

**CONTINUOUS PRODUCTION OF MICROCELLULAR FOAMS**

DISSERTATION

Presented in Partial Fulfillment of the Requirements for  
the Degree Doctor of Philosophy in the Graduate  
School of The Ohio State University

By

Xiangmin Han, M.E.

\* \* \* \*

The Ohio State University

2003

Dissertation Committee:

Professor K. W. Koelling, Adviser

Professor D. L. Tomasko

Professor L. James Lee

Approved by

---

Adviser

Chemical Engineering Graduate Program

## **ABSTRACT**

Microcellular foams, characterized by cell size smaller than 10  $\mu\text{m}$  and cell density larger than  $10^9$  cells/cm<sup>3</sup>, are drawing increased attention. It has been shown that by keeping the foam cell size uniformly less than 10  $\mu\text{m}$ , one can reduce the material usage and improve mechanical properties simultaneously. In this study, supercritical carbon dioxide (CO<sub>2</sub>), a potential replacement of the traditional foaming agents (chlorofluorocarbons), is applied to produce microcellular foams of polystyrene and polystyrene nanocomposites continuously on a two-stage single screw extruder.

The contraction flow in the extrusion die is simulated with the FLUENT computational code to predict profiles of pressure, temperature, viscosity, and velocity. The location of nucleation onset is determined based on the pressure profile and equilibrium solubility. It is shown that a high CO<sub>2</sub> concentration or a high foaming temperature induces an earlier nucleation near the die entrance. The pressure profile and the position of nucleation onset are then correlated to the cell nucleation and growth, which helps understand the effects of operating conditions on the cell structure qualitatively.

To perform these simulations, the necessary physical properties of the CO<sub>2</sub>/polymer system, such as the viscosity and solubility, are characterized and fitted to various theoretical models, which are latterly substituted into the flow simulation. The solubility is measured using a volumetric method at 120 and 200°C. The Sanchez-Lacombe equation of state is applied to represent the phase equilibrium. Shear viscosities of polystyrene at different temperatures and pressures with and without CO<sub>2</sub> are measured using both parallel-plate and slit die rheometers. Effects of temperature, pressure, and CO<sub>2</sub> content on the shear viscosity are analyzed by the traditional shifting technique and further explained based on the free volume theory.

Systematic experiments are performed to verify effects of three key operating conditions: CO<sub>2</sub> content, pressure drop or pressure drop rate, and foaming temperature on the foam cell structure. Experimental results are compared with simulations and both are used to gain insight into the foaming process. When the pressure drop in the die is larger than 16 MPa and the pressure drop rate is around 10<sup>9</sup> Pa/sec at a foaming temperature of 160°C, closed microcells with cell size less than 10 μm and cell density greater than 10<sup>9</sup> cells/cm<sup>3</sup> are successfully extruded. Studies in operating conditions exhibits that a higher pressure drop or pressure drop rate results in smaller cells and greater cell density. Below the CO<sub>2</sub> solubility, cell size decreases and cell density increases with an increase of CO<sub>2</sub> concentration, which is also favorable for producing open cell foams. Die temperature affects both cell size and cell structure (open or closed).

To obtain microcellular foams with even smaller cell size and larger cell density, and to create versatile properties, nanocomposite foams were produced. The resulting foam structure is compared with that of pure polystyrene and polystyrene/talc composite. At a screw rotation speed of 10 rpm and a die temperature of 200°C, the addition of a small amount (i.e., 5 wt.%) of intercalated nano-clay greatly reduces cell size from 25.3 to 11.1  $\mu\text{m}$  and increases cell density from  $2.7 \times 10^7$  to  $2.8 \times 10^8$  cells/cm<sup>3</sup>. Once exfoliated, the nanocomposite exhibits the highest cell density ( $1.5 \times 10^9$  cells/cm<sup>3</sup>) and smallest cell size (4.9  $\mu\text{m}$ ) at the same particle concentration. Open cell structure was observed in intercalated nanocomposite foams at high clay concentration. The structure of heterogeneous nucleated cells is affected by the orientation and dispersion of the clay. Nanocomposite foams provide superior performance, including high tensile modulus, better surface quality, enhanced fire retardance, and improved barrier properties. The effects of nano-clay dispersion on the polymer melt rheology are discussed. Combining nano-clay compounding with supercritical CO<sub>2</sub> foaming provides a new technique for the design and control of foam structure and property.

Dedicated to my family

## ACKNOWLEDGMENTS

I would like to thank my advisers, Dr. Kurt W. Koelling, Dr. David L. Tomasko, and Dr. L. James Lee for their intellectual support, encouragement, and advice on my research. Their insight and guidance has made this dissertation possible.

I thank Paul Green, Carl Scott, Leigh Evrard, and Chris Gecik for their exceptional help with the various equipment and repairs that took place over the past five years. I also wish to thank Cameron Begg in the Campus Electron Optics Facility for his help in SEM. I would like to thank Roland Loh from Owens-Corning for our cooperation.

I would also like to thank former group members, Mark Elkovitch, Jose Garcia, Jason Vititoe, and Adam Baxter, for their technical support and valuable discussion, and all current group members, especially Changchun Zeng, Hongbo Li, and Max Wingert.

I thank my parents, sisters, and brothers for their continued support and encouragement. Finally, I would like to thank my wife, Jun Luo, for her understanding, patience, support and encouragement.

## VITA

February 6, 1973 ..... Born – Laiwu, China

July, 1994 ..... B. E. Chemical Engineering  
Tsinghua University  
Beijing, China

July, 1997 ..... M. E. Chemical Engineering  
Tsinghua University  
Beijing, China

1997- present ..... Graduate Teaching and Research  
Assistant, Chemical Engineering  
The Ohio State University

## PUBLICATIONS

X. Han, K. W. Koelling, D. L. Tomasko, and L. J. Lee, Continuous Microcellular Polystyrene Foam Extrusion with Supercritical CO<sub>2</sub>. *Polymer Engineering and Science*, 42(11), 2094-2106, 2002.

X. Han, C. Zeng, K. W. Koelling, D. L. Tomasko, and L. J. Lee, Polymer Nanocomposite Foams by Using Supercritical CO<sub>2</sub>, PPS-18, Guimaraes, Portugal, 6/2002.

X. Han, C. Zeng, K. W. Koelling, D. L. Tomasko, and L. J. Lee, Polymer Nanocomposite Foams Prepared by Microfabrication and Supercritical Fluid Foaming Technology, MRS Spring meeting, San Francisco, California, 4/2002.

X. Han, C. Zeng, K. W. Koelling, D. L. Tomasko, L. J. Lee, Processing and Cell Structure of Nano-Clay Modified Microcellular Foams. SPE-ANTEC, 1915-19, 2002.

X. Han, K. W. Koelling, D. L. Tomasko, L. J. Lee, Influence of Solubility and Viscosity in the Polystyrene/CO<sub>2</sub> Microcellular Foaming Extrusion. SPE-ANTEC, 1910-14, 2002.

X. Han, K. W. Koelling, D. L. Tomasko, L. J. Lee, Process Optimization in Microcellular Foam Extrusion. SPE-ANTEC, 1741-45, 2001.

X. Han, K. W. Koelling, D. L. Tomasko, L. J. Lee, Extrusion of Polystyrene Microcellular Foam with Supercritical CO<sub>2</sub>. SPE-ANTEC, 1857-61, 2000.

X. Han, P. Hu, R. Lu, S. Guo, Study on Blend of Chloroprene Rubber/Ultrahigh-Molecular-Weight PVC. Synthesized Rubber Industry, 20(3), 174, 1997.

## **FIELDS OF STUDY**

Major Field: Chemical Engineering  
Polymer Engineering and Science  
Polymer Processing and Composites  
Rheology  
Supercritical Fluids

## TABLE OF CONTENTS

	<u>Page</u>
Abstract .....	ii
Dedication .....	v
Acknowledgments .....	vi
Vita .....	vii
List of Tables .....	xv
List of Figures .....	xvi
Chapters:	
1. Introduction .....	1
1.1. Microcellular Thermoplastic Foams .....	1
1.2. Supercritical CO <sub>2</sub> as the Foaming Agent .....	3
1.3. Scope and Objectives of Research .....	4
1.3.1. Viscosity Characterization .....	5
1.3.2. Measurement of CO <sub>2</sub> Solubility in Polystyrene .....	5
1.3.3. Computational Simulation of the Foaming Extrusion .....	6
1.3.4. Relationship between Operating Conditions and Cell Structure .....	6
1.3.5. Nanocomposite Foams .....	7
1.4. Outline .....	8

2. Literature Review .....	9
2.1. Polymeric Foams .....	9
2.2. Microcellular Plastic Foams .....	13
2.2.1. Procedure .....	14
2.2.1.1. Batch Foaming .....	15
2.2.1.2. Semicontinuous Foaming .....	16
2.2.1.3. Continuous Extrusion Foaming .....	17
2.2.1.4. Injection Molding Foaming .....	18
2.2.2. Overview of Microcellular Polymers .....	20
2.2.3. Mechanical Properties .....	25
2.2.3.1. Impact Strength .....	25
2.2.3.2. Fatigue Life .....	26
2.2.3.3. Tensile Strength .....	27
2.2.4. Foam Structure and Foaming Conditions .....	27
2.2.4.1. Foaming Pressure .....	28
2.2.4.2. Gas Concentration .....	28
2.2.4.3. Foaming Temperature .....	28
2.2.4.4. Foaming Time and Shear Stress .....	34
2.2.5. Innovations and Applications .....	35
2.2.5.1. Ultramicrocellular Foams .....	35
2.2.5.2. Nanocomposite Foams .....	35
2.2.5.3. Scaffolds for Tissue Engineering .....	36
2.2.5.4. Open-Cell Foams .....	37
2.2.5.5. On-Line CO <sub>2</sub> Concentration Detection .....	39
2.3. Supercritical Carbon Dioxide and Its Interactions with Polymers .....	40
2.3.1. Supercritical Carbon Dioxide .....	40
2.3.2. Interaction between Supercritical Carbon Dioxide and Polymers .....	41
2.3.3. Solubility of CO <sub>2</sub> in Polymers (S-L EOS) .....	43
2.3.3.1. Solubility of CO <sub>2</sub> in Polystyrene .....	43
2.3.3.2. Sanchez-Lacombe Equation of State (S-L EOS) .....	44
2.3.4. Glass Transition and Crystallization .....	46
2.3.4.1. Glass Transition Temperature (T <sub>g</sub> ) .....	46
2.3.4.2. Crystallization .....	48
2.3.5. Diffusivity and Interfacial Tension .....	49
2.3.5.1. Diffusivity .....	49
2.3.5.2. Interfacial Tension .....	50
2.3.6. Viscosity Reduction .....	50
2.3.6.1. Shear Viscosity Measurement .....	51
2.3.6.2. Shear Viscosity Prediction .....	54
2.3.6.3. Extensional Viscosity Measurement .....	56

2.4. Foam Cell Nucleation and Growth .....	57
2.4.1. Cell Nucleation .....	58
2.4.1.1 Homogeneous Nucleation Theory .....	60
2.4.1.2 Heterogeneous nucleation theory .....	61
2.4.1.3 Other Theoretical Considerations .....	63
2.4.2. Cell Growth .....	63
2.4.2.1. Modeling .....	64
2.4.2.2. Effect of Transient Extensional Strain Hardening Viscosity on Bubble Growth .....	67
2.4.3. Cell Coalescence .....	68
3. Continuous Microcellular polystyrene Foam Extrusion with supercritical CO <sub>2</sub> .....	82
3.1. Introduction .....	82
3.1.1. Art and Science of Microcellular Foaming Polymers .....	82
3.1.2. Continuous Production Essential for Economic Viability .....	83
3.2. Experimental .....	87
3.3. Computations .....	89
3.3.1. Sanchez-Lacombe Calculation of CO <sub>2</sub> Saturation Solubility as A Function of Temperature and Pressure .....	89
3.3.2. FLUENT Simulation of Contraction Flow in Die .....	90
3.4. Results and Discussion .....	91
3.4.1. Simulated Pressure, Temperature, Viscosity, and Velocity Profiles in Die .....	91
3.4.2. Calculated Rate of Pressure Drop and Pressure in the Die as a Function of Position .....	92
3.4.3. Calculated Solubility of CO <sub>2</sub> in PS and T <sub>g</sub> as a Function of CO <sub>2</sub> Concentration. ....	93
3.4.4. Calculated Position of Nucleation Onset .....	95
3.4.5. Calibration of Experimental Mass Flow Rate and Pressure .....	96
3.4.6. Effect of CO <sub>2</sub> Content on Cell Size and Cell Density .....	97
3.4.7. Effect of Die Pressure on Cell Nucleation .....	98
3.5. Conclusions .....	99

4. Effect of Die Temperature on The Morphology of Microcellular Foams .....	114
4.1. Introduction .....	114
4.1.1. Effects of Foaming Temperature in a Batch Foaming Process.....	116
4.1.2. Effects of Foaming Temperature in a Continuous Foaming Extrusion Process .....	120
4.2. Experimental .....	122
4.2.1. Setup and Procedure .....	122
4.2.2. Foam Structure Analysis .....	123
4.3. Flow Simulation in the Die: Effect of Temperature .....	124
4.4. Results and Discussion .....	125
4.4.1. Simulated Pressure Profile and Nucleation Position .....	125
4.4.2. Effect of Temperature on Nucleation Rate Calculated from the Classical Nucleation Theory .....	127
4.4.3. Effect of Temperature on Mass Flow Rate and Pressure .....	129
4.4.4. Effect of Die Temperature on Cell Size and Cell Density .....	130
4.4.5. Effect of Die Temperature on Cell Morphology .....	132
4.4.6. Effect of Temperature and CO <sub>2</sub> Concentration on Cell Coalescence .....	134
4.5. Conclusions .....	135
5. Extrusion of Polystyrene Nanocomposite Foams with Supercritical CO <sub>2</sub> .....	152
5.1. Introduction .....	152
5.2. Experimental .....	156
5.2.1. Synthesis and Characterization of Nanocomposites .....	156
5.2.2. Preparation and Analysis of Nanocomposite Foams .....	157
5.3. Results and Discussion .....	160
5.3.1. Intercalated and Exfoliated PS/Clay Nanocomposites .....	160
5.3.2. Continuous Foaming Extrusion .....	161
5.3.2.1. Effects of Clay Dispersion .....	162
5.3.2.2. Effects of Clay Concentration .....	164
5.3.2.3. Effect of Operating Conditions .....	166
5.3.3. Cell Nucleation and Growth .....	167
5.3.4. Properties of Nanocomposite Foams .....	168
5.3.5. Shear Viscosity of PS Nanocomposites .....	170
5.4. Conclusions .....	170

6. Influences of Solubility and Viscosity on the Polystyrene/CO <sub>2</sub> Microcellular Foaming Extrusion .....	189
6.1. Introduction .....	189
6.1.1. Solubility Measurement of CO <sub>2</sub> in PS .....	189
6.1.2. Viscosity Characterization of CO <sub>2</sub> /PS .....	191
6.2. Experimental .....	193
6.2.1. Materials .....	193
6.2.2. Measurement of Solubility by Volumetric Method .....	194
6.2.3. Shear Viscosity Characterization .....	195
6.2.4. Microcellular Foaming and Cell Structure Analysis .....	196
6.3. Results and Discussion .....	197
6.3.1. Solubility of CO <sub>2</sub> in Pure Polystyrene .....	197
6.3.2. Shear Viscosity of PS/CO <sub>2</sub> Solution .....	199
6.3.2.1. Viscosity Measurement .....	199
6.3.2.2. Viscosity Prediction .....	200
6.3.3. Comparison Between Three Polystyrenes .....	202
6.3.4. Effect of Nano-clay on CO <sub>2</sub> Sorption and Viscosity .....	203
6.3.4.1. CO <sub>2</sub> Sorption of PS/Nano-Clay Composites .....	204
6.3.4.2. Shear Viscosity of PS/20A Nanocomposite .....	205
6.4. Conclusions .....	206
7. Conclusions and Recommendations .....	231
7.1. Conclusions .....	231
7.2. Recommendations .....	236
References .....	239
Appendices .....	260
A. Mixing Rules of the Sanchez-Lacombe Equation of State for a Binary System .....	260
B. Fortran Code to Determine $\delta_{ij}$ by Knowing Solubility .....	263
C. Fortran Code to Compute Solubility by Knowing $\delta_{ij}$ .....	270
D. Development of Viscosity Prediction Model .....	276
E. Design of the Capillary Foaming Die .....	279

F. Flow Simulation in the Die: Effect of Temperature .....	285
F.1. Computations .....	286
F.1.1. Fluent Simulation of Contraction Flow .....	286
F.1.2. Calculation of CO <sub>2</sub> Solubility .....	287
F.2. Flow Simulation in the Die .....	288
F.2.1. Pressure Drop .....	288
F.2.2. Position of Nucleation Onset .....	289
F.2.3. Consistency between Simulation and Experimental Observations .....	290
F.3. Estimation of Critical Size of Nucleated Cells .....	292
G. Microcellular Foam Extrusion with Fillers: Talc and Alumoxane Nano-Particle .....	301
G.1. Talc .....	302
G.2. Alumoxane Nano-Particle .....	303
G.3. Formation of Bimodal Cell Size Distribution .....	303
G.4. Shear Viscosity .....	304
H. Foam Extrusion with H142B/22 .....	317
I. Batch Foaming .....	327

## LIST OF TABLES

<u>Table</u>	<u>Page</u>
2.1. Common Extrusion Processes .....	69
2.2. Comparison of different methods to determine solubility of CO <sub>2</sub> in polymers .....	70
2.3. Characteristic Sanchez-Lacombe EOS parameters for CO <sub>2</sub> /PS system ...	71
3.1. Parameters in the Carreau model (175°C) .....	101
4.1. Parameters in the Carreau model (5 wt.% CO <sub>2</sub> ) .....	138
5.1. Void fraction of PS nanocomposite foams extruded at 4 wt.% CO <sub>2</sub> and 200°C (calculated based on the cell size and cell density in Figure 5.7 and 5.9) .....	172
6.1. Parameters in the viscosity prediction model .....	208
6.2. Shear viscosity prediction .....	209
F.1. Parameters in the Carreau model .....	293
F.2. Influence of the operation conditions on the pressure drop rate and the nucleation position (the up arrow means an increase in the specific value or a earlier nucleation) .....	294

## LIST OF FIGURES

<u>Figure</u>	<u>Page</u>
2.1. Microcellular foaming .....	72
2.2. Microcellular foaming by a batch process .....	73
2.3. Izod impact strength as a function of relative density compared with the unfoamed PC samples .....	74
2.4. Stress-strain curves for unfoamed and microcellular PC at different relative densities.....	75
2.5. Liquid-vapor phase diagram of CO <sub>2</sub> .....	76
2.6. Solubility of CO <sub>2</sub> in polystyrene (the thick lines are fitted by Sanchez-Lacombe model) .....	77
2.7. T <sub>g</sub> reduction of PS with sorption of CO <sub>2</sub> .....	78
2.8. The diffusion coefficient at three temperatures (100, 150, and 200°C) ...	79
2.9. Dependence of interfacial tension between PS/CO <sub>2</sub> and CO <sub>2</sub> on pressure .....	80
2.10. Schematic diagram of bubble growth in a liquid shell .....	81
3.1. Experimental setup for microcellular foaming .....	102
3.2. Saturation CO <sub>2</sub> content at different pressures and temperatures (the thick line on the surface is the T <sub>g</sub> ) .....	103

3.3. Simulation results for distributions of (a) Pressure (Max = $1.957 \times 10^7$ Pa, min = $-1.250 \times 10^6$ Pa); (b) Temperature (Max = 459.5 K, min = 448.2 K); (c) Viscosity (Max = 334.4 Pa.sec, min = $1.720 \times 10^{-5}$ Pa.sec); and (d) Velocity (Max = 1.058 m/s, min = 0 m/s) when the die temperature is 175°C and the CO <sub>2</sub> content is 5.1 wt%. The horizontal direction to the right is the flow direction. The die insert contains two sections: the guiding hollow tube and the capillary nozzle	104
3.4. Profiles of pressure and saturation CO <sub>2</sub> weight fraction along the die nozzle with different CO <sub>2</sub> content (1 and 5 wt.%) at the same die temperature (175°C). Points a and d: weight fraction that the solution becomes saturated; b and e: local pressure when the solution becomes saturated; c and f: nucleation onset position	105
3.5. The influence of CO <sub>2</sub> content on the pressure drop and pressure drop rate	106
3.6. Effects of CO <sub>2</sub> content and die temperature on the nucleation onset position and the cell growth length	107
3.7. Pressure drop rate in the die as a function of CO <sub>2</sub> content at different screw rotation speed (die temperature: 180°C)	108
3.8. Cell morphology influenced by CO <sub>2</sub> content: (a) 1%, 12.1 MPa; (b) 2.5%, 11.3 MPa; (c) 4%, 11.4 MPa; (d) 6%, 11.5 MPa; (e) 8 wt%, 11.3 MPa (die temperature: 180°C; screw rotation speed: 10 rpms)	109
3.9. Cell size and cell density affected by CO <sub>2</sub> content (foaming temperature: 180°C; screw rotation speed: 10 rpm)	110
3.10. Cell morphology influenced by pressure change: (a) 10; (b) 15; (c) 20; (d) 25; (e) 30 rpms (die temperature: 180°C; CO <sub>2</sub> content: 2.5 wt%)	111
3.11. Relation between cell size, cell density, and pressure drop at 180°C with the same CO <sub>2</sub> content (2.5 wt%)	112
3.12. Relation between cell size, cell density, and pressure drop rate at 180°C with the same CO <sub>2</sub> content (2.5 wt%)	113
4.1. Relationship between parameters in a continuous extrusion foaming process	139
4.2. Experimental setup of microcellular foaming extrusion	140

4.3. Profiles of pressure and saturation CO <sub>2</sub> weight fraction along the die nozzle at different die temperatures (150 and 175°C) and same CO <sub>2</sub> concentration (5 wt.%). Points a and d: saturation concentration; b and e: local pressure when the solution becomes saturated; c and f: nucleation onset position .....	141
4.4. Nucleation rate calculated from the classical nucleation theory by changing ± 1% of the mean value of four variables .....	142
4.5. Calibration of melt flow rate .....	143
4.6. Die pressure drop rate at different screw rotation speeds .....	144
4.7. SEM micrographs of foam cells at 30 rpm, 1 wt.% CO <sub>2</sub> , and different foaming temperatures: (a) 240°C (dp=9.9 MPa, dp/dt=6.1×10 <sup>8</sup> Pa/s); (b) 220°C (dp=11.3 MPa, dp/dt=9.2×10 <sup>8</sup> Pa/s); (c) 200°C (dp=12.6 MPa, dp/dt=9.6×10 <sup>8</sup> Pa/s); (d) 180°C (dp=13.8 MPa, dp/dt=1.2×10 <sup>9</sup> Pa/s); (e) 160°C (dp=17.3 MPa, dp/dt=2.0×10 <sup>9</sup> Pa/s) .....	145
4.8. (a) Relationship between cell size and pressure drop <i>rate</i> at different foaming temperatures with the same CO <sub>2</sub> content (1 wt%). (b) Relationship between cell density and pressure drop <i>rate</i> at different foaming temperatures with the same CO <sub>2</sub> content (1 wt%) .....	146
4.9. Why the pressure drop rate (dP/dt) is important .....	148
4.10. SEM pictures of polystyrene samples foamed at different temperatures at 10 rpm and 1 wt.% CO <sub>2</sub> : (a) 240°C (dp=6.7 MPa, dp/dt=2.5×10 <sup>8</sup> Pa/s); (b) 220°C (dp=7.9 MPa, dp/dt=2.8×10 <sup>8</sup> Pa/s); (c) 200°C (dp=9.7 MPa, dp/dt=3.5×10 <sup>8</sup> Pa/s); (d) 180°C (dp=12.1 MPa, dp/dt=3.8×10 <sup>8</sup> Pa/s); (e) 160°C (dp=15.0 MPa, dp/dt=4.6×10 <sup>8</sup> Pa/s); and (f) 140°C (dp=23.6 MPa, dp/dt=5.7×10 <sup>8</sup> Pa/s) .....	149
4.11. Foam density change with foaming temperature(1 wt.% CO <sub>2</sub> ) .....	150
4.12. SEM pictures of polystyrene samples foamed at 160°C: (a) 1 wt%, 10 rpm (dp=15.0 MPa, dp/dt=4.6×10 <sup>8</sup> Pa/s); (b) 1 wt%, 20 rpm (dp=16.1MPa, dp/dt=1.0×10 <sup>9</sup> Pa/s); (c) 1 wt%, 30 rpm (dp=17.3 MPa, dp/dt=2.0×10 <sup>9</sup> Pa/s); (d) 6 wt%, 10 rpm (dp=14.5 MPa, dp/dt=4.2×10 <sup>8</sup> Pa/s); (e) 6 wt%, 20 rpm (dp=16.2 MPa, dp/dt=1.2×10 <sup>9</sup> Pa/s); and (f) 6 wt%, 30 rpm (dp=16.9 MPa, dp/dt=1.8×10 <sup>8</sup> Pa/s) .....	151

5.1. Experimental setup of microcellular foaming extrusion .....	173
5.2. Wide angle X-ray diffraction (XRD) patterns: (a) intercalated PS/5 wt.% 20A nanocomposite; (b) exfoliated PS/5 wt.% MHABS nanocomposite .....	174
5.3. TEM images: (a) intercalated PS/5 wt.% 20A nanocomposite; (b) exfoliated PS/5 wt.% MHABS nanocomposite .....	175
5.4. Changes of pressure drop (a) and pressure drop rate (b) at different melt flow rates (die temperature: 200°C; CO <sub>2</sub> concentration: 4 wt.%) .....	176
5.5. Foam structure measured by SEM: (a) PS/5 wt.% talc (dP = 11.03 MPa, dP/dt = 4.75 × 10 <sup>8</sup> Pa/sec), (b) PS/5 wt.% 20A (dP = 11.53 MPa, dP/dt = 4.90 × 10 <sup>8</sup> Pa/sec), and (c) PS/5 wt.% MHABS (dP = 15.10 MPa, dP/dt = 8.04 × 10 <sup>8</sup> Pa/sec). Foaming conditions: die temperature: 200°C; CO <sub>2</sub> concentration: 4 wt.%; screw rotation speed: 10 rpm .....	178
5.6. Interaction of foam cells and particles measured by TEM: (a) PS/5 wt.% talc, (b) PS/5 wt.% 20A, and (c) PS/5 wt.% MHABS. The foaming conditions are the same as those in Figure 5.5 .....	179
5.7. Effect of clay concentration on the cell size and cell density (die temperature: 200°C; CO <sub>2</sub> concentration: 4 wt.%; screw rotation speed: 20 rpm) .....	180
5.8. Cell morphology of PS/20A nanocomposite foams at 200°C, 4 wt.% CO <sub>2</sub> , 20 rpm, and different clay concentration: (a) 0 wt.% (dP = 12.7 MPa, dP/dt = 1.15 × 10 <sup>9</sup> Pa/sec); (b) 2.5 wt.% (dP = 3.2 MPa, dP/dt = 1.14 × 10 <sup>9</sup> Pa/sec); (c) 5 wt.% (dP = 12.8 MPa, dP/dt = 1.10 × 10 <sup>9</sup> Pa/sec); and (d) 7.5 wt.% (dP = 12.7 MPa, dP/dt = 1.07 × 10 <sup>9</sup> Pa/sec). .....	181
5.9. Effect of pressure drop rate on (a) foam cell size and (b) foam cell density (die temperature: 200°C; CO <sub>2</sub> concentration: 4 wt.%) .....	182
5.10. Relationship between cell size, cell density, and void fraction .....	184
5.11. Reduced tensile modulus of different foamed samples extruded at 200°C and 4 wt.% CO <sub>2</sub> (PS and PS/5 wt.% MHABS: 10 rpm; PS/5 wt.% talc and PS/5 wt.% 20A: 20 rpm) .....	185
5.12. Burning test of (a) PS foam sample, and (b) PS/5 wt.% 20A nanocomposite foam sample .....	186

5.13. CO <sub>2</sub> desorption from PS and PS nanocomposites at room temperature .....	187
5.14. Shear viscosity of PS and PS/clay nanocomposites at 200°C without CO <sub>2</sub> .....	188
6.1. Volumetric method for solubility measurement .....	210
6.2. Side view of the slit die used for viscosity characterization under pressure .....	211
6.3. Sorption curve of CO <sub>2</sub> in polystyrene at 120°C and 15 MPa .....	212
6.4. Solubility data of CO <sub>2</sub> in polystyrene (solid lines: fitting curves using the Sanchez-Lacombe equation of state) .....	213
6.5. (a) Shear viscosities of polystyrene at different temperatures; (b) master curve shifted to T <sub>g</sub> .....	214
6.6. Effect of backpressure on the shear viscosity of pure polystyrene at 180°C (PS-rms means the measurement was performed on RMS 800) .....	216
6.7. (a) Effect of CO <sub>2</sub> content on the shear viscosity of polystyrene at 180°C; (b) Master curve shifted to 0%; and (c) Shift factors .....	217
6.8. Viscosity prediction at different temperatures (a), pressures (b), and CO <sub>2</sub> concentrations (c) .....	220
6.9. Shear viscosity of three polystyrene resins at 200°C without CO <sub>2</sub> and backpressure .....	223
6.10. Cell size (solid symbols) and cell density (open symbols) versus pressure drop (a) and pressure drop rate (b) at 200°C for three polystyrenes with different shear viscosities .....	224
6.11. Cell morphology of the three polystyrenes at 200°C and different screw rotation speeds: (a) high viscosity, 10 rpm; (b) medium viscosity, 10 rpm; (c) low viscosity, 10 rpm; (d) high viscosity, 30 rpm; (e) medium viscosity, 30 rpm; and (f) low viscosity, 30 rpm .....	226
6.12. CO <sub>2</sub> desorption from PS and PS nanocomposites .....	227

6.13. Shear viscosity of PS and PS/clay nanocomposites at 180°C with (a) 1 wt.%; (b) 2 wt.%; and (c) 3 wt.% CO <sub>2</sub> .....	228
E.1. Pressure drop and pressure drop rate with different diameter of the capillary die (PS, Power Law Model: $m=17,420 \text{ Pa}\cdot\text{s}^{0.30}$ , $n=0.30$ , length $L=10 \text{ mm}$ , $q = 1 \text{ lb/hr}$ ) .....	282
E.2. Pressure drop and pressure drop rate with different flow rate (PS, Power Law Model: $m=17,420 \text{ Pa}\cdot\text{s}^{0.30}$ , $n=0.30$ , $L=10 \text{ mm}$ , $D = 0.5 \text{ mm}$ ) .....	283
E.3. Dimension of the designed capillary die .....	284
F.1. Geometry and grid in the Fluent simulation .....	295
F.2. Profiles of pressure and saturation CO <sub>2</sub> weight fraction along the die nozzle at different die temperatures (150 and 175°C) and same CO <sub>2</sub> concentration (5 wt.%). Points a and d: saturation concentration; b and e: local pressure when the solution becomes saturated; c and f: nucleation onset position .....	296
F.3. The influence of CO <sub>2</sub> content on the pressure drop and pressure drop rate (5 wt.% CO <sub>2</sub> ) .....	297
F.4. Effects of die temperature on the nucleaion onset position and the cell growth length (5 wt.% CO <sub>2</sub> ) .....	298
F.5. Profiles of pressure, solubility, and glass transition temperature in the die during flow .....	299
F.6. Estimation of critical cell size at different supersaturation pressures .....	300
G.1. TEM pictures of PS foams with (a) 5 wt.% alumoxane nano-particle and (b) 5 wt.% talc at 200°C, 4 wt.% CO <sub>2</sub> and 20 rpm (The black dots in the pictures are the filler particles) .....	305
G.2. Cell size and cell density with different talc concentration at 200°C, 4 wt.% CO <sub>2</sub> and 20 rpm .....	306
G.3. SEM pictures of PS foams with different talc concentration at 200°C, 4 wt.% CO <sub>2</sub> and 20 rpm: (a) 0, (b) 0.5, (c) 2.5, (d) 5, and (e) 7.5 wt.% .....	307

G.4. SEM pictures of PS foams with 5 wt.% talc at 200°C, 4 wt.% CO <sub>2</sub> and different screw rotation speeds: (a) 10, (b) 15, (c) 20, (d) 25, and (e) 30 rpm .....	308
G.5. Comparison of PS foams with 5 wt.% of different fillers at 200°C, 4 wt.% CO <sub>2</sub> (except one data point of MHABS is at 240°C): (a) cell size vs. pressure drop, (b) cell density vs. pressure drop, (c) cell size vs. pressure drop rate, and (d) cell density vs. pressure drop rate .....	309
G.6. SEM pictures of PS foams with 5 wt.% alumoxane at 200°C, 4 wt.% CO <sub>2</sub> and different screw rotation speeds: (a) 10, (b) 15, (c) 20, (d) 25, and (e) 30 rpm .....	313
G.7. SEM pictures of PS foam with (a) 5 wt.% alumoxane and (b) 5 wt.% talc at 200°C, 4 wt.% CO <sub>2</sub> and different magnifications .....	314
G.8. SEM pictures of PS foam with (a) 5 wt.% 20A and (b) 5 wt.% MHABS at 200°C, 4 wt.% CO <sub>2</sub> and different magnifications .....	315
G.9. Shear viscosity of PS with different fillers at 200°C .....	316
H.1. Experimental setup for PS foam extrusion on a twin-screw extruder by using H142B/22 as the foaming agent: (a) entire setup, and (b) enlargement of the foaming die and shaping die .....	320
H.2. Comparison between CO <sub>2</sub> and H142B/22 as foaming agent .....	321
H.3. Comparison of cell structure between CO <sub>2</sub> and H142B/22 as foaming agent .....	322
H.4. SEM pictures of PS foam with talc and nano-clay by using H142B/22 as the foaming agent: (a) 0.8 wt.% talc, (b) 0.5 wt.% 15A, and (c) 2.5 wt.% 15A (pilot plant products of Owens-Corning) .....	324
H.5. Cell size and cell density of PS foam with talc and nano-clay by using H142B/22 as the foaming agent (pilot plant products of Owens-Corning) .....	325
H.6. Strut structure of PS foam by using H142B/22 as the foaming agent: (a) PS/1% talc/10% H143B/22, and (b) PS/0.8 wt.% talc (pilot plant product of Owens-Corning) .....	326

I.1. Batch foaming at 120°C and 2000 psi saturation pressure to determine the effect of nano-clay dispersion on PS nanocomposite foams by using CO <sub>2</sub> as foaming agent: (a) PS, (b) PS/5 wt.% 20A intercalated nanocomposite, and (c) PS/5 wt.% MHABS exfoliated nanocomposite ....	330
I.2. Cell size and cell density of different PS nanocomposite foams (batch foaming at 120°C and 2000 psi saturation pressure by using CO <sub>2</sub> as foaming agent) .....	331
I.3. Batch foaming at 120°C and 2000 psi saturation pressure to determine the effect of nano-clay dispersion on PMMA nanocomposite foams by using CO <sub>2</sub> as foaming agent: (a) PMMA, (b) PMMA/5 wt.% 20A intercalated nanocomposite, and (c) PMMA/5 wt.% MHABS exfoliated nanocomposite .....	332
I.4. Cell size and cell density of different PMMA nanocomposite foams (batch foaming at 120°C and 2000 psi saturation pressure by using CO <sub>2</sub> as foaming agent) .....	333

## **CHAPTER 1**

### **INTRODUCTION**

#### **1.1. Microcellular Thermoplastic Foams**

Polymeric foams are commonly considered standard consumer products such as packaging, insulation, cushions, and absorbents. In fact, foams are also used in “high-tech” applications such as scaffolds for tissue engineering. Because of so many applications, research in foams is drawing increased attention. Polymer foaming technology requires the knowledge base of several different scientific fields including polymer processing, thermodynamics, rheology, fluid dynamics, mass and heat transfer, and equipment design. Although basic principles governing the foaming process are understood, the design of a foaming process is still mainly experimental. As a result, researchers are interested in fully understanding the governing parameters in both foam cell nucleation and growth.

Polymeric foams are found in many applications due to their numerous excellent properties, including lightweight, good strength-to-weight ratio, superior insulation abilities, and energy or material absorbing ability. Based on the size of fully-grown cells in a cellular polymer, polymeric foams can be classified as macrocellular ( $>100\ \mu\text{m}$ ), microcellular ( $1\sim 100\ \mu\text{m}$ ), ultra-microcellular ( $0.1\sim 1\ \mu\text{m}$ ), and nanocellular ( $0.1\sim 100\ \text{nm}$ ) foams.

Traditionally, microcellular foams are characterized as plastic foams with cell size smaller than 10 microns and cell density (number of cells per unit volume) larger than  $10^9\ \text{cells}/\text{cm}^3$ . This definition is still being debated because it is difficult to relate the properties of polymer foams directly to the cell size and cell density. However, it has been found that microcellular foams can improve some mechanical properties, such as impact strength [1]. Therefore, by applying the microcellular foaming technique, one can produce lightweight polymeric products with high mechanical strength. Microcellular foams can greatly save the material usage and are thus economically favorable. It is a good choice to apply microcellular foams when making thin-wall products, such as bottles, sheets, pipes, and films. Furthermore, the cellular structure itself may have unique applications, e.g., capsulation, filtration, and absorption.

In this dissertation, we focus on a physical foaming procedure in which a physical foaming agent, supercritical carbon dioxide ( $\text{CO}_2$ ), is applied to a batch or a continuous extrusion foaming process. The foaming procedure can be divided into three steps: 1) mixing, the formation of a homogeneous solution composed of the foaming agent and polymer melt; 2) cell nucleation, the phase separation induced by a thermodynamic instability, usually a temperature increase or a pressure decrease, to form

nuclei with critical size; 3) cell growth, the spontaneous expansion of the nuclei with critical size controlled by mass and heat transfer, fluid dynamics, and rheological properties.

## **1.2. Supercritical CO<sub>2</sub> as the Foaming Agent**

Since the traditional foaming agent, chlorofluorocarbons (CFCs), are proven to contribute to the destruction of the Earth's ozone layer and will be gradually eliminated as a foaming agent in the coming years (2010 in US), replacement technologies have been under intensive investigation. Three choices currently have the highest potential: hydrogenated chlorofluorocarbons/fluorocarbons, hydrocarbons/alcohols, and inert gases (CO<sub>2</sub>, N<sub>2</sub>, argon, or water). Among these, CO<sub>2</sub> seems to be one of the most favorable replacements because it is environmentally benign, non-combustible, chemically stable and economically low-cost. More important, CO<sub>2</sub> exhibits relatively high solubility in polymers compared with other inert gases, and correspondingly shows high nucleation ability.

The critical point of CO<sub>2</sub> is relatively low, 31.0°C and 7.38 MPa, above which CO<sub>2</sub> is at the supercritical state with liquid-like density and gas-like diffusivity and viscosity. Supercritical CO<sub>2</sub> has a lot of potential applications in polymer processing, such as extraction, particle formation, surface modification, coating, impregnation, blending, and foaming. Therefore, study of the interaction between CO<sub>2</sub> and polymers, including the phase behavior and the plasticization effect, becomes important in guiding the experimental design.

The high-pressure operation and the fast gas escape during the foaming process are two major challenges when CO<sub>2</sub> is used as the foaming agent. Compared with these difficulties, the advantages of CO<sub>2</sub> are greater in number, especially for the microcellular foaming process, in which high volume expansion is not emphasized.

### **1.3. Scope and Objectives of Research**

In this study, the continuous production of polystyrene microcellular foams with supercritical CO<sub>2</sub> is achieved on a two-stage single screw extruder. The contraction flow in the extrusion die is simulated with the FLUENT computational code to predict profiles of pressure, temperature, viscosity, and velocity. The location of nucleation onset is determined based on the pressure profile and equilibrium solubility. To perform these simulations, the necessary physical properties of the CO<sub>2</sub>/polymer system, such as the viscosity and solubility, are characterized and fitted to various theoretical models, which are latterly substituted into the flow simulation. Systematic experiments are performed to verify effects of three key operating conditions: CO<sub>2</sub> content, pressure drop or pressure drop rate, and foaming temperature on the foam cell structure. Experimental results are compared with simulations and both are used to gain insight into the foaming process. To obtain improved cell structure and properties, noncomposite foams are produced.

### **1.3.1. Viscosity Characterization**

Because of the pivotal role of viscosity in equipment design and process simulation, various methods are designed to measure the viscosity of polymer melts under conditions with and without CO<sub>2</sub>. The viscosity measurement focuses on determining the shear viscosity of CO<sub>2</sub>/polymer melt systems at different shear rates, temperatures, pressures, and CO<sub>2</sub> contents. The experimental data are fitted in various rheological models and then the models are substituted in the flow simulation. Effects of temperature, pressure, and CO<sub>2</sub> content on the shear viscosity are analyzed by the traditional shifting technique and further explained based on the free volume theory.

### **1.3.2. Measurement of CO<sub>2</sub> Solubility in Polystyrene**

Solubility represents the upper limit of CO<sub>2</sub> amount that can be dissolved in the polymer, which directly affects the cell nucleation rate and cell growth. Solubility also influences the viscosity, interfacial tension, and other important physical properties. Based on the value of the solubility, one can predict the foaming expansion ratio and estimate the compatibility between CO<sub>2</sub> and polymers. Here, a volumetric method is designed to measure the solubility of CO<sub>2</sub> in polystyrene and polystyrene nanocomposites at various temperatures and pressures. The Sanchez-Lacombe equation of state is used to represent the phase equilibrium between CO<sub>2</sub> and CO<sub>2</sub>/polystyrene solutions.

### **1.3.3. Computational Simulation of the Foaming Extrusion**

After the viscosity and solubility for the CO<sub>2</sub>/polystyrene system are characterized, a simulation using FLUENT computational code is performed to predict the pressure profile and the position of nucleation onset in an extrusion capillary die. The simulation is accomplished by combining the equations of motion, the energy balance, and the Carreau viscosity model to characterize the flow field in the die and modeling the phase equilibria with the Sanchez-Lacombe equation of state. Profiles of pressure, temperature, viscosity and velocity for the contraction flow in the extrusion die are calculated and then the position of nucleation onset is determined based on the pressure profile and equilibrium solubility.

Furthermore, the pressure profile and the position of nucleation onset are correlated to the cell nucleation and growth, which helps understand the effects of operating conditions on the cell structure qualitatively. Therefore, the simulation results can help us to select the right operating conditions for producing foams with desired cell structure.

### **1.3.4. Relationship between Operating Conditions and Cell Structure**

Systematic experiments are performed to explore effects of three key operating conditions: CO<sub>2</sub> content, pressure drop or pressure drop rate, and foaming temperature on the microcellular foam structure. Experimental results are compared with simulations and both are used to gain insight into the foaming process.

Microcellular foam structure is represented by foam cell size, cell density, cell shape, and open or closed cell morphology. Cell size, the average diameter of the foam

cells, and cell density, the number of cells per unit volume, are determined by analyzing images obtained from scanning electron micrographs (SEM). The open or closed cell morphology and the cell shape can be directly observed from the SEM micrographs.

Foam properties, including tensile modulus, fire retardance, surface quality, and barrier property are studied for some foam samples.

### **1.3.5. Nanocomposite Foams**

Two nucleation mechanisms, homogeneous nucleation and heterogeneous nucleation, coexist in a foaming process. To obtain cells with desired cell structure and uniform cell size distribution, some organic, inorganic, or metal powders, which are called nucleating agents, are necessary to act as ‘hot spots’ and thus nucleate foam cells by reducing the nucleation energy. Commonly, the nucleation efficiency is affected by the size, shape, distribution, and surface treatment of the nucleating agents.

In this study, nanometer-sized particles, mainly nano-clays, are used to nucleate micrometer-sized foam cells. Intercalated and exfoliated polystyrene/nano-clay composites are prepared with mechanical blending and in-situ polymerization, respectively. The composites are then foamed in an extrusion foaming process. Compared with conventional micron-sized nucleating agents used in the foaming process, nanometer-sized clay particles offer unique properties. The extremely fine dimensions and large surface area of nanoparticles and the intimate contact between particles and polymer matrix may greatly alter the cell nucleation and growth. It is shown that the addition of nano-clay benefits both the foam structure and the property. The nano-clay can facilitate to obtain high cell density and to change the cell

morphology (open or closed). The nano-clay also improves the barrier properties (low diffusion coefficient for both mass and heat), mechanical strength, and heat resistance, offering opportunities for foams in various new applications.

H142B/22 (foaming agent) and talc (nucleating agent) are also used as comparison.

#### **1.4. Outline**

This dissertation includes seven chapters, starting with this introduction (Chapter 1) and a literature review (Chapter 2) to gain an overview of this research and the current situation in microcellular foaming studies. Chapter 3 focuses on the computational simulation and the influence of pressure and CO<sub>2</sub> content on the foaming extrusion. To continue the discussion on the relationship between operating conditions and foam structures, Chapter 4 addresses the effect of foaming temperature. In Chapter 5, our work on the nanocomposite foams is summarized. To better understand a foaming process, the sorption of CO<sub>2</sub> in polymers and the viscosity reduction are also studied and the results are shown in Chapter 6. In Chapter 7, the major conclusions are emphasized again and some future work is recommended. Finally, nine appendices are attached to supplement the main content.

## **CHAPTER 2**

### **LITERATURE REVIEW**

#### **2.1. Polymeric Foams**

Polymeric foams [2-5], defined as materials consisting of gaseous voids surrounded by a denser matrix of polymeric materials, have brought increasing interest in both academia and industry due to its interdisciplinary nature and multiple applications. Foaming technology requires the knowledge of several different scientific fields including polymer science and engineering, thermodynamics, rheology, fluid dynamics, mass and heat transfer, and equipment design. Although researchers have understood a lot of basic principles governing the foaming process, the design of a foaming process is still mainly experimental. Nowadays, the foam industry is challenged by issues ranging from waste disposal, recyclability, flammability, and the depletion of earth's ozone layer by the chlorofluorocarbon blowing agents, to the demands of new concept foam materials, such as the microcellular foams. More important, it is necessary to know the exact governing parameters in both foam cell nucleation and growth for directing the design of foam structure and foam production. As a result, fundamental study in related areas, such as foam cell nucleation thermodynamics and cell growth dynamics, becomes crucial.

A variety of polymers are foamed to low densities for applications that derive from weight-reduction, high strength-to-weight ratio, heat and sound insulation, buoyancy, energy dissipation, high absorption, convenience, and comfort. Polymeric foams can be divided into two classes based on the polymeric materials: reprocessable thermoplastic foams (polystyrene, poly(vinyl chloride), polyacetal, acrylonitrile-butadiene-styrene (ABS), polyester (ex., poly(butylene terephthalate)), polyetherimide, polyolefins (ex., polyethylene, polypropylene), etc.) and crosslinked non-reprocessable thermoset foams (polyurethane, polyisocyanurate, phenolics, epoxy, silicone, urea-formaldehyde (UF), etc.). Some polymeric foams and their corresponding applications can be found in literatures [2-4]. Among them, polyurethane, polystyrene, and poly(vinyl chloride) occupy the largest market share.

In 2001, the total foamed plastics demand in the United States was 7,420 million pounds, including 3,910 million pounds of urethane foams, 1,900 million pounds of polystyrene foams, and 1,610 millions pounds of other foamed polymer [5]. Another source [6] says that the foam sales in North America in year of 2,000 is 1.7 billion dollars, including 400 million dollars of extruded polystyrene foam (XPS), 450 million dollars of expanded polystyrene foam (EPS) around, and 950 million dollars of polyiso (PI and PU) foam.

Depending on the material composition, foam morphology, and physical and thermal properties (glass transition temperature, crystallinity, degree of crosslinking, etc.), polymeric foams can be further classified as rigid and flexible foams. Rigid foams are found in applications of building and construction, appliance, tanks/pipes, transportation, packaging, furniture, flotation, moldings, and food and drink containers.

In contrast, flexible foams are usually used as furniture, transportation, bedding, carpet underlay, packaging, textile, toys, gaskets, sports applications, shock and sound attenuation, and shoes. We can see that most polymeric foams are used for automotive, construction, packaging, and consumer products applications.

Foams can consist of either closed cells or open cells. Closed cell foams have complete cell walls around each cellular structure, while in the open cell foams, cell walls totally disappear and only ribs and struts are left. Commonly, open cell foams have a higher absorptive capacity for water and moisture, a higher permeability to gas and vapor, less effective insulation capabilities for either heat or electricity, and a better ability to absorb and damp sound than closed cell foams. Also, closed cell foams are usually rigid and open cell foams are usually flexible. The formation of open cells or closed cells depends on the material selection and the foaming process control.

Typical foaming techniques include extrusion, compression molding, injection molding, reaction injection molding, and the solid-state method (where pressurized gas is forced into a solid polymer at room followed by depressurization at a high temperature above the  $T_g$ ).

A typical formulation of a foaming system is composed of the polymer (or polymer monomer), foaming agent (or blowing agent), nucleating agent, and other necessary additives (fire retardant, surfactant, catalyst, etc.).

There are two types of foaming agents that form the gaseous phase in the foam cells: chemical foaming agent and physical foaming agent. The chemical foaming agent can give off gases, usually CO<sub>2</sub> and N<sub>2</sub>, under the foaming conditions by chemical reactions or thermal decomposition. The physical foaming agents are chlorofluorocarbons (freons), volatile hydrocarbons/alcohols, and inert gases (CO<sub>2</sub>, N<sub>2</sub>, argon, or water).

The traditional foaming agents, freons, are proven to contribute to the destruction of the Earth's ozone layer and gradually being eliminated (2010 in US). At present, three choices, hydrogenated chlorofluorocarbons/fluorocarbons (HCFC/HFCs), hydrocarbons or alcohols, and inert gases (CO<sub>2</sub>, N<sub>2</sub>, argon, or water), have the highest potential as replacements of the traditional physical foaming agents. Among these, CO<sub>2</sub> is the most favorable replacement because of its unique properties. Compared with freons, a nearly equivalent amount of CO<sub>2</sub> in volume can be dissolved in polymer melt at elevated pressures. The diffusivity of CO<sub>2</sub> in polymer melt is large, which ensures a quick mixing process. Moreover, CO<sub>2</sub> is environmentally benign, non-flammable, chemically stable, and economically low-cost. The challenges of CO<sub>2</sub> as a foaming agent mainly come along with the high-pressure operation, fast gas escape, and dimensional instability during the foaming process.

In a typical foaming process, both homogeneous nucleation and heterogeneous nucleation may exist simultaneously. To obtain cells with controlled cell structure and uniform cell size distribution, some organic, inorganic, or metal powders, which are called nucleating agents, are necessary to act as 'hot spots' to reduce the nucleation energy. Among them, the inorganic nucleating agents are mostly commonly used, such

as talc, silicon oxide, titanium oxide, diatomaceous earth, and kaolin. A fine dispersion of these nucleating agents can assist the formation of nucleation centers for a gaseous phase. Talc is heavily used as the nucleating agent in the extrusion of polystyrene insulation foams. The nucleation efficiency is affected by the size, shape, distribution, and surface treatment of nucleating agents.

In this work, we will focus on a microcellular foaming process by using supercritical CO<sub>2</sub> as the physical foaming agent, although other methods, such as phase separation [7], precipitation with a compressed fluid antisolvent [8], and polymerization of monomers [9], were also reported to make microcellular foams. The nucleation effect of various micrometer and nanometer particles is also our interest.

## **2.2. Microcellular Plastic Foams**

Microcellular foams are usually defined as plastic foams characterized by cell sizes smaller than 10 μm and cell density larger than 10<sup>9</sup> cells/cm<sup>3</sup> [10, 11]. Although the definition is still in argument because it is difficult to relate the foam properties directly to the cell size and cell density, three major advantages determine there would be many potential applications for microcellular foams. First, microcellular foams can greatly reduce the material usage and improve some mechanical properties simultaneously. The densities of microcellular foams can be 3 to 99 % of the density of the solid non-foamed polymers. Second, environmentally friendly inert gases, primarily carbon dioxide (CO<sub>2</sub>) and nitrogen (N<sub>2</sub>), are used as foaming agents. Third, microcellular foams may create unique properties that are not possessed by the conventional foams or the original, solid polymers, such as the small cell size for filtration and separation.

The concept to create many small bubbles in plastics by gas nucleation was initially introduced by Professor Nam P. Suh of the Massachusetts Institute of Technology in early 1980s as a means to reduce the cost of many mass-produced plastic items [10, 12]. If the bubble size is small enough, the essential mechanical properties should be conserved while the weight is reduced.

A microcellular foaming process follows the basic principles of the conventional foaming processes. Thus, by studying the microcellular foaming process, we can get information that is also appropriate for the conventional foaming processes. Of course, the microcellular foaming process has its own unique requirements to create extremely small bubbles and a huge quantity of bubbles.

### **2.2.1. Procedure**

As shown in Figure 2.1 [13], the basic microcellular foaming process consists of three steps: mixing, cell nucleation, and cell growth. To ensure that all cells are created by nucleation, good mixing is necessary to form a homogeneous solution composed of the foaming agent and polymer melt. Next, cell nucleation, a phase separation phenomenon, is induced by a thermodynamic instability to form nuclei with the critical size. Such an instability is usually a temperature increase or pressure decrease, which can reduce the solubility. Compared with the cell nucleation, determining the cell density, cell growth, starting with the critical size, decides the cell size. Cell growth is a complex procedure controlled by fluid dynamics, mass and heat transfer, and polymer rheology.

Following these basic steps, microcellular foams can be produced by a batch, a semicontinuous, a continuous extrusion, a rotation molding, or an injection molding foaming process.

### **2.2.1.1. Batch Foaming**

In the batch foaming process (Figure 2.2) [14-16], pre-shaped samples are placed in a pressurized autoclave and saturated with the foaming agent (CO<sub>2</sub>, N<sub>2</sub>, etc.) at a selected saturation temperature and pressure. The saturation time varies from several hours to several days according to the gas diffusivity and the sample dimension. After saturation, there are two choices possessing different driving forces for cell nucleation.

If the saturation temperature is relatively high (near or above the glass transition temperature ( $T_g$ ) of the sample), this saturation temperature can be treated as the foaming temperature. The sample can be foamed at such a temperature when the pressure is rapidly released. Here, the nucleation is induced by the pressure drop ( $\Delta P$ ) and pressure drop rate ( $\Delta P/\Delta t$ ). Otherwise, if the saturation temperature is very low and far below  $T_g$ , the sample cannot nucleate when the pressure is released due to the rigidity of the polymer matrix. The saturated sample can be then dropped in a high temperature water (oil) bath to get foamed. This high temperature is the foaming temperature; and correspondingly, the nucleation driving force is the temperature increase ( $\Delta T$ ) and temperature increase rate ( $\Delta T/\Delta t$ ). The advantage of the second choice is that the gas solubility is high at the low saturation temperatures. Combinations of the two choices can be also used to nucleate samples.

After cell nucleation, cell growth is controlled by the cell growth temperature and time, and then stopped by quenching the sample at a temperature below its  $T_g$ .

#### **2.2.1.2. Semicontinuous Foaming**

A semicontinuous foaming process, in which the foaming was uncoupled from the shaping, was developed from the batch foaming process by Kumar et al. [17, 18] to produce sheets or strips of microcellular polymers at solid state.

First, a roll of solid polymer sheet with a gas channeling material interleaved between the layers of polymers is prepared. The gas channeling material should consist of a layer of flexible gas permeable material, such as porous paper sheet, particulate material, and fabrics. Next, the roll of polymer sheet and gas channeling material is exposed to the high-pressurized foaming agent (i.e.,  $\text{CO}_2$ ) for a period of time sufficient to achieve the desired gas concentration, usually at room temperature. For example, when saturating a 0.02 inch thick sheet of poly(ethylene terephthalate) (PET) with  $\text{CO}_2$  a saturation time of 15 to 30 hours is needed. Finally, the pressure is released and the saturated polymer roll is gradually unwound, separated from the gas permeable material, and heated by drawing under tension through a heating station, a water or oil bath which temperature is higher than  $T_g$ .

This process is suitable for the polymers whose  $T_g$  is above the room temperature, such as polystyrene (PS), poly(vinyl chloride) (PVC), ABS, poly(methyl methacrylate) (PMMA), PET, and poly(ethylene terephthalate glycol) (PETG) foams.

### **2.2.1.3. Continuous Extrusion Foaming**

Compared with the batch process, a continuous extrusion foaming process is more economically favorable because of its high productivity, easy control, and flexible product shaping. A traditional extrusion process is suitable for foam manufacture after a few modifications, such as a venting port for CO<sub>2</sub> injection, a special mixing element for creating a homogeneous solution, and a specific foaming die.

The extrusion foaming can be performed on a single screw extruder, a twin-screw extruder, or tandem extruders where two extruders are connected together and the mixing and temperature cooling control are independent procedures on each extruder. The comparison of these three common extrusion foaming processes is listed in Table 2.1 [5].

A typical foaming extrusion [11, 19-21] begins with the plasticization of polymer resin after which CO<sub>2</sub> is injected into the extruder barrel. A decreasing temperature profile from the hopper to the die is usually applied for the foaming extrusion. High temperatures from the hopper to the gas injection port ensure the complete melt of the polymer resin. Once the gas is injected in the barrel, low barrel temperatures can be applied due to the viscosity reduction. A low foaming temperature (or die temperature) is always favorable to get good foam structure. Mixing elements, such as static mixers, can be attached to the extruder to further improve the mixing effect and pre-control the melt temperature. A homogeneous single-phase solution consisting of the polymer melt and the foaming agent is created by the screw rotation and the on-line mixers.

The rapid, large pressure drop through the die induces cell nucleation, although a device to create a sudden temperature increase in the extrusion die was also reported

[22]. Again, the purpose of the pressure drop or temperature increase is to reduce the gas solubility in the polymer melt and therefore induce the phase separation. The continuous extrusion foaming process is different from the batch foaming process in these aspects: first, a metered amount of gas, instead of the saturation amount of gas, is dissolved in the system; second, the pressure gradient which is the major nucleation driving force is decided by the flow instead of the saturation pressure; and third, the foaming temperature is always the temperature of the extrusion die.

After the nucleation die, a shaping die is usually necessary to control the product shape and the foam expansion. Once the extrudate temperature is lowered below its  $T_g$ , the foam structure is vitrified and the foam sample can be collected.

#### **2.2.1.4. Injection Molding Foaming**

Foam injection molding is another commonly used polymer processing technique that combines gas dissolution, cell nucleation, and cell growth, with product shaping. Compared with the extrusion foaming process, foam injection molding has its own advantages. For example, it is convenient to produce parts with complex geometry. By choosing the right size of the injection nozzle or mold gate, the pressure drop (or pressure drop rate) through them can be very high, which provides the high thermodynamic instability for cell nucleation. Currently, foam injection molding using  $\text{CO}_2$  as the foaming agent is applied to produce lightweight products with strong mechanical strength. When one considers the preservation of polymer molecular

structure at high melt temperature, CO<sub>2</sub> is a better choice than the thermal degradable chemical blowing agents. Applying MuCell molding technology invented by Suh et al. [10], Trexel [23] has successfully commercialized this technique to injection mold microcellular foams.

Xu et al. [24] used injection molding to make microcellular foam after a series of modifications on certain components of a standard reciprocating-screw injection molding machine, such as the plasticizing unit, injection unit, hydraulic unit, clamping unit, and gas delivery unit. To successfully produce microcellular foams a new screw designed for better mixing and a new sealed barrel with gas injectors were used. The injection unit requires a fast injection speed to get the high pressure drop rate. It was found that a finer cell structure and more uniform cell size distribution can be achieved by controlling the pressure drop rate at the mold gate than at the injection nozzle. Of course, the injection speed should be controlled below the shear limit to prevent the melt fracture.

Generally, foaming injection molding achieves increased melt flowability, lower injection pressures, faster cycle times, and greater dimensional stability and weight savings in molded parts [25, 26]. The reduced viscosity after the addition of supercritical CO<sub>2</sub> allows faster injection speed, lower injection pressure, and lower clamp tonnage. The shot size for the microcellular foam process is usually smaller than that for the solid molding process, which brings shorter recovery time. The pack and hold time is eliminated due to the internal gas pressure and the significantly less mass of material that needs to be cooled. The uniform cell distribution and expansion allow improved dimensional stability and diminish the surface flaws (ex. sink marks). However, to

obtain a perfect surface finish, other techniques, such as a venting mold or co-injection, are needed. A new potential application of foaming injection molding is to make fiber-filler articles [27]. The viscosity reduction after introducing the foaming agent can prevent the fibers to break during flowing in the mold and reduce the fiber orientation.

### 2.2.2. Overview of Microcellular Polymers

Both amorphous and semicrystalline polymers have been successfully microcellular foamed. Various foamed polymers are summarized below.

**Polystyrene (PS)** PS and high impact PS (HIPS) are the most common foaming materials and they are heavily used in today's life. As early as 1982, Martini et al. [10, 12] first produced microcellular foams of HIPS by using N<sub>2</sub> as the foaming agent. Since then, study in PS foams can be found in many literatures [19, 28-31].

**Polycarbonate (PC)** Kumar et al. [16] foamed PC at 150°C in a batch system. Cell density in a range of 1~10×10<sup>9</sup> cells/cm<sup>3</sup> was achieved. Bubble nucleation at 60°C, which is 90°C below the T<sub>g</sub> of original polymer, was observed.

**Poly(methyl methacrylate) (PMMA)** Handa et al. [32, 33] applied the phenomenon of retrograde vitrification of PMMA/CO<sub>2</sub> system on the batch foaming study. By optimizing the foaming temperature (20~90°C), PMMA sub-micron foam with cell size of 0.35 μm, cell density of 4.4×10<sup>13</sup> cells/g, and foam density of 0.116 g/cm<sup>3</sup> was obtained after saturating the sample in CO<sub>2</sub> at -0.2°C and 34 atm. Cell size of 0.5 μm and cell density of 10<sup>12</sup> cells/cm<sup>3</sup> were also reported by Goel et al. [34-38] when PMMA was saturated with CO<sub>2</sub> at 40°C and 272 atm.

**Poly(vinyl chloride) (PVC)** Kumar et al. [15] obtained microcellular foams of PVC at foaming temperatures varying from 56 to 115°C. Holl et al. [39] studied the effect of additives on microcellular PVC foams. It was found the solubility of CO<sub>2</sub> in the additives (lubricants) is lower than in the PVC matrix. The presence of lubricants shows no adverse effect on the foam and makes it possible to process PVC at a lower temperature. Matuata et al. [40, 41] found that microcellular foamed PVC/wood-fiber composites have higher impact strength and poorer tensile properties than the unfoamed samples. The addition of wood-fibers reduces the concentration of CO<sub>2</sub>, the foaming agent, in the composites because wood-fibers do not absorb CO<sub>2</sub>.

**Polyethersulfone (PES) and Polysulfone (PSF)** PES and PSF, thermally stable non-crystalline polymers, were foamed by Itoh et al. [42] at various foaming temperatures and saturation pressures of CO<sub>2</sub>. PES exhibits a very small cell size of 0.2 μm for a saturation temperature of 5.7 MPa, which is small compared to that of PSF (2.5~4 μm). Cell density ranging from 10<sup>11</sup> to 10<sup>14</sup> cells/cm<sup>3</sup> for PES was achieved at saturation pressure of 2.0~5.7 MPa.

PES and **Poly(ether imide) (PEI)** were batch foamed by Krause et al. [43, 44] using CO<sub>2</sub> as the foaming agent at foaming temperatures ranging from 120 to 240°C. An interesting phenomenon is that there is a critical CO<sub>2</sub> content above which closed-cell morphologies no longer develop and nanoporous open foams are formed. Cell size as small as 40 nm and cell density over 10<sup>14</sup> cells/cm<sup>3</sup> for both polymers were obtained above a CO<sub>2</sub> concentration threshold.

Batch foaming of PSF, **polyethersulphone (PESF)**, **polyphenylsufone (PPSF)**, and PEI were also reported by Sun et al. [45, 46]. PSFs are clear, rigid, and tough engineering thermoplastics with  $T_g$  between 180 and 250°C. They have been widely used in membrane supports for reverse osmosis, ultrafiltration, and gas separation. Therefore, the microcellular foams of such material may exhibit excellent mechanical properties and good thermal stabilities.

**Poly(ethylene terephthalate) (PET)** Baldwin et al. [47] foamed both crystalline and amorphous PET/CO<sub>2</sub> systems in a batch at foaming temperatures ranging from 80 to 230°C. It was found that CO<sub>2</sub> induces crystallization of PET once a critical concentration is reached. The crystallization increases cell density due to the heterogeneous nucleation at the amorphous/crystal interface. However, the crystallization also results in a lower solubility, increased matrix stiffness, and lower diffusivity. The cell size is larger at a higher foaming temperature due to the lower matrix viscosity.

**Poly(ethylene terephthalate glycol) (PETG)** PETG was batch-foamed by Kumar et al. [48, 49] by using CO<sub>2</sub> as the foaming agent. The relative density decreases as the foaming temperature increases from 40 to 120°C.

**Polypropylene (PP)** Park et al. [50] used isopentane and CO<sub>2</sub> as foaming agents to foam both linear and branched PP in an extrusion process. A slightly lower nucleation was observed on the branched PP than the linear PP. However, the branched PP produces closed cells because the branched structure enhances the melt strength or the melt elasticity. As a result, cell coalescence is eliminated.

**Acrylonitrile-Butadiene-Styrene (ABS)** Microcellular foams of PP, HIPS, and ABS were extruded by Park et al. [22] to study the foaming effect of both CO<sub>2</sub> and N<sub>2</sub>. Cell density of about 10<sup>8</sup>~10<sup>10</sup> cells/cm<sup>3</sup> was achieved when CO<sub>2</sub> was applied, while 10<sup>7</sup>~10<sup>8</sup> cells/cm<sup>3</sup> for N<sub>2</sub>. The lower cell density was explained as the lower solubility of N<sub>2</sub> in these polymers.

**Polyethylene (PE)** High Density PE (HDPE) was successfully foamed using CO<sub>2</sub> as foaming agent in an extrusion process by Behravesht et al. [51]. The lower the melt temperature and the die temperature, the higher the volume expansion ratio. A large volume expansion ratio was achieved by freezing the extrudate surface in order to prevent the gas diffusing out of the sample. The lowest practical die temperature for HDPE was found to be 121°C with 7 wt.% of CO<sub>2</sub>. Blend of PE and PS was also foamed when Lee et al. [52] studied the CO<sub>2</sub> assisted blending in a twin-screw extruder. Doroudiani et al. [14] applied blend of HDPE and isotactic PP (iPP) for microcellular foaming with CO<sub>2</sub> and obtained finer and more uniform cells than neat HDPE or iPP.

**Polybutylene (PB)** Doroudiani et al. [53] studied the effect of the crystallinity of HDPE, PB, PP, and PET on the microcellular foam structure. The crystallinity and the crystal morphology were changed based on different heat treatment history. Then, in a batch foaming system, such samples were saturated by CO<sub>2</sub> at room temperature and foamed at different temperatures, i.e., 133°C for HDPE, 117°C for PB, 159°C for PP, and 150°C for PET. In general, compared with amorphous polymers, microcellular foaming of semicrystalline polymers is more difficult to control since the gas does not dissolve much in the crystallites. As a result, a non-uniform distribution of foam cell size and density is common and the bubble nucleation is not homogeneous due to the

heterogeneous nature of the semicrystalline polymer. Furthermore, because of the existence of the melting temperature ( $T_m$ ) for the semicrystalline polymer, the foaming temperature window is narrow in the extrusion foaming process.

**Polybutylene succinate (PBS)** PBS, a long chain branched biodegradable polyester, was extrusion foamed to obtain fortyfold expansion by Park et al. [54]. Proper operating conditions were selected to get such a high volume expansion ratio and offset the relatively high diffusivity of  $\text{CO}_2$ . An optimum foaming temperature range exists, below which the foam could not expand much because the stiffness of the PBS matrix is not favorable for the cell growth, while above which  $\text{CO}_2$  is easy to escape out of the foam to the environment. It is also found that the optimum temperature to produce the maximum volume expansion ratio decreases as the  $\text{CO}_2$  concentration increases, mainly due to the plasticization of  $\text{CO}_2$ .

**Polyamide 11 (PA 11)** PA 11 may have a higher  $\text{CO}_2$  solubility than PA 6 because it has fewer hydrogen bond pairs along the polymer chains and thus its carbonyl groups can be accessible to the interaction with  $\text{CO}_2$ . Martinache et al. [55] foamed PA 11 by using  $\text{CO}_2$  as the foaming agent at an extruder die temperature of  $165^\circ\text{C}$ ,  $25^\circ\text{C}$  lower than the melting temperature of the pure material. Cell size of  $30\ \mu\text{m}$  and cell density of  $10^7$  cells/ $\text{cm}^3$  were achieved. At the same time, the volume swelling and the viscosity reduction were studied. They also reported a method to produce foamed materials by the aid of surfactants [56].

**Poly(vinylidene fluoride) (PVDF)** PVDF and its blends with amorphous PS or PMMA were foamed by Siripurapu et al. [57] using CO<sub>2</sub> as the foaming agent at an extrusion die temperature around 175°C. Poor cell structure was observed for neat PVDF and PVDF/PS immiscible blends. Miscible blends of PVDF and PMMA yield foams with vastly improved morphologies.

### **2.2.3. Mechanical Properties**

One of the original rationales for developing microcellular foams is that mechanical properties like impact strength and fatigue life would be significantly improved. The small voids in the microcellular foams could relieve the triaxial stress at the tip of cracks, behaving like the rubber particle cavitation [58-62] in a plastics/rubber toughening system. Recently, with the development in microcellular foaming studies, more and more mechanical properties are available, although still limited. Experimental data on the impact strength, fatigue life, and tensile strength of microcellular foams of PC, PVC, PS, and styrene-acrylonitrile copolymer (SAN) are available.

#### **2.2.3.1. Impact Strength**

Barlow et al. [63, 64] studied the impact strength of high density solid-state microcellular PC foams. The Izod impact strength was found to be a strong function of both foam density and cell size. As shown in Figure 2.3, foams with relative densities

(foam density/unfoamed density) of 0.62 and above all demonstrates an improvement in impact strength, compared with the unfoamed PC samples. The impact strength decreases in a linear manner with the decrease of density. The impact strength is also observed to decrease with the decrease of cell size (ranging from 7 to 18  $\mu\text{m}$ ).

Collias et al. [65-67] studied both the tensile toughness and the impact toughness of microcellular foams of PS, SAN, and PC by using  $\text{N}_2$  as foaming agent. It is found that the gas dissolved in the polymer matrix has a great influence on the mechanical properties. Microcellular PS foams showed some limited improvement over unfoamed PS in terms of tensile and impact toughness, while microcellular PC foams with cell size of 40  $\mu\text{m}$  and void fraction of 28% was indeed able to increase the notched impact toughness dramatically. The notched Izod impact strength of microcellular foamed PVC was also found to increase as the void fraction increases by Matuana et al. [68].

Kumar et al. [69, 70] recently presented an opposite result that the Gardner impact strength from a falling-weight impact tester decreases linearly with the decrease of the foam relative density. A decrease in impact strength of crystallizable PET (CPET) [71] was also observed after microcellular foaming, although a close value of impact strength between foamed and virgin non-foamed CPET was obtained at a high  $\text{CO}_2$  saturation pressure due to the gas induced crystallization.

#### **2.2.3.2. Fatigue Life**

The fatigue life test determines the failure of samples under repeating, usually sinusoidal, tension forces. Seeler and Kumar [72-74] have performed extensive studies on the fatigue life of microcellular PC foams. When the relative density of the foamed

sample is 0.90, a same value of fatigue life as that of the unfoamed sample was obtained. When the relative density increases to 0.97, a fatigue life, one order of magnitude higher than that of the unfoamed sample, was observed.

### **2.2.3.3. Tensile Strength**

In general, the tensile properties, including tensile strength at break and yield strength, were found to be directly proportional to the foam density for both PC/CO<sub>2</sub> [75] and PVC/CO<sub>2</sub> [40, 41, 68, 76, 77] systems. As shown in Figure 2.4, the microcellular structure is inefficient in carrying the tensile load. An interesting tensile behavior for microcellular PS foams is that it exhibits a clear yield point in the stress-extension curve, instead of a brittle break for the unfoamed sample. The percent elongation at yield and break are higher, although the tensile strength at break and the modulus are still lower than those of the unformed PS.

### **2.2.4. Foam Structure and Foaming Conditions**

The relationship between foam structure and foaming conditions is one of most interesting topics that researchers focus on. The goal is to provide experimental data for the fundamental study in cell nucleation and growth. Here, the foam structure mainly indicates foam cell size, cell density, and cell morphology. Several important foaming conditions include pressure, temperature, gas concentration, foaming time, and shear stress.

#### **2.2.4.1. Foaming Pressure**

Overall, it is found that the higher the saturation pressure or the larger the pressure releasing rate, the higher the nucleation rate and the smaller the cell size for both batch and continuous foaming process [16, 19, 28, 29, 34-37, 78]. The pressure drop rate plays an important role in deciding the cell density since cell nucleation is affected by the time period over which a thermodynamic instability is induced [11, 20].

#### **2.2.4.2. Gas Concentration**

In general, more nucleation is expected at a higher gas concentration because it provides more nucleation sites and enlarges the thermodynamic instability, which is the driving force for cell nucleation.

Park et al. [50] studied the microcellular foaming of PP. It was found that a higher cell density was observed when more CO<sub>2</sub> was dissolved in the polymer melt. However, the cell density levels off and becomes independent of CO<sub>2</sub> concentration when it is beyond a certain value, very like the solubility limit.

The solubility was found to play a vital role in controlling cell density and cell size when Handa et al. [32] was making ultramicrocellular foams of PMMA. At 34 atm, the solubility of CO<sub>2</sub> drops dramatically from 22.5 wt.% at -0.2°C to 7.9 wt% at 24°C. The cell density increases and cell size decreases with the increase of CO<sub>2</sub> solubility.

#### **2.2.4.3. Foaming Temperature**

The influence of foaming temperature is very complex and it seems there is no simple answer about how the cell structure changes with foaming temperature. It

depends on the specific foaming system because nearly the physical properties, such as viscosity, surface tension, solubility, diffusivity, etc., are all sensitive functions of temperature. The final change in cell size, cell density, and cell morphology is a result of the comprehensive interaction of all these parameters.

In a batch microcellular foaming process [79, 80], a polymer specimen is placed in a high pressure vessel and then the vessel is pressurized to a certain pressure at a certain saturation temperature. After a period of saturation time (usually longer than 24 hours), the pressure is rapidly released to atmospheric and the nucleated cells are allowed to grow for a period of time, then stopped by a temperature quench lower than the glass transition temperature. The saturation temperature is usually treated as the foaming temperature although some experiments were designed to saturate the polymer sample at one temperature and foam it at another temperature. Because the polymer sample has been saturated before nucleation, any change in the foaming temperature or saturation temperature always causes a change in solubility, interfacial tension and diffusivity.

By modifying the classical homogeneous nucleation theory, Goel and Beckman [34, 35, 37] calculated the nucleation rate in the CO<sub>2</sub>/PMMA system. It was found that the interfacial tension, treated as a function of CO<sub>2</sub> concentration, increases with an increasing foaming temperature in a range of 40 to 80°C due to the decrease in solubility. As a result, increasing temperature leads to a gradual increase in the nucleation energy barrier and thus a decrease in the nucleation rate although the effect is not as dramatic as for pressure. Experimental results at different saturation temperatures (40, 50, 60, and 70°C) and a constant saturation pressure (34.47 MPa) show that the

observed cell density (number of cells per unit volume) decreases and the cell size increases with an increase of foaming temperature. The simulation predicted a similar trend. Here, the decrease of CO<sub>2</sub> solubility in PMMA with the increase of saturation temperature is the major reason for a decreasing cell density.

Sumarno et al. [28] presented a similar opinion for the polystyrene/nitrogen system. The cell density is minimum and the cell size is maximum at about 77°C (350 K), which corresponds to the minimum solubility of nitrogen in polystyrene with the variation of saturation temperature. Predictions based on the classical homogeneous nucleation theory agree with experimental results up to 120°C (393 K), above which the experimental results show that the cell density decreases and the cell size increases again. The volume expansion ratio also shows a minimum with an increase in saturation temperature for both the predicted ideal value as obtained from the solubility and the measured actual value. However, the actual value is lower than the predicted value because only part of the dissolved gas is used for cell nucleation and growth, while the remainder diffuses directly out of the polymer.

Arora et al. [29, 30] prepared microcellular polystyrene foams processed in supercritical CO<sub>2</sub> in a batch system where the foaming temperature changed from 40 to 120°C. Larger and fewer cells were also found at a higher foaming temperature. They attributed this phenomenon to the viscosity reduction of the substrate material at a higher temperature, causing the cell growth rate to increase (apparently due to the decrease of

the retractive force which confines the cell growth and the increase of the CO<sub>2</sub> diffusivity). Of course, the lower solubility of CO<sub>2</sub> in polystyrene at a higher saturation temperature (and thus fewer nuclei generated) is another reason for formation of the large cells.

Exceptions were found by Itoh et al. [42] when they studied the CO<sub>2</sub> foamed thermally stable non-crystalline polymers (polyether sulfone (PES) and polysulfone (PSF)). The cell sizes foamed at 230°C (503 K) were smaller than those at 170°C (443 K) and 200°C (473 K) for PSF/CO<sub>2</sub> system, although other results maintain that the cell size increases with the foaming temperature.

By considering that the surface tension decreases with an increasing temperature and using a theoretical model based on the classical homogeneous nucleation theory, Rodeheaver and Colton [81] obtained the opposite trend: that increasing both the temperature and pressure causes the nucleation density to increase. They studied the formation of an open-cell microcellular foam structure in a temperature range from 150 to 200°C for the polystyrene/nitrogen system. Although the majority of their experimental data indicates a decrease in bubble density with an increase in foaming temperature, a reasonable explanation of the discrepancy between the experimental results and the prediction is that higher foaming temperature promotes cell coalescence which reduces the final cell density. A foaming temperature of 200°C was found to favor the formation of both internal and surface porosity in a batch foaming process.

The classical nucleation theory was also found unable to describe the observed data even in a qualitative way by Kumar and Weller [15, 16] when they studied the effect of foaming temperature on the cell nucleation of a polycarbonate/CO<sub>2</sub> system.

Observed data show that in the experimental temperature range (60 to 160°C), the cell density only changes between 1 and  $5 \times 10^9$  cells/cm<sup>3</sup>. This is far from the Arrhenius-type temperature dependence in the classical nucleation theory that predicts the number of cells nucleated should be reduced about 3 orders of magnitude from 160 to 60°C. Furthermore, the cell density has a maximum at around 110°C. However, the cell size keeps increasing with increasing foaming temperature. In the experiment, 60°C was found to be the lowest temperature at which cell nucleation can be observed and substantially below the glass transition temperature of the original polymer. At this temperature, the cells nucleate non-uniformly and arrange along certain lines. When they studied the foaming behavior of a PVC/CO<sub>2</sub> system, the cell density was found to increase between 56 and 90°C, and then level off up to 120°C because of the cell coalescence at the relatively high foaming temperature region. However, the cell size kept nearly constant in the test temperature region due to the gas usage competition between the cell nucleation and cell growth. The foam density has a minimum around 105°C, above which the CO<sub>2</sub> loss by diffusion out of the sample increases instead of supports the cell nucleation.

When crystalline polymers are used for microcellular foaming, the situation becomes more complicated. Baldwin et al. [47] foamed polyesters at different temperatures to study the influence of crystallization on the foaming process. A bimodal cell size distribution was observed with larger uniform cells in the surface region (~20 μm) and very small cells in the center region (~1 μm) due to combined effects of heat transfer and molecular orientation.

In a continuous microcellular foaming process [11], a metered amount of gas (CO<sub>2</sub>) is injected in the barrel of an extruder. The mixing of CO<sub>2</sub> with a polymer melt depends on the shear force generated by the screw rotation and other special mixing elements (e.g. static mixers). The cells are nucleated after the rapid pressure drop when the mixture flows through the die, and the cells keep growing until vitrification. The three main differences between a continuous extrusion foaming process and a batch foaming process are that in the continuous process: (1) a metered amount of gas (instead of the saturation amount of gas) is dissolved in the system, (2) the pressure gradient as the major nucleation driving force is determined by the flow instead of the saturation pressure, and (3) the foaming temperature is always the extrusion die temperature.

By controlling the temperature of the melt before flowing into the die and the temperature of the die itself, Park et al [31, 51, 82] investigated the effects of both melt temperature and the die temperature on the foam morphology of high impact polystyrene with CO<sub>2</sub> as the foaming agent. They pointed out that the formation of excellent microcellular structure comes at the cost of a decrease in volume expansion. When the melt temperature is high (170°C), cell coalescence is severe and cell size is not uniform irregardless of the die temperature. At a moderate melt temperature (150°C), cell morphology ranges from a partial cell coalescence structure at a high die temperature of 175°C, to a highly open cell structure at a medium die temperature of 135°C, and then to a uniform closed cell structure at a low die temperature of 110°C. At a low melt temperature (120°C), the cell coalescence occurs less and less with the decrease of the die temperature until it disappears at the lowest die temperature. A similar study was conducted on the HDPE/CO<sub>2</sub> system. The degree of cell coalescence was again found to

be related to both the melt temperature and the die temperature. To decrease cell coalescence, it was shown that the melt temperature should be lowered substantially. The authors conclude that improving the melt strength by decreasing melt temperature is an effective way to reduce cell coalescence and preserve high cell density.

#### **2.2.4.4. Foaming Time and Shear Stress**

The effect of foaming time was heavily studied in a batch process where it is usually treated as the time that the sample is put in the high-temperature bath. In a continuous extrusion foaming process, because it is a dynamic flowing and cooling procedure, the exact foaming time could not be determined easily. As a result, a qualitative estimation is applied. In batch foaming [15, 39, 42], cell size was observed to grow rapidly in the first several seconds and then reach a limiting value after the driving force for growth is depleted. On the contrary, the cell density decreases first and then levels off. The change in void fraction or bulk foam density depends on the comprehensive effect of both cell size and cell density. A long foaming time also renders foam cells to interfere with each other and the cell structure to change from spherical to polyhedral [16].

Saturation time, the time in a batch foaming process for which a polymer sample is exposed to the high pressure CO<sub>2</sub> prior to the pressure release, also affects the cell morphology. A short saturation time always represents a low CO<sub>2</sub> concentration absorbed. As a result, low cell nucleation densities were observed for shorter saturation time [34-36].

Chen et al. [83] designed a simulator that can be used to test the effect of shear stress on a foaming process. They state that introducing shear stress significantly reduces the amount of gas for sufficient nucleation. Therefore, shear stress can help to create more nucleation sites.

## **2.2.5. Innovations and Applications**

### **2.2.5.1. Ultramicrocellular Foams**

Recently, cell size as small as 0.35 micron and cell density as high as  $4.4 \times 10^{13}$  cell/g was produced by Handa et al. [32, 33, 84] utilizing the phenomenon of retrograde vitrification documented earlier by Condo et al. [85, 86]. The large CO<sub>2</sub> solubility at 0°C and 34 atm in PMMA, which is about 30 wt.%, provides the major driving force for foaming. Potential applications of this ultramicrocellular foam of sub-micron in diameter are still under investigation.

### **2.2.5.2. Nanocomposite Foams**

Comparing to conventional micron-sized filler particles used in the foaming process, nanometer-sized clay particles [87-92] may offer unique properties. The extremely fine dimensions, large surface area of nanoparticles, and intimate contact between particles and polymer matrix may greatly alter cell nucleation and growth. Therefore, both the structure and the properties of microcellular foam may benefit from the nano-clay. The nano-clay can facilitate the formation of more cells at the same pressure drop, and change the cell structure (open or closed). The nano-clay may improve the barrier properties (low diffusion coefficient for both mass and heat),

mechanical strength, and heat resistance, offering new opportunities for foams in various applications. Limited work has been done in this area. Via a batch process, Nam et al. [93, 94] foamed polypropylene/clay nanocomposites and studied their influence on cell density, cell size, cell wall thickness, and bulk density. Transmission electron microscopy observations show that biaxial flow during cell growth induces the alignment of clay particles along the cell boundary. Several patents also mention the potential applications of nano-clays in various polymer processing operations, including foaming [95-97].

#### **2.2.5.3. Scaffolds for Tissue Engineering**

Scaffolds for tissue engineering can be made by different techniques [98], such as fiber bonding, solvent casting/particulate leaching, gas foaming, and phase separation. Because CO<sub>2</sub> is a green foaming agent and biocompatible, new applications can be found in foaming biodegradable or biocompatible polymers to make porous scaffolds or other medical devices. This prevents the residue of harmful materials that can be induced by the other scaffold manufacturing methods. Mooney et al. [99, 100] used CO<sub>2</sub> to foam highly porous amorphous biodegradable copolymer of polylactide and polyglycolide as three-dimensional tissue engineering scaffolds. The porosity was found to be as high as 95%.

Kumar [101] also described the potential applications of porous microcellular polymers in biomaterials research. These porous microcellular polymers could act 'hosts' to the live creature body cells where they can attach and grow without common reaction of rejection. A good starting material is the polymer already approved for use inside the body, such as PE, PTFE, PMMA, PC, PET, etc.

#### **2.2.5.4. Open-Cell Foams**

Open-cell foams in which cells are connected with each other, cell walls are dissipated, and only cell struts and ribs are left, have been found in such applications as absorption, separation, filtration, insulation in vacuum environment, scaffolds for tissue engineering, and biomedical devices. Traditionally, open-cell foams are produced from thermoset or highly crosslinked polymers directly from the polymerization that depends on the phase separation, such as open-cell polyurethane foams [2] and the high internal phase emulsion (HIPE) polymerized open-cell foams [102]. Salt extraction, in which water-soluble salt is blended into polymers and then washed out after foaming to get the open pores occupied by the salt molecules, was also reported to make open-cell foams [99, 103]. Recently, research in thermoplastic open-cell foams by extrusion is popular, especially using CO<sub>2</sub> as the foaming agent, because it is recyclable, low-cost, biocompatible, and environmentally friendly.

However, the extrusion process to create open-cell foams is highly empirical, complex, and difficult, determined by various factors. A common agreement is that the foaming temperature to give open structures is relatively higher than that of closed structure [31, 81, 104, 105]. The foaming temperature must be high enough to prevent

cell structure freezing before the rupture of cell walls. On the other hand, an excessively high foaming temperature may cause cell collapse due to rapid loss of blowing agent and reduced ability of cell struts to resist pressure. Furthermore, a high foaming temperature also reduces the die pressure that is important for cell nucleation. Therefore the most desirable foaming temperature for making open-cell foams will be the lowest foaming temperature at which the foam can be made and still maintain the open cell structure. Consequently, the operating window for open-cell foaming temperature is narrow.

A high concentration of the foaming agent is also important for the production of open-cell foams. Such open-cell foams are very sensitive to balances of rates of diffusion of the foaming agent out of the resin and out of the cells and air into such cells [106].

Besides the techniques described above, other methods were also found to be effective to obtain open-cell foams. Mechanical stretching the extruded foams may elevate contents of open cells because elongation can increase the average size of the existing open pores and thinner the cell wall along the elongation direction [107, 108]. Blending two polymers together may help the formation of open structures at the interface. For example, in making a polystyrene foam, minor amounts of polyethylene or ethylene/vinyl acetate copolymer may be employed. Crosslinking is an effective means to make flexible open foams, especially for polyolefins [109-112]. Compared with polystyrene foams that are lightweight and have both rigidity and good shape retention, polyolefin foams can offer flexibility, compressive recovery, and capacity to absorb repeated impacts. However, polyolefins are usually semicrystalline polymers and the viscosity changes dramatically above and below the melting point. For this reason, the

temperature for foaming polyolefins is narrow. Crosslinking can be used to highly improve this problem so that the material may be able to withstand the expansion pressure. Addition of surfactant in the foam formulations may stabilize the foam structure and may also change the resulting foam material from hydrophobic to hydrophilic [107, 108].

Rodeheaver et al. [81] presented a theoretical model of the formation of open-cell microcellular foam and open-cell polystyrene foam was produced by carefully selecting the processing conditions. Two mechanisms, cell impingement and cell coalescence, were combined to explain the formation of open cells. In the cell impingement model, the neighboring bubbles must be close enough to impinge so that a critical nucleation density exists for different bubble sizes. On the contrary, the cell coalescence depends on the rapture of the cell wall, a free film suspended between nearby struts. Therefore the foaming time is important. It was estimated that the foaming time should be on the order of 32 seconds to allow the free film to rapture, and then bubbles to coalesce. Park et al. [31] found a medium foaming temperature of 135°C is desirable to create open cells for HIPS. Huang et al. [105] obtained PC open-cell foams at a relatively high temperature of 170°C. All of these applied CO<sub>2</sub> as the foaming agent.

#### **2.2.5.5. On-Line CO<sub>2</sub> Concentration Detection**

Near infrared (NIR) spectroscopy was applied by Nagata et al. [113, 114] to detect the CO<sub>2</sub> concentration in an extrusion foaming line. For PP, LDPE, and polybutylene succinate (PBS), CO<sub>2</sub> concentration was successfully correlated to the light absorbance peak at a wavelength of 2019 nm, which comes from the combination of

different bond vibrations of CO<sub>2</sub>. It was found that the operating temperature, pressure, and flow rate, could change the amplitude of the NIR spectra. Therefore, the baseline of the spectra was corrected using special treatments.

An ultrasonic sensor is another means to study the foaming process. It has been reported that ultrasonic sensors can be used to detect T<sub>g</sub> reduction, solubility, cell nucleation and cell growth [115].

### **2.3. Supercritical Carbon Dioxide and Its Interactions with Polymers**

#### **2.3.1. Supercritical Carbon Dioxide**

Supercritical carbon dioxide (scCO<sub>2</sub>) can be defined as a substance for which both temperature and pressure are above the critical values [116]. For CO<sub>2</sub>, the critical temperature is 31.1°C and the critical pressure is 7.38 MPa (1074 psi). The corresponding critical density is 0.47 grams/cm<sup>3</sup>. A more practical definition for supercritical fluid is given as ‘any substance, the temperature and pressure of which are higher than their critical values, and which has a density close to or higher than its critical density’. Compared with high-pressure gas, scCO<sub>2</sub> cannot liquefy under any pressure once the temperature is higher than its critical point.

As shown in Figure 2.5 [117], scCO<sub>2</sub> is highly compressible and its density can be adjusted in a wide range only by changing the pressure. Supercritical CO<sub>2</sub> also exhibits high solubility (liquid-like solubility), high diffusivity (gas-like diffusivity), and low viscosity. Furthermore, compared with other volatile organic solvents, CO<sub>2</sub> is clean, low-cost, non-toxic, non-flammable, and environmentally friendly (low ozone-depletion potential and low contribution to the green house effect). The fact that CO<sub>2</sub> is a gas at

ambient conditions makes its removal from polymeric products very easy, avoiding the costly separation processes like drying and solvent removal. On the other hand, the difficulties with use of scCO<sub>2</sub> are mainly due to its requirement of high pressures.

The above advantages provide a variety of potential applications of scCO<sub>2</sub> on polymer synthesis and processing. Polymer polymerization, polymer fractionation and extraction, impregnation and surface modification, foaming and blending, polymer particle formation, coating, and microlithography are applications that have been reviewed in the literatures [116-119].

### **2.3.2. Interaction between Supercritical Carbon Dioxide and Polymers**

To predict the solubility and T<sub>g</sub> reduction in different polymer/CO<sub>2</sub> systems, one must generally understand interactions between a polymer and scCO<sub>2</sub> on a molecular level. This can also provide guidance about how to select the right polymer to get the best foam structure.

In general, interactions between CO<sub>2</sub> and polymers can be described as Lewis acid/Lewis base where CO<sub>2</sub> is the Lewis acid. The electron-short carbon atom in CO<sub>2</sub> could be of an electron acceptor, so that any polymer possessing electron-donating groups, such as carbonyl groups, ether groups, phenyl groups, fluoro groups, or nitrogen atoms, could exhibit specific interactions with CO<sub>2</sub>. As a result, CO<sub>2</sub> was found to be miscible with fluoroether or silicone (polydimethylsiloxane) polymers and show a decreasing solubility in polymers such as PMMA, PVC, PS, and polyolefins.

Kazarian et al. [120-123] studied specific intermolecular interactions of carbon dioxide with polymers by using infrared spectroscopy (IR). It has been demonstrated

that PMMA, polymer that possesses carbonyl groups show favorable interactions with CO<sub>2</sub>. They used the bending mode ( $\nu_2$ ) of CO<sub>2</sub> to probe polymer-CO<sub>2</sub> interactions. The evidence of the interaction is the observation of the splitting, shift, or broadening of the band corresponding to the CO<sub>2</sub>  $\nu_2$  mode. The splitting was not observed for polymers lacking electron-donating functional groups like polyethylene.

To make the mixing of CO<sub>2</sub> in a polymer a favorable process, the free energy of mixing must be negative. The entropy of mixing of a long-chain polymer with CO<sub>2</sub> will increase as the flexibility and hence the number of configurations available to the chain molecule increases. Interactions between CO<sub>2</sub> and polymers can reduce the enthalpy of mixing. From this point of view, Drohmann and Bechman [124] explained how the nature of monomeric unit, the degree of polymerization, the end group effect, the composition of copolymers, and the temperature influence the miscibility between CO<sub>2</sub> and polyethers. It is shown that polymers of propylene oxide are more 'CO<sub>2</sub>-philic' than those of ethylene oxide or tetrahydrofuran. The ether oxygen exhibits interactions with CO<sub>2</sub> when it is in a readily accessible position. Hydrogen bonds between polymer molecules may decrease such accessibility.

Furthermore, Shieh et al. [125-127] investigated the interaction between supercritical CO<sub>2</sub> and nine crystalline polymers and eleven amorphous polymers by testing the change in appearance, weight, thermal and mechanical properties before and after the sorption of CO<sub>2</sub>. At 3000 psi and 40°C PMMA absorbed 12.96 wt.% of CO<sub>2</sub> while polystyrene absorbed 4.48 wt.% of CO<sub>2</sub>. The treatment time for all reported samples was one hour. These results were compared to those from semi-crystalline polymers under the same conditions of CO<sub>2</sub> treatment. High-density polyethylene

(HDPE) absorbed 1.22 wt.% of CO<sub>2</sub>, low-density polyethylene absorbed 1.36 wt.% of CO<sub>2</sub>, polypropylene absorbed 1.98 wt.%, and Teflon absorbed 0.51 wt.% of CO<sub>2</sub>. Semi-crystalline polymers always absorb less CO<sub>2</sub> than the amorphous polymers.

### **2.3.3. Solubility of CO<sub>2</sub> in Polymers (S-L EOS)**

#### **2.3.3.1. Solubility of CO<sub>2</sub> in Polystyrene**

The solubility of CO<sub>2</sub> in polymers, the upper limit of CO<sub>2</sub> dissolved into polymers, is an important consideration in various polymer processes. For examples, the solubility of the CO<sub>2</sub> in one polymer directly affects the foaming ability, the viscosity reduction, and the amount of a particular substance that can be impregnated into the polymer. Table 2.2 compares the advantages of three techniques to measure the solubility, which are gravimetric, pressure decay, volumetric, and on-line visualization.

Wissinger et al. [128, 129] studied the sorption behavior of CO<sub>2</sub> in various polymers at relatively low temperatures (35, 50, and 65°C) and pressures up to 100 atm. Sato et al. [130, 131] characterized both solubility and diffusion coefficients of CO<sub>2</sub> and N<sub>2</sub> in polypropylene, high-density polyethylene, and polystyrene under high temperatures and a wider pressure range by using one gravimetric method. Zhang et al. [132] monitored the phase separation of the CO<sub>2</sub>/PS system at 215°C by attaching an in line optical window on an extruder. They all presented a linear relation between the solubility and the saturation pressure, or a Henry's law ( $C = HP$ ) behavior. The experimental data are compared in Figure 2.6.

### 2.3.3.2. Sanchez-Lacombe Equation of State (S-L EOS)

The Sanchez-Lacombe equation of state [133-135] was developed based on lattice-fluid theory, and therefore it can model the sorption of CO<sub>2</sub> in non-crystalline, non-crosslinked or slightly crosslinked polymers above their glass transition temperature. Researchers [136-138] have successfully applied the S-L EOS to model the sorption of high-pressure gases into solid, amorphous polymers, and molten polymers. Compared with Henry's law ( $C = HP$ ) that gives a linear relation between the solubility ( $C$ ) and the saturation pressure ( $P$ ), S-L EOS can fit the solubility curve better in a wider pressure range. At low-pressure region, Henry's law may be accurate enough, but when the pressure changes over a large range, as during a microcellular foaming process, the solubility will not completely follow Henry's Law. The Sanchez-Lacombe equation of state was found to correlate well the CO<sub>2</sub> solubility data in polystyrene.

The Sanchez-Lacombe equation of state is:

$$\tilde{\rho}^2 + \tilde{P} + \tilde{T} \left\{ \ln(1 - \tilde{\rho}) + \left(1 - \frac{1}{r}\right) \tilde{\rho} \right\} = 0 \quad (2.1)$$

The number of lattice sites occupied by a molecule is represented by  $r$ , which for polymers assumes a value near infinity. The reduced properties, temperature ( $\tilde{T}$ ), pressure ( $\tilde{P}$ ), and density ( $\tilde{\rho}$ ) are given as follows.

$$\begin{aligned} \tilde{P} &= P/P^*, \quad P^* = \varepsilon^*/v^*; \\ \tilde{T} &= T/T^*, \quad T^* = \varepsilon^*/R; \\ \tilde{\rho} &= \rho/\rho^*, \quad \rho^* = M/rv^*; \\ \tilde{v} &= 1/\tilde{\rho} = V/V^*, \quad V^* = N(rv^*) \end{aligned} \quad (2.2)$$

$T^*$ ,  $P^*$ , and  $\rho^*$  are characteristic parameters given for each individual gas and polymer.  $\varepsilon^*$  is the interaction energy per mer,  $R$  is the gas constant,  $v^*$  is the close-packed volume of a mer,  $M$  is the molecular weight, and  $N$  is number of molecules in a system.

For a binary mixture, such as CO<sub>2</sub> and polystyrene, these parameters are determined from pure component parameters using the mixing rules [133, 134]. One major advantage of S-L EOS is that only one adjustable parameter, the binary interaction parameter ( $\delta_{ij}$ ), which is used in the mixing rules to correct the deviation of the characteristic pressure of the mixture,  $P^*_{i2}$ , from the geometric mean, is required to fit. This binary interaction parameter ( $\delta_{ij}$ ) can be adjusted to fit the experimental data. Regarding the use of the S-L EOS to model gas-polymer systems, the following assumptions are made: 1) The solubility of the gas in the polymer represents equilibrium data; 2) The solubility of the polymer in the high-pressure gas phase is essentially zero; 3) The amorphous polymer above its  $T_g$  can be modeled as a liquid. The solubility is determined by equating the chemical potential of CO<sub>2</sub> in the polymer to that in the gas phase at a given temperature and pressure.

Table 2.3 shows the characteristic EOS parameters for the CO<sub>2</sub>/polystyrene system [136].

### **2.3.4. Glass Transition and Crystallization**

It has been well documented that carbon dioxide is an effective plasticizing agent for polymers, affecting both the glass transition and crystallization.

#### **2.3.4.1. Glass Transition Temperature ( $T_g$ )**

$T_g$  is the transition temperature of a homopolymer from the glassy state to the rubbery state. In general,  $T_g$  is the onset of coordinated molecular motion of polymer chains. At temperatures below  $T_g$ , only vibrational motions are possible, and as a result the polymer is hard and glassy. As the temperature is increased, the polymer chains get enough free volume for large-scale movements and the polymer shows rubber-like properties [139].

From a thermodynamic point of view, two approaches are commonly applied to determine the value of  $T_g$ .

##### **(1) Zero Entropy**

Based on the assumption of infinitely slow cooling, DiMarzio and Gibbs [85, 86, 140-142] pointed out that, the polymer essentially becomes ‘frozen’ and has zero entropy at an ideal glass transition temperature  $T_2$ . It is reasonable to assume that the entropy should also be zero at  $T_g$  if the decrease in entropy is the cause of the glass transition. This is called Gibbs-DiMarzio criterion of the glass transition.

##### **(2) Transition of Second-order properties**

$T_g$  is usually measured experimentally by determining the heat capacity ( $C_p$ ), volume expansion coefficient ( $\alpha$ ), or compression coefficient ( $K$ ), which change with temperature. The temperature at the point of discontinuity on the curve is treated as the

glass transition temperature [142]. When a polymer is in the glass transition stage, a sharp jump of these properties at  $T_g$  is expected. The above variables can be expressed as the second-order derivatives of the free energy.

$$\begin{aligned} \left( \frac{\partial^2 G}{\partial T^2} \right)_P &= \left( \frac{\partial S}{\partial T} \right)_P = \frac{C_P}{T} \\ \left( \frac{\partial^2 G}{\partial P^2} \right)_T &= \left( \frac{\partial V}{\partial P} \right)_T = -KV \\ \left( \frac{\partial}{\partial T} \left( \frac{\partial G}{\partial P} \right)_T \right)_P &= \left( \frac{\partial V}{\partial T} \right)_P = \alpha V \end{aligned} \quad (2.3)$$

### (3) Plasticization of Glassy Polymers by CO<sub>2</sub>

Due to the high solubility in polymers compared with other gases such as N<sub>2</sub>, CO<sub>2</sub> can cause significant plasticization resulting in substantial decreases in  $T_g$ . The lowering of the glass transition temperature can be closely related to the interaction between CO<sub>2</sub> and polymers.

Chiou and coworkers [143] studied the effect carbon dioxide on the glass transition temperature of various polymers, including PMMA, polystyrene, PVC, PC, and PET. They used the differential scanning calorimeter (DSC) equipped for high pressure and found that at 20 atm, the  $T_g$  of PMMA was reduced by 45°C at that pressure, while that of PS was reduced by 22°C. Calculation results, from a theoretical relation developed by Chow [144, 145] for estimating the depression of  $T_g$  caused by diluents, were compared with the experimental data. Winssinger and Paulaitis [146]

applied another experimental technique to determine the  $T_g$  changing with  $\text{CO}_2$  concentration and pressure. The glass transition temperature was determined from measurements of creep compliance as a function of time for PS and PMMA in the presence of  $\text{CO}_2$  at a constant temperature and pressure.

A new device was designed by Hwang and Cha [147] to measure the  $T_g$  reduction of PS and ABS by applying the concept that the modulus of elasticity will change near the glass transition temperature. It was found that the glass transition temperature of both polymers drops to room temperature with the increase of  $\text{CO}_2$  solubility.

A new phenomenon of retrograde vitrification that a transition directly from liquid to glass occurs with increasing temperature was predicted and experimentally confirmed by Condo et al. [85, 86] for PMMA. Based on the study, three glass transition temperatures take place for Poly(MMA-co-St) upon changing the temperature isobarically in a narrow pressure range. It is unique for PMMA. For PS, only one  $T_g$  for each pressure is present. This phenomenon was further studied and applied to make sub-microcellular foams by Handa et al. [32, 33] using high-pressure DSC.

Figure 2.7 gives the  $T_g$  reduction of PS determined by the high-pressure DSC technique [148-150].

#### **2.3.4.2. Crystallization**

The sorption and diffusion of  $\text{CO}_2$  in polymer lead to plasticization that increases the motions of polymeric segments. As a result, the rearrangement of such segments into crystals becomes kinetically possible. As early as 1985, Chiou et al. [151] found that the

sorption of CO<sub>2</sub> can induce crystallization in PVF<sub>2</sub>/PMMA blends and causes appearance of a secondary melting endothermic peak on DSC spectrums. Induced crystallization of PET was also discussed. Baldwin et al. [47, 152] and Kumar et al. [153, 154] also reported the crystallization of PET due to sorption of CO<sub>2</sub> during the microcellular foaming process.

For the crystallization rate, Mizoguchi et al. [155] observed that the crystallization rate of PET increases in the presence of CO<sub>2</sub>. Similarly, Handa et al. [156] reported the crystallization of sPS was significantly accelerated by CO<sub>2</sub> dissolution. Takada et al. [157] further studied the crystallization kinetics of PP with the sorption of CO<sub>2</sub>. They found that the presence of CO<sub>2</sub> does not change the crystalline structure, however, does change the crystallization rate. When the polymer is isothermally crystallized in the crystal growth controlled temperature region, CO<sub>2</sub> dissolution accelerates the crystallization rate by reducing the interchain interactions and increasing the chain mobility. Otherwise, due to the same reason, in the nucleation controlled temperature region, the overall crystallization rate decreases with the sorption of CO<sub>2</sub>.

### **2.3.5. Diffusivity and Interfacial Tension**

#### **2.3.5.1. Diffusivity**

No doubt it is important to know the diffusivity of CO<sub>2</sub> in polymers, especially in polymer melts because either the sorption rate of CO<sub>2</sub> in polymers or the foam cell growth rate are affected by the CO<sub>2</sub> diffusion rate.

In Figure 2.8, the mutual diffusion coefficient is given at three temperatures (100, 150, and 200°C). Sato et al. [130, 131] obtained these data by using a magnetic

suspension balance. During the experiment, the weight change with the sorption time of CO<sub>2</sub> was recorded and a one-dimensional diffusion in the polymer sample sheet was assumed. The diffusion coefficient was treated as independent of gas concentration and the sample thickness was assumed to be constant. Other measurement methods and diffusivity of CO<sub>2</sub> in other polymers can be seen in literatures [158-160].

### **2.3.5.2. Interfacial Tension**

The interfacial tension between polymer and CO<sub>2</sub> is very important in understanding the CO<sub>2</sub> assisted polymer processing, such as foaming and blending. The Axisymmetric Drop Shape Analysis (ADSA) technique was applied by Li et al. [148, 161] to measure the interfacial tension between PS and CO<sub>2</sub> over the pressure range 1-140 atm and at 3 different temperatures ( 210, 220, 230°C). As shown in Figure 2.9, at 210 °C, the interfacial tension decreases quickly from 24.32 to 14.55 dyn/cm as the pressure of CO<sub>2</sub> increases from 1 atm to 70.5 atm and then decreases at much slower rate to 13.60 as pressure further increases to 137.0 atm. A similar trend was found at the other temperatures.

### **2.3.6. Viscosity Reduction**

Because of its pivotal role in equipment design and process simulation, increased attention has been given to understand the rheological properties of CO<sub>2</sub>/polymer melt systems.

In general, the viscosity is observed to decrease as CO<sub>2</sub> is dissolved into various polymer melts. This viscosity reduction is greatly favorable for processing the high

molecular weight polymers where the high viscosity is the major obstacle. It also facilitates the processing of temperature sensitive polymers at lower temperatures to prevent thermal degradation and save energy.

### **2.3.6.1. Shear Viscosity Measurement**

To measure the viscosity of CO<sub>2</sub>/polymer solutions, traditional rheometers are modified and two issues must be emphasized: one is to ensure the formation of a homogeneous solution before the measurement; the other is to prevent phase separation during the measurement. Early work for foaming researches demonstrated many experimental devices capable of measuring viscosities of polymer/blowing agent mixtures under high pressures, based on which new devices are specially developed for the CO<sub>2</sub>/polymer solutions. These devices are classified into two categories: 1) pressure driven, and 2) drag driven.

Pressure driven devices can be either a capillary or a slit extrusion rheometer controlled by a back-pressure regulator. This method was originally designed for viscosity measurement of polymers with fluorocarbon blowing agents [162, 163].

Recently, a capillary rheometer was used by Gerhardt et al. [164-166] to measure the shear viscosity of polydimethyl siloxane (PDMS) containing dissolved CO<sub>2</sub>. A sealed loading apparatus helps the transfer of an equilibrated sample to the rheometer and a back-pressure assembly at the exit holds the gas in the solution. Corrections for back-pressure, wall friction, and entrance/exit pressure drop, were considered in the viscosity calculation. A similar rheometer was used by Kwag et al. [167] to measure the shear viscosity of polystyrene (PS) with dissolved CO<sub>2</sub> and several refrigerants. Lee et

al. [168, 169] applied a foaming extrusion apparatus to determine the viscosity of PS/CO<sub>2</sub> solutions. A capillary tube die with two pressure transducers mounted along the flow stream was used and the phase separation was prevented by maintaining a high pressure in the die. Using a positive displacement pump, a metered amount of gas was injected into the extrusion barrel and then mixed with polymer melts. Such a capillary rheometer was also applied by Areerat et al [170, 171] to measure the viscosities of low-density polyethylene (LDPE) and polypropylene (PP) with CO<sub>2</sub> concentration monitored on-line by the near-infrared spectroscopy.

By using the similar extrusion apparatus, a slit die can also be used to measure the shear viscosity of polymer/CO<sub>2</sub> solutions. The pressure drop along the flow streamline can be directly measured without worrying about the entrance/exit pressure correction or pressure measurement error created by the curvature of the capillary die. However, the total pressure drop may be lower than that in a capillary die, which may affect the measurement accuracy. Elkovitch et al. [172-174] applied a slit die to measure the viscosity reduction for CO<sub>2</sub>/PS and CO<sub>2</sub>/poly(methyl methacrylate) (PMMA) without back-pressure control. Royer et al. [175, 176] attached nozzles of different sizes on the slit die to hold the high pressure and measured shear viscosities of PS, PMMA, PP, LDPE, and poly(vinylidene fluoride) (PVDF) with dissolved CO<sub>2</sub>. Lee et al. [177] also applied a wedge die mounted on a twin-screw extruder to measure the viscosities of CO<sub>2</sub>/polymers. Gendron et al. [178-180] examined the rheological behavior of PS and PP with dissolved CO<sub>2</sub> by using a commercial on-line rheometer, basically a slit contraction, mounted on a twin-screw extruder.

Overall, the pressure driven devices have been found convenient to provide accurate rheological data. Their limitation is that the large pressure drop across the capillary or slit die limits the CO<sub>2</sub> concentration dissolved in the polymer melts and as a result viscosities are usually measured at low CO<sub>2</sub> concentration to ensure the formation of a single phase solution. Also in the low shear rate region, the small pressure drops detected, regardless of the large absolute pressure, may cause uncertainties in the raw data.

On the other hand, drag driven devices can be used to measure shear viscosities at low shear rates near the Newtonian plateau. They are usually operated at or near equilibrium CO<sub>2</sub> concentration and a steady uniform distribution of pressure, stress and deformation rate can be created. However, such devices are usually difficult to design because the signals (ex. torque, force, and displacement) have to be transferred under pressure through a dynamic seal, although a magnetic sensor may improve the design.

A magnetically levitated sphere rheometer was designed by Royer et al [181] to study the viscosity of PDMS/CO<sub>2</sub> solution. In this design, the sphere is held stationary at a fixed height through magnetic levitation while the cylindrical sample chamber is moved vertically to generate different shear rates. The device provides a non-homogeneous flow field and needs to be calibrated against a known fluid viscosity. Recently, a Couette viscometer was designed by Oh et al. [182] to measure the viscosity of PS/CO<sub>2</sub>. A magnetic transmission has been used to eliminate dynamic seals and reduce torque losses in the drive train. The viscosity near the Newtonian plateau was evaluated from the torque and the rate of rotation.

### 2.3.6.2. Shear Viscosity Prediction

As discussed above, the viscosity decreases as the dissolved CO<sub>2</sub> concentration increases for various polymer melts. It is also found that the viscosity curves (i.e., shear viscosity versus shear rate) of the polymer/CO<sub>2</sub> solution are usually similar in shape to that of pure polymer, and are therefore analogous to the effect of increasing temperature or decreasing pressure. These analogies imply that carbon dioxide affects the viscosity of polymer melts following a similar mechanism to the temperature and pressure, predominantly through a change in free volume. Other factors, such as the improvement in polymer chain mobility, the dilution of polymer chains, and the reduction of chain entanglement upon CO<sub>2</sub> plasticization, also contribute to the viscosity reduction.

As a consequence, the traditional scaling techniques can be used and a scaling factor  $a_c$ , similar to the familiar temperature-dependent shift factor  $a_T$  employed in time-temperature superposition, can be applied to represent the influence of the CO<sub>2</sub> concentration [165-167, 169, 175, 176, 181].

Although power law or Cross-Carreau models can fit the shear thinning behavior easily, extensive research has been focused on how to predict the effect of CO<sub>2</sub> concentration on viscosity of various polymer/CO<sub>2</sub> solutions. Doolittle's free volume theory [183] is always used as the starting point:

$$\eta_0 = A \exp\left(\frac{B}{f(T, P, \omega_g)}\right) \quad (2.4)$$

where  $\eta_0$  is the zero shear viscosity; A and B are unique constant parameters for the polymer.  $f(T, P, \omega_g)$  denotes the free volume fraction which is given as a function of temperature, pressure and dissolution of gas:

$$f(T, P, \omega_g) = \frac{V(T, P, \omega_g) - V^0(\omega_g)}{V(T, P, \omega_g)} \quad (2.5)$$

where  $V(T, P, \omega_g)$  is the specific volume of the polymer at temperature T, pressure P, and gas concentration  $\omega_g$ , and  $V^0$  is the hardcore specific volume.

By applying an extension of Doolittle's free volume theory, originally developed by Kelly and Bueche [184], Gerhardt et al. [165, 166] calculated the scaling factor  $a_c = \eta_o(\omega_g)/\eta_o(\text{pure polymer})$  for PDMS/CO<sub>2</sub> mixtures. Both Sanchez-Lacombe and Panayiotou-Vera equations of state, which model the  $P$ - $V$ - $T$  properties, were used to calculate the specific volumes of the pure polymer melt and polymer-gas mixture. The prediction was found to be in very good agreement with the experimental data.

Areerat et al. [170, 185] approaches this problem by substituting Doolittle's equation in the Cross-Carreau model to get a generalized equation to relate viscosity to shear rate, temperature, pressure and CO<sub>2</sub> concentration. All the model coefficients except the one corresponding to CO<sub>2</sub> concentration can be determined from the  $P$ - $V$ - $T$  data and the molten viscosity data of the pure polymer. The Sanchez-Lacombe equation of state was used to calculate the specific volume of the polymer/CO<sub>2</sub> solution and then the free volume fraction. The viscosity of LDPE/CO<sub>2</sub> and PP/CO<sub>2</sub> solutions was successfully predicted by this model.

Lee et al. [169] also started from Doolittle's equation and expressed the fractional free volume as a power law series in terms of temperature, pressure and CO<sub>2</sub> concentration. A seven-parameter model, a generalized Arrhenius equation, was built to predict the zero-shear viscosity of the neat PS melt to accommodate the effects of temperature and pressure. Further, an eight-parameter model was built to include the effect of CO<sub>2</sub> concentration.

Royer et al. [175, 176] adopted the WLF equation, a direct descendant of Doolittle's equation, to relate the viscosity scaling factors corresponding to pressure and CO<sub>2</sub> concentration to the glass transition temperature ( $T_g$ ) when the temperature is in the range from  $T_g$  to  $T_g + 100^\circ\text{C}$ . Then the effects of CO<sub>2</sub> concentration and pressure can be directly incorporated as the  $T_g$  depression, which was predicted by the Chow's model [144]. On the other hand, when the temperature is higher than  $T_g+100^\circ\text{C}$  and beyond the effective range of the WLF equation, Arrhenius analogues were applied to build the relation between shift factors and  $T_g$ . Systems of PS, PP, LDPE, and PVDF with dissolved CO<sub>2</sub> were studied by applying these models.

### **2.3.6.3. Extensional Viscosity Measurement**

Extensional viscosity is important to help understand the entrance pressure drop, foam bubble growth, and other processes related to elongational deformation. Ladin et al. [186] applied a contraction slit die attached to a foaming extrusion system to measure the entrance pressure drop, which was then converted to the extensional viscosity according to the Cogswell's analysis [187] for PBS/CO<sub>2</sub> solutions. The extensional viscosity was found to significantly depend on the CO<sub>2</sub> concentration and a large

reduction was obtained with the dissolution of CO<sub>2</sub>. Tension thinning behavior, where extensional viscosity decreases with an increase of extensional rate, was observed. The extensional viscosity was also observed to decrease as the temperature increased. By applying a similar design, Xue et al. [188, 189] studied the entrance pressure drop and extensional viscosity of PS/CO<sub>2</sub> solution. Extensional viscosity reduction and tension-thinning behavior were also reported. The entrance pressure drop was found to be a strong function of pressure. Of course, such a design can be used to measure the shear viscosity simultaneously.

#### **2.4. Foam Cell Nucleation and Growth**

A foaming process can be usually divided into two steps: cell nucleation and cell growth. Different theories or models have been used to describe both steps. Among these theories and models, a lot of physical properties, such as viscosity, solubility, surface tension, diffusivity, and glass transition temperature, are found to play important roles. The situation becomes more complex when one considers that these parameters are all functions of temperature, pressure, and CO<sub>2</sub> concentration, the major operating conditions that are also included in the models of cell nucleation and cell growth. Computational simulation is a useful tool to understand interactions between the operating conditions, the physical properties, and the cell nucleation and cell growth.

### 2.4.1. Cell Nucleation

Nucleation exists in several phase separation processes, such as bubble formation from a gas/polymer solution, water droplets formation from its vapor, and crystal formation from its amorphous phase. During nucleation, molecules conquer an activation energy barrier to accumulate together to create new phase. This is achieved by spontaneous fluctuations in density to form the embryo of the new phase. When such an embryo is less than some critical size, it will collapse back into the old phase. Otherwise, the embryo that exceeds the critical size can spontaneously grow to macroscopic size. Obviously, nucleation is different from the spinodal phase separation process in which no activation energy barrier needs to be surmounted and phase separation is a spontaneous process.

The difficulties of studying nucleation come from both theoretical analysis and experimental techniques. The nucleation is induced by the energy fluctuation, so that any changes in local temperature, pressure, and concentration, or the existence of impurities can affect the repeatability of the experiment. Most of the nucleation theories about the liquid droplets-vapor start from the following reaction:



where  $A_1$  is the monomer and  $A_i$  is the  $i$ -mer cluster [190, 191].

The classical nucleation theory (phenomenological approaches) treats the cluster as a macroscopic spherical droplet with bulk surface tension. Here, the equilibrium constant from above reaction (Eq. 2.6) is related to the Gibbs free energy and monomers collide with the cluster surface at the gas kinetic rate for an ideal gas. The classical nucleation theory can predict critical supersaturations successfully for most gases, while it is in error when predicting actual nucleation rate.

Another theory, the kinetic approaches, evaluates the forward and backward rate constants without direct reference to formation free energies of clusters. The nucleation rates can be calculated from the interaction potential between particles. In practice, the uncertainties in these potentials for real systems forces the theories to fit their parameters using experimental data for surface tension, the liquid density, or even the nucleation rates themselves. This limits the testing of any theoretical result.

The microscopic approach is the third choice that involves computer simulation with molecular dynamics and Monte Carlo techniques. This avoids many of the limitations in phenomenological approaches; however, the typical volume and time in computation work restrict simulation to the properties of isolated clusters, which requires the definition of a cluster.

Specifically, the foaming process belongs to binary nucleation where bubbles are formed from a binary homogeneous solution. The classical nucleation theory is commonly used to describe this process. Below we will focus on the homogeneous classical nucleation theory and its modification, heterogeneous nucleation theory. Finally, we will mention some other theoretical approaches.

### 2.4.1.1. Homogeneous Nucleation Theory

Without effective heterogamous nucleation sites, homogeneous nucleation is dominant. The homogeneous nucleation rate (number of clusters which grow beyond the critical cluster size per unit volume and unit time) [192-198] can be expressed as:

$$N_0 = C_0 f_0 \exp\left(-\frac{\Delta G_{crit}}{k_B T}\right) \quad (2.7)$$

Where  $C_0$  is the number of gas molecules dissolved per unit volume of the primary phase,  $k_B$  is the Boltzmann's constant,  $T$  is the temperature,  $\Delta G_{crit}$  is the critical free energy to form a nucleus of critical size, and  $f_0$  is a kinetic preexponential factor that is believed to be weakly dependent upon temperature.

$f_0$  can be expressed as

$$f_0 = \left(\frac{2\sigma}{\pi m}\right)^{1/2} \quad (2.8)$$

in which  $\sigma$  is the surface tension and  $m$  is the mass of the gas molecule. The Gibbs free energy  $\Delta G$  for a spherical cluster of radius  $R$  (corresponding to the formation of new volume and new surface) is given as

$$\Delta G = -\frac{4\pi}{3} R^3 (P^G - P^L) + 4\pi R^2 \sigma \quad (2.9)$$

As a result, the critical free energy when  $\frac{\partial(\Delta G)}{\partial R} = 0$  is expressed as

$$\Delta G_{crit} = \frac{16\pi\sigma^3}{3(P^G - P^L)^2} \quad (2.10)$$

and the corresponding critical bubble size is

$$R_{crit} = \frac{2\sigma}{(P^G - P^L)} \quad (2.11)$$

where  $P^G$  is the pressure inside the critical bubble and  $P^L$  is the pressure of the surrounding liquid.

Goel and Beckman [34, 36] demonstrated that classical nucleation theory could be used to model the effects of saturation pressure, temperature, and time on the cell density when foaming PMMA. The diluent effects of CO<sub>2</sub> on the surface tension were taken into account. The product of the Zeldovich factor times the impingement rate was treated as a fitted parameter, for which  $f_0 = Z(4\pi R_{crit}^2)R_{impingement}$ . Agreement between prediction and data was found at high saturation pressures.

Based on classical nucleation theory, Xu and Wu [199, 200] simulated computationally the relationship between the pressure drop rate and the nucleation rate. When the pressure drop rate is small, the nucleation is proportional to the pressure drop rate. However it becomes independent of pressure drop rate at high pressure drop rates.

#### **2.4.1.2. Heterogeneous Nucleation Theory**

In a polymer system, heterogeneous nucleation is usual because of the existence of impurities (i.e., nucleating agents, additives, initiator residue, etc.). Bubbles prefer to

nucleate on the interface of the polymer matrix and the foreign particles because lower activation energies need to be surmounted. Colton and Suh [192-194] presented a model, based on the classical nucleation theory, for the heterogeneous nucleation in a polymer melt.

The rate of heterogeneous nucleation,  $N_I$ , is given as

$$N_I = C_1 f_1 \exp\left(-\frac{\Delta G_{crit}^{het}}{k_B T}\right) \quad (2.12)$$

where  $C_1$  is the concentration of heterogeneous nucleation sites,  $f_1$  is the frequency factor similar to  $f_0$ , and represents the frequency that gas molecules impinge upon the embryo nucleus. It is a complex function of the vibrational frequency of the atoms, the activation energy for diffusion in the polymer, and the surface area of the critical nucleus.

The critical free energy  $\Delta G_{crit}^{het}$  for heterogeneous nucleation is given as

$$\Delta G_{crit}^{het} = \frac{16\pi\sigma^3}{3(P^G - P^L)} S(\theta) \quad (2.13)$$

$S(\theta)$  is a function depending only on the wetting angle  $\theta$  of the particle-gas interface, and has values of less than or equal to 1. an expression of  $S(\theta)$  is as follows:

$$S(\theta) = (1/4)(2 + \cos\theta)(1 - \cos\theta)^2 \quad (2.14)$$

Colton and Suh [192-194] also considered the free volume change caused by the dissolved gas and the surface tension change caused by the presence of a third phase and their influence on the Gibbs free energy. They got acceptable qualitative agreement between the theory and the experimental results for the polystyrene-zinc stearate system.

### **2.4.1.3. Other Theoretical Considerations**

Ramesh et al. [201, 202] explained the nucleation phenomenon from a different point of view. They emphasized that the nucleation ‘concentrates’ on the stresses and voids for a high impact polystyrene (HIPS) system. The bubble nucleation depends on the survival of the pre-existing microvoids to grow rather than the formation of a new phase as modeled by the classical nucleation theory. If the pressure inside a microvoid exceeds the resistance offered by the surface and elastic energy, it will result in nucleation of a cell, which relies on a statistical distribution. Excellent agreement between theory and experimental data was obtained.

Lee [203, 204] attempted to apply cavitation to describe nucleation in polymer melts. Pre-existing cavities were found to play a critical role in enhancing bubble formation. This model successfully explains the effects of shear stress on nucleation in a foaming extrusion.

### **2.4.2. Cell Growth**

Cell growth is a process that involves mass, momentum, and heat transport, and complex rheological behavior of fluids. A lot of efforts [205-212] have been put in modeling a bubble growth procedure that evolves from single bubble growth models, a single bubble surrounded by an infinite sea of fluid with an infinite amount of gas available for growth, to the ‘cell model’, swarm of bubbles growing without interaction. In the ‘cell model’, the foam is divided into spherical microscopic unit cells of equal and constant mass, each consisting of a liquid envelope surrounding a single bubble. Thus the gas available for growth is limited.

To model a bubble growth process in a foaming process is still a very difficult problem, determined by the nature of the real foaming process, which may be in a batch, an extruder die, or an injection mold. To our knowledge, we have not found a solution from the commercial computational codes, such as Fluent, Polyflow, or C-mold, to solve a foaming process.

#### 2.4.2.1. Modeling [37, 213-217]

Reference [213] lists a complete historical development of bubble growth models that evolves from single bubble growth models to the ‘cell model’.

A schematic figure of the cell model is shown in Figure 2.10. If an isothermal environment is assumed for bubble growth, the problem can be highly simplified by neglecting unsteady and inertial terms in the equations of motion. Here, the viscosity of the gas is also omitted, but the interfacial tension is included.

First, the integrated momentum equation reduces to the following:

$$P_G - P_L - \frac{2\sigma}{R} + 2 \int_R^{R_f} (\tau_{rr} - \tau_{\theta\theta}) \frac{dr}{r} = 0 \quad (2.15)$$

Here,  $P_G$  and  $P_L$  are the pressures in the bubble and in the polymer melt respectively.  $\sigma$  is the interfacial tension.  $R$  and  $R_f$  are the radius of the bubble and the polymer shell respectively.  $\tau_{rr}$  and  $\tau_{\theta\theta}$  are the stresses.

If the fluid is Newtonian, a more practicable format is obtained

$$\tau_{rr} = 4\eta \frac{\dot{R}}{R} = P_G - P_L - \frac{2\sigma}{R} \quad (2.16)$$

where the bubble growth rate  $\dot{R} = \frac{dR}{dt}$ , and the Newtonian viscosity is denoted by  $\eta$ .

Otherwise, a rheological constitutive equation to describe the viscoelastic behavior of the fluid is needed, for example, the upper-convected Maxwell (UCM) equation:

$$\tau + \lambda \overset{\nabla}{\tau} = 2\eta_0^* \underline{D} \quad (2.17)$$

where the zero shear viscosity  $\eta_0^*$  could be a function of temperature, pressure, and concentration of the foaming agent.  $\underline{D}$  is the deformation gradient matrix.

1.1.1.1.1 Second, the mass balance over a bubble can be expressed as

$$\frac{d}{dt} \left[ \frac{4\pi}{3} \rho_g R^3 \right] = 4\pi R^2 D \left. \frac{\partial c}{\partial r} \right|_{r=R} \quad (2.18)$$

Third, the gas diffusion in the surrounding polymer (the control volume) is

$$\frac{\partial c}{\partial t} + \frac{\dot{R} R^2}{r^2} \frac{\partial c}{\partial r} = \frac{D}{r^2} \frac{\partial}{\partial r} \left( r^2 \frac{\partial c}{\partial r} \right) \quad (2.19)$$

where diffusivity ( $D$ ) is also a function of temperature and concentration of foaming agent.

Finally, proper initial conditions and boundary conditions need to be selected carefully according to the modeling requirement. For example, an initial condition could be a pseudo equilibrium followed by Henry's law:

$$c(r,0) = c_0^* = K_H P_{G0} \quad (2.20)$$

The boundary condition could be either with or without gas loss at the moving boundary ( $r = S(t)$ ). When the foam expansion occurs in a closed mold, such as an injection molding process, boundary conditions without foaming agent loss are reasonable. However, in an extrusion foaming process, especially when the extruded shape is thin, the influence of gas loss on the foaming efficiency must be considered.

The initial bubble radius from which bubbles begin to grow is always conveniently assumed to be the critical radius of cell nucleation.

$$R(0) = \frac{2\sigma}{(P_{G0} - P_c)} \quad (2.21)$$

where  $P_{G0}$  is the saturation pressure before nucleation and  $P_c$  is the polymer resin pressure during flowing.

In some simulations, an influence volume around each bubble is defined where the dissolved gas concentration at the edge of the influence volume is assumed to be equal to  $0.95 c_0^*$ . Here,  $c_0^*$  is the initial dissolved gas concentration before nucleation. This concentration is also treated as the nucleation threshold gas concentration below which no nucleation occurs. The bubble nucleation stops when the average gas concentration becomes less than the threshold concentration or the summation of the influence volume of all the bubbles nucleated equals the polymer initial volume.

To model an extrusion foaming process, it is still necessary to combine the macroscopic flow models with the models of microscopic behavior of the bubble shown above. Baldwin [214] modified the power law model of the flow through a constant cross-section slit die with a height  $2B$  and a width  $W$ . In the model, the influence of gas phase was included in the flow rate and viscosity. In other words, the apparent volumetric flow rate and viscosity are functions of volume fraction of bubbles in the flow.

$$\frac{dP_c}{dz} = - \left[ \frac{2+1/n}{2WB^2} Q \right]^n \frac{m}{B} \left( 1 - \frac{V_G}{Q} \right) \quad (2.22)$$

where  $Q = V_G + V_P$ , and  $V_G$  is the volume flow rate of gas.

#### **2.4.2.2. Effect of Transient Extensional Strain Hardening Viscosity on Bubble Growth**

It is not surprising that viscosity, especially the extensional viscosity, plays an important role in deciding the bubble growth. The extensional viscosity of many polymers, such as polystyrene, shows dependence on both extensional rate and time [218, 219]. The extensional viscosity increases with time and finally reaches a steady state. Also it exhibits pronounced extensional thickening; that is, the transient extensional viscosity for larger extensional rates lies above that for smaller extensional rates.

Experiments show that a bubble growth takes about 60-120 seconds in a batch process, while in a continuous extrusion foaming process, only 1-2 seconds [213]. In such a short time scale for (1-2 seconds), the effect of transient extensional strain hardening viscosity on bubble growth would be very noteworthy.

To understand this effect, simulation was done by Arefmanesh et al. [212] based on complex constitutive equations. Simulation results indicate that increasing the melt elasticity (longer relaxation time) enhances bubble growth compared with a Newtonian medium with the same zero-shear-rate viscosity. The effect of the elasticity is more pronounced at the beginning of the bubble growth when it is mainly controlled by the hydrodynamic forces. The stresses that oppose bubble growth are much smaller in a viscoelastic fluid than those in a Newtonian fluid.

### **2.4.3. Cell Coalescence**

Cell coalescence is an unfavorable phenomenon to produce closed cell structure, as the microcellular foams or insulation foams. When cells are coalesced, cell density will be deteriorated, mechanical strength will be weaker, and heat transport will be enhanced. The conjugated cells tend to coalesce because it is free energy favorable and the shear stress during the flow tends to stretch the cells, which worsens the coalescence. The most feasible way to suppress the cell coalescence is to increase the melt strength by branching, cross-linking, temperature reduction, control of molecular weight and its distribution, and blending of polymers [82].

<b>Type</b>	<b>Advantages</b>	<b>Disadvantages</b>
Long Single Extruder L/D* : 38-42	<ul style="list-style-type: none"> <li>• Less leaking point</li> <li>• Less investment</li> </ul>	<ul style="list-style-type: none"> <li>• Narrow melting/cooling control</li> <li>• Precise screw design</li> <li>• Long screw length</li> </ul>
Tandem Extruder L/D: 24-32 and 28-30	<ul style="list-style-type: none"> <li>• Independent melting/cooling control</li> <li>• Can process high-melt polymers</li> </ul>	<ul style="list-style-type: none"> <li>• More leaking points</li> <li>• High investment</li> <li>• More power consumption</li> </ul>
Twin-Screw Extruder L/D: around 25	<ul style="list-style-type: none"> <li>• Easy to control</li> <li>• Good mixing</li> <li>• Good heat transfer</li> </ul>	<ul style="list-style-type: none"> <li>• Cooling limited</li> <li>• Narrow melting/cooling range</li> </ul>

\* L/D: Screw length/screw diameter

Table 2.1. Common Extrusion Processes [5].

<b>Method</b>	<b>Description</b>
On-line clouding point [132]	<ul style="list-style-type: none"> <li>• Observation</li> <li>• High temperature, high pressure measurement</li> <li>• Slow response</li> </ul>
Pressure decay [220]	<ul style="list-style-type: none"> <li>• Indirect measurement</li> <li>• Volume Correlated by EOS</li> <li>• High temperature, high pressure measurement</li> <li>• Long measurement time</li> <li>• Large amount of sample</li> <li>• Accurate pressure reading needed</li> </ul>
Volumetric	<ul style="list-style-type: none"> <li>• Indirect measurement</li> <li>• Volume correlated by EOS</li> <li>• High temperature, high pressure</li> <li>• Long measurement time</li> <li>• Large amount of sample</li> <li>• Accurate volume and pressure reading needed</li> </ul>
Gravimetric – microbalance [128-131]	<ul style="list-style-type: none"> <li>• Direct measurement</li> <li>• Buoyancy correction by EOS</li> <li>• Low temperature only</li> <li>• Special design needed for high temperature</li> <li>• Quick measurement</li> <li>• Small amount of sample</li> <li>• Good repeatability</li> </ul>

Table 2.2. Comparison of different methods to determine solubility of CO<sub>2</sub> in polymers.

<b>Substance</b>	$\rho^*$ (g/cm <sup>3</sup> )	$T^*$ (K)	$P^*$ (atm)
CO <sub>2</sub>	1.510	305	5670
PS	1.105	735	3523

Table 2.3. Characteristic Sanchez-Lacombe EOS parameters for CO<sub>2</sub>/PS system [136].

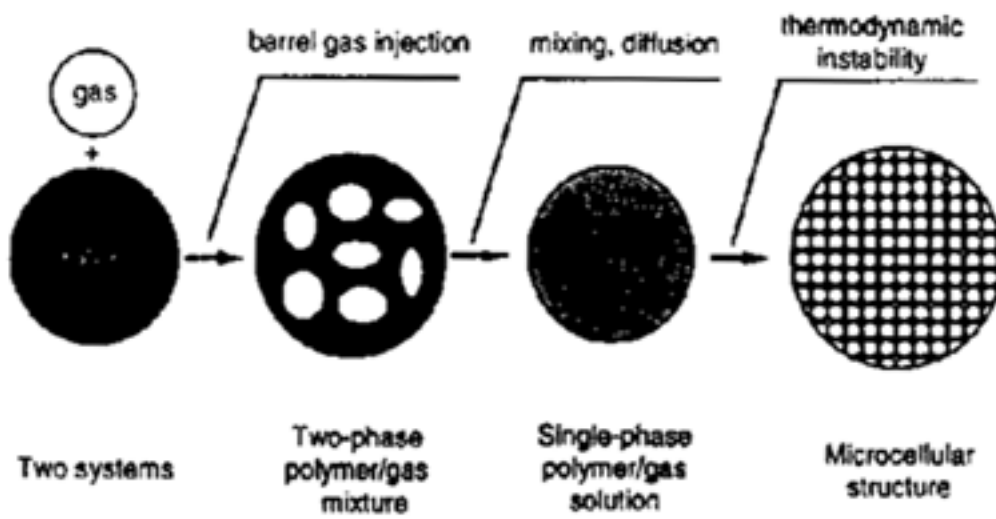


Figure 2.1. Microcellular foaming [13].

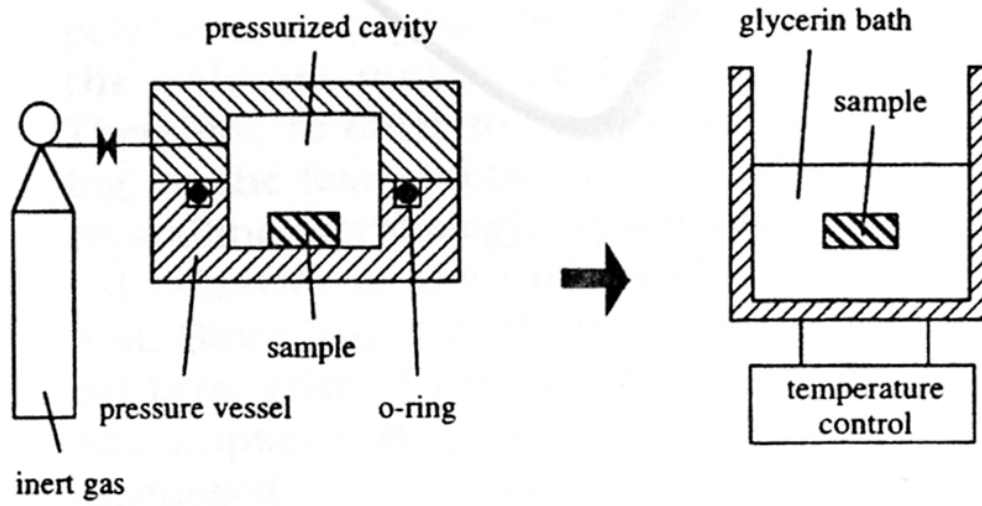


Figure 2.2. Microcellular foaming by a batch process [14].

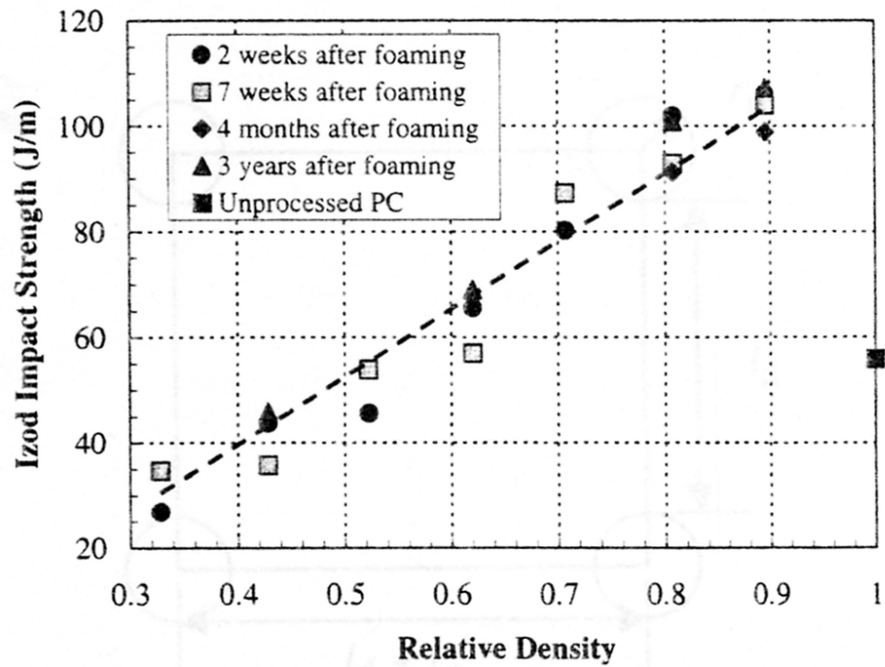


Figure 2.3. Izod impact strength as a function of relative density compared with the unfoamed PC samples [64].

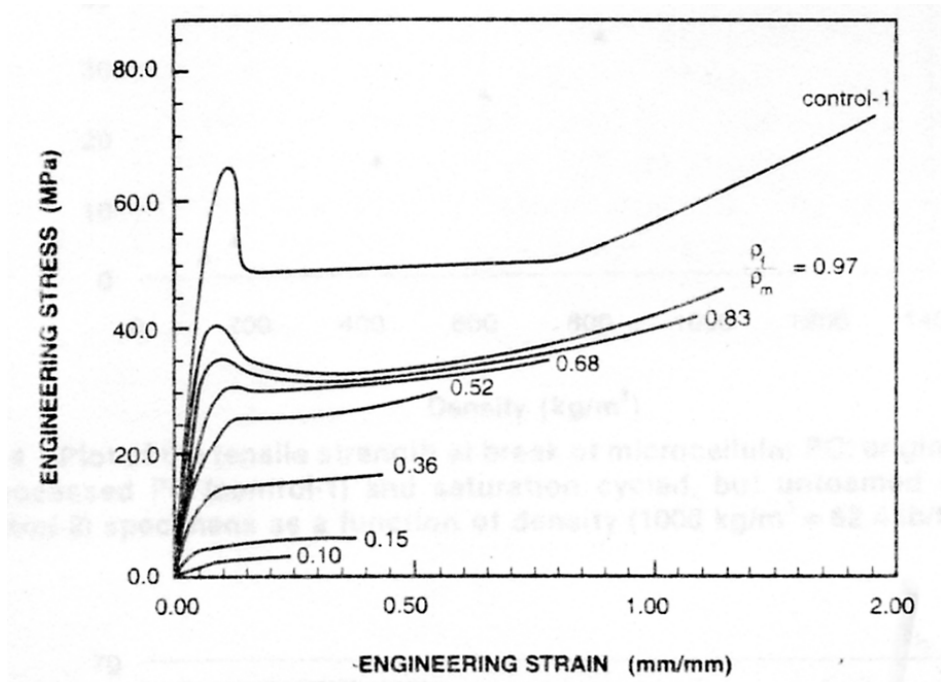


Figure 2.4. Stress-strain curves for unfoamed and microcellular PC at different relative densities [75].

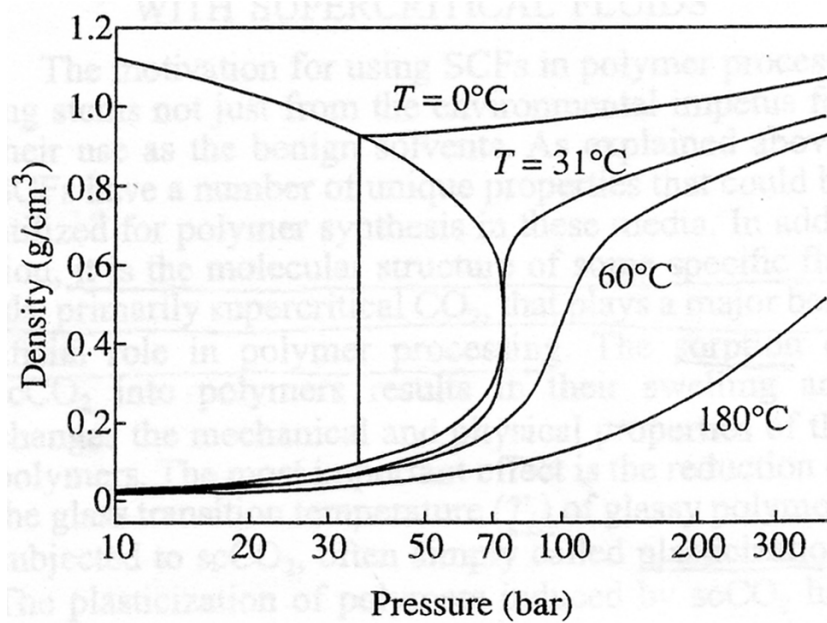


Figure 2.5. Liquid-vapor phase diagram of CO<sub>2</sub> [117].

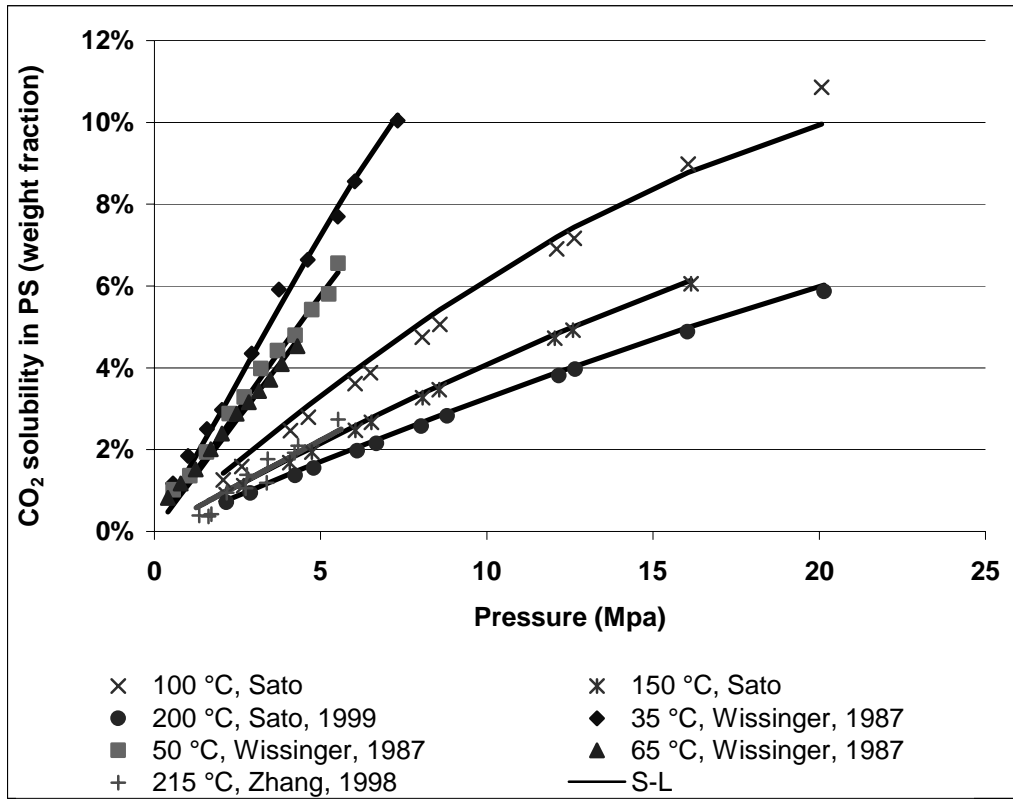


Figure 2.6. Solubility of CO<sub>2</sub> in polystyrene [128-132, 221] (the thick lines are fitted by Sanchez-Lacombe model).

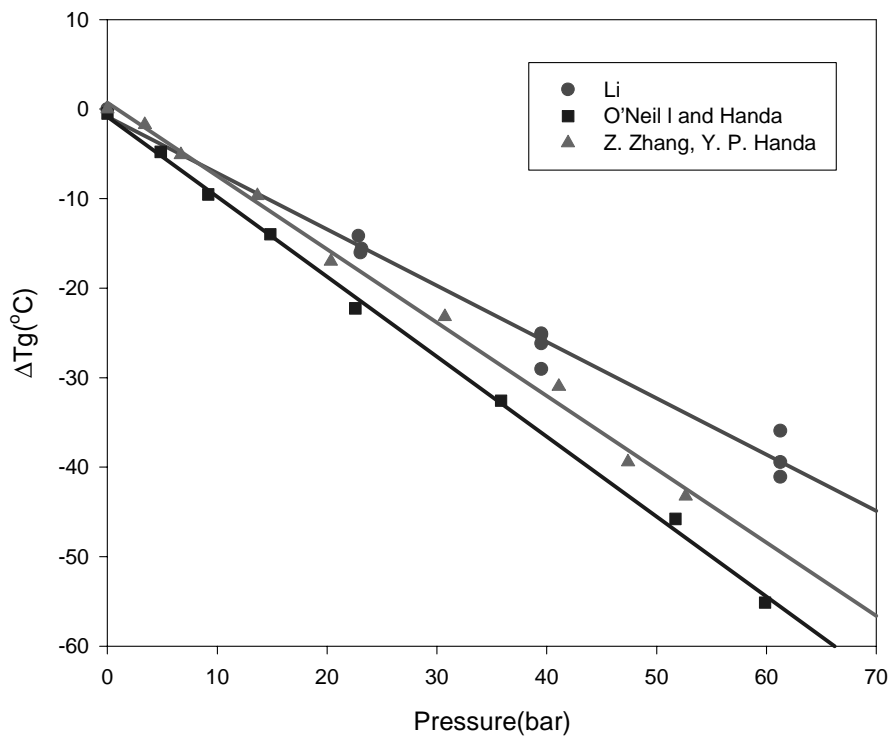


Figure 2.7.  $T_g$  reduction of PS with sorption of CO<sub>2</sub> [148-150].

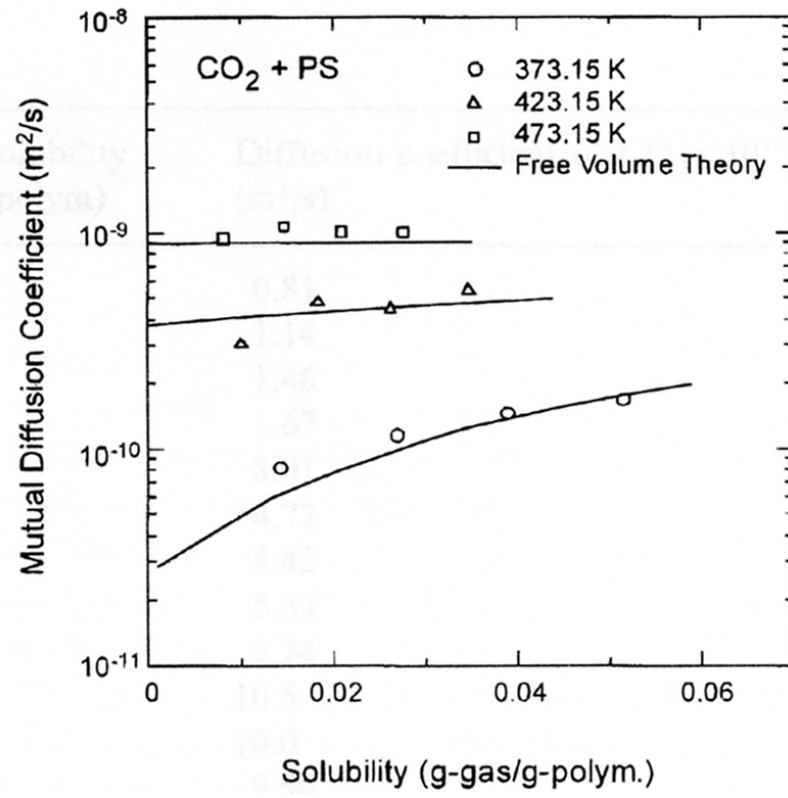


Figure 2.8. The diffusion coefficient at three temperatures (100, 150, and 200°C) [131].

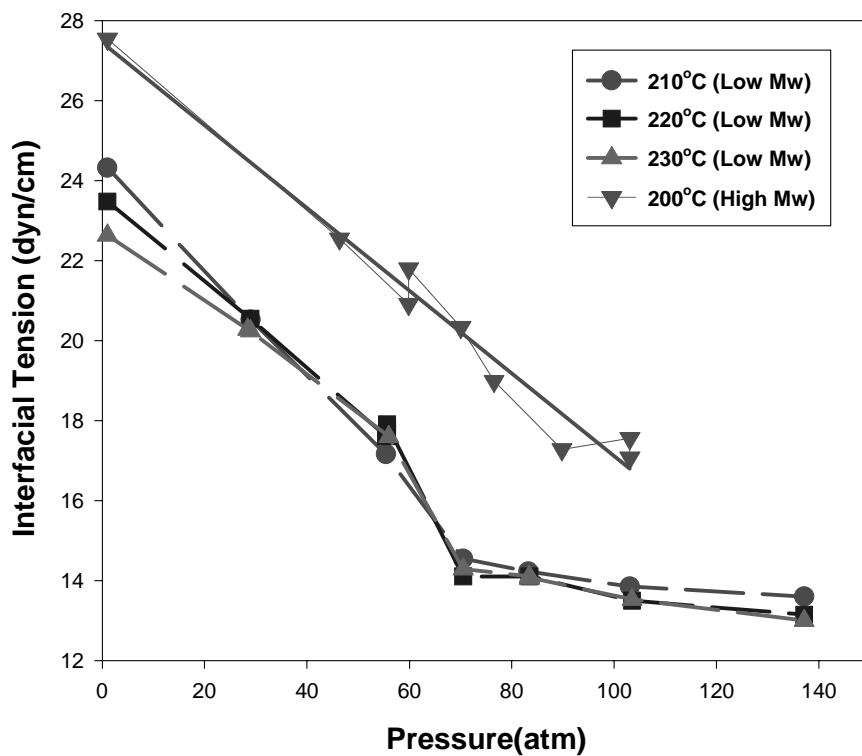


Figure 2.9. Dependence of interfacial tension between PS/CO<sub>2</sub> and CO<sub>2</sub> on pressure [148, 161].

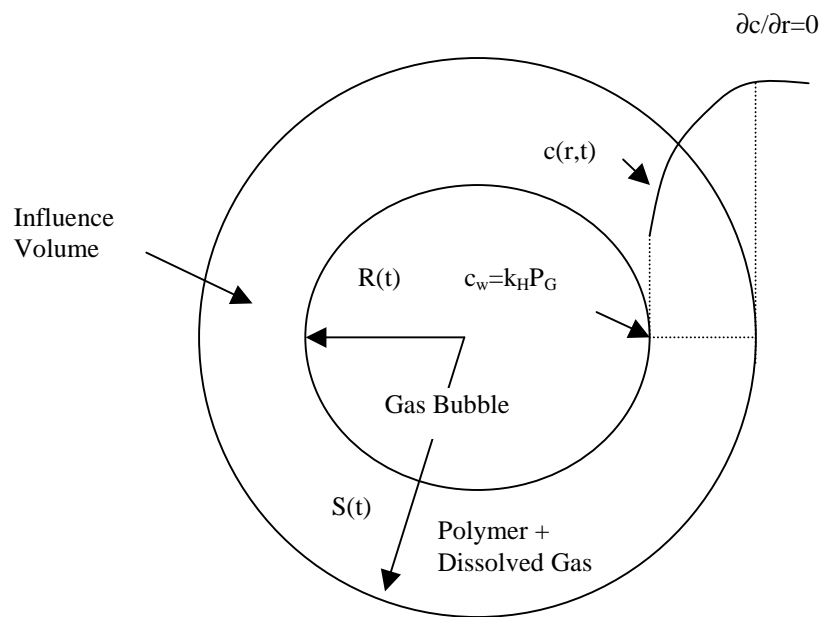


Figure 2.10. Schematic diagram of bubble growth in a liquid shell [215-217].

## **CHAPTER 3**

### **CONTINUOUS MICROCELLULAR POLYSTYRENE FOAM EXTRUSION WITH SUPERCRITICAL CO<sub>2</sub>**

#### **3.1. Introduction**

##### **3.1.1. Art and Science of Microcellular Foaming Polymers**

Foamed polymers are found in applications ranging from insulation to adsorbents [2]. Depending on the application, various foam structures are produced by applying specially designed foaming processes. Research in this area typically focuses on the correlation between foaming conditions, foam structures and final foam properties. The basic principle of foaming is to mix a blowing agent (typically a gas) into a polymer melt and induce a thermodynamic instability through a temperature or pressure change to nucleate bubbles of the blowing agent. After nucleation, the bubble growth is controlled by reducing the temperature lower than the glass transition temperature of the polymer. While traditional foaming processes have relied on hydrocarbon or chlorofluorocarbon blowing agents there has been renewed interest in reducing emissions of these volatile organic components (VOC's) to the atmosphere. A popular approach has involved the use of benign blowing agents such as nitrogen or carbon dioxide.

It is challenging to replace traditional foaming agents with CO<sub>2</sub> since CO<sub>2</sub> is usually processed at higher pressures and CO<sub>2</sub> easily escapes from the polymer matrix, which induces processing instability and shaping contraction. However, CO<sub>2</sub> has several advantages for producing microcellular foams. The liquid-like solubility and gas-like diffusivity [116] make it possible to dissolve sufficient CO<sub>2</sub> in a polymer quickly, and the high self-nucleation ability helps to create large quantity of bubbles without the aid of nucleation agents.

Microcellular foams, characterized by cell sizes smaller than 10 μm [10], are foamed polymers with special constraints. It has been shown that by keeping the cell (or bubble) size uniformly less than 10 microns in diameter, one can greatly reduce material usage without compromising mechanical properties because the bubbles are smaller than the preexisting flaws in a polymer matrix. Typical microcellular plastics exhibit high impact strength or toughness [40, 66-68, 222], and high fatigue life [73, 74]. More importantly, microcellular polymers are light in weight and consequently, they have higher mechanical strength to weight ratio than common structural foams at equivalent densities [75]. In order to realize these advantages people prefer to reduce the cell size and increase the cell density as much as possible.

### **3.1.2. Continuous Production Essential for Economic Viability**

Extensive efforts have been made in the batch microcellular foaming process [14-16, 34, 35, 39, 53, 79, 80], which involves rapidly depressurizing a saturated solution of polymer and CO<sub>2</sub> contained in a batch vessel. Compared with the batch process, a continuous extrusion foaming process [11] is more economically favorable

because of its high productivity, easy control and flexible product shaping. The axiomatic approach was applied by Suh to design an overall microcellular extrusion process [13, 22, 223] concluding that a large pressure gradient is necessary to a microcellular foaming process. Some work has been done on the influence of processing conditions to the foam size or density. Effects of processing pressure were studied when the maximum amount of CO<sub>2</sub> was injected into a high impact polystyrene (HIPS) melt at each processing pressure. The cell density was found to increase with the processing pressure since the solubility of gas increases [19]. The pressure drop rate also plays an important role in deciding the cell size and cell density since cell nucleation time period is affected by the time period over which the thermodynamic instability is induced [20, 21]. Cell coalescence is a competing phenomenon that reduces the cell density during the cell growth process. It was found that low melt temperatures and low die temperatures [31, 51] as well as improving the melt strength [224, 225] can reduce the cell coalescence.

One major reason why the foaming process is so complex is that the key physical variables, such as viscosity, glass transition temperature, surface tension, CO<sub>2</sub> solubility and diffusivity, are all functions of temperature, pressure, and CO<sub>2</sub> content as well. A good example of this complexity is the pressure drop and the pressure drop rate in the die, which is controlled by the viscosity, the die dimension, the die temperature, and the screw rotation speed (or the flow rate). It is a well-known phenomenon that CO<sub>2</sub> can greatly reduce the viscosity of a polymer melt. In addition to shear rate and temperature,

the viscosity greatly depends on CO<sub>2</sub> content and pressure that are changing continuously along the foaming die. Therefore, the pressure in the die determines the CO<sub>2</sub> solubility and the viscosity, but the viscosity dictates how high a pressure can be created.

Recently, the rheological behavior for mixtures of polymer and supercritical CO<sub>2</sub> has been reported. Gerhardt and Kwag et al. [165, 167] used a capillary rheometer with a special loading assembly and a back pressure assembly to measure the viscosity of polymers with dissolved CO<sub>2</sub> and several refrigerants. The sorption of CO<sub>2</sub> and the viscosity measurement are two separate procedures and the data from different shear rates (1-2000 s<sup>-1</sup>), temperatures (150 and 175°C), pressures, and CO<sub>2</sub> contents, were shifted to one master curve, and the curve was correlated by the Cross model. Lee et al. [168, 169] applied a foaming extrusion apparatus to determine the viscosity of a polystyrene/supercritical CO<sub>2</sub> solution. A capillary tube die with two pressure transducers mounted along the flow stream was used and phase separation was prevented by maintaining a high pressure in the die. The shear thinning behavior was described by the generalized Cross-Carreau equation and the influence of temperature, pressure and CO<sub>2</sub> content was integrated into the zero-shear viscosity using the Arrhenius form. Elkovitch [226, 227] applied a slit die to measure the viscosity reduction for CO<sub>2</sub>/PS and CO<sub>2</sub>/PMMA without backpressure control. Experimental viscosity data at 175°C and different CO<sub>2</sub> concentrations from Kwag et al. [167] are selected in this paper to represent the rheological behavior of polystyrene in the simulation.

The solubility of CO<sub>2</sub> in the polymer melt determines the concentration limit and the position of nucleation onset in the die. Wissinger [128, 129] studied the sorption behavior of CO<sub>2</sub> in various polymers at relatively low temperatures (35, 50 and 65°C) and pressures up to 100 atm. Sato [130, 131] characterized both solubility and diffusion coefficients of CO<sub>2</sub> and N<sub>2</sub> in polypropylene, high-density polyethylene, and polystyrene under high temperatures and a wider pressure range by using one gravimetric method. Zhang [132] monitored the phase separation of the CO<sub>2</sub>/PS system at 215°C by attaching an in line optical window along an extruder. They all presented linear relations between the solubility and the saturation pressure, or Henry's law ( $C = HP$ ) behavior. At low-pressure region, Henry's law is accurate enough, but when the pressure changes over a large range, as during a microcellular foaming process, the solubility will not completely follow Henry's Law. The Sanchez-Lacombe equation of state [136, 137] was found to correlate well the CO<sub>2</sub> solubility data in polystyrene.

In this paper, the contraction flow in the extrusion die was simulated with FLUENT computational code to predict profiles of pressure, temperature, viscosity and velocity. The location of nucleation onset was determined based on the pressure profile and equilibrium solubility. Systematic experiments were performed to unveil effects of three key operating conditions: CO<sub>2</sub> content, processing pressure and pressure drop rate, on the cell size and cell density. Experimental results were compared with simulations and both were used to gain insight into the foaming process.

### 3.2. Experimental

The polymeric material used in this study is polystyrene resin (Styron 685D) from Dow Chemical. The physical foaming agent, bone-dry grade carbon dioxide (99%), is provided by Praxair.

Experiments were carried out on a two-stage single-screw extruder (Rheomex 252p) from Haake (Figure 3.1). The screw has a diameter of 3/4 inches and a length to diameter ratio (L/D) of 25. CO<sub>2</sub> was injected in the barrel from a port initially designed for venting, located between the two screw stages where the barrel pressure is relatively low. A static mixer (Omega, FMX8441S), with 6 elements, 0.28" in diameter and 2.7" long, was attached to the end of the extruder to provide extra mixing intensity. A capillary die with a 0.5 mm diameter and 10 mm length nozzle was custom made to generate high and rapid pressure drops. Two pressure transducers (Dynisco PT422A-10M-6/18) were installed at the end of barrel and in the die to measure the highest pressure of the system and the pressure just at the entrance of the nozzle, respectively.

CO<sub>2</sub> was delivered from a syringe pump (ISCO 260D) with a cooling jacket. The pump was run in either constant pressure or constant volumetric flow rate mode. The CO<sub>2</sub> pressure and volumetric flow rate can be read precisely from the pump controller. Just before the injection port, another pressure gauge was installed to accurately measure the gas pressure injected into the barrel.

CO<sub>2</sub> is compressed to a certain pressure in the syringe pump at 40°C reaching a supercritical state. Upon injection into the barrel, it is preliminarily mixed with the polystyrene melt by the screw rotation. A one-phase solution is formed when the mixture flows through the static mixer. Nucleation occurs in the die because of the solubility reduction due to the quick and large pressure drop realized by the narrow capillary nozzle. The foamed extrudate flows freely out to the air and vitrifies.

The amount of CO<sub>2</sub> injected into the polymer melt is adjusted by the syringe pump which is normally running at a constant volumetric flow rate. At steady state, the gas pressure will also be constant. By measuring the mass flow rates of polystyrene melt at different screw rotation speeds, the weight fraction of CO<sub>2</sub> in polymer melt is known. To increase the pressure drop in the die, the screw rotation speed is increased. The chosen screw rotation speeds used in this work are 10,15,20, 25, and 30 rpm, which correspond to mass flow rates of polymer of 3.8, 5.4, 7.2, 9.1 and 10.9 grams/min.

Cell size ( $D_f$ ), which is characterized by the diameter of the foam cells, and cell density ( $N_f$ ), which is the number of cells per unit volume, are determined by analyzing images obtained from scanning electron micrographs (SEM) using Scion image software. A micrograph showing 20-50 bubbles is chosen, and the number of bubbles,  $n$ , in the micrograph is determined by the software. If the area of the micrograph is  $A$  cm<sup>2</sup> and the magnification factor is  $M$ , the cell density can be estimated by

$$N_f = \left( \frac{nM^2}{A} \right)^{3/2} \quad (3.1)$$

The cell size is the average circle equivalent diameter for all the bubbles in the micrograph.

### 3.3. Computations

#### 3.3.1. Sanchez-Lacombe Calculation of CO<sub>2</sub> Saturation Solubility as a Function of Temperature and Pressure

Instead of Henry's law ( $C = HP$ ), the Sanchez-Lacombe equation of state, which has been shown successfully model the sorption of high-pressure gases in amorphous polymers or polymer melts, was applied to represent the solubility as a function of temperature and pressure. The solubility is determined by equating the chemical potential of CO<sub>2</sub> in the polymer to that in the gas phase at a given temperature and pressure. For the calculation, the gas phase is assumed pure, i.e., the polymer is insoluble in the gas. The binary interaction parameters ( $\delta_{ij}$ ) were selected by fitting the Sanchez-Lacombe EOS with the literature solubility experimental data (38 - 41) at different temperatures. Then the fitting  $\delta_{ij}$  values were averaged to obtain 0.0249 because we found they change irregularly in a narrow range (0.0165 to 0.0359) for temperature varying from 35 to 200°C. At a typical foaming condition (175°C and 10.34 MPa), the solubility is calculated to be 3.82%, 3.62%, and 3.36% when the  $\delta_{ij}$  is the lowest (0.0165), the average (0.0249) and the highest (0.0359) respectively. Therefore not a big error was introduced by applying the average value for all the temperatures. This value was assumed independent of temperature and was used to generate the solubility surface shown in Figure 3.2.

### 3.3.2. FLUENT Simulation of Contraction Flow in Die

To determine pressure and temperature distributions in the die and, as a first approximation, to locate the nucleation position, the FLUENT computational fluid dynamics program was applied to combine the equations of motion with the energy balance and the rheological viscosity model. Because FLUENT cannot handle two-phase flows, the simulation assumes that the CO<sub>2</sub>/PS solution flows through the die without phase separation. The capillary die insert used in this work contains two sections: a guiding hollow tube (D=7.8mm, L=56.12mm) and a capillary nozzle (D=0.5mm, L=10mm), so a contraction flow exists through the insert.

The shear-thinning behavior of the CO<sub>2</sub>/PS solution was expressed by the Carreau model [228]:

$$\frac{\eta - \eta_{\infty}}{\eta_0 - \eta_{\infty}} = \frac{1}{\left(1 + \left(\lambda \dot{\gamma}\right)^2\right)^{(1-n)/2}} \quad (3.2)$$

Where  $\eta$ ,  $\eta_0$ ,  $\eta_{\infty}$ , are shear viscosity, zero shear viscosity and infinite shear viscosity respectively.  $n$  is the power law index and  $\lambda$  is a constant.

Based on the experimental viscosity data obtained by Kwag et al. at 175°C [167], we determined the parameters in the Carreau model, as shown in Table 1.  $\eta_{\infty}$  was set to be zero. This model was then substituted into the Fluent computational code to characterize the rheological behavior of the CO<sub>2</sub>/polystyrene mixture.

Other parameters are listed below: the heat capacity was a function of temperature ( $C_p$  (J/kg.K) = 1182.03 + 1.7714 T (K)), and the thermal conductivity was a constant ( $k = 0.15$  W/m.K) [229]. The temperature on the wall and at the entrance was set to be 175°C and an exit flow rate of 0.4536 kg/hr (1 lb/hr) was selected.

### **3.4. Results and Discussion**

#### **3.4.1. Simulated Pressure, Temperature, Viscosity, and Velocity Profiles in Die**

The simulated pressure, temperature, viscosity, and velocity profiles in the die are shown in Figure 3.3 for a die wall temperature of 175°C and CO<sub>2</sub> concentration of 5.1 wt%. The rheology is described by the Carreau model and the average outlet velocity is 0.651 m/sec. The pressure gradient (Figure 3.3 (a)) is concentrated in the capillary nozzle because there is a large ratio between the diameters of the guiding tube and the capillary nozzle. Viscous heating induces a significant temperature (Figure 3.3 (b)) rise (11 °C) near the wall at the exit of the capillary nozzle where the shear rate is the largest. However, the temperature at other points does not change very much and as a first approximation, the flow in the die can be treated as isothermal. The viscosity distribution, highest at the center and lowest near the wall, exhibits shear-thinning behavior, based on which the shear rate at every location in the die can be determined. The velocity profile (Figure 3.3 (d)) is parabolic with a maximum velocity (1.058 m/sec) at the centerline. From this simulation information, the operation conditions for a microcellular foaming extrusion process, such as die temperature and screw rotation speed, can be selected to give different pressure distributions.

### **3.4.2. Calculated Rate of Pressure Drop and Pressure in the Die as a Function of Position**

Figure 3.4 demonstrates the effect of CO<sub>2</sub> content (1 or 5.1 wt.%) on the pressure drop at 175°C. As noted, the pressure drops mainly across the capillary nozzle. The entire die insert (guiding tube + capillary nozzle) is 66.12 mm long. The pressure is nearly constant from the insert entrance to the capillary nozzle entrance (0 to 56.12 mm), and then it drops quickly through the nozzle, from 56.12 to 66.12 mm. In the calculations, we only considered the shear viscosity for simplicity even although extensional viscosity is sometimes important in a contraction flow.

In Figure 3.4, we also tried to label the nucleation onset, which is defined as the position that the solution becomes saturated. The actual concentration of CO<sub>2</sub> in the polymer is fixed by the experimental conditions. At some point in the die the actual concentration will become greater than the saturation concentration due to the latter decreasing with the pressure in the die. The point at which these concentrations are equal is where the polymer begins to be supersaturated with CO<sub>2</sub> and nucleation becomes theoretically possible. The saturated CO<sub>2</sub> content, indicated by thicker lines in the figure, was calculated with the Sanchez-Lacombe equation of state according to the local pressure (the thinner lines) at different positions along the centerline and the corresponding die temperature. The horizontal dashed lines represent the actual CO<sub>2</sub> concentration in polystyrene (1 wt.% or 5.1 wt.%), and the intersection of the vertical

dashed lines and the length-axis represents the onset position where the solution becomes saturated. This position can be treated as the point where bubble nucleation and growth begin. The influence of the CO<sub>2</sub> content on the nucleation onset position will be discussed in detail latter.

Figure 3.5 shows that both the pressure drop and the average pressure drop rate decrease with the increasing CO<sub>2</sub> content under the same flow rate. In other words, a higher CO<sub>2</sub> content creates larger supersaturation ratios for nucleation, however, a large pressure drop or pressure drop rate cannot be developed. Fortunately, the pressure reduction due to the dissolution of CO<sub>2</sub> at high CO<sub>2</sub> content region (2 - 5.1 wt%) is not as dramatic as that at low CO<sub>2</sub> content region (0 - 2 wt%). Therefore a higher CO<sub>2</sub> content is expected to promote the formation of more bubbles.

### **3.4.3. Calculated Solubility of CO<sub>2</sub> in PS and T<sub>g</sub> as a Function of CO<sub>2</sub> Concentration.**

Applying the Sanchez-Lacombe equation of state, the solubility of CO<sub>2</sub> in polystyrene was calculated from 40 to 260°C under pressures from 0 to 20.7 MPa (0~3000 psi). A 3-dimensional surface (Figure 3.2) is plotted to express the relation between CO<sub>2</sub> solubility, temperature and saturation pressure. As expected, more CO<sub>2</sub> can be dissolved into polystyrene at low temperature and high pressure. Below the surface, polystyrene and CO<sub>2</sub> exist as a single-phase solution, while it becomes a two-phase vapor-liquid system above the surface.

The solid thick line on the 3-D surface represents the glass transition temperature. Condo et al. [85, 86] studied the dependence of the glass transition

temperature of the CO<sub>2</sub>/polystyrene system on its saturation concentration or saturation pressure. Based on their simulation results, glass transition temperatures and the corresponding saturation pressures were used to calculate the CO<sub>2</sub> content and the data were overlaid on the 3-dimensional surface. It is shown that T<sub>g</sub> decreases significantly with the addition of CO<sub>2</sub>. For example, for pure polystyrene, T<sub>g</sub> is 105°C, while it is about 46.4 °C with 5.9 wt.% CO<sub>2</sub> dissolved in polystyrene.

We use this 3-dimensional representation to guide the experiments and understand the continuous extrusion foaming process from a new point of view. After the single-phase solution forms and flows into the die, an approximately isothermal procedure begins. We can draw a line parallel to the pressure-axis below the surface, which means the temperature and CO<sub>2</sub> concentration remain constant. The intersection of the line and the surface represents the saturation condition. Once the line penetrates the surface, a non-equilibrium condition exists and the solution wants to lower its free energy by reducing the CO<sub>2</sub> content in the polymer to that represented by the surface. We can therefore treat this intersection point as the onset of nucleation. Based on homogeneous nucleation theory, the nucleation rate is ‘proportional’ to the supersaturation ratio (actual pressure/saturation pressure) and to produce microcellular foams we desire to maximize the nucleation rate and minimize growth. To maximize nucleation rate we would like the intersection to occur at a point where the surface is steep (i.e. changing rapidly with pressure) so that supersaturation is immediately large. Secondly, we can design different paths to control the cell growth. The basic idea is to lower the die temperature, so that when T<sub>g</sub> increases rapidly due to loss of CO<sub>2</sub> from the solution, the extrudate temperature is suddenly lower than the T<sub>g</sub>, and cells stop growing.

Therefore, to get ideal microcellular foams with small cell sizes and larger cell densities, we must 1) choose the intersection point to maximize nucleation rate; 2) optimize the cooling procedure to control the cell growth. The purpose is to freeze the cell structure once the cell is formed.

#### **3.4.4. Calculated Position of Nucleation Onset**

For a batch foaming system, the sample is placed in a pressurized vessel for a long period of time to become saturated before the pressure is released, and the processing pressure is always the saturated pressure at the given temperature. But for a continuous foaming process, the pressure at the die entrance is always higher than the saturated pressure to maintain a single-phase solution. Therefore, nucleation does not occur until the solution becomes saturated at some position in the die. We believe the nucleation rate is highest just beyond this point because of the highest concentration of the gas. In Figure 3.4, the total pressure drop is large for the 1 wt.% CO<sub>2</sub>/polystyrene solution, but the effective pressure drop for the nucleation beyond the nucleation onset point, which is far downstream near the exit, is low. On the contrary, the nucleation onset position for the 5.1wt% solution is near the entrance of the capillary nozzle and the effective pressure drop is high. Combination of the high CO<sub>2</sub> concentration with the high effective pressure drop means that a large thermodynamic instability can be induced and as a result, more nuclei can be created. This trend is more obvious in Figure 3.6. The more CO<sub>2</sub> in the melt, the earlier the bubbles begin to nucleate and grow. In other words, a high CO<sub>2</sub> content gives more nuclei, but a longer time for bubble growth.

Although the flow simulation in the die was done at 175°C, experiments were performed at 180°C. It is hypothesized that the trends obtained from simulation will hold true for other temperature ranges.

#### **3.4.5. Calibration of Experimental Mass Flow Rate and Pressure in the Die**

During the experiments, at a certain screw rotation speed and die temperature (180°C), the CO<sub>2</sub> contents were chosen to be 1, 2.5, 4, 6, and 8 wt%. Then the same procedure was repeated at another screw rotation speed, which was 10, 15, 20, 25, and 30 rpms. Without CO<sub>2</sub> dissolved in polystyrene, it was observed that the melt hardly flows through the small die at 180°C. Thus calibrations were performed with polystyrene/CO<sub>2</sub> solutions to obtain how mass flow rate, die pressure and pressure drop rate vary with screw rotation speed quantitatively.

The mass flow rate was measured by weighing the melt flowing out during a certain period of time. A pressure transducer mounted near the die entrance recorded the pressure. As expected, the mass flow rate is nearly proportional to the screw rotation speed. Higher screw rotation speeds shorten the residence time of the CO<sub>2</sub>/polystyrene mixture in the extruder, and to some extent, impact the mixing and formation of a single-phase solution.

Surprisingly, experiments show that both the pressure and pressure drop rate are independent of CO<sub>2</sub> content. Here, only the changes of pressure drop rate with the CO<sub>2</sub> content are plotted in Figure 3.7. This is abnormal because generally it is believed that the higher the CO<sub>2</sub> content, the lower the viscosity and as a result, the lower the pressure drop. One explanation is based on simulation results. The viscosity reduction in the high

CO<sub>2</sub> content region is not as dramatic as the low CO<sub>2</sub> content region, therefore, the pressure reduces slowly once a little amount of CO<sub>2</sub> is dissolved in the melt. Another explanation involves the more complex flow in the die, such as the phase separation during the foaming process and the contraction flow at the die entrance. From the point of view of controlling pressure or pressure drop rate, it is not an effective means to vary CO<sub>2</sub> content only. A certain die pressure can be created by speeding up or slowing down the screw rotation speed.

#### **3.4.6. Effect of CO<sub>2</sub> Content on Cell Size and Cell Density**

Figure 3.8 shows the cell morphology at different CO<sub>2</sub> content with a screw rotation speed of 10 rpms and foaming temperature of 180°C. Besides the trend that the cell size decreases and cell density increases with increasing CO<sub>2</sub> content, the nearby cells tend to coalesce at this low screw rotation speed (or low mass flow rate). The low mass flow rate provides a long residence time for cells to grow and the viscosity is not high enough to prevent the dissipation of cell walls. If the images are analyzed quantitatively by the method described in the experimental section, the cell size (left vertical axis) and cell density (right vertical axis) were determined and plotted versus CO<sub>2</sub> content in Figure 3.9. It is found that at low CO<sub>2</sub> concentrations, cell size decreases with an increase of CO<sub>2</sub> content; while at high CO<sub>2</sub> concentrations, cell size tends to be independent of CO<sub>2</sub> content. Accordingly, cell density increases at the beginning and then levels off.

From homogeneous nucleation theory, the nucleation rate, number of nucleation sites per unit volume and unit time, is proportional to the concentration of gas molecules.

When more CO<sub>2</sub> is dissolved in the polymer melt, it initiates more nucleation sites. However, the CO<sub>2</sub> concentration in polystyrene is limited by the solubility. CO<sub>2</sub> solubility is elevated when the saturation pressure is high and temperature is low. For our experimental range, the pressure rises from about 900 to 2000 psi (6.2 ~ 13.8 MPa). From Figure 3.2 the solubility is approximately from 2% to 4% correspondingly. Obviously, when the CO<sub>2</sub> content approaches or exceeds its solubility, the extra gas is not used to nucleate cells. Cell size and cell density do not change any more. Furthermore, ultrahigh gas injection usually causes unstable polymer flow with oscillating pressure or flow rate. Compared with the simulation of nucleation onset position, high CO<sub>2</sub> content makes the nucleation onset move to the die entrance at the same flow rate and die temperature. The predicted limit is where the saturation pressure is equal to the processing pressure at the entrance to the capillary nozzle.

#### **3.4.7. Effect of Die Pressure on Cell Nucleation**

As mentioned before, the pressure drop and the pressure drop rate in the die can be varied effectively by changing the screw rotation speed. Figure 3.10 shows the cell morphology foamed at the same die temperature (180°C) and CO<sub>2</sub> content (2.5 wt%) but different mass flow rates. Cells are more closed at high flow rates, which is consistent with our former explanation that short residence time in the die accelerates the freezing of cell structure. Furthermore, the competition between cell nucleation and cell growth exists so that a large part of gas is used for nucleation instead of growth when a large number of nuclei are created at a high flow rate which is corresponding to a high pressure drop and a high pressure drop rate.

Similarly, the cell size and cell density are plotted against the pressure drop and pressure drop rate in Figure 3.11 and 3.12 respectively. Cell size decreases with an increase in the pressure drop, and conversely, cell density increases (Figure 3.11). Because the pressure drop is not an instantaneous process, the rate of pressure drop is also essential to the nucleation. Assuming that the density of all CO<sub>2</sub>/polystyrene mixtures is 1000 kg/m<sup>3</sup>, the residence time of the mixture flowing through the die can be calculated by knowing the length and cross-sectional area of the die along with the mass flow rate. Then the pressure drop rate equals the pressure drop over the residence time. Figure 3.12 shows a similar trend as Figure 3.11. The quicker the die pressure drops, the smaller the cells.

It is seen that a large pressure drop or pressure drop rate is favorable for our purposes. A high processing pressure provides the capability to dissolve more CO<sub>2</sub> in the polymer. A large and fast pressure drop passing through the saturation pressure early leads to a lower activation energy that causes a higher nucleation rate, and results in a higher cell nucleation density.

### **3.5. Conclusions**

The solubility of CO<sub>2</sub> in polystyrene was accurately modeled with the Sanchez-Lacombe equation of state at different temperatures and pressures. A three dimensional surface was created to represent the temperature-pressure-CO<sub>2</sub> saturation composition behavior. The glass transition temperature as a function of pressure and CO<sub>2</sub> content was also overlaid on the surface.

The Carreau viscosity model was used in a computational fluid dynamics code (FLUENT) to represent the CO<sub>2</sub>/polystyrene rheological behavior. The distributions of pressure, temperature, viscosity, and velocity in the die were calculated and nucleation onset position was studied based on the pressure distribution and solubility. It was shown that a higher CO<sub>2</sub> content could move the nucleation onset position to the inlet of the die.

Microcellular foams of PS are produced continuously and the influences of the operation conditions were studied systematically. The flow rate and die pressure were controlled by changing the screw rotation speed. A higher pressure drop or pressure drop rate in the die results in smaller cells and greater cell density. Below the solubility limit, cell size decreases and cell density increases with higher concentrations of CO<sub>2</sub> in the polystyrene melt.

<b>CO<sub>2</sub> content</b>	<b>1 wt%</b>	<b>2 wt%</b>	<b>3 wt%</b>	<b>3.5 wt%</b>	<b>4.5 wt%</b>	<b>5.1 wt%</b>
$\eta_0$ (Pa.sec)	1969.4	1577.9	1139.3	614.2	548.5	334.4
$\lambda$	0.07102	0.0584	0.04956	0.02292	0.02614	0.01496
<b>N</b>	0.4099	0.3703	0.428	0.4271	0.4409	0.4553

Table 3.1. Parameters in the Carreau model (175°C)

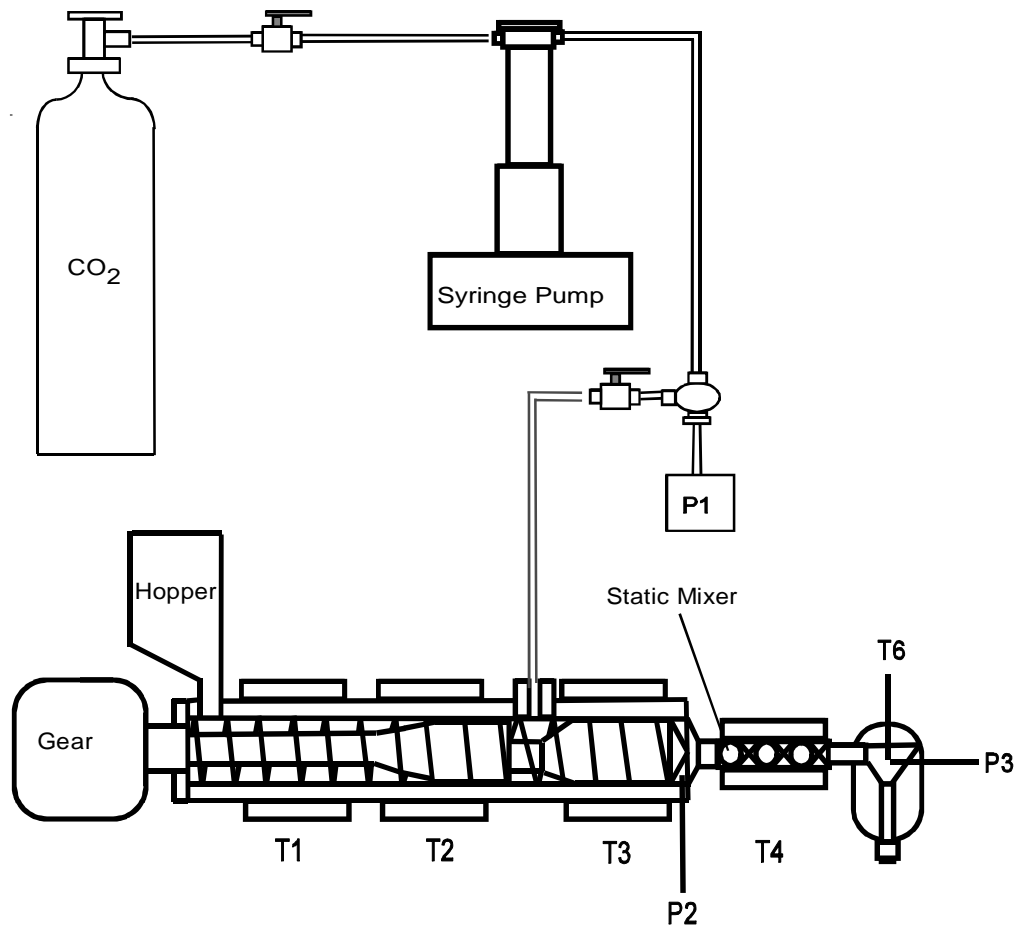


Figure 3.1. Experimental setup for microcellular foaming.

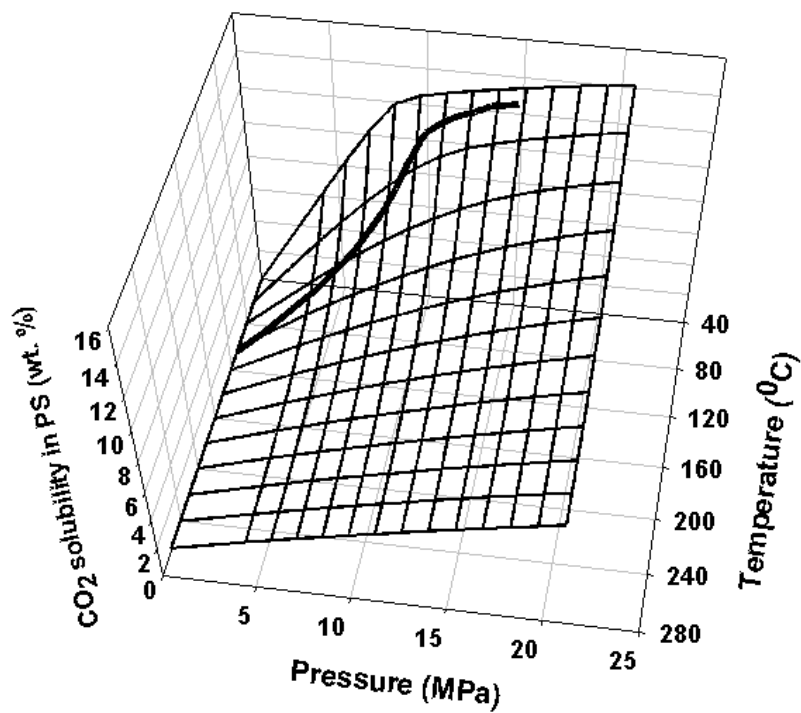


Figure 3.2. Saturation CO<sub>2</sub> content at different pressures and temperatures (the thick line on the surface is the T<sub>g</sub>).

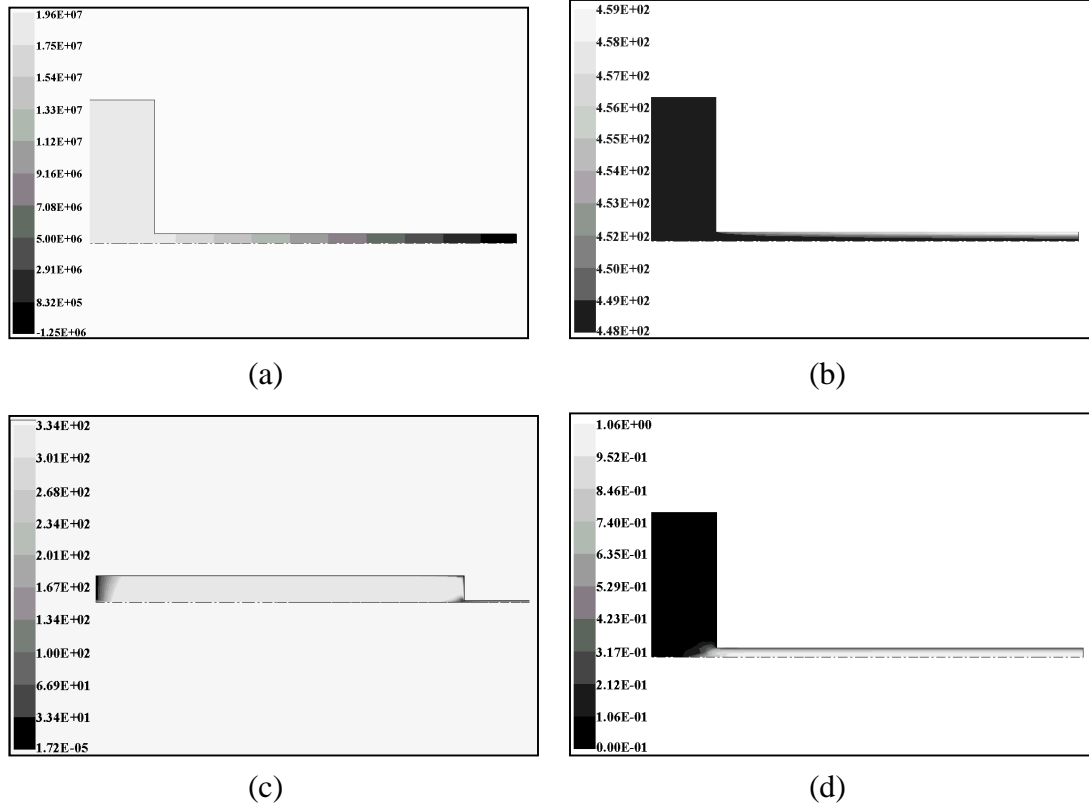


Figure 3.3. Simulation results for distributions of (a) Pressure (Max =  $1.957 \times 10^7$  Pa, min =  $-1.250 \times 10^6$  Pa); (b) Temperature (Max = 459.5 K, min = 448.2 K); (c) Viscosity (Max = 334.4 Pa.sec, min =  $1.720 \times 10^{-5}$  Pa.sec); and (d) Velocity (Max = 1.058 m/s, min = 0 m/s) when the die temperature is  $175^\circ\text{C}$  and the  $\text{CO}_2$  content is 5.1 wt%. The horizontal direction to the right is the flow direction. The die insert contains two sections: the guiding hollow tube ( $R = 3.9$  mm,  $L = 56.12$  mm) and the capillary nozzle ( $R = 0.25$  mm and  $L = 10$  mm).

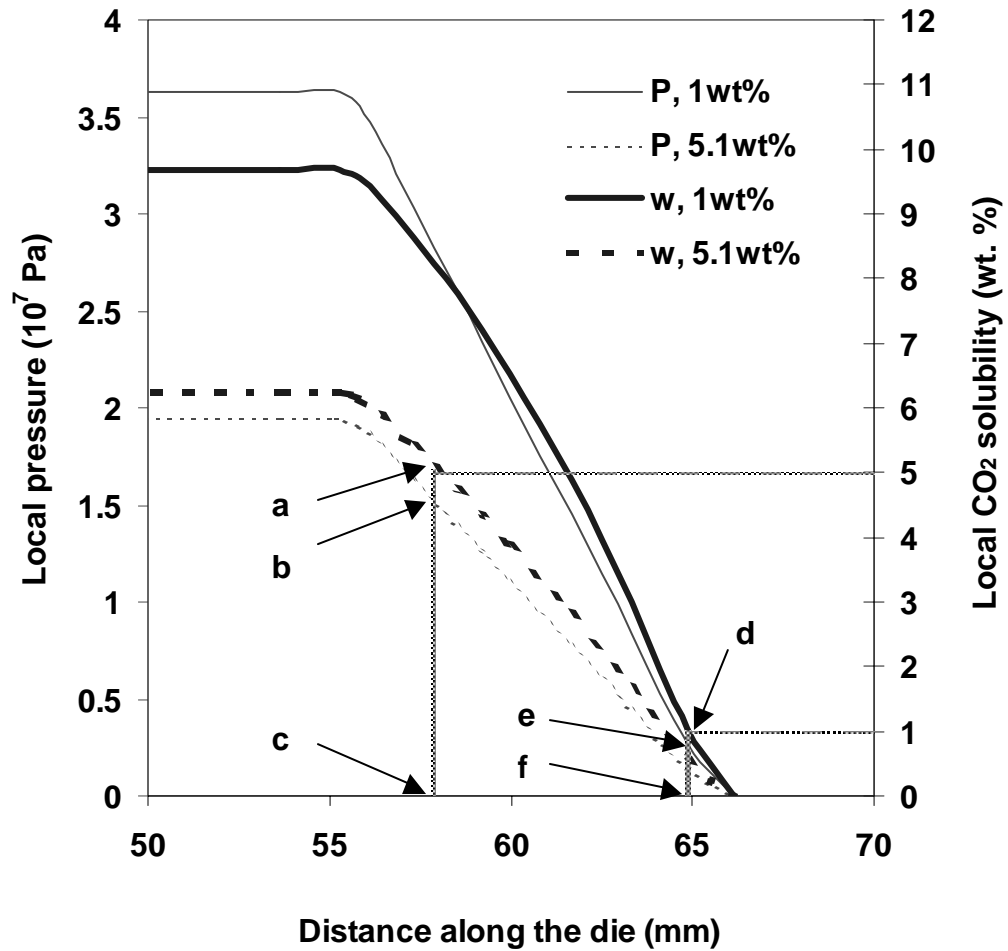


Figure 3.4. Profiles of pressure and saturation CO<sub>2</sub> weight fraction along the die nozzle with different CO<sub>2</sub> content (1 and 5 wt.%) at the same die temperature (175°C). Points a and d: weight fraction that the solution becomes saturated; b and e: local pressure when the solution becomes saturated; c and f: nucleation onset position.

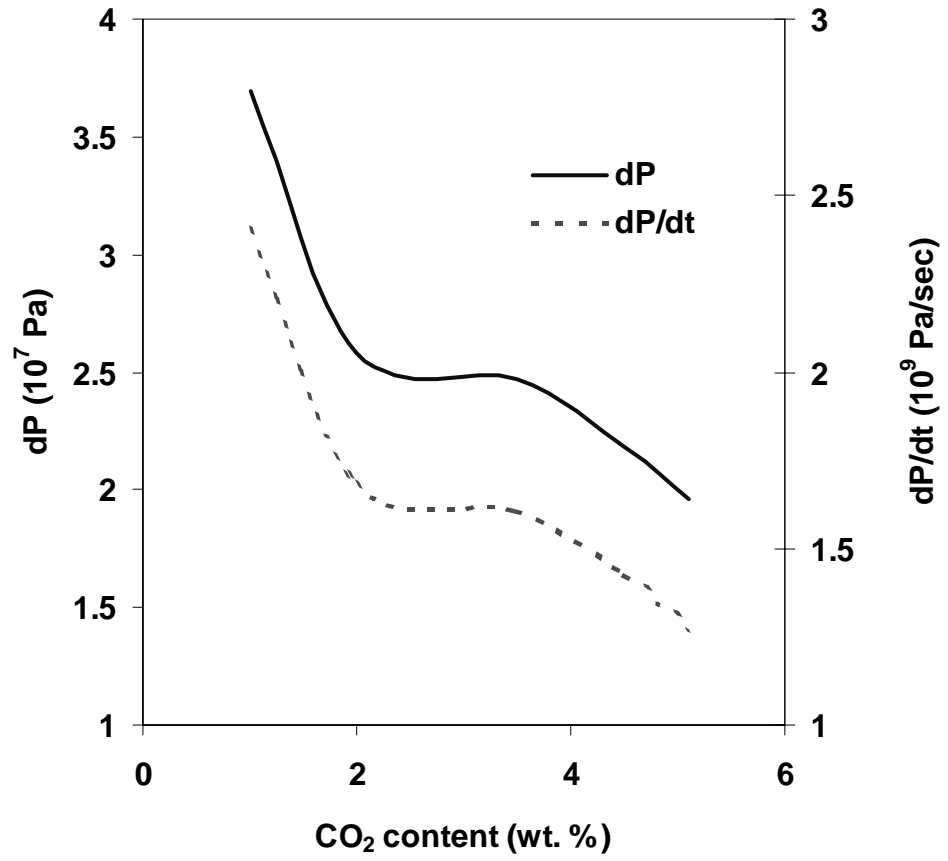


Figure 3.5. The influence of CO<sub>2</sub> content on the pressure drop and pressure drop rate.

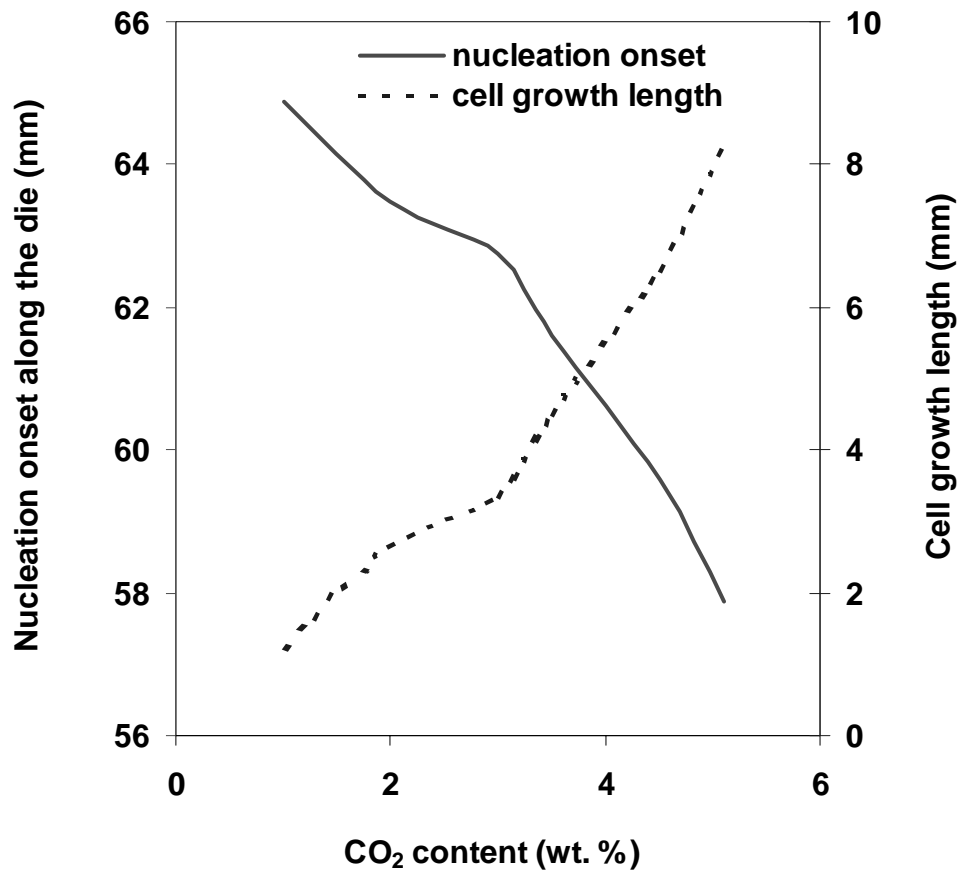


Figure 3.6. Effects of CO<sub>2</sub> content and die temperature on the nucleaion onset position and the cell growth length.

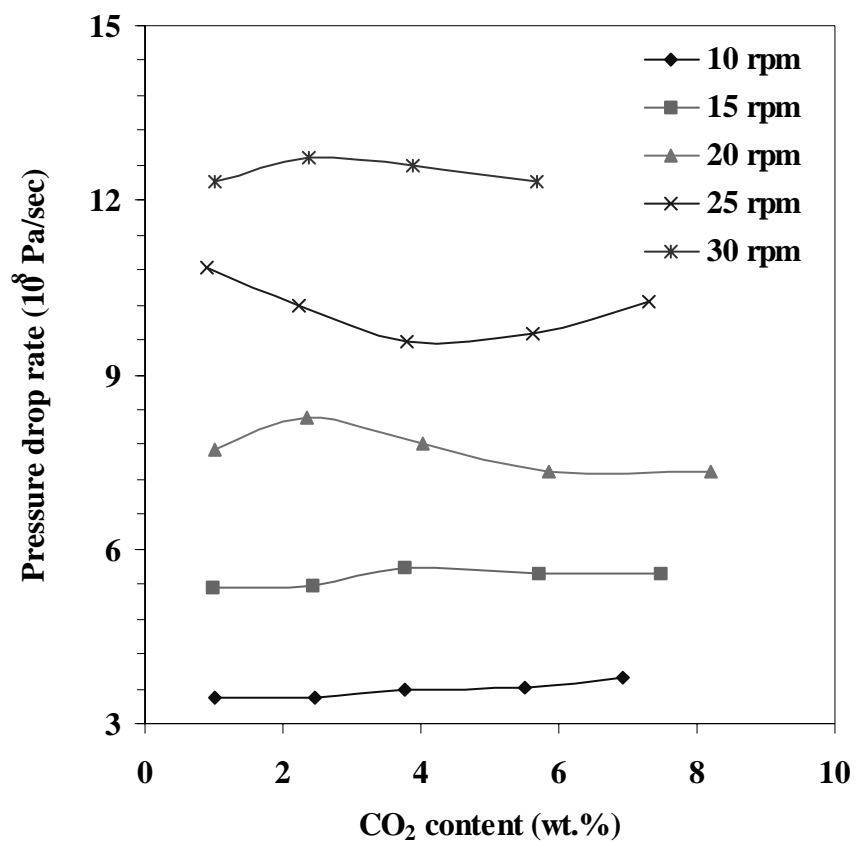


Figure 3.7. Pressure drop rate in the die as a function of CO<sub>2</sub> content at different screw rotation speed (die temperature: 180°C).

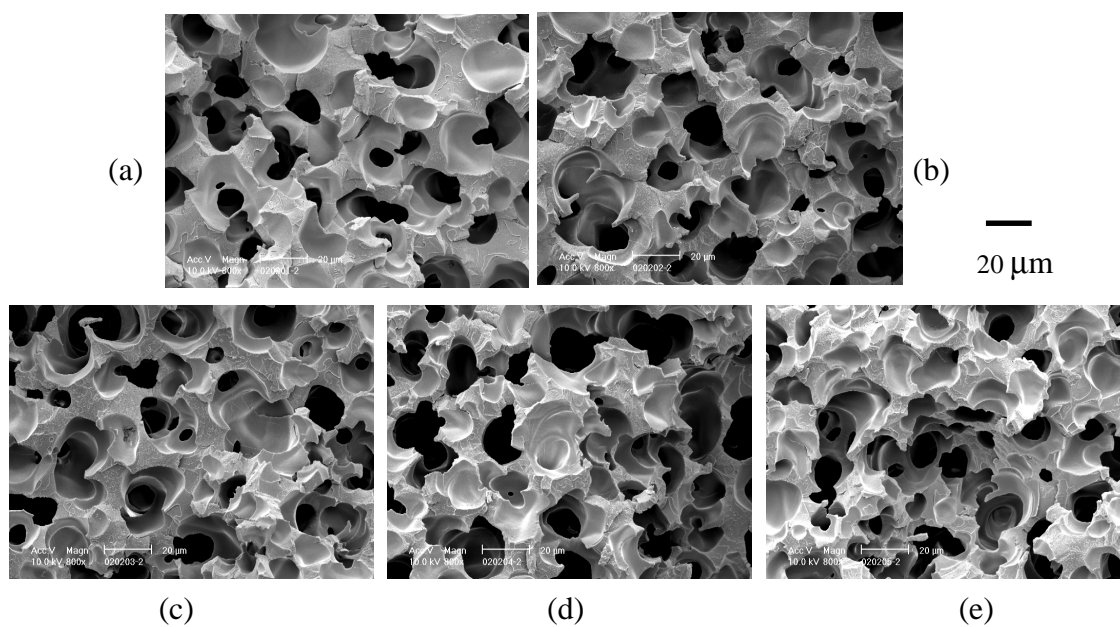


Figure 3.8. Cell morphology influenced by CO<sub>2</sub> content: (a) 1%, 12.1 MPa; (b) 2.5%, 11.3 MPa; (c) 4%, 11.4 MPa; (d) 6%, 11.5 MPa; (e) 8 wt%, 11.3 MPa (die temperature: 180°C; screw rotation speed: 10 rpms).

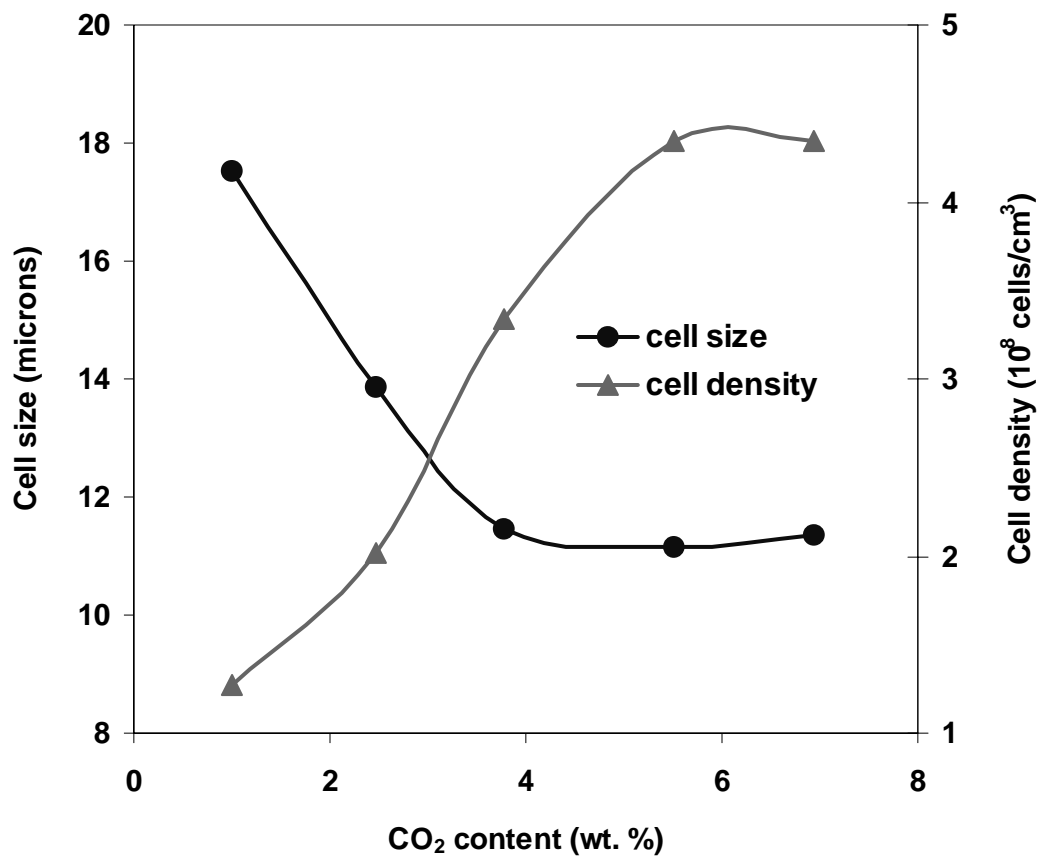


Figure 3.9. Cell size and cell density affected by CO<sub>2</sub> content (foaming temperature: 180°C; screw rotation speed: 10 rpm).

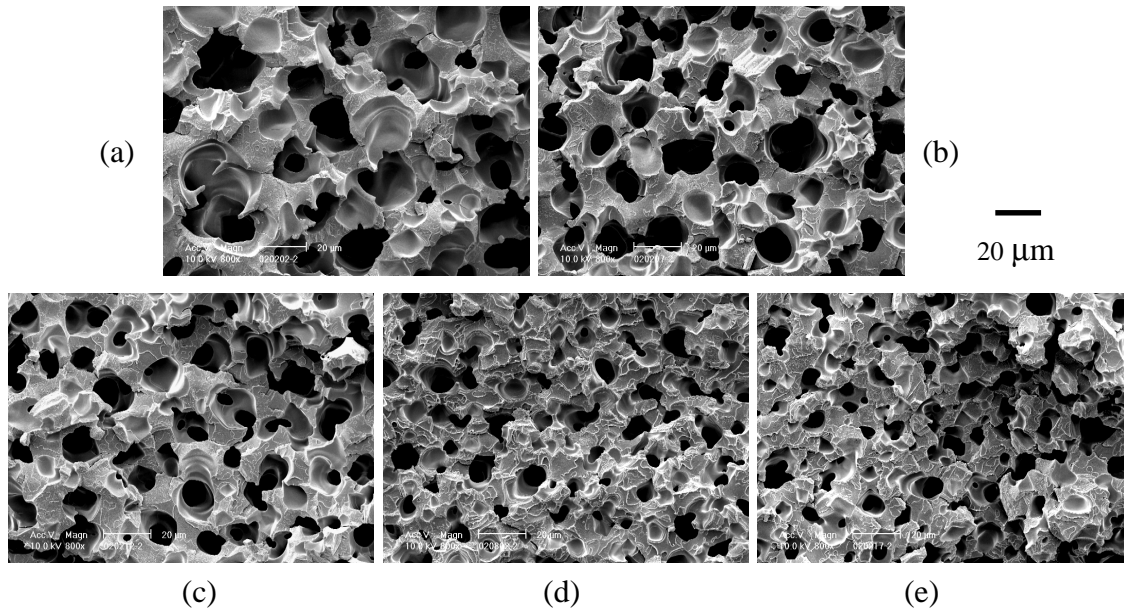


Figure 3.10. Cell morphology influenced by pressure change: (a) 10; (b) 15; (c) 20; (d) 25; (e) 30 rpms (die temperature: 180°C; CO<sub>2</sub> content: 2.5 wt%).

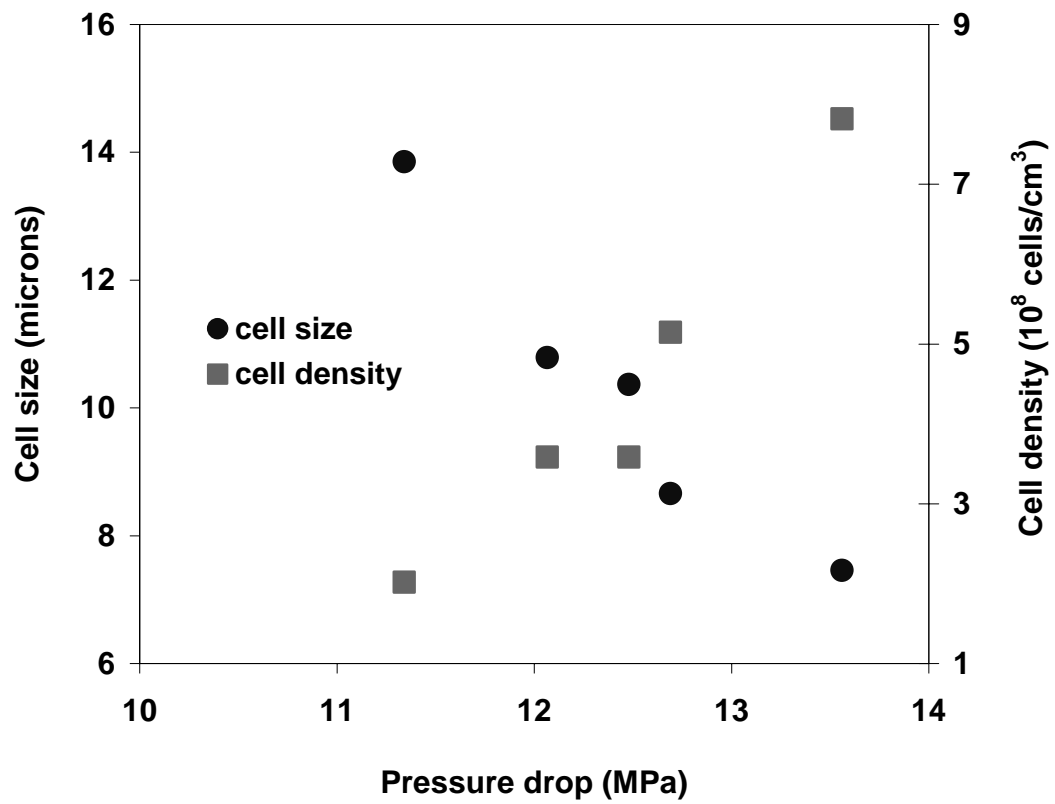


Figure 3.11. Relation between cell size, cell density, and pressure drop at 180°C with the same CO<sub>2</sub> content (2.5 wt%).

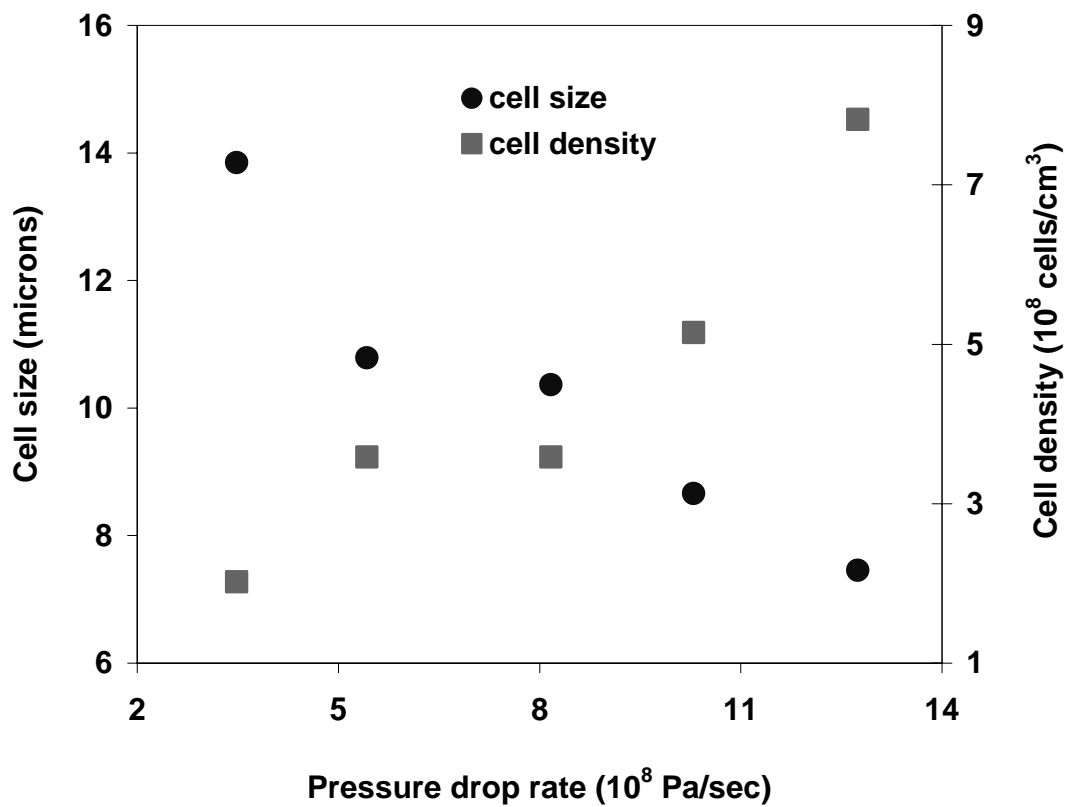


Figure 3.12. Relation between cell size, cell density, and pressure drop rate at 180°C with the same CO<sub>2</sub> content (2.5 wt%).

## CHAPTER 4

### EFFECT OF DIE TEMPERATURE ON THE MORPHOLOGY OF MICROCELLULAR FOAMS

#### 4.1. Introduction

Microcellular foams, typically defined as foamed plastics with a cell size smaller than 10  $\mu\text{m}$  and a cell density larger than  $10^9$  cells/cm<sup>3</sup> [10], have aroused tremendous research interest due to their unique properties and potential applications. Microcellular foams with a closed cell structure are believed to have higher mechanical strength-to-weight ratio, higher impact strength and toughness [40, 66-68, 222], and longer fatigue life [73, 74]. They may be applied to replace pure materials and save material, or to produce thin-wall foamed products (e.g. building siding). An open cell structure may be favorable as well [108] for application as an absorbent media, a separation media, or scaffolds for tissue engineering.

Carbon dioxide, as a possible replacement of traditional physical foaming agents such as chlorofluorocarbons (CFCs), is environmentally friendly, non-flammable, and low cost. Compared to traditional foaming agents, CO<sub>2</sub> has a relatively low mass

solubility and high diffusivity in polymer melts, causing the volume expansion ratio (defined as the volume ratio between the foamed and non-foamed sample) to be low. However, these characteristics are advantageous for producing microcellular foams with small cell size, high cell density, and low volume expansion ratio.

The design of foams with a desired cell structure mainly depends on the selection of proper operating conditions. Figure 4.1 lists the major parameters in a continuous extrusion foaming process. Among them, foaming temperature, pressure drop or pressure drop *rate*, and CO<sub>2</sub> concentration are three key variables that need to be addressed. These three variables determine the changes in the viscosity, solubility, surface tension, diffusivity, and other physical properties, as well as playing important roles in mechanisms of cell nucleation and cell growth. Experimentally, it is a good strategy to study the correlation between the three key variables and the physical properties separately from their effect on cell nucleation and growth. The combination of all these parameters, including the three key variables and the physical properties, into models of cell nucleation and growth to fully understand a foaming process depends on simulations involving thermodynamics of nucleation, mass, momentum and heat transport, and selection of constitutive equations.

The concept of creating many small bubbles in plastics by gas nucleation was initially introduced by Professor Nam P. Suh in early 1980s as a means to reduce the cost of many mass-produced plastic items [10, 12]. Fundamental study in the foaming area involves the measurement and characterization of solubility [128, 130, 131], shear viscosity [162, 163, 167, 169, 174], and bubble nucleation [192-198] of various gas/polymer systems. In recent literature, much attention has been given to the influence

of pressure gradient or pressure drop *rate* on batch or continuous foaming processes. It was shown that a high pressure drop and a high pressure drop *rate* are the necessary conditions to nucleate a great number of small cells because the pressure drop provides the direct driving force for phase separation [11, 19, 20, 230]. Furthermore, a high CO<sub>2</sub> concentration is favorable to produce microcellular foams [50]. However, the effect of foaming temperature on the foam structure (cell size, cell density, and cell morphology) is poorly understood, especially for a continuous foaming process.

#### **4.1.1. Effects of Foaming Temperature in a Batch Foaming Process**

In a batch microcellular foaming process [79, 80], a polymer specimen is placed in a high pressure vessel and the vessel is pressurized to a certain pressure at a certain saturation temperature. After a period of time (usually longer than 24 hours), the pressure is rapidly released to atmospheric and the nucleated cells are allowed to grow for a period of time. Growth is stopped by quenching to a temperature lower than the glass transition temperature. The saturation temperature is usually treated as the foaming temperature although some experiments were designed to saturate the polymer sample at one temperature and foam it at another temperature. Because the polymer sample has been saturated before nucleation, any change in the foaming temperature or saturation temperature always causes a change in solubility, interfacial tension and diffusivity.

Although there are still uncertainties in the cell nucleation mechanism, a great deal of work has been done in this area. Classical homogeneous nucleation theory [192-198] is usually applied to describe the foaming process qualitatively or semi-quantitatively.

The homogeneous nucleation rate  $N_0$  (i.e. the number of cells created per unit time and unit volume) can be expressed as:

$$N_0 = f_0 C_0 \exp(-\Delta G^* / k_B T) \quad (4.1)$$

in which the Gibbs free energy barrier  $\Delta G^*$  for the formation of a critical bubble nucleus is

$$\Delta G^* = 16 \pi \sigma^3 / (3 \Delta P_i^2) \quad (4.2)$$

In these equations,  $f_0$  is the frequency factor ( $f_0 = (\frac{2\sigma}{\pi m})^{1/2}$ ),  $C_0$  is the number of gas molecules per unit volume,  $k_B$  is the Boltzmann's constant,  $T$  is the absolute temperature,  $\sigma$  is the interfacial tension,  $\Delta P_i$  is the difference between the actual pressure and the saturation pressure, and  $m$  is the mass of a gas molecule.

The influence of foaming temperature is very complex because nearly all the physical properties, such as viscosity, surface tension, solubility, and diffusivity, are functions of temperature. The final change in cell size and cell density with temperature depends on the specific foaming system as a result of the comprehensive interaction of all these parameters. There are conflicting reports of temperature effect in the literature.

By modifying the classical homogeneous nucleation theory, Goel and Beckman [34, 35, 37] calculated the nucleation rate in a CO<sub>2</sub>/PMMA system. It was found that the interfacial tension, treated as a function of CO<sub>2</sub> concentration, increases with an increasing foaming temperature in a range from 40 to 80°C due to the decrease in solubility. As a result, increasing temperature leads to a gradual increase in the nucleation energy barrier ( $\Delta G^*$ ) and thus a decrease in the nucleation rate. However the effect is not as dramatic as for an increase in saturation pressure. Sumarno et al. [28]

presented a similar opinion for the polystyrene/nitrogen system. The cell density is minimum and the cell size is maximum at about 77°C (350 K), which corresponds to the minimum solubility of nitrogen in polystyrene with the variation of saturation temperature. Arora et al. [29, 30] prepared microcellular polystyrene foams processed in supercritical CO<sub>2</sub> in a batch system where the foaming temperature ranged from 40 to 120°C. Larger and fewer cells were also found at a higher foaming temperature. They attributed this phenomenon to the viscosity reduction of the substrate material at a higher temperature, causing the cell growth rate to increase (apparently due to the decrease of the radial stresses which confines bubble growth and also the increase of CO<sub>2</sub> diffusivity).

Exceptions were found by Itoh et al. [42] when they studied the thermally stable non-crystalline polymers polyether sulfone (PES) and polysulfone (PSF) foamed with CO<sub>2</sub>. The cell sizes at 230°C (503 K) were smaller than those at 170°C (443 K) and 200°C (473 K) for the PSF/CO<sub>2</sub> system, although results at other temperatures maintain that the cell size increases with the foaming temperature.

By considering that the surface tension decreases with an increasing temperature and using a theoretical model based on the classical homogeneous nucleation theory, Rodeheaver and Colton [81] obtained the opposite trend: that increasing both the temperature and pressure causes the nucleation density to increase. Although the majority of their experimental data indicates a decrease in bubble density with an increase in foaming temperature, a reasonable explanation of the discrepancy between the experimental results and the prediction is that higher foaming temperature promotes cell coalescence that reduces the final cell density.

The classical nucleation theory was not able to describe the observed data even in a qualitative way by Kumar and Weller [15, 16] when they studied the effect of foaming temperature on the cell nucleation of a polycarbonate/CO<sub>2</sub> system. The data show that in the experimental temperature range from 160 to 60°C, the cell density lies between 1 and  $5 \times 10^9$  cells/cm<sup>3</sup> and exhibits a maximum at around 110°C, which is different from the Arrhenius-type temperature dependence in the classical nucleation theory that predicts the number of cells nucleated should reduce about three orders of magnitude when reducing the foaming temperature from 160 to 60°C. However, the cell size keeps increasing with increasing foaming temperature. In their study of a PVC/CO<sub>2</sub> system, the cell density was found to increase between 56 and 90°C, and then level off up to 120°C because of cell coalescence at the relatively high foaming temperature. However, the cell size remained constant in the test temperature region due to competition for gas molecules between the cell nucleation and cell growth.

When crystalline polymers are used for microcellular foaming, the situation becomes more complicated. Baldwin et al. [47] foamed polyesters at different temperatures to study the influence of crystallization on the foaming process. A bimodal cell size distribution was observed with larger uniform cells in the surface region (~20 μm) and very small cells in the interior region (~1 μm) due to combined effects of heat transfer and molecular orientation.

#### **4.1.2. Effects of Foaming Temperature in a Continuous Foaming Extrusion Process**

In a continuous microcellular foaming process [11], a metered amount of gas (CO<sub>2</sub>) is injected in the barrel of an extruder. The mixing of CO<sub>2</sub> with a polymer melt depends on the shear force generated by the screw rotation and other special mixing elements (e.g. static mixers). The cells are nucleated by the rapid pressure drop generated when the mixture flows through the die, and the cells keep growing until vitrification. The three main differences between a continuous extrusion foaming process and a batch foaming process are that in the continuous process: (1) a metered amount of gas (instead of the saturation amount of gas) is dissolved in the system, (2) the pressure gradient as the major nucleation driving force is determined by the flow instead of the saturation pressure, and (3) the foaming temperature is always the extrusion die temperature (although the melt temperature before the die also has an effect).

By controlling the temperature of the melt before flowing into the die and the temperature of the die itself, Park et al. [31, 51, 82] investigated the effects of both melt temperature and the die temperature on the foam morphology of high impact polystyrene with CO<sub>2</sub> as the foaming agent. They pointed out that the formation of excellent microcellular structure comes at the cost of a decrease in volume expansion. When the melt temperature is high (170°C), cell coalescence is severe and cell size is not uniform regardless of the die temperature. At a moderate melt temperature (150°C), cell morphology ranges from a partially open structure at a high die temperature of 175°C, to a highly open cell structure at a medium die temperature of 135°C, and then to a uniform closed cell structure at a low die temperature of 110°C. At a low melt temperature (120°C), cell coalescence decreases with die temperature until it disappears at the lowest

die temperature. A similar study was conducted on the HDPE/CO<sub>2</sub> system. The degree of cell coalescence was again found to be related to both the melt temperature and the die temperature. To decrease cell coalescence, it was shown that the melt temperature should be lowered substantially. The authors conclude that improving the melt strength by decreasing melt temperature is an effective way to reduce cell coalescence and preserve high cell density.

In this work, we focused on the effect of foaming temperature on the cell size, cell density, and cell morphology in a continuous microcellular extrusion foaming process. Effects of the other two key variables (pressure and CO<sub>2</sub> concentration) have been summarized in Chapter 3 [231]. The contraction flow in the extrusion die was simulated with FLUENT computational fluid dynamics code at two temperatures (150 and 175°C) to predict profiles of pressure and temperature. The location of nucleation onset was determined based on the pressure profile and equilibrium solubility. Systematic experiments were performed to unveil effects of foaming temperature on cell size, cell density and cell morphology at a series of screw rotation speeds. Experimental results were compared with simulations and both were used to gain insight into the foaming process. Our aim is to connect processing variables to foam structure and facilitate the selection of operating conditions for producing microcellular foams. It should be noted that the extrusion die used in this study was a capillary die with a small diameter (0.5 mm) to achieve the high pressure drop and pressure drop rate required to nucleate microcellular foam cells. Additional study is needed to scale up this procedure to larger equipment and foam products.

## 4.2. Experimental

### 4.2.1. Setup and Procedure

Polystyrene (Styron 685D) from Dow Chemical was foamed at different conditions. Bone-dry grade carbon dioxide (99% purity), provided by Praxair, was applied as the physical foaming agent.

Figure 4.2 shows a schematic of the foaming system. Experiments were carried out on a two-stage single-screw extruder (Rheomex 252p) from Haake. The screw has a diameter of 3/4 inches and a length to diameter ratio ( $L/D$ ) of 25.  $\text{CO}_2$  was injected in the barrel from a port initially designed for venting, located in the middle of the two screw stages where the barrel pressure is relatively low. A static mixer (Omega, FMX8441S) containing 6 elements, 0.28" in diameter and 2.7" long, was attached to the end of the extruder to provide extra distributive mixing. A separate temperature control system controlled the static mixer temperature. A capillary die with a 0.5 mm diameter and 10 mm length nozzle was custom-made to generate high and rapid pressure drops. Pressure transducers (Dynisco PT422A-10M-6/18) were installed at the end of the barrel and in the die to monitor the highest pressure of the system and the pressure at the entrance of the die nozzle, respectively. Two thermocouples were mounted in the die: one in the die block to control temperature, and the other extending into the flow to measure the temperature of the polymer melt. A negligible discrepancy ( $1\sim 2^\circ\text{C}$ ) exists between the two temperatures. Therefore, the melt temperature can be controlled effectively by only changing the die temperature.

$\text{CO}_2$  was first pumped from a gas cylinder to a syringe pump (ISCO 260D) with a cooling jacket. The pump was run in either constant pressure or, most often, constant

volumetric flow rate mode. The CO<sub>2</sub> volumetric flow rate can be read with high precision from the pump controller. Just before the injection port, another pressure gauge was installed to measure the gas pressure.

CO<sub>2</sub> is compressed to a certain pressure in the syringe pump at 40°C reaching a supercritical state. Upon injection into the barrel, it is preliminarily mixed with the polystyrene melt by the screw rotation. A one-phase solution is formed after the mixture flows through the static mixer. Nucleation occurs in the die due to the quick and large pressure drop realized by the narrow nozzle. The foamed extrudate flows out of the die and vitrifies freely in the air.

The amount of CO<sub>2</sub> injected into the polymer melt is adjusted through the volumetric flow rate setting on the syringe pump. At steady state, the gas pressure will also be constant even though it is not controlled. By measuring the mass flow rates of polystyrene melt at different screw rotation speeds, the weight fraction of CO<sub>2</sub> in the polymer melt is known. To increase the pressure drop in the die, either the screw rotation speed is increased or the die temperature is lowered. The chosen screw rotation speeds were 10, 15, 20, 25, and 30 rpm. The die temperature ranged from 140 to 240°C and the melt temperature before the die was fixed to be 235°C. The CO<sub>2</sub> concentration was selected to be 1, 2.5, 4, 6, and 8 wt.%.

#### **4.2.2. Foam Structure Analysis**

Cell size  $D_f$  is characterized by the diameter of the foam cells while the cell density  $N_f$  is the number of cells per unit volume.  $D_f$  and  $N_f$  were determined by analyzing images obtained from scanning electron micrographs (SEM) using Scion

image software. The foam samples were frozen in liquid nitrogen and then fractured to expose the microstructures. Then the exposed cross-section was coated with gold and observed in a scanning electron microscope. A micrograph showing at least 50 bubbles was chosen, and the number of bubbles  $n$  in the micrograph was determined with the software. If the area of the micrograph is  $A \text{ cm}^2$  and the magnification factor is  $M$ , the cell density can be estimated:

$$N_f = \left( \frac{nM^2}{A} \right)^{3/2} \quad (4.3)$$

The cell size is the average circle equivalent diameter for all of the bubbles in the micrograph.

The foam density is determined by measuring the volume and weight of the sample.

### **4.3. Flow Simulation in the Die: Effect of Temperature**

To understand the extrusion foaming process, it is important to know what happens in the foaming die. As discussed in Chapter 3 [231], the position of nucleation onset and the pressure drop rate were determined at two  $\text{CO}_2$  concentrations and  $175^\circ\text{C}$ . It was shown that the position of nucleation onset moves upstream (i.e., an earlier nucleation) and the pressure drop rate decreases as the  $\text{CO}_2$  concentration increases. By applying the same analysis, we studied how foaming temperature affects the position of nucleation onset and the pressure drop rate. Two temperatures, 150 and  $175^\circ\text{C}$ , are selected with a constant  $\text{CO}_2$  concentration of 5wt.%.

Via a computational fluid dynamics code (Fluent), the pressure profile in the die was determined at the two temperatures by assuming that the phase separation does not affect the polymer foam rheology (a poor but necessary assumption in our CFD code). The shear-thinning behavior of the CO<sub>2</sub>/PS solution is represented using the Carreau model [228]. By fitting the experimental viscosity data obtained by Kwag et al. [167], we determined the parameters in the Carreau model, which are shown in Table 1. The infinite shear viscosity in the model is set to be zero. Subsequently, the Sanchez-Lacombe equation of state [136, 137] was applied to calculate the CO<sub>2</sub> saturation concentration (solubility) at each pressure obtained above. The position of nucleation onset is where the real CO<sub>2</sub> concentration that is physically injected into the polymer melt becomes higher than the saturation concentration at the local pressure.

## **4.4. Results and Discussion**

### **4.4.1. Simulated Pressure Profile and Nucleation Position**

Because of the large ratio in diameter between the guiding tube and the capillary nozzle, the pressure drop concentrates in the capillary nozzle. The pressure is nearly constant from the insert entrance to the capillary nozzle entrance (0 to 56.12 mm), and then it drops quickly through the nozzle (56.12 to 66.12 mm). In the calculations, we only considered the shear viscosity in the calculation, although extensional viscosity is also important in a contraction flow. Figure 4.3 demonstrates the effect of die temperature on the pressure drop (thin lines) with 5 wt.% of CO<sub>2</sub> dissolved in the

polystyrene. When the die temperature decreases from 175 to 150°C, both the pressure drop and the pressure drop rate through the die increase at the same flow rate as a result of the viscosity increase.

In Figure 4.3, the position of nucleation onset is also labeled (point c for 175°C and f for 150°C), which we define as the position that the solution reaches saturation. The actual concentration of CO<sub>2</sub> in the polymer is determined by the experimental condition. At some point in the die the actual concentration will become greater than the saturation concentration due to the pressure decrease in the die and the dependence of saturation concentration on pressure. The point at which these concentrations are equal is where the polymer begins to be supersaturated with CO<sub>2</sub> and nucleation becomes theoretically possible. The saturated CO<sub>2</sub> content, represented by the thick lines in the figure, was calculated with the Sanchez-Lacombe equation of state according to the local pressure (the thin lines) at different positions along the centerline and the corresponding die temperature. The horizontal dashed lines represent the actual CO<sub>2</sub> concentration in polystyrene (5 wt.%), and the intersection of the vertical dashed lines and the length-axis represents the onset position where the solution becomes saturated. This position can be treated as the point where bubble nucleation and growth begin. Although the influence of temperature to the nucleation is complex, a lower die temperature postpones nucleation to a position nearer the die exit at the same CO<sub>2</sub> content and flow rate.

For a microcellular foaming process, in which the purpose is to form cells as small as possible, a nucleation position near the die exit may be favorable. The cell structure can be frozen right after nucleation to limit cell growth due to the temperature decrease outside the die. However, the complexity of a foaming procedure ensures that

one cannot simply relate the cell structure directly to the nucleation position. Cell nucleation and cell growth are competitive processes for gas consumption. When the available amount of gas is shared by more nucleated cells growing simultaneously, smaller cell size is possible. Therefore, one can infer that smaller cells can be obtained when two conditions are satisfied: (1) a late nucleation (i.e., a short cell growth time), and (2) a large nucleation rate.

Next, using calculations from homogeneous nucleation theory, we want to show that a low die temperature can increase the nucleation rate mainly because a low die temperature creates a high pressure drop (or pressure drop *rate*) across the die.

#### **4.4.2. Effect of Temperature on Nucleation Rate Calculated from the Classical Nucleation Theory**

From the classical nucleation theory (Equation 1), the nucleation rate is a function of four variables: concentration of nucleation sites ( $C_0$ ), interfacial tension, supersaturation ( $\Delta P_i$ ), and temperature ( $T$ ). Calculations according to the classical nucleation theory are usually difficult because the variables are highly correlated. For example, for a PS/CO<sub>2</sub> system, the interfacial tension is known to be a sensitive function of CO<sub>2</sub> concentration, which itself can be treated as the concentration of nucleation sites ( $C_0$ ). To simplify the complexity, we first select a mean value for each of the four variables. Then a  $\pm 1\%$  change of the mean value was introduced to each variable and the variation in nucleation rate was calculated. Thus we can determine which variable is more influential in determining the nucleation rate. Here, we assume that a small 1% change in one variable does not change significantly the value of other variables.

The calculation results are shown in Figure 4.4. The mean values of CO<sub>2</sub> concentration (in weight fraction), interfacial tension ( $\sigma$ ), supersaturation ( $\Delta P_i$ ), and temperature ( $T$ ) were 3%, 0.0173 N/m, 16 MPa, and 473.2 K (200°C) respectively. Obviously, the increase in CO<sub>2</sub> concentration, supersaturation, and temperature, as well as the decrease in interfacial tension is favorable to obtain a high nucleation rate. The nucleation rate is most sensitive to the change in the interfacial tension and least sensitive to the change in the CO<sub>2</sub> concentration. A more interesting result is that the influence of supersaturation is greater than that of temperature.

As shown in our flow simulation, a decrease in foaming temperature (i.e., die temperature) causes an increase in pressure drop and pressure drop *rate*, which in turn enlarges the supersaturation. This enlargement in supersaturation would dominate the change in nucleation rate.

Up to this point, at the same CO<sub>2</sub> concentration and the same flow rate, it has been shown that a low die temperature can give a late nucleation (i.e., a short cell growth time) and a large nucleation rate simultaneously. Therefore, small cell size and large cell density are expected at a low die temperature.

#### 4.4.3. Effect of Temperature on Mass Flow Rate and Pressure

To determine the relationships between the processing conditions and the foam structure, the effects of die temperature (i.e., the foaming temperature) on the pressure profile in the die, the cell size and cell density, and cell morphology were investigated experimentally. With CO<sub>2</sub> as a foaming agent, polystyrene was foamed at a series of die temperatures and we focus below on the experimental results using low CO<sub>2</sub> concentration.

To increase the pressure drop in the die, one usually increases the screw rotation speed or reduces the die temperature. Because the polystyrene melt/CO<sub>2</sub> system is a shear-thinning fluid, it is not always possible to generate a high pressure in the die only by increasing the screw rotation speed or the mass flow rate. Therefore, increasing the viscosity (and hence the pressure drop) by reducing the die temperature becomes important.

The mass flow rate of the polystyrene/CO<sub>2</sub> mixture was measured by weighing the melt flowing out the die over a certain period of time. A pressure transducer mounted near the die entrance recorded the pressure. Figure 4.5 shows that the mass flow rate is nearly linearly proportional to the screw rotation speed at all temperatures. Higher screw rotation speeds shorten the residence time of the CO<sub>2</sub>/polystyrene mixture in the extruder. Generally, decreasing die temperature can slow the mass flow rate at the same screw rotation speed due to the increasing viscosity.

Figure 4.6 shows that the pressure drop rate increases with the increase of the screw rotation speed and the decrease of the die temperature. The pressure drop rate was calculated by assuming the CO<sub>2</sub>/PS solution has a constant density of 1 grams/cm<sup>3</sup>,

which is a reasonable approximation for such a low CO<sub>2</sub> concentration. Because the pressure drop through the die is used to create a supersaturated state and cell nucleation rapidly depletes the supersaturation of gas, the rate of pressure drop must be large to maintain a high level of supersaturation. Therefore, we surmise that the pressure drop rate may exhibit better correlation with the foam structure than the pressure drop. We discuss this in greater detail in the following section.

#### **4.4.4. Effect of Die Temperature on Cell Size and Cell Density**

In order to study the effect of temperature at constant CO<sub>2</sub> concentration, polystyrene was foamed at a series of die temperature with a low CO<sub>2</sub> concentration of only 1 wt%, far below its solubility limit at any foaming temperature applied. In Figure 4.7, the cell structures at different die temperatures are shown for a high screw rotation speed (30 rpm). The pressure drop and pressure drop rate are also labeled for each condition. In the range of foaming temperature explored in these experiments, cell size decreases and cell density increases with a decrease of the temperature, which is consistent qualitatively with the prediction that a low temperature gives a late nucleation (i.e., a short cell growth time) and a high pressure drop (i.e., a large nucleation rate), and thus a small cell size and a large cell density.

Somewhat surprisingly, when the cell size and cell density are plotted versus the pressure drop *rate* (Figure 4.8a and 4.8b), all of the data start to collapse onto one line, which indicates that the cell size and cell density correlate more strongly with the pressure drop rate than with the foaming temperature. Foams with the same cell size and cell density can be generated at the same pressure drop rate regardless of the foaming temperature. The dependence on pressure drop is similar but more scattered.

Why is the pressure drop rate important in determining the cell density? Figure 4.9 gives a qualitative explanation, adapted from reference [20]. Two processes with the same pressure drop across the die are shown in the figure. Here we assume that the pressure profile in the die is linear but the pressure drop rate ( $dP/dt$ ) of process 1 is higher than that of process 2. The amount of  $CO_2$  dissolved in the system is indicated by the saturation pressure ( $P_{sat}$ ). Above the saturation pressure, the mixture is a single phase and below it, nucleation begins. If the two processes have an identical nucleation time ( $\Delta t$ ), the pressure decrease ( $\Delta P_1$  and  $\Delta P_2$ ) during  $\Delta t$  is the real thermodynamic instability that induces the cell nucleation or phase separation. Obviously  $\Delta P_1$  is larger than  $\Delta P_2$ , which indicates that process 1 has a higher nucleation rate based on the classical nucleation theory (Equation 1). This illustrates that the pressure drop and pressure drop *rate* presented thus far are only the operating conditions, not the real thermodynamic instability ( $\Delta P_i$ ) in the classical nucleation theory, although they correlate with each other. Consequently, a higher pressure drop rate can always create a higher thermodynamic instability ( $\Delta P_i$ ) and a higher nucleation rate.

The dependence of the cell size and cell density on the pressure and the pressure drop rate show similar trends for other CO<sub>2</sub> concentrations (2.5, 4, and 6 wt%), which are not shown here.

#### **4.4.5. Effect of Die Temperature on Cell Morphology**

Although the foaming temperature was found to be not as significant as the pressure drop or the pressure drop *rate* in deciding the cell size and cell density, it indeed affects the cell morphology dramatically, especially at a low screw rotation speed (10 rpm) when the residence time in the die is longer and foam cells have time to grow. Figure 4.10 demonstrates the gradual change of the cell morphology with a decrease of the foaming temperature from 240 to 140°C. The CO<sub>2</sub> content and the screw rotation speed were kept constant at 1 wt% and 10 rpm respectively. Obviously the pressure drop and the pressure drop *rate* are different for these samples because they increase with the decrease of the foaming temperature.

At high foaming temperatures (240 or 220°C), the foamed samples have separate, spherical micron-sized cells with thick cell walls. With a decrease of the foaming temperature from 200 to 160°C, cell coalescence becomes more pronounced at this low screw rotation speed. At 200°C, the cells begin to combine locally (i.e. the walls of several nearby cells vanish). This trend is more obvious at 180°C. However, the cells can be still treated as closed at this condition. An open cell structure was created at 160°C in that the cells coalesce into an interconnected pore space and we cannot identify a complete cell wall. At this moderate temperature and low screw rotation speed, the number of nucleated cells increases only gradually with decreasing foaming temperature,

and sufficient gas is available for cell growth with the same CO<sub>2</sub> concentration because of the lower diffusivity. At the same time, the viscosity or the rigidity of the polymer matrix is still not high enough to stop the cell coalescence through vitrification. Therefore, more and more cells nucleate and combine together to form the open structure.

At the low foaming temperature (140°C), the cell morphology changes greatly and the cells become large, closed and conjugated with each other. The cell wall is relatively thin and the shape of most cells is polygonal because of the space limitation to the cell growth. At this temperature, the viscosity and the rigidity rise up quickly and dramatically when the extrudate flows out of the die due to the decrease of temperature. Furthermore, the glass transition temperature increases with the loss of CO<sub>2</sub>, which accelerates the vitrification of the cell structure. For example, the glass transition temperature of PS/1 wt.% CO<sub>2</sub> and pure PS is approximately 98°C and 105°C respectively. As a result, the cell structure is frozen before the cell coalescence occurs. We obtained well-structured cells with decreasing cell density. Due to the limitation of our experimental apparatus where the small-sized die creates extremely high pressure at this temperature, no systematic study has been done. However, there is no doubt that more efforts are needed to study this interesting transition region, so that we can increase our understanding of why the cell size increases and the cell density decreases suddenly.

Additionally, the foam bulk density (Figure 4.11) was found to decrease proportionally with the foaming temperature at a low screw rotation speed (10 rpm), which means that the volume expansion ratio increases with decreasing foaming temperature. However, such a trend becomes less obvious at a higher screw rotation speed (30 rpm), where the residence time in the die is short and the cell structure is quickly vitrified after flowing out of the die.

#### **4.4.6. Effect of Temperature and CO<sub>2</sub> Concentration on Cell Coalescence**

As mentioned before, both closed and open micron-sized cell structures have potential applications. Different cell structures may be achieved by controlling the operating conditions. Based on the experimental results, it was found that both structures could be created at a foaming temperature of 160°C. The open cell structure described here is more likely the early and middle stages of cell coalescence, which is different from the traditional description of open-cellness where the cell walls totally disappear and only ribs and struts are left.

Figure 4.12 shows the foam morphology at 160°C with three screw rotation speeds (10, 20, and 30 rpm) and two CO<sub>2</sub> concentrations (1 and 6 wt%). The formation of open cell structure is favorable with a low screw rotation speed and a high CO<sub>2</sub> concentration. In Figure 4.12, the foam generated at 10 rpm and 6 wt.% CO<sub>2</sub> content has the most open structure. Similarly, the high CO<sub>2</sub> content samples exhibit more cell coalescence than those with low CO<sub>2</sub> content. However, with the increase of the screw rotation speed, the cell coalescence becomes less severe and a closed micron-sized cell structure is created.

Therefore, we can see that two conditions are important for the formation of open cell structure. One is to nucleate enough cells to obtain a high cell density, and the other is to provide sufficient driving force and time for cell growth. A lower screw rotation speed always gives a lower mass flow rate and as a result, a longer residence time in the die, which is essentially equivalent to the cell growth time because the extrudate is vitrified very quickly after flowing out of the die at such a low die temperature. Further, the higher CO<sub>2</sub> concentration provides more available gas for cell growth if we consider that cell nucleation and cell growth are competitive processes in CO<sub>2</sub> consumption. These are the major reasons why open cells are generated at a low screw rotation speed and a high CO<sub>2</sub> concentration.

#### **4.5. Conclusions**

A study on the microcellular foaming extrusion of polystyrene at different foaming temperatures was carried out using CO<sub>2</sub> as the foaming agent. The relationship between the operating conditions and the foam structure was discussed based on simulation results and experimental observations. The following conclusions can be drawn.

The location of nucleation onset can be determined based on the pressure profile and equilibrium solubility. When the die temperature decreases from 175 to 150°C, both the pressure drop and the pressure drop rate through the die increase as a result of viscosity increase at the same flow rate. A lower die temperature also postpones the

nucleation to a position near the exit at the same CO<sub>2</sub> content and flow rate. Thus, large cell density and small cell size are expected at a low foaming temperature since the high pressure drop (or pressure drop rate) induces a high nucleation rate and the late nucleation position means a short cell growth time.

The variation in nucleation rate was calculated based on the classical homogeneous nucleation theory after a  $\pm 1\%$  change of the mean value was introduced to each variable among CO<sub>2</sub> concentration, interfacial tension, supersaturation pressure, and temperature. It was shown that the influence of supersaturation ( $\Delta P_i$ ) is greater than that of temperature on the nucleation rate.

Experimentally, at a CO<sub>2</sub> concentration of 1 wt.% and a screw rotation speed of 30 rpm, a lower foaming temperature (ranging from 240 to 160°C) results in a smaller cell size and a greater cell density. Microcellular foams of PS, with cell sizes smaller than 10  $\mu\text{m}$  and cell densities greater than  $10^9$  cells/cm<sup>3</sup>, were created when the die temperature is 160°C, where the pressure drop through the die was greater than 16 MPa and the pressure drop *rate* was higher than  $10^9$  Pa/sec.

The influence of temperature on cell size and cell density is complex because temperature affects nearly all of the parameters in cell nucleation and growth. However, the cell size and cell density exhibit greater dependence on the pressure than on the foaming temperature. This can be observed by the fact that when the cell size or cell density at different foaming temperatures is plotted versus the pressure drop *rate*, all the data roughly merge onto one curve. A higher pressure drop *rate* generates smaller cell size and higher cell density.

The foaming temperature has a large influence on the foam morphology. Open and closed cell structures were generated by changing the foaming temperature. At a low screw rotation speed of 10 rpm, with a decrease in the foaming temperature (ranging from 240 to 160°C), cell coalescence becomes more severe due to an increase of the cell density. An open structure was obtained at 160°C and a high CO<sub>2</sub> concentration of 6 wt.%. Two conditions appear to be important in the formation of open cell structure. One is to nucleate enough cells (high cell density); the other is to provide sufficient gas and time to support cell growth.

Temperature	150°C	175°C
$\eta_0$ (Pa.sec)	2972.6	334.4
$\lambda$	0.1358	0.01496
n	0.3738	0.4553

Table 4.1. Parameters in the Carreau model

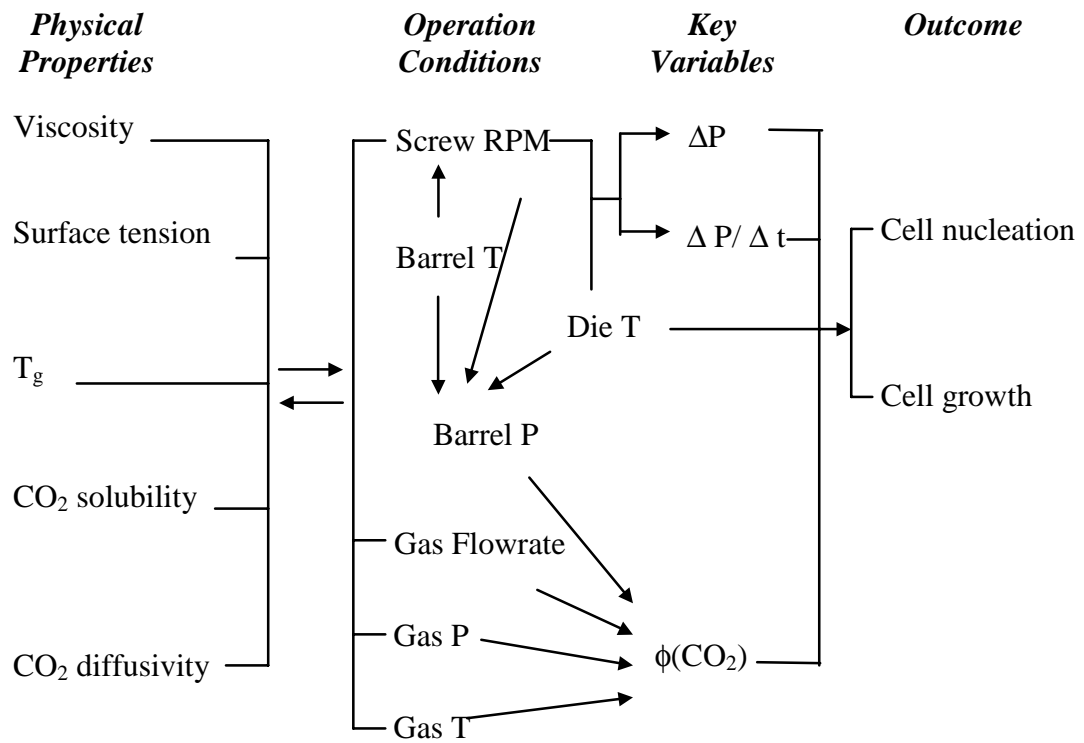


Figure 4.1. Relationship between parameters in a continuous extrusion foaming process

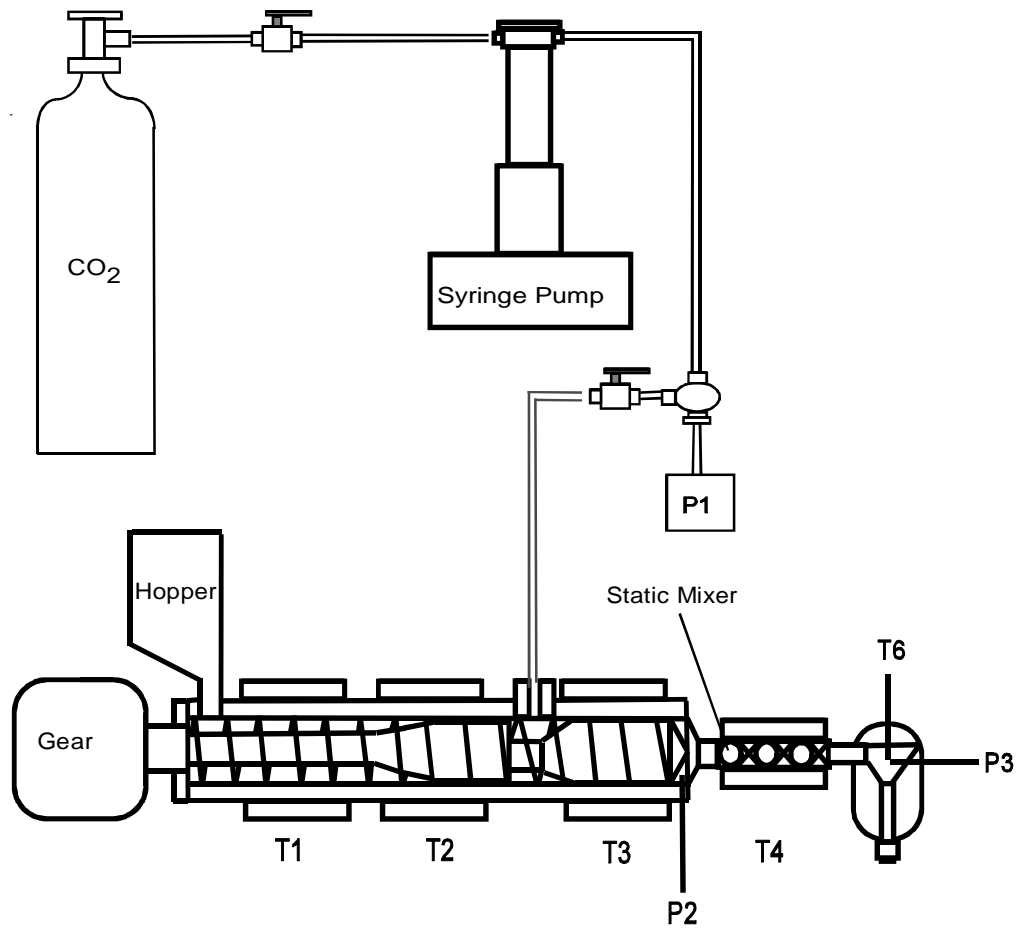


Figure 4.2. Experimental setup of microcellular foaming extrusion.

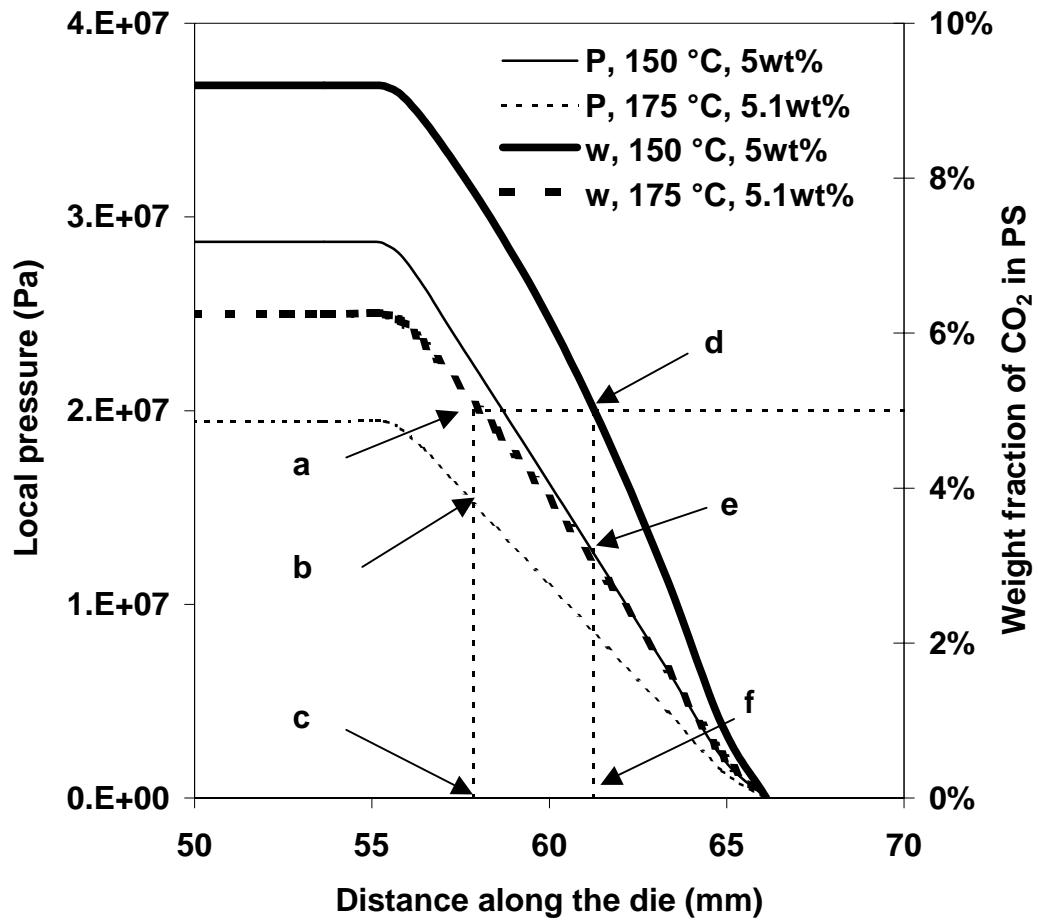


Figure 4.3. Profiles of pressure and saturation CO<sub>2</sub> weight fraction along the die nozzle at different die temperatures (150 and 175 °C) and same CO<sub>2</sub> concentration (5 wt.%). Points a and d: saturation concentration; b and e: local pressure when the solution becomes saturated; c and f: nucleation onset position.

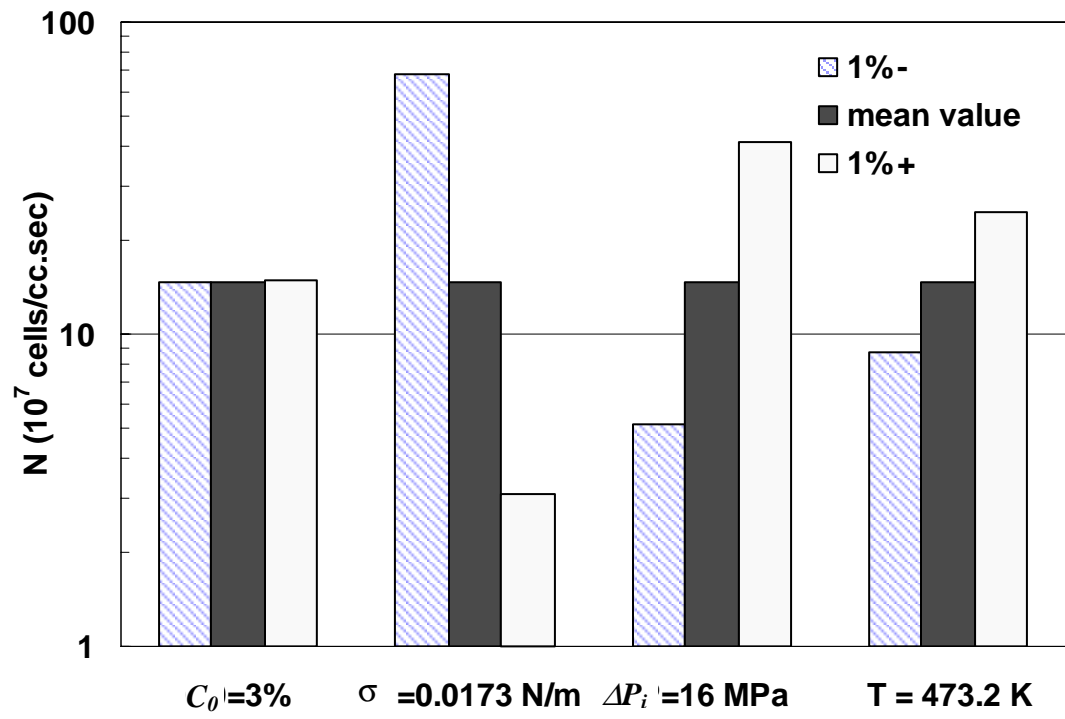


Figure 4.4. Nucleation rate calculated from the classical nucleation theory by changing  $\pm$  1% of the mean value of four variables.

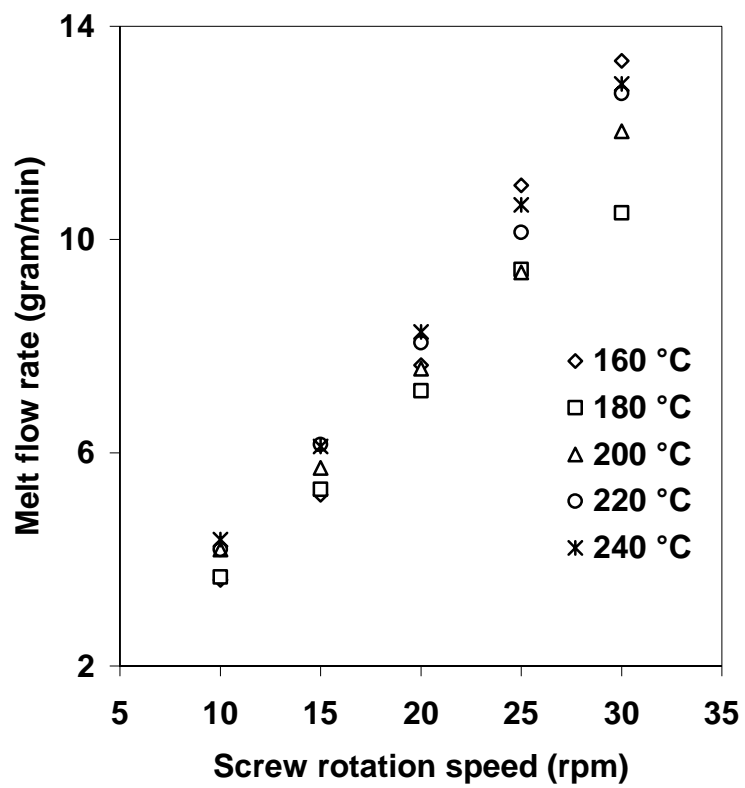


Figure 4.5. Calibration of melt flow rate.

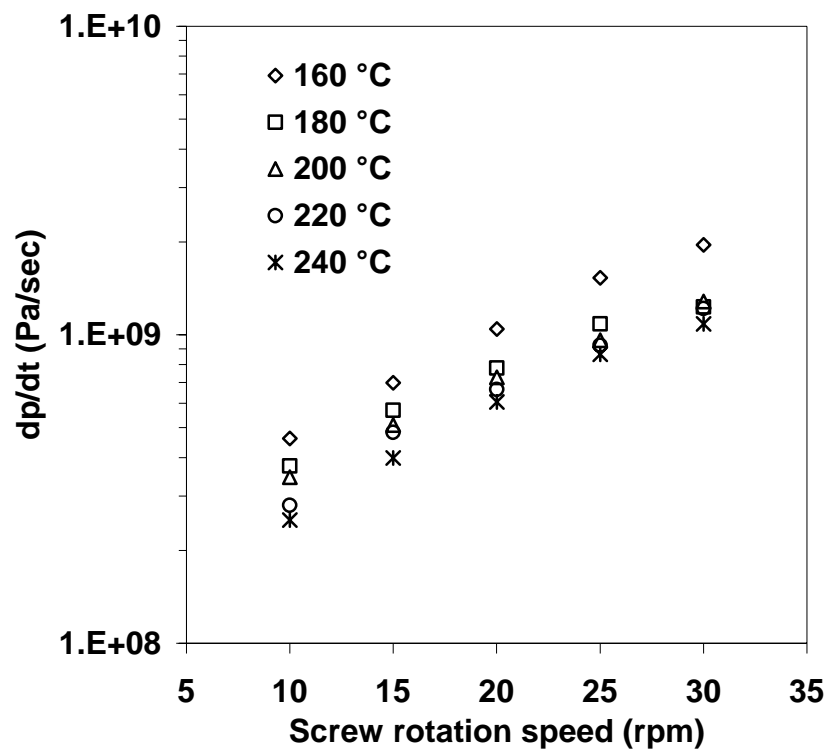


Figure 4.6. Die pressure drop rate at different screw rotation speeds.

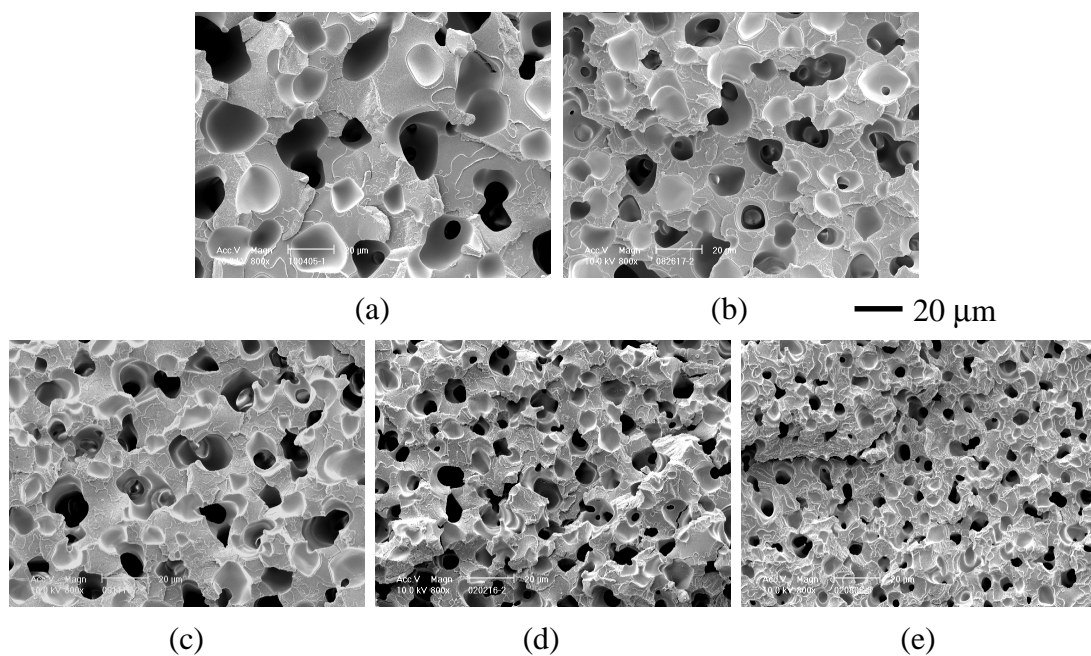
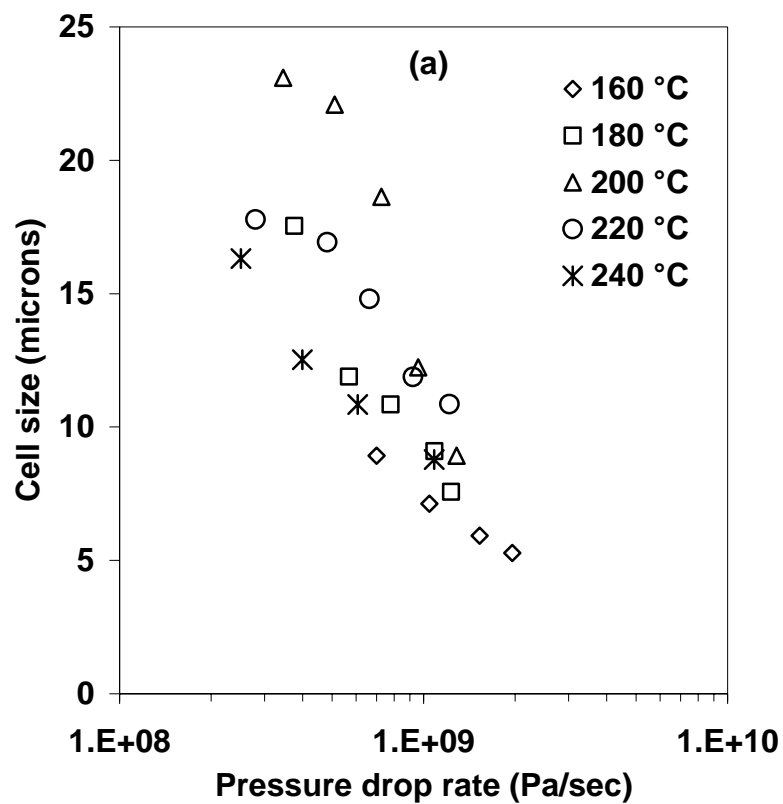


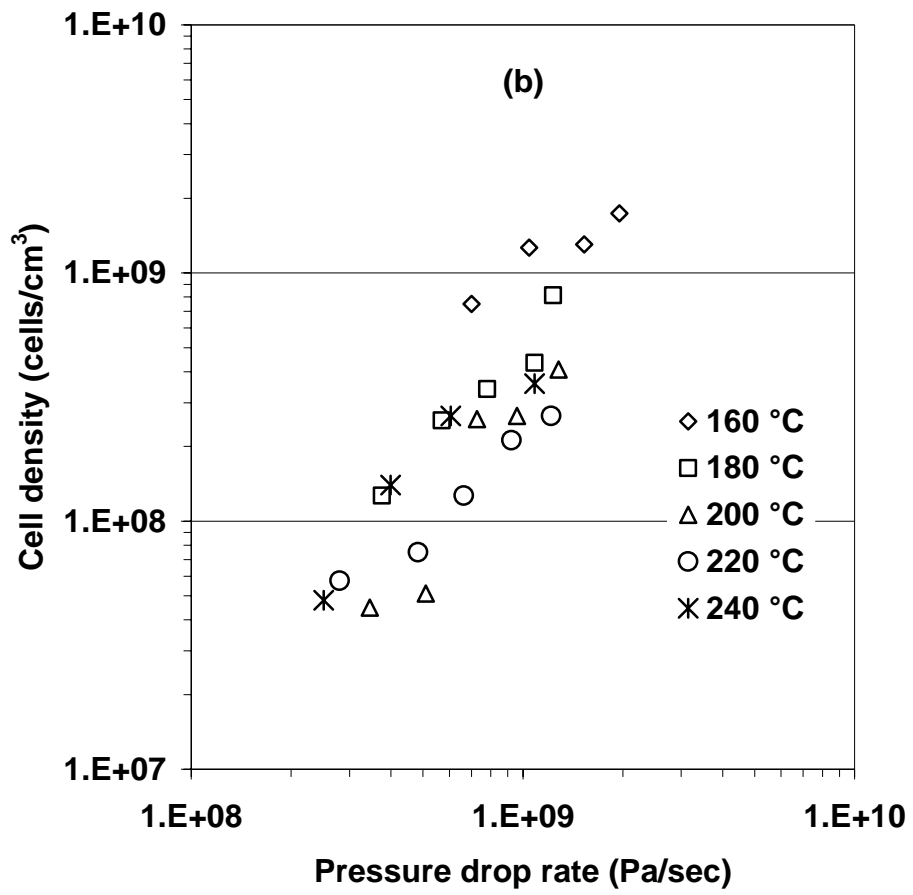
Figure 4.7. SEM micrographs of foam cells at 30 rpm, 1 wt.% CO<sub>2</sub>, and different foaming temperatures: (a) 240°C ( $dp=9.9$  MPa,  $dp/dt=6.1\times 10^8$  Pa/s); (b) 220°C ( $dp=11.3$  MPa,  $dp/dt=9.2\times 10^8$  Pa/s); (c) 200°C ( $dp=12.6$  MPa,  $dp/dt=9.6\times 10^8$  Pa/s); (d) 180°C ( $dp=13.8$  MPa,  $dp/dt=1.2\times 10^9$  Pa/s); (e) 160°C ( $dp=17.3$  MPa,  $dp/dt=2.0\times 10^9$  Pa/s).



( continued )

Figure 4.8. (a) Relationship between cell size and pressure drop *rate* at different foaming temperatures with the same CO<sub>2</sub> content (1 wt%). (b) Relationship between cell density and pressure drop *rate* at different foaming temperatures with the same CO<sub>2</sub> content (1 wt%).

Figure 4.8 continued



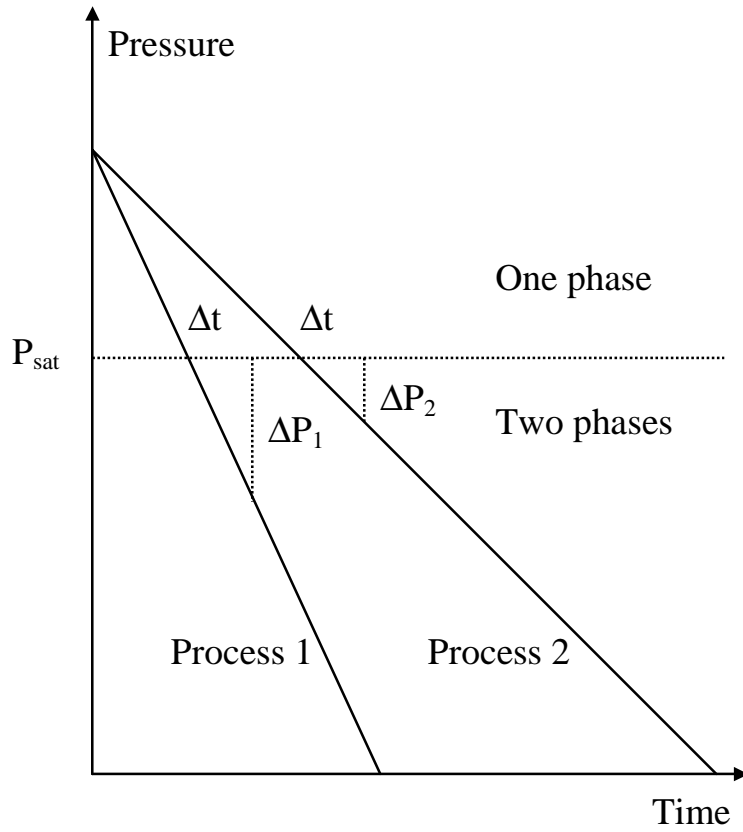


Figure 4.9. Why the pressure drop rate ( $dP/dt$ ) is important (adapted from ref. [20]).

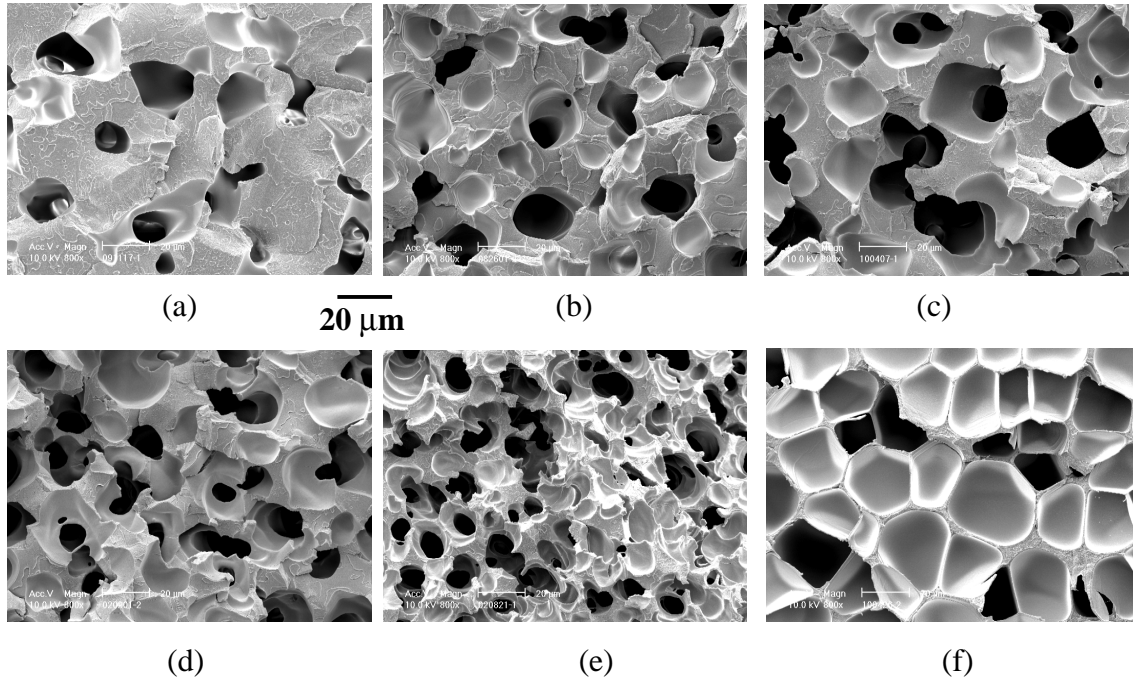


Figure 4.10. SEM pictures of polystyrene samples foamed at different temperatures at 10 rpm and 1 wt.% CO<sub>2</sub>: (a) 240°C ( $dp=6.7$  MPa,  $dp/dt=2.5\times 10^8$  Pa/s); (b) 220°C ( $dp=7.9$  MPa,  $dp/dt=2.8\times 10^8$  Pa/s); (c) 200°C ( $dp=9.7$  MPa,  $dp/dt=3.5\times 10^8$  Pa/s); (d) 180°C ( $dp=12.1$  MPa,  $dp/dt=3.8\times 10^8$  Pa/s); (e) 160°C ( $dp=15.0$  MPa,  $dp/dt=4.6\times 10^8$  Pa/s); and (f) 140°C ( $dp=23.6$  MPa,  $dp/dt=5.7\times 10^8$  Pa/s).

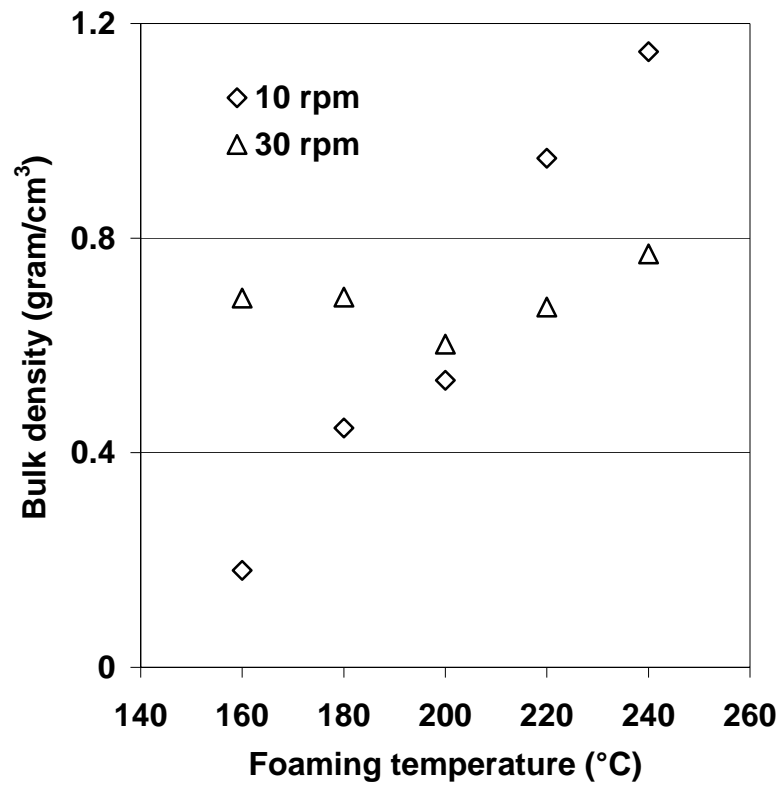


Figure 4.11. Foam density change with foaming temperature (1 wt.% CO<sub>2</sub>).

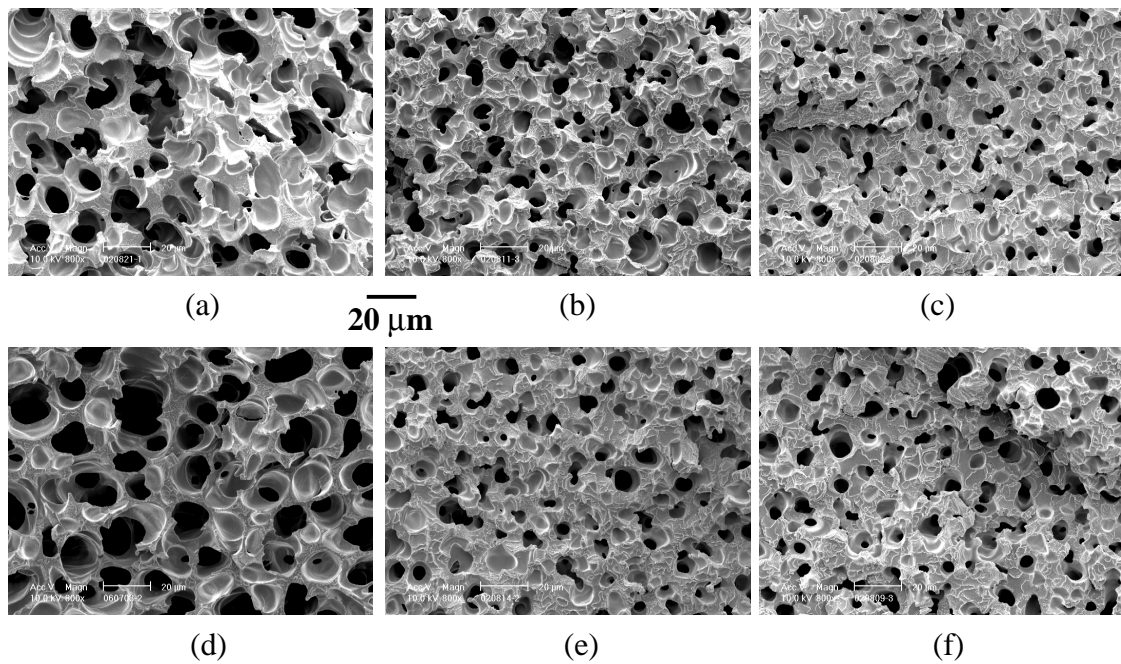


Figure 4.12. SEM pictures of polystyrene samples foamed at 160°C: (a) 1 wt%, 10 rpm ( $dp=15.0$  MPa,  $dp/dt=4.6\times 10^8$  Pa/s); (b) 1 wt%, 20 rpm ( $dp=16.1$  MPa,  $dp/dt=1.0\times 10^9$  Pa/s); (c) 1 wt%, 30 rpm ( $dp=17.3$  MPa,  $dp/dt=2.0\times 10^9$  Pa/s); (d) 6 wt%, 10 rpm ( $dp=14.5$  MPa,  $dp/dt=4.2\times 10^8$  Pa/s); (e) 6 wt%, 20 rpm ( $dp=16.2$  MPa,  $dp/dt=1.2\times 10^9$  Pa/s); and (f) 6 wt%, 30 rpm ( $dp=16.9$  MPa,  $dp/dt=1.8\times 10^8$  Pa/s).

## CHAPTER 5

### EXTRUSION OF POLYSTYRENE NANOCOMPOSITE FOAMS WITH SUPERCRITICAL CO<sub>2</sub>

#### 5.1. Introduction

Polymeric foams are found in applications ranging from packaging, insulation, cushions, and adsorbents [2], to scaffolds for tissue engineering [99]. Recently, microcellular foams generated by using supercritical CO<sub>2</sub> as the foaming agent have drawn a great deal of attention and interest in industry and academia [11, 14, 16, 19, 20, 34, 35, 53, 79, 80, 231]. Compared with traditional foaming agents (hydrocarbons or chlorofluorocarbons), CO<sub>2</sub> at its supercritical state ( $T_c = 31^\circ\text{C}$  and  $P_c = 73.8$  bar, or 1074 psi) exhibits several advantages [116]. The high diffusivity makes it possible to dissolve sufficient CO<sub>2</sub> in a polymer melt quickly. CO<sub>2</sub> can reduce the viscosity and surface tension of polymer melts, which assists many polymer processing operations. Moreover, CO<sub>2</sub> is low-cost, non-flammable, environmentally friendly, and chemically benign.

Microcellular foams, characterized by cell sizes smaller than 10  $\mu\text{m}$  and cell densities larger than  $10^9$  cells/cm<sup>3</sup> [10], can greatly reduce material use without compromising mechanical properties. Typical microcellular plastics exhibit high impact strength or toughness [40, 66-68, 222] and high fatigue life [73, 74]. Microcellular

polymers are light in weight and consequently, they have a higher mechanical strength to weight ratio than common structural foams at equivalent densities. However, the operating windows are very narrow for the microcellular foaming of pure polymers, usually requiring an extremely high pressure drop or pressure drop rate and a very low foaming temperature near the glass transition temperature  $T_g$ . The addition of nucleation agents can reduce the cell size and increase the cell density at less stringent operating conditions.

To obtain plastic foams with controlled cell structure, organic, inorganic, or metal powders can act as nucleation agents or ‘hot spots’ in order to reduce the nucleation energy. Solubility [128, 130, 131], shear viscosity [162, 163, 167, 169, 174], and nucleation [192-198] for various gas/polymer systems have been studied in the past. In classical nucleation theory [192-194], the heterogeneous nucleation is expressed as

$$N_I = f_I C_I \exp(-\Delta G_{het}^* / kT) \quad (5.1)$$

where  $N_I$  is the rate of heterogeneous nucleation,  $f_I$  is the frequency factor of gas molecules joining the nucleus,  $C_I$  is the concentration of heterogeneous nucleation sites,  $k$  is the Boltzmann's constant,  $T$  is the temperature, and the nucleation energy  $\Delta G_{het}^*$  is related to the interfacial tension  $\sigma$ , wetting angle  $\theta$  at the polymer-additive-gas interface, and the pressure difference  $\Delta P$  in and out of the cell (bubble) by:

$$\Delta G_{het}^* = 16 \pi \sigma^3 f(\theta) / (3 \Delta P^2) \quad (5.2)$$

in which  $f(\theta)$  is a function of  $\theta$ .

Although the nucleation mechanism is still not well understood, it is generally known that the size, shape, and distribution of the particles, as well as the surface

treatment can affect the nucleation efficiency. Ramesh et al. [201, 202] developed a model for heterogeneous nucleation in the blend of polystyrene (PS) and high impact polystyrene (HIPS) based on a micro-void theory that assumes micro-voids exist at the filler-polymer interface. A polystyrene-zinc stearate system was selected by Colton et al. [192-194] to investigate nucleation phenomenon. The homogeneous nucleation theory was extended to a heterogeneous case. They considered the free volume change caused by the dissolved gas and the surface tension change caused by the presence of a third phase and their influence on the Gibbs free energy of nucleation. Park et al. [232] studied the effect of talc on the cell nucleation of polypropylene foamed by CO<sub>2</sub> and isopentane. They found that when isopentane is used as the foaming agent, bubble nucleation is dominated by the talc concentration and not affected too much by the isopentane concentration. In contrast, the effect of talc is significant only at low CO<sub>2</sub> content and then the CO<sub>2</sub> content primarily determines the cell nucleation. Recently, Chen et al. [233] stated that the filled polymers (i.e. high density polyethylene (HDPE)/talc, and poly(vinyl chloride) (PVC)/CaCO<sub>3</sub>) absorb more CO<sub>2</sub> compared to the unfilled ones since the gas tends to accumulate on the filler-polymer interface and helps create nucleation sites. Furthermore, foams with finer fillers show a higher cell density at a high saturation pressure and a lower cell density at a low saturation pressure. All these studies are based on micron-sized particles.

In this work, nano-sized particles, nano-clays, are applied to modify the microcellular foams in a continuous extrusion foaming process. It has been shown that with the addition of a very small amount of nano-clay into the polymer matrix, the nanocomposites exhibit substantial increase in many physical properties, including

mechanical strength (e.g. tensile modulus and strength, flexural modulus and strength), thermal stability, flame retardance, and barrier resistance [87-92]. Smectite clays, such as montmorillonite (MMT), are of particular interest because they offer a high aspect ratio (100-1000) and a high surface area. Montmorillonite is hydrophilic in nature, which hinders its dispersion in the organic polymer phase. Ion exchange of the interlayer inorganic cations ( $\text{Na}^+$ ,  $\text{Ca}^{2+}$ ) with an organic cation renders the hydrophilic clay surface organophilic. The reduction in surface energy improves the wetting characteristics of the clay surface with polymers or monomers.

Depending on the dispersion of clay, nanocomposites may possess two idealized structures: intercalated and exfoliated. Intercalation results from limited insertion of polymer chains into the interlayer region and interlayer expansion. Usually the ordered layer structure of the clay is preserved and can be detected by wide angle X-ray diffraction (WXRd). By contrast, extensive polymer penetration and delamination of clay crystallites lead to exfoliated nanocomposites, in which the nanometer-thick silicate platelets are randomly dispersed in the polymer matrix. Exfoliated nanocomposites usually provide the best property enhancement due to the large aspect ratio and surface area of the clay. It is therefore interesting to explore how this difference in particle dispersion affects cell morphology in plastic foams.

Comparing to conventional micron-sized filler particles used in the foaming process, nanometer-sized clay particles may offer unique properties. The extremely fine dimensions and large surface area of nanoparticles and the intimate contact between particles and polymer matrix may greatly alter the cell nucleation and growth. Therefore, the addition of nano-clay may benefit both microcellular foam structure and properties.

Limited work has been done in this area. Via a batch process, Nam et al. [93, 94] foamed polypropylene/clay nanocomposites and studied their influence on cell density, cell size, cell wall thickness, and bulk density. Transmission electron microscopy observations show that biaxial flow during cell growth induces the alignment of clay particles along the cell boundary. Several patents also mentioned the potential applications of nanoclays in various polymer processing operations, including foaming [95-97].

In this study, we synthesized a series of polystyrene (PS)/clay nanocomposites by extrusion compounding and in-situ polymerization, and used them to prepare nanocomposite foams. Continuous extrusion was conducted to make the microcellular foams by using supercritical CO<sub>2</sub> as the foaming agent. The foam structure and some properties were measured.

## **5.2. Experimental**

### **5.2.1. Synthesis and Characterization of Nanocomposites**

To prepare the intercalated nanocomposites, different amounts of Cloisite 20A provided by Southern Clay (0.5, 2.5, 5, 7.5, 10 wt.%) was pre-mixed with a polystyrene resin (AtoFina CX 5197, melt index: 4.5) and then mechanically blended in a Leistritz ZSE-27 twin-screw extruder (L/D = 40, D = 27mm). Cloisite 20A is a montmorillonite based clay with a surface modifier, dimethyl dihydrogenated tallow quaternary ammonium chloride. The blending temperature varied between 180 and 220°C and the extruder was running in the co-rotating mode at relatively high rotation speeds (200-300 rpm) to provide sufficient mixing.

As described in our previous work [90, 234, 235], in-situ polymerization was carried out to prepare exfoliated nanocomposites. The process can be divided into two major steps: synthesis of the surface modified clay and in-situ polymerization of the composite. Na<sup>+</sup>-montmorillonite (cation exchange capacity CEC = 90meq/100g) was provided by Southern Clay. A reactive cationic surfactant, 2-methacryloyloxyethylhexadecyldimethyl ammonium bromide (MHAB) was synthesized in-house and ion-exchanged with Na<sup>+</sup>-montmorillonite to prepare the organophilic clay. The modified clay is denoted as MHABS. After that, the monomer styrene (Aldrich), the initiator 2,2'-azobisisobutyronitrile (AIBN), and the modified clay were mixed together using a high shear mixer. The mixture was then reacted at 60°C for 20 hrs, after which the temperature was raised to 105°C for another 30 min for complete reaction. Up to 20 wt.% MHABS can be added to create a fully exfoliated nanocomposite masterbatch [235].

The nanocomposite structure was characterized by both wide angle X-ray diffraction (WXR) and transmission electron microscopy (TEM).

### **5.2.2. Preparation and Analysis of Nanocomposite Foams**

The basic principle of a physical foaming process is to mix a blowing agent (typically a gas) into a polymer matrix and then reduce the solubility of the blowing agent by thermodynamic instabilities, usually a temperature increase or a pressure decrease, to induce the nucleation. After nucleation, the bubble growth starts, which is mainly controlled by the temperature. The foam cells are finally vitrified when the temperature is reduced below than  $T_g$  of the polymer.

The continuous foaming extrusion process was performed on a two-stage single-screw extruder (HAAKE Rheomex 252P) shown in Figure 5.1. A static mixer (Omega, FMX8441S) was attached to the end of the extruder to provide extra distributive mixing. A capillary die with a 0.5 mm diameter and 10 mm long nozzle was custom-made to generate a high and rapid pressure drop. CO<sub>2</sub> was delivered from a syringe pump (ISCO 260D) with a cooling jacket. The CO<sub>2</sub> pressure and volumetric flow rate can be controlled precisely by the pump controller.

CO<sub>2</sub> was compressed to the required pressure in the syringe pump at 40°C reaching a supercritical state. Then approximately 4 wt.% CO<sub>2</sub> was injected into the extruder barrel by carefully controlling the pressure and the volumetric flow rate. Upon injection into the barrel, CO<sub>2</sub> is mixed with the polystyrene melt by screw rotation. A one-phase solution is formed when the mixture flows through the static mixer. Nucleation occurs in the die due to the quick and large pressure drop realized by the narrow capillary nozzle. The foamed extrudate flows freely out of the nozzle and vitrifies in the ambient air.

Cell size ( $D_f$ ), which is characterized by the diameter of the foam cells, and cell density ( $N_f$ ), which is the number of cells per unit volume, are determined by analyzing images obtained from scanning electron micrographs (SEM) using Scion image software.

A micrograph showing more than 50 bubbles is chosen, and the number of bubbles,  $n$ , in the micrograph is determined by the software. If the area of the micrograph is  $A \text{ cm}^2$  and the magnification factor is  $M$ , the cell density can be estimated as

$$N_f = \left( \frac{nM^2}{A} \right)^{3/2} \quad (5.3)$$

The foam density was measured by evaluating both the mass and the volume of the sample. The void fraction of foam samples was estimated by knowing the cell size and cell density from SEM micrographs.

The tensile modulus of the foam samples was measured using the Rheometrics Solids Analyzer (RSA II). All samples were 2.5 cm round rods with diameters from 0.5 to 1.5 mm. The applied crosshead speed was 0.15 mm/sec.

A burning test was also carried out to test the fire resistance. A piece of soft paper soaked with ethanol was placed on the table and the rod-like foam samples were ignited and burned above the soft paper. If the burning sample drips, the soft paper will catch fire quickly.

To study the effect of nano-clay on  $\text{CO}_2$  solubility and diffusivity, experiments of  $\text{CO}_2$  sorption and desorption were performed. At high temperatures, temperature control and the accurate reading of pressure and volume are very difficult, so the absorption measurement was carried out at  $50^\circ\text{C}$  and the desorption was characterized at room temperature. Although the testing temperatures are not the actual foaming temperature,  $200^\circ\text{C}$ , the results can provide some general trend. The experimental procedure was similar to that employed by Berens et al. [236]. Flat plate samples (44~51 mm in length,

8.1~8.8 mm in width, and 0.37~0.43 mm in thickness) of PS or PS/nano-clay composites were placed in a high-pressure vessel that was connected to a syringe pump. The samples were saturated with CO<sub>2</sub> at 10 MPa and 50°C for 24 hours. They were then quickly taken out of the high-pressure vessel and placed on a high-resolution balance. The CO<sub>2</sub> desorption curve (weight loss with time) was recorded. From this desorption curve, CO<sub>2</sub> solubility at 50°C was obtained by extrapolating the data back to time zero and CO<sub>2</sub> diffusivity at room temperature was also calculated.

The shear viscosity of PS and PS/clay composites without CO<sub>2</sub> was measured at 200°C under the dynamic frequency sweep mode using the Rheometrics Mechanical Spectrometer (RMS 800).

### **5.3. Results and Discussion**

#### **5.3.1. Intercalated and Exfoliated PS/Clay Nanocomposites**

Each montmorillonite clay particle contains thousands of individual layers with a thickness dimension of ~1 nm and a lateral dimension of ~1000 nm. To take advantage of its high aspect ratio (100-1000) and large surface area, the layers should be separated as far as possible.

It has been shown that the formation of nanocomposites relies on the penetration of polymer chains into the interlayer region to separate the layers [237-239]. The layer separation, especially exfoliation, depends on the establishment of favorable interactions between the polymer and the clay surface, and the subsequent system energy reduction. Limited interaction resulted in limited polymer chain penetration, leading to intercalated nanocomposites. Figure 5.2 shows the WXR patterns of PS/clay nanocomposites.

PS/5 wt.% 20A nanocomposite exhibits two strong and one weak diffraction peaks, corresponding to (d001), (d002) and (d003) basal reflections. Clay 20A has an interlayer spacing of 2.3 nm. Upon PS intercalation, the basal spacing increases to 3.5 nm. The TEM micrograph (Figure 5.3a) shows that large clay aggregates are still present in the matrix. Face-to-face layer stacking and low angle intergrowth of tactoids are observable.

On the other hand, by using the reactive surfactant MHAB, the copolymerization of MHAB and the styrene monomer forces layer separation and an exfoliated nanocomposite was synthesized with a clay concentration up to 20 wt.%. The WXRd of PS/5%MHABS shows a featureless pattern (Figure 5.2(b)). A TEM micrograph of PS/5%MHABS is shown in Figure 5.3(b). The tactoids have been completely delaminated and uniformly dispersed in the matrix, while stacks of a few layers are also observable in some regions. As discussed in our previous work [90, 234], the copolymerization of an interlayer surfactant with styrene monomer provides the driving force for delamination of clay crystallite.

### **5.3.2. Continuous Foaming Extrusion**

For a batch foaming process, where the polymer samples are saturated by CO<sub>2</sub> in a high-pressure vessel and then foamed by the pressure release, the foam cell size is typically large and the cell density is low due to the relatively low and uncontrolled pressure drop rate, on the order of 10<sup>6</sup> Pa/sec. By contrast, continuous extrusion can create a high pressure drop and pressure drop rate. For the die used in this work, the residence time of the polymer in the die is typically shorter than 0.1 second; as a result,

the pressure drop rate can be larger than  $10^9$  Pa/sec when the die entrance pressure is from 6.9 to 20.7 Mpa (1000 – 3000 psi). This provides a greater thermodynamic instability to induce the nucleation of foam cells.

Figures 5.4a and 5.4b show the pressure drop and the pressure drop rate across the die at different mass flow rates resulting from different screw rotation speeds. It is clear that the nanocomposites, either intercalated or exfoliated, create a higher pressure drop (Figure 5.4a) and a higher pressure drop *rate* (Figure 5.4b) compared with pure PS at the same temperature and flow rate. The exfoliated PS/5 wt.% MHABS gives the highest pressure drop rate due to its highest viscosity at the same screw rotation speed (10 rpm). The three lowest flow rates in the figures were at the same screw rotation speed for the three materials.

#### **5.3.2.1. Effects of Clay Dispersion**

Intercalated and exfoliated PS/5 wt.% clay nanocomposites as well as the PS/5 wt.% talc blend were foamed at a die temperature of 200°C, a screw rotation speed of 10 rpm, and a CO<sub>2</sub> concentration of 4 wt.%. The cell morphology is shown in Figure 5.5. The cell size in PS/talc is larger and the cell density is lower than those in PS/20A at the same particle concentration. Once exfoliated, the nanocomposite foam has the smallest cell size and highest cell density. In contrast to some open cell structures observed in Figure 5.5b, the exfoliated composite (Figure 5.5c) shows a perfect microcellular foam structure in which cells are round in shape, closed, and well separated. Very little cell coalescence was observed. The calculated average cell size and cell density are 4.9

microns and  $1.5 \times 10^9$  cells /cm<sup>3</sup> respectively. In addition, the exfoliated composite extrudate exhibits a very smooth and shiny surface that comes from the small cell size and the few flaws created by well-dispersed clay particles in the polymer matrix.

Figure 5.6 shows the TEM photos of the three samples. At the same particle concentration, a few talc particles (the black points on the image) are dispersed on the cell wall and all of them are aggregates. For intercalated nano-clay, both well dispersed and tactoid clay layers are observed and the foam cells are found to nucleate and grow around the clay particles to form many small ( $\sim 2 \mu\text{m}$ ) and irregular-shaped cells (labeled by arrows) on the cell wall. On the other hand, exfoliated clay disperses uniformly through the polymer matrix and small features can be seen on the cell wall. The clay is found to align along the boundary of the cells, perhaps due to the biaxial extensional flow pattern during the cell growth, as reported by Nam et al. [93, 94]. Such an alignment may improve the barrier properties and slow down gas diffusion in and out of the sample.

Particles are added to induce heterogeneous nucleation. The available surface area and particle sites affect nucleation. In nanocomposites, particles are much better dispersed in the matrix and therefore expose more surface area than micron-sized particles. In intercalated nanocomposites, most clay exists as stacks of layers or tactoids, serving as nucleation sites. In exfoliated nanocomposites, clay is present mostly as separated layers and usually the distance between the layers is greater than the effective radius of gyration of a polymer chain. Unlike in intercalated nanocomposites where polymer chain penetration is limited and the major contact area is the outer surface of the tactoids, in exfoliated nanocomposites the separated layers are in direct contact with the

matrix, providing much larger interfacial area for CO<sub>2</sub> adsorption and cell nucleation. As a result, the exfoliated nanocomposite foam provides the highest cell density and the smallest cell size.

The PS matrix in three blends is different. The exfoliated nanocomposite were prepared from in-situ polymerization of styrene monomer, while the others were from extrusion compounding of particles with a commercial polystyrene. Our previous work [240] showed that the molecular weight itself has little influence on the cell size and cell density. When the cell size and cell density are plotted versus the pressure drop rate (dP/dt), all polystyrenes with different molecular weights merge into one single curve, which implies that the same cell size and cell density will be obtained at the same dP/dt for all polystyrenes. The molecular weight difference affects the viscosity, and thus the pressure drop rate. Therefore, we may conclude that the reduction in cell size and the increase in cell density after the addition of nano-clay mainly result from the heterogeneous nucleation.

#### **5.3.2.2. Effects of Clay Concentration**

To explore the effect of nano-clay concentration on the microcellular foaming extrusion, four nanocomposites with different 20A concentrations (0.5, 2.5, 5, and 7.5 wt.%) were prepared by extrusion blending and then foamed in the single screw extruder under the same operating conditions (200°C foaming temperature, 20 rpm screw rotation speed, and 4 wt.% CO<sub>2</sub> concentration).

As shown in Figure 5.7, the cell size decreases greatly with a small amount of nano-clay (~ 2.5 wt%) blended in and then levels off at high clay concentrations. However, the cell density increases nearly linearly.

Comparing the SEM images (Figure 5.8) of these samples, it can be seen that the cells tend to coalesce together as more 20A is blended in PS. Cells in the pure PS are mostly round in shape and well separated from each other. The cell size is large and the cell density is relatively low. Cell coalescence is not observed for the 2.5 wt.% 20A sample. However, when the concentration of 20A increases to 5 wt.%, coalescence of cells appears, and it becomes more obvious for the 7.5 wt.% 20A sample. A possible explanation is that when a large amount of 20A is blended in the polymer matrix, the plate-like particles tend to orient parallel with each other, especially in a high shear stress field as found in the extrusion die. The parallel orientation and connection creates a sandwich structure in the micro domain that consists of arrays of nano-clay particles with the polystyrene matrix in between. The cell growth is confined to the space between the arrays and the cells grow along the orientation direction of the nano-clay particles. Because of this, elongated open cells with a cigar shape are common in more concentrated polystyrene/20A composites. This provides a good method to produce open-cell foams when desired.

### 5.3.2.3. Effect of Operating Conditions

PS and PS/5% 20A intercalated nanocomposites were also foamed at different pressure drops by changing the screw rotation speed, i.e., the mass flow rate of the polymer/CO<sub>2</sub> mixture. The foaming temperature was the same (200°C) and the CO<sub>2</sub> concentration was kept at 4 wt.%. The exfoliated PS/5% MHABS was only foamed at one screw rotation speed (10 rpm) due to the limited amount of material.

The results are summarized in Figure 5.9, which exhibits how cell size and cell density change with increasing the pressure drop rate. A similar trend is obtained when plotted versus the pressure drop. An interesting observation is that the decrease of the cell size becomes slower at high pressure drop rates, while the cell density increases nearly linearly. The cell size of nanocomposites is smaller than 10 μm and the cell density larger than 10<sup>9</sup> cells/cm<sup>3</sup> when the pressure drop rate is greater than 10<sup>9</sup> Pa/sec. The exfoliated nanocomposite creates the smallest cells and largest cell density at the lowest screw rotation speed. On the contrary, no pure PS foam has a cell density higher than 10<sup>9</sup> cells/cm<sup>3</sup> at these operating conditions, although cell sizes smaller than 10 μm can be obtained.

Compared with pure PS, nanocomposites broaden the operating windows to make microcellular foams. To achieve the same cell size and cell density, the nanocomposites require lower pressure drop rates, which means a larger die opening can be used at the same flow rate. This is important when making large parts in the extrusion foaming process. The foaming temperature applied in this study is far beyond the T<sub>g</sub> of

PS (~ 105°C). With a decrease of the foaming temperature, a higher pressure drop rate can be obtained due to increased melt viscosity. As a result, smaller cell size and higher cell density may be achievable.

### 5.3.3. Cell Nucleation and Growth

Based on the above experimental results, it was found that the cell density increases nearly linearly with an increase of clay concentration or pressure drop rate. However, the cell size decreases rapidly in the region of low clay concentration or low pressure drop rate, then tends to level off in the region of high clay concentration or high pressure drop rate.

The cell density directly corresponds to the number of cell nucleation sites. The addition of nano-clay increases the nucleation sites and thus the nucleation rate according to heterogeneous nucleation theory (Eq. 1). A better dispersion of the clay particles may provide more nucleation sites than less well-dispersed clay particles at the same conditions. A combination of these factors determines how clay dispersion, clay concentration and the pressure drop rate affect cell density.

From a simple mass balance, a relation exists between the cell size  $D$  (diameter) and cell density  $N$  (number of cells per unit volume) as:

$$\begin{aligned} \text{void fraction} &= \frac{\text{volume of cells}}{\text{volume of foam}} \\ &= N(\text{cells} / \text{cm}^3) \left( \frac{4}{3} \pi \left( \frac{D(\text{cm})}{2} \right)^3 \right) \end{aligned} \quad (5.4)$$

At the same void fraction, the cell size is inversely proportional to  $N^{1/3}$ . For example, at a constant void fraction of 0.6, the cell density needs to increase from  $1.15 \times 10^9$  cells/cm<sup>3</sup> to  $1.15 \times 10^{15}$  cells/cm<sup>3</sup> in order to reduce the cell size from 10  $\mu\text{m}$  to 0.1  $\mu\text{m}$ . As schematically shown in Figure 5.10, the cell size decreases quickly in the region of low cell density and then tends to level off, which is consistent with our experimental observation.

The void fraction itself changes with many parameters. By substituting the cell size and cell density data in Figure 5.7 and Figure 5.9 in equation (4), the addition of nano-clay is found to increase the void fraction when its concentration is higher than 2.5 wt.%, while an increase of the pressure drop rate decreases the void fraction. The calculated void fractions are included in Table 5.1 and the trend is schematically shown in Figure 5.10.

#### **5.3.4. Properties of Nanocomposite Foams**

The tensile modulus of the foam samples was measured using the Rheometrics Solids Analyzer (RSA II). All samples are 2.5 cm round rods with diameters from 0.5 to 1.5 mm. The applied crosshead speed was 0.15 mm/sec. For comparison, a reduced tensile modulus (i.e., tensile modulus divided by the density of the sample) is calculated. As shown in Figure 5.11, the nanocomposite foams exhibit a higher reduced modulus, although it is still lower than that of non-foamed pure PS. Among the three foam samples, PS/talc, PS/5 wt.% 20A, and PS/5 wt.% MHABS, the densities are close while the exfoliated nanocomposite foam has the highest reduced modulus. Compared to the non-foamed PS sample, the exfoliated nanocomposite foam sample has about 31%

weight reduction with a sacrifice in the reduced modulus of about 19% from 2.6 to 2.1 GPa/g/cm<sup>3</sup>. In comparison, the PS/talc foam has about 29% weight reduction and a decrease of 43% in reduced modulus.

Nanocomposite foams also show enhanced fire retardance. A simple burning test was performed as shown in Figure 5.12. A piece of soft paper soaked with ethanol was placed on the table and the rod foam samples were ignited and burned above it. For the pure PS foam (Figure 5.12a), the burning sample dripped down quickly and ignited the paper. On the contrary, the nanocomposite foam sample (PS/5 wt.% 20A) forms a char during burning without dripping, preventing fire spreading (Figure 5.12b).

Figure 5.13 shows CO<sub>2</sub> desorption curves of three samples, PS, PS/5% 20A, and PS/5% MHABS. After releasing the pressure in the high-pressure vessel, the samples remained unfoamed at low temperatures, and thus the dimensions of the samples remained unchanged. By extrapolating the desorption data back to time zero, the solubility of CO<sub>2</sub> in PS, PS/5% 20A, and PS/5% MHABS at 50°C and 10 MPa was found to be 8.5, 8.5, and 8.8 wt.%, respectively. Carbon dioxide exhibits a slightly higher solubility in the exfoliated PS nanocomposite. The diffusivity at room temperature was calculated based on the three desorption curves by assuming a one-dimensional diffusion since the sample thickness is much smaller than the other two dimensions). The results are  $5 \times 10^{-7}$ ,  $3 \times 10^{-7}$ , and  $3 \times 10^{-7}$  cm<sup>2</sup>/sec for PS, PS/5% 20A, and PS/5% MHABS respectively. Obviously, the addition of nano-clay can slow down the CO<sub>2</sub> diffusion out of the sample.

### **5.3.5. Shear Viscosity of PS Nanocomposites**

In the foaming extrusion process, shear viscosity is one of the most important parameters that determines the pressure drop and pressure drop rate in the die. Shear viscosities of non-foamed PS and PS/clay nanocomposites were measured at 200°C under the dynamic frequency sweep mode by using the Rheometrics Mechanical Spectrometer (RMS 800). The shear rates applied were from 0.1 to 100 1/sec. As shown in Figure 5.14, the addition of the clay increases the shear viscosity of the polymer melt. The more clay added, the higher the viscosity. The exfoliated nanocomposite shows the highest shear viscosity. With the same flow rate and same dimension of the extrusion die, a higher shear viscosity can create a larger pressure drop that benefits the formation of more nucleation sites.

### **5.4. Conclusions**

Intercalated and exfoliated PS nanocomposites were synthesized and continuous extrusion foaming was conducted to prepare nanocomposite foams. At a screw rotation speed of 10 rpm and a die temperature of 200°C, the addition of a small amount (i.e., 5 wt.%) of intercalated nano-clay greatly reduces cell size from 25.3 to 11.1  $\mu\text{m}$  and increases cell density from  $2.7 \times 10^7$  to  $2.8 \times 10^8$  cells/cm<sup>3</sup>. Once exfoliated, the nanocomposite exhibits the highest cell density ( $1.5 \times 10^9$  cells/cm<sup>3</sup>) and smallest cell size (4.9  $\mu\text{m}$ ) at the same particle concentration.

Open cell structure was observed in intercalated nanocomposite foams at high clay concentration. The structure of heterogeneous nucleated cells is affected by the orientation and dispersion of the clay. To decrease the cell size linearly, a third order of power increase in cell density is required at the same void fraction.

Compared with the polystyrene foams, nanocomposite foams can provide superior performance, including high tensile modulus, better surface quality, enhanced fire retardance, and better barrier property.

The addition of nano-clay was found to increase the shear viscosity of polymer melts.

Screw rotation speed of 20 rpm					
20A content (wt. %)	0	0.5	2.5	5.0	7.5
Void fraction	8.6%	8.1%	6.6%	9.8%	12.7%
PS with 5 wt.% 20A					
Screw rotation speed (rpm)	10	15	20	25	30
Void fraction	20.5%	12.7%	13.6%	13.7%	7.1%

Table 5.1. Void fraction of PS nanocomposite foams extruded at 4 wt.% CO<sub>2</sub> and 200°C (calculated based on the cell size and cell density in Figure 5.7 and 5.9).

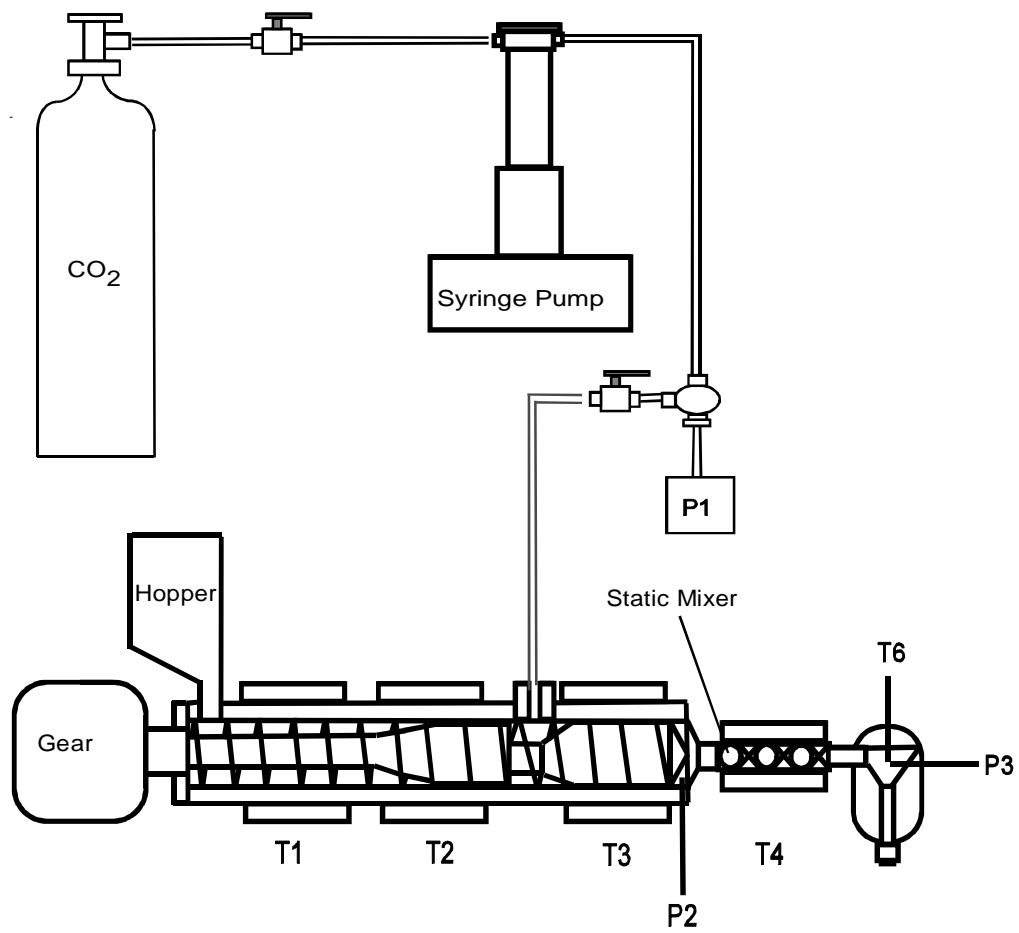


Figure 5.1. Experimental setup of microcellular foaming extrusion.

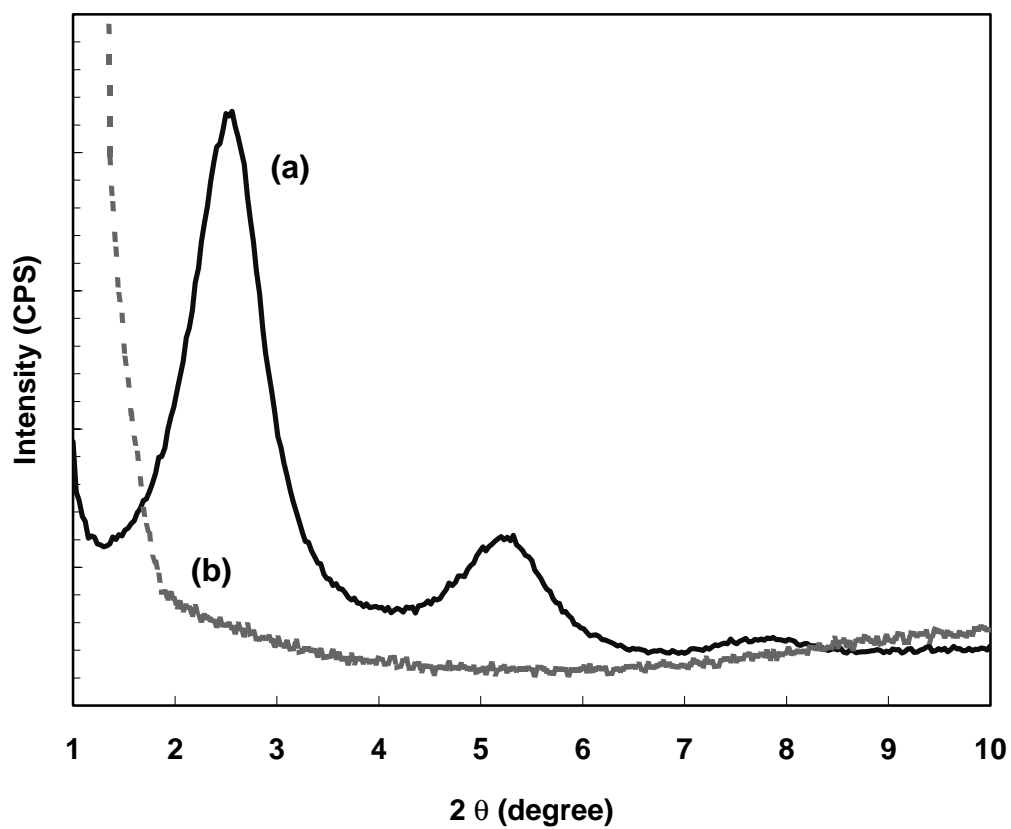


Figure 5.2. Wide angle X-ray diffraction (WAXRD) patterns: (a) intercalated PS/5 wt.% 20A nanocomposite; (b) exfoliated PS/5 wt.% MHABS nanocomposite.

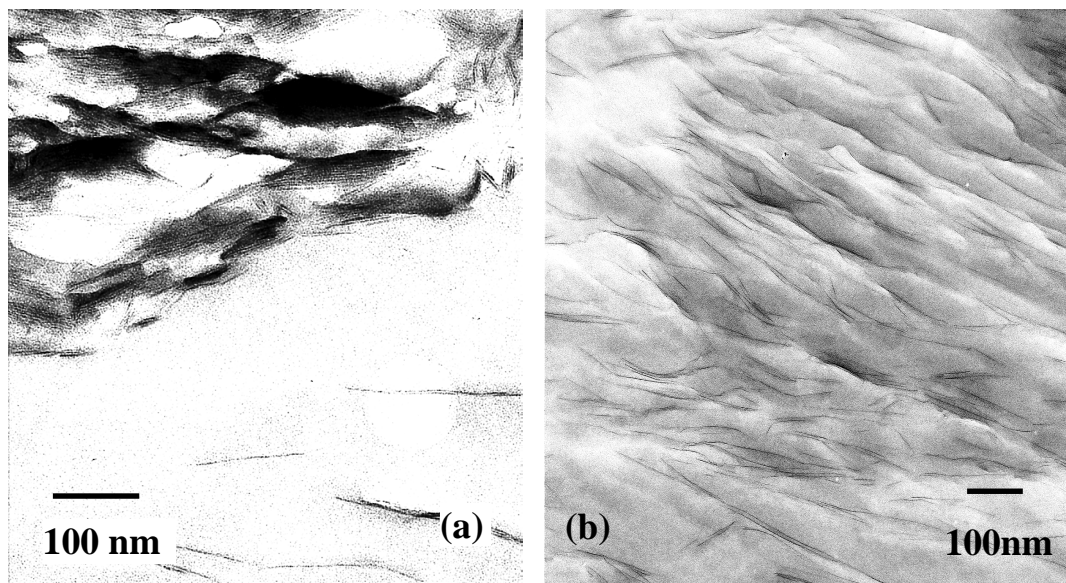
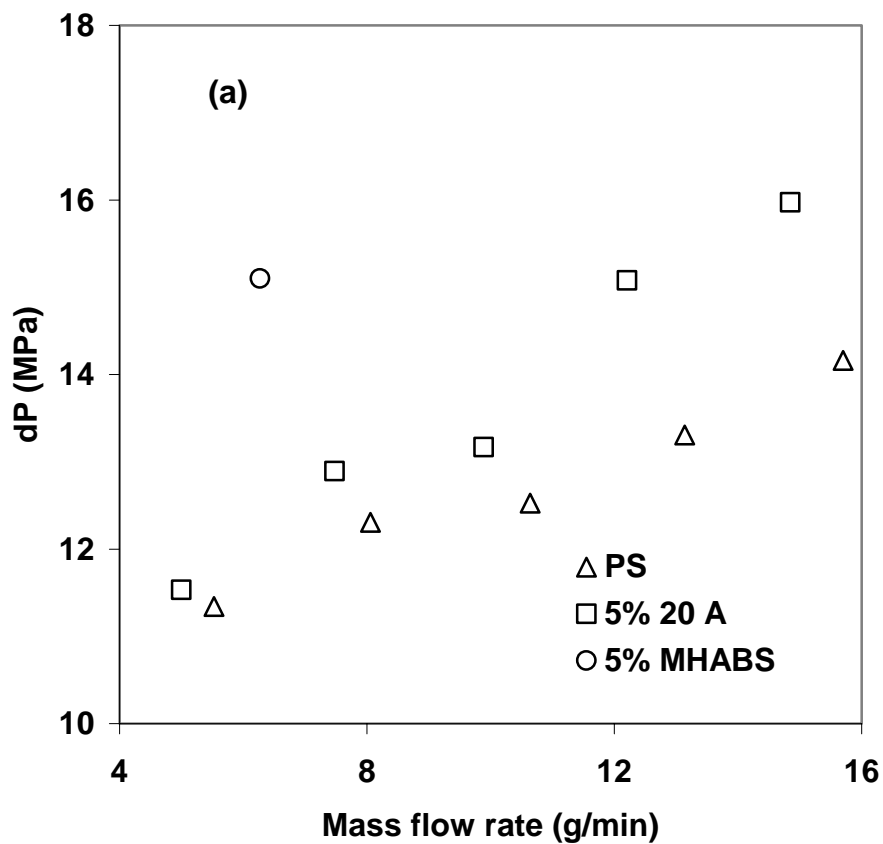


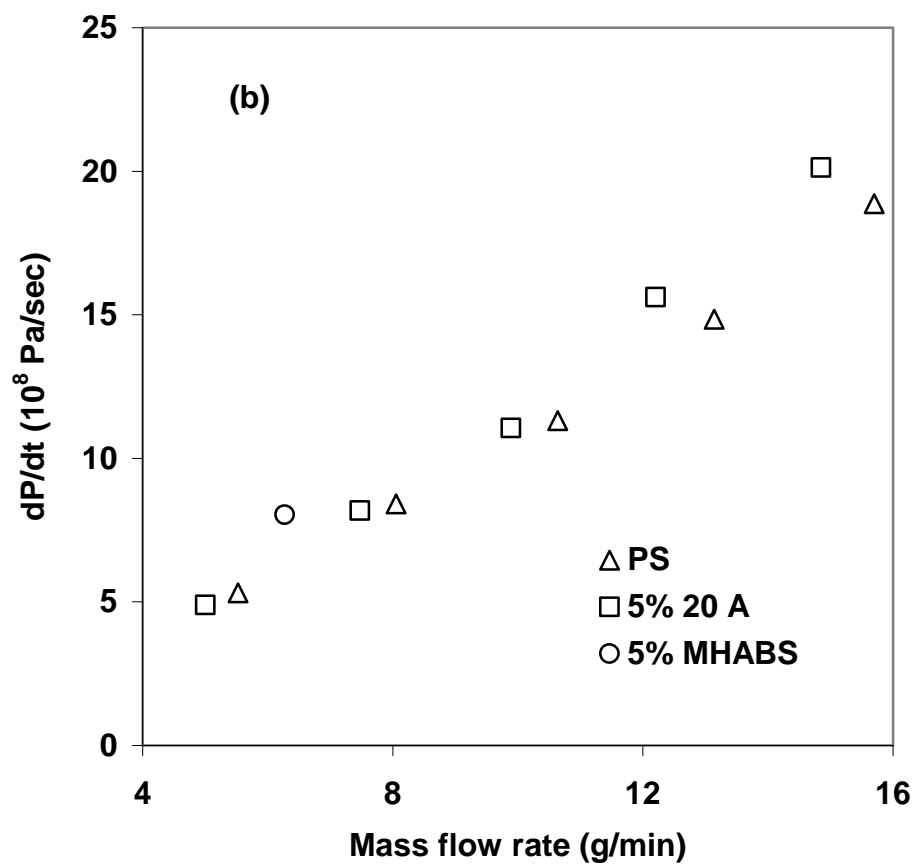
Figure 5.3. TEM images: (a) intercalated PS/5 wt.% 20A nanocomposite; (b) exfoliated PS/5 wt.% MHABS nanocomposite.



(continued)

Figure 5.4. Changes of pressure drop (a) and pressure drop rate (b) at different melt flow rates (die temperature: 200°C; CO<sub>2</sub> concentration: 4 wt.%).

Figure 5.4 continued



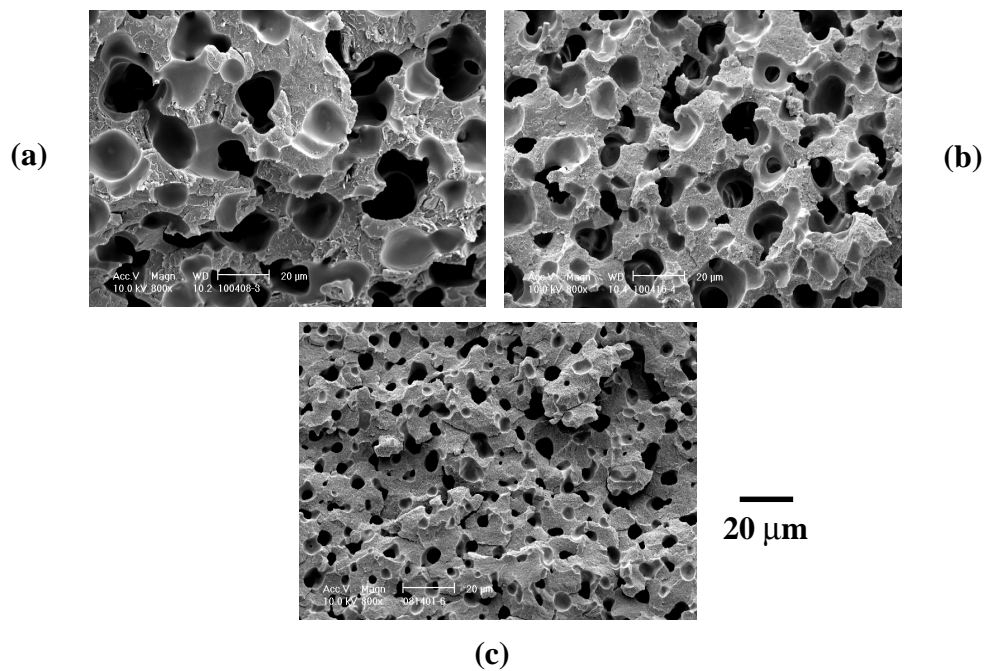


Figure 5.5. Foam structure measured by SEM: (a) PS/5 wt.% talc ( $dP = 11.03$  MPa,  $dP/dt = 4.75 \times 10^8$  Pa/sec), (b) PS/5 wt.% 20A ( $dP = 11.53$  MPa,  $dP/dt = 4.90 \times 10^8$  Pa/sec), and (c) PS/5 wt.% MHABS ( $dP = 15.10$  MPa,  $dP/dt = 8.04 \times 10^8$  Pa/sec). Foaming conditions: die temperature:  $200^\circ\text{C}$ ;  $\text{CO}_2$  concentration: 4 wt.%; screw rotation speed: 10 rpm.

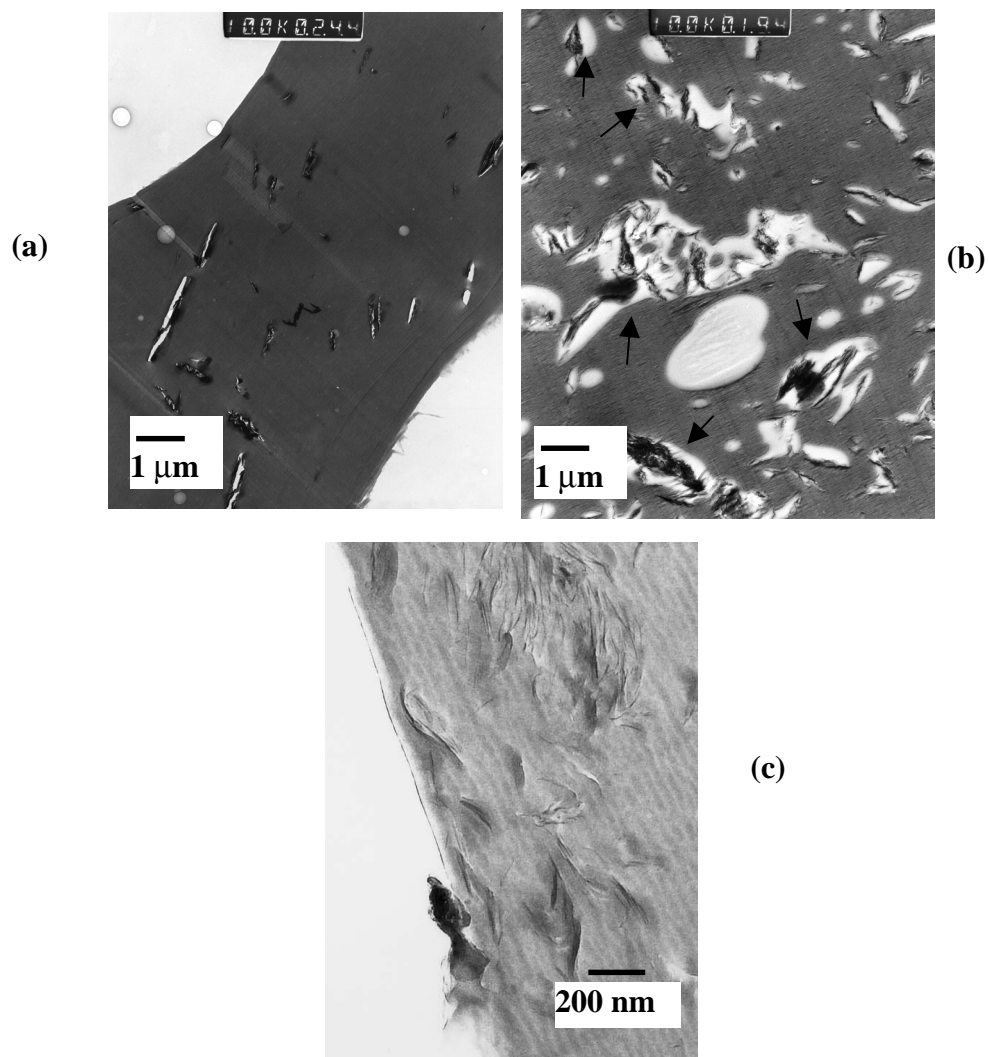


Figure 5.6. Interaction of foam cells and particles measured by TEM: (a) PS/5 wt.% talc, (b) PS/5 wt.% 20A, and (c) PS/5 wt.% MHABS. The foaming conditions are the same as those in Figure 5.5.

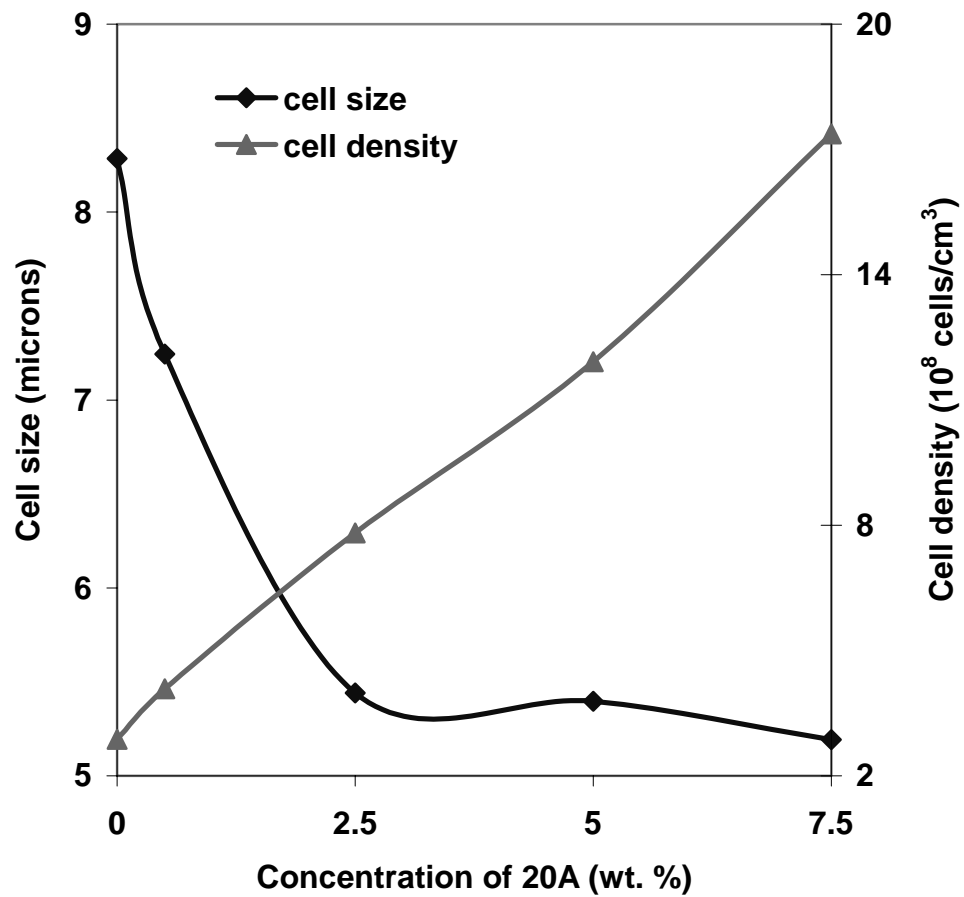


Figure 5.7. Effect of clay concentration on the cell size and cell density (die temperature: 200°C; CO<sub>2</sub> concentration: 4 wt.%; screw rotation speed: 20 rpm).

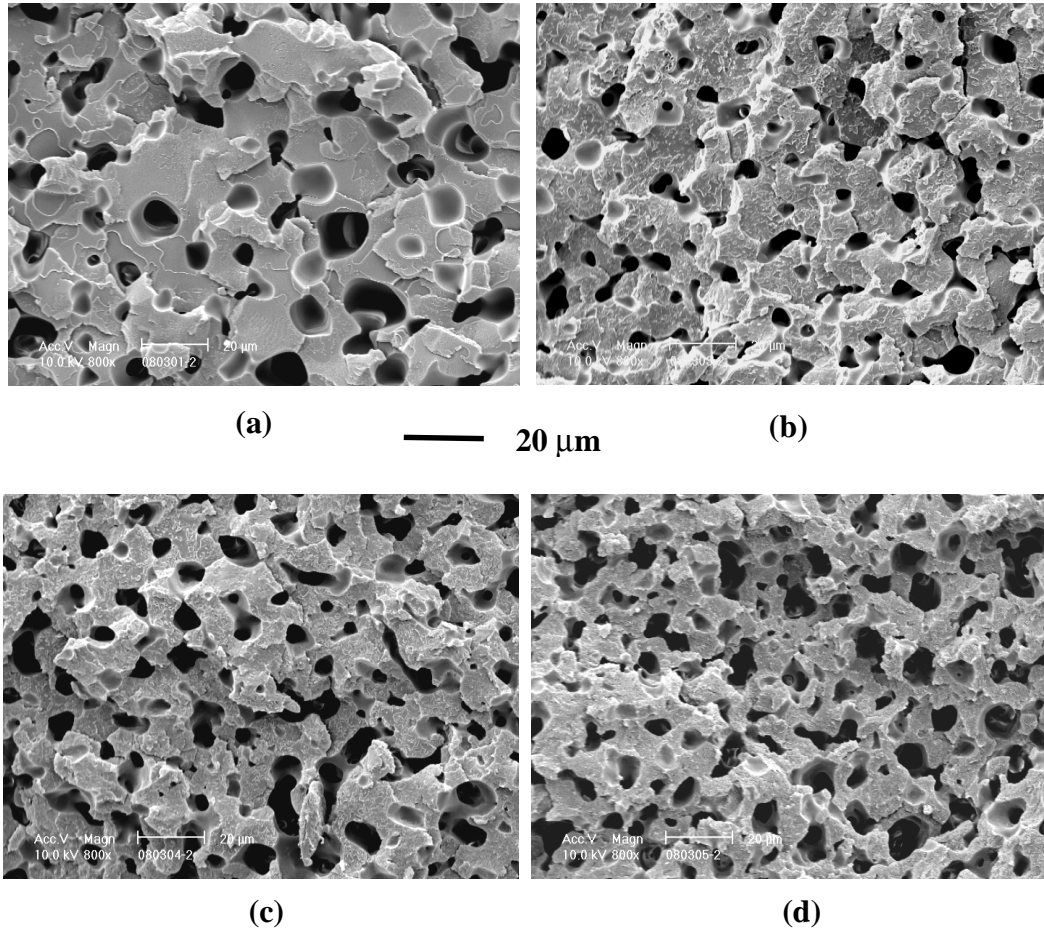
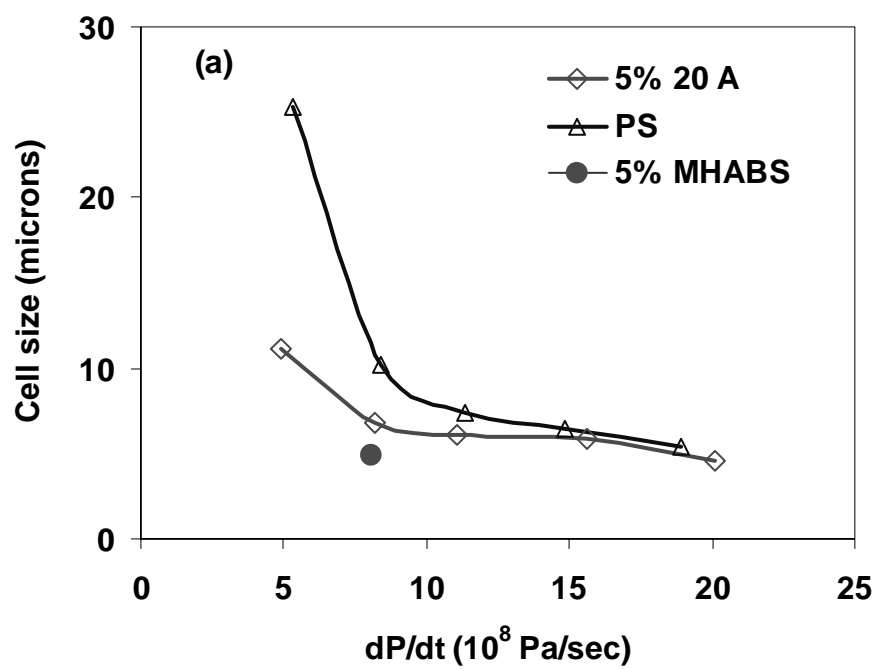


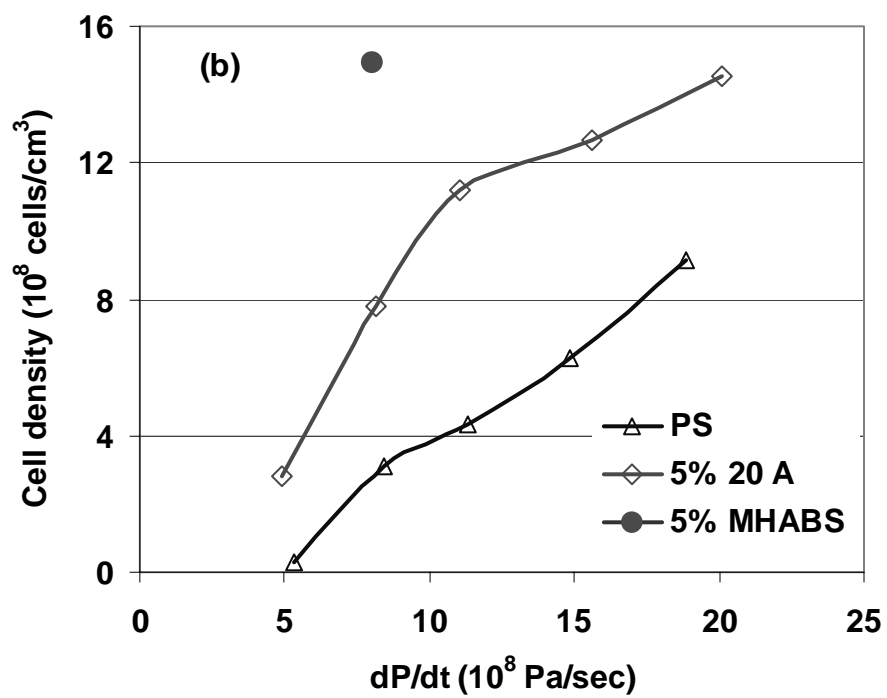
Figure 5.8. Cell morphology of PS/20A nanocomposite foams at 200°C, 4 wt.% CO<sub>2</sub>, 20 rpm, and different clay concentration: (a) 0 wt.% ( $dP = 12.7$  MPa,  $dP/dt = 1.15 \times 10^9$  Pa/sec); (b) 2.5 wt.% ( $dP = 13.2$  MPa,  $dP/dt = 1.14 \times 10^9$  Pa/sec); (c) 5 wt.% ( $dP = 12.8$  MPa,  $dP/dt = 1.10 \times 10^9$  Pa/sec); and (d) 7.5 wt.% ( $dP = 12.7$  MPa,  $dP/dt = 1.07 \times 10^9$  Pa/sec).



(continued)

Figure 5.9. Effect of pressure drop rate on (a) foam cell size and (b) foam cell density (die temperature: 200°C; CO<sub>2</sub> concentration: 4 wt.%).

Figure 5.9 continued



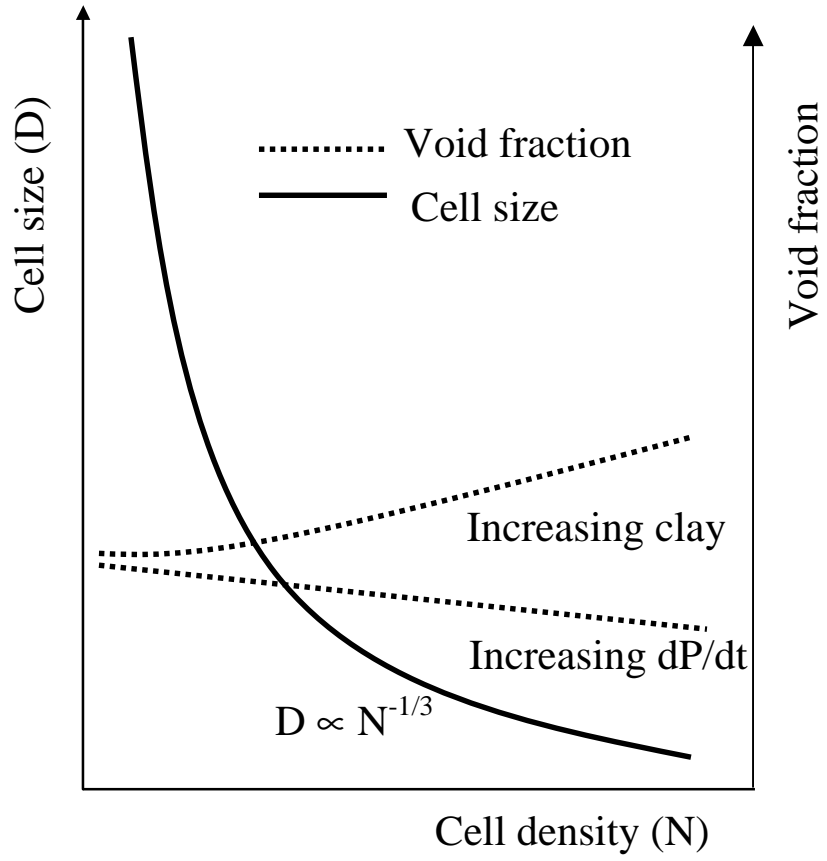


Figure 5.10. Relationship between cell size, cell density, and void fraction.

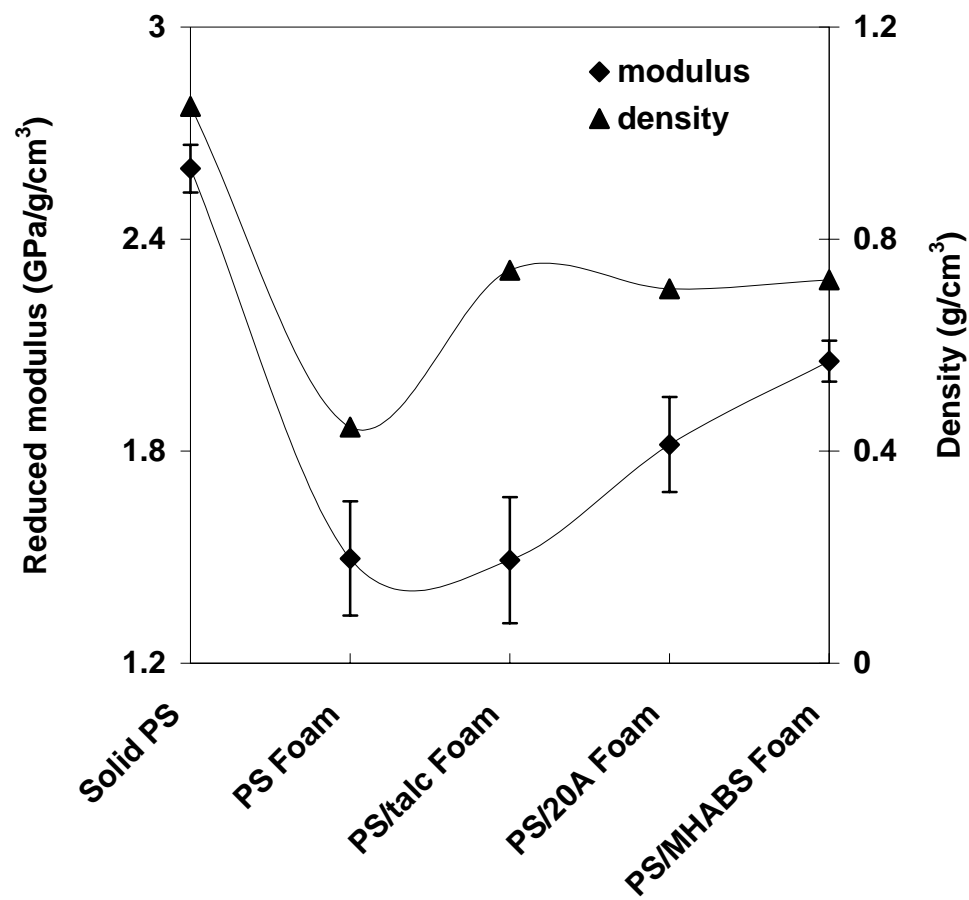
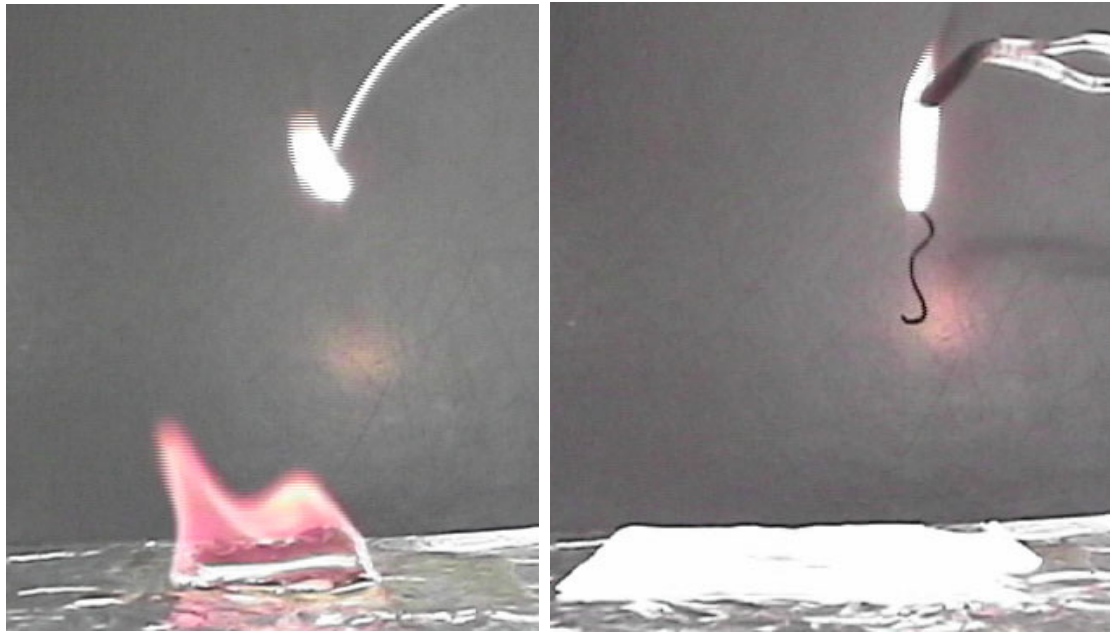


Figure 5.11. Reduced tensile modulus of different foamed samples extruded at 200°C and 4 wt.% CO<sub>2</sub> (PS and PS/5 wt.% MHABS: 10 rpm; PS/5 wt.% talc and PS/5 wt.% 20A: 20 rpm).



(a)

(b)

Figure 5.12. Burning test of (a) PS foam sample, and (b) PS/5 wt.% 20A nanocomposite foam sample.

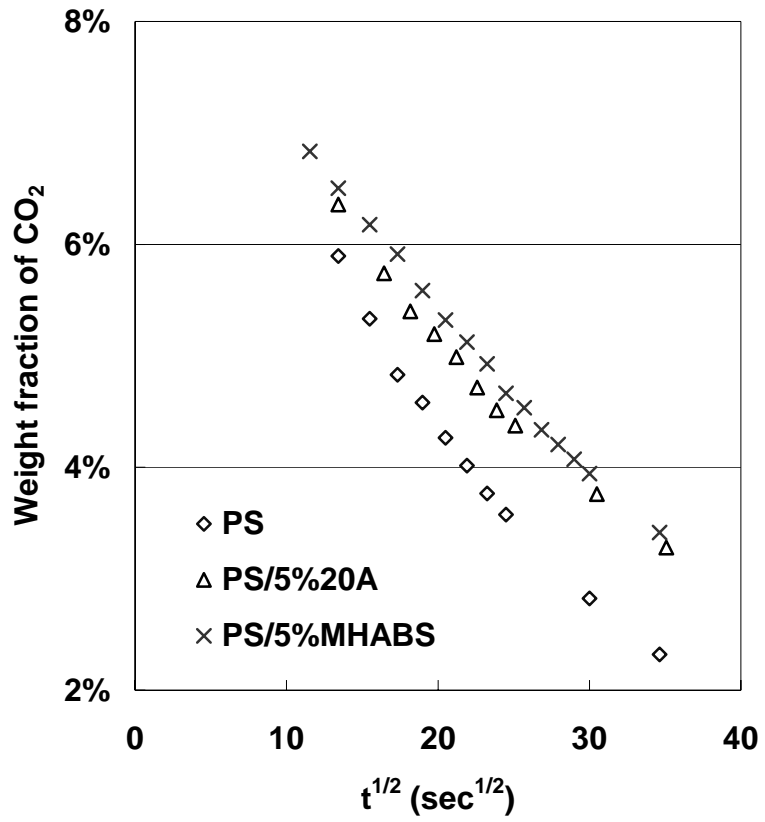


Figure 5.13. CO<sub>2</sub> desorption from PS and PS nanocomposites at room temperature.

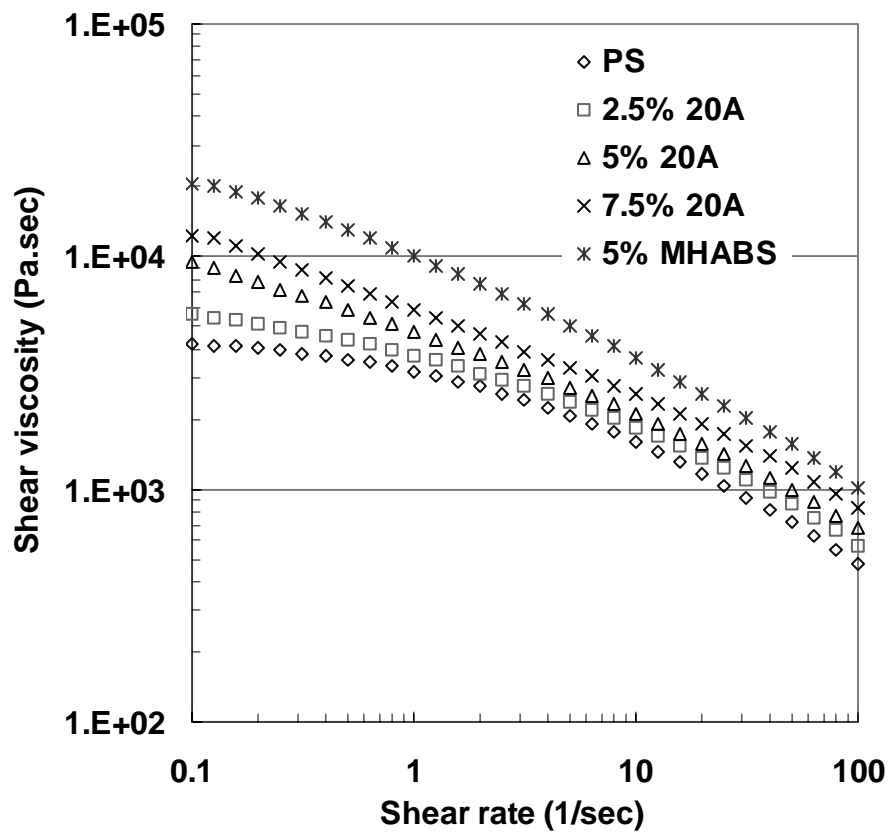


Figure 5.14. Shear viscosity of PS and PS/clay nanocomposites at 200°C without CO<sub>2</sub>.

## CHAPTER 6

### INFLUENCES OF SOLUBILITY AND VISCOSITY ON THE POLYSTYRENE/CO<sub>2</sub> MICROCELLULAR FOAMING EXTRUSION

#### 6.1. Introduction

Solubility and viscosity are two important parameters in determining cell nucleation and cell growth. Solubility is the upper limit how much CO<sub>2</sub> can be dissolved in a polymer, which indicates the phase equilibrium behavior of CO<sub>2</sub>/polymer systems. Viscosity influences both the pressure profile in an extrusion die and the cell growth. After the addition of CO<sub>2</sub>, the viscosity is affected by shear rate, temperature, pressure, and CO<sub>2</sub> concentration as well. To facilitate the process design, it is necessary to understand fundamental phenomena about the phase equilibrium and the viscosity.

##### 6.1.1. Solubility Measurement of CO<sub>2</sub> in PS

At present, three methods are commonly used to measure the solubility of CO<sub>2</sub> in polymers: on-line measurement method, gravimetric method, and volumetric method.

By applying the on-line measurement method [132] in an extrusion foaming line, a view cell with optical windows was mounted between the mixing elements and the die. A microscope was used to monitor the phase separation of the polymer melt/CO<sub>2</sub>

mixture. This method highly reflects the degree of mixing, although this value may not agree with the solubility at equilibrium because of the short mixing time and the hysteretic response of the equipment.

The gravimetric method is perhaps the most popular one, where a microbalance, located in a pressurized chamber, is applied to weigh directly the sample mass change with the CO<sub>2</sub> sorption. Wissinger et al. [128] studied the sorption behavior of CO<sub>2</sub> in various polymers in glassy state. Sato et al. [130] characterized both solubility and diffusion coefficient of CO<sub>2</sub> and N<sub>2</sub> in several polymers at high temperatures. A lot of advantages can be listed for this method. It is a direct measurement of mass change, highly accurate and reproducible. However, its operation is sometimes not easy due to the high sensitivity. The temperature control may be also a problem, especially at a high temperature. A buoyancy correction is needed to offset the volume swelling of polymers in CO<sub>2</sub>.

The third method, volumetric method, currently has very little experimental data published because it is an indirect method. The mass solubility is calculated from the change in the gas volume (or pressure). By knowing the density of both CO<sub>2</sub> and polymer/CO<sub>2</sub> mixture at any temperature and pressure, the solubility can be calculated based on the mass balance. The advantage of this volumetric method lies in its simplicity and ease of operation. The challenges are that it requires precise measurement of pressure, temperature, and volume, a relatively large amount of polymer sample, and absolutely no leaks.

Both Henry's law and the Sanchez-Lacombe equation of state [137] are frequently used to fit the experimental solubility data.

### 6.1.2. Viscosity Characterization of CO<sub>2</sub>/PS

Because of its pivotal role in equipment design and process simulation, increased attention has been given to understand the rheological properties of CO<sub>2</sub>/polymer melt systems. In general, viscosity is observed to decrease as CO<sub>2</sub> is dissolved into various polymer melts. This viscosity reduction is greatly favorable for the processing of high molecular weight polymers where the high viscosity is the major obstacle. When processing temperature sensitive polymers, one can apply this advantage to select a low processing temperature to prevent thermal degradation.

To measure the viscosity of CO<sub>2</sub>/polymer solutions, traditional rheometers are modified and two issues must be emphasized: one is to ensure the formation of a homogeneous solution before the measurement; the other is to prevent phase separation during the measurement. Early research in foaming demonstrated many experimental devices capable of measuring viscosities of polymer/blowing agent mixtures under high pressures, based on which new devices are specially developed for the CO<sub>2</sub>/polymer solutions. These devices are classified into two categories: 1) pressure driven, and 2) drag driven.

Pressure driven devices can be either a capillary [164-171] or a slit extrusion rheometer [172-176] controlled by a backpressure regulator. This method was originally designed for viscosity measurement of polymers with fluorocarbon blowing agents [162, 163]. Overall, the pressure driven devices have been found convenient to provide accurate rheological data. The limitation is that the large pressure drop across the capillary or slit die limits the CO<sub>2</sub> concentration dissolved in the polymer melts and as a result viscosities are usually measured at low CO<sub>2</sub> concentration to ensure the formation

of a single phase solution. Also in the low shear rate region, the small pressure drops detected, regardless of the large absolute pressure, may cause uncertainties in the raw data.

On the other hand, drag driven devices can be used to measure shear viscosities at low shear rates near the Newtonian plateau. They are usually operated at or near the equilibrium CO<sub>2</sub> concentration and a steady uniform distribution of pressure, stress and deformation rate can be created. However, such devices are usually difficult to design because the signals (ex. torque, force, and displacement) have to be transferred under pressure through a dynamic seal, although a magnetic sensor may improve the design. A magnetically levitated sphere rheometer was designed by Royer et al [181] to study the viscosity of PDMS/CO<sub>2</sub> solution. Recently, a new Couette viscometer was designed by Oh et al. [182] to measure the viscosity of PS/CO<sub>2</sub>.

Commonly, the viscosity decreases as the dissolved CO<sub>2</sub> concentration increases for various polymer melts. It is also found that the viscosity curves (i.e., shear viscosity versus shear rate) of the polymer/CO<sub>2</sub> solution are usually similar in shape to that of pure polymer, and are therefore analogous to the effect of increasing temperature or decreasing pressure. These analogies imply that carbon dioxide affects the viscosity of polymer melts following a similar mechanism to the temperature and pressure, predominantly through a change in free volume. Other factors, such as the improvement in polymer chain mobility, the dilution of polymer chains, and the reduction of chain entanglement upon CO<sub>2</sub> plasticization, also contribute to the viscosity reduction.

As a consequence, the traditional scaling techniques can be used and a scaling factor  $a_c$ , similar to the familiar temperature-dependent shift factor  $a_T$  employed in time-temperature superposition, can be applied to represent the influence of the CO<sub>2</sub> concentration [165-167, 169, 175, 176, 181]. To understand the effect of CO<sub>2</sub> concentration on viscosity of various polymer/CO<sub>2</sub> solutions, predictions from the change in free volume based on the Doolittle's free volume theory [183, 184] were also reported [165, 166, 169, 170, 175, 176, 185].

In the chapter, an investigation has been conducted to analyze the influences of two important parameters, solubility and viscosity, on the polystyrene/CO<sub>2</sub> extrusion foaming process. The solubility was measured by an open volumetric method. Experimental data were then fitted to the Sanchez-Lacombe equation of state. The viscosity reduction after dissolving CO<sub>2</sub> in polystyrene and polystyrene nanocomposites was studied by attaching a slit die to an extruder with backpressure control. Therefore, the viscosity at any temperature, pressure, CO<sub>2</sub> content, and shear rate can be obtained.

## **6.2. Experimental**

### **6.2.1. Materials**

Three polystyrene resins, Dow 685D, AtoFina CX 5197, and Nova 1037C, were applied to study the solubility and viscosity in this work. Additionally, intercalated and exfoliated nanocomposites consisting of polystyrene and nano-clays were also prepared to investigate the influence of nano-clays on the solubility and viscosity.

To prepare the intercalated nanocomposites, different amounts of Cloisite 20A provided by Southern Clay (0.5, 2.5, 5, 7.5, 10 wt.%) was pre-mixed with a polystyrene

resin (AtoFina CX 5197, melt index: 4.5) and then mechanically blended in a Leistritz ZSE-27 twin-screw extruder ( $L/D = 40$ ,  $D = 27\text{mm}$ ). As described in literatures [90, 234, 235], in-situ polymerization of styrene monomers was carried out to prepare exfoliated nanocomposites.

Among these materials, the solubility measurements focus on the Dow 685D polystyrene resin, while shear viscosities were characterized using another polystyrene resin (AtoFina CX 5197) and its intercalated nanocomposite consisting of 5 wt.% 20A.

The physical foaming agent, bone-dry grade  $\text{CO}_2$  (99% purity), was provided by Praxair.

### **6.2.2. Measurement of Solubility by Volumetric Method**

As shown in Figure 6.1, the apparatus for the volumetric method of solubility measurement consists of a syringe pump (ISCO 500D) for  $\text{CO}_2$  delivery and a high-pressure vessel for polymer loading. The temperature of the syringe pump was controlled at  $40^\circ\text{C}$  by water circulation and the pressure was kept constant. The high-pressure vessel was emerged in an oil bath to obtain the desired equilibrium temperature. The decrease of the gas volume in the syringe pump was recorded from the start of the gas absorption to the end of the equilibrium. The density of  $\text{CO}_2$  was calculated based on its equation of state and the density of the polymer/ $\text{CO}_2$  solution was estimated according to the density of pure polystyrene at the same temperature.

The mass balance before and after equilibrium, described below, was used to calculate the solubility.

$$\begin{aligned}
 m \text{ (before sorption)} &= \rho(40^0 \text{ C}, P)V_{\text{pump}}^{\text{before}} + \rho(25^0 \text{ C}, P)V_{\text{tubing}} \\
 &= \rho(40^0 \text{ C}, P)V_{\text{pump}}^{\text{after}} + \rho(25^0 \text{ C}, P)V_{\text{tubing}} + \rho(T, P)(V_{\text{vessel}} - V_{\text{polymer}}) + m_{\text{polymer}} w \\
 &= m \text{ (after sorption)}
 \end{aligned} \tag{6.1}$$

where  $\rho$  is the CO<sub>2</sub> density at the corresponding temperature and pressure;  $V$  is the volume of pump, tubing, high-pressure vessel, or polymer respectively; and  $w$  is the weight fraction of CO<sub>2</sub> in polymers. Here the volume of polymer ( $V_{\text{polymer}}$ ) was calculated by the mass of polymer ( $m_{\text{polymer}}$ ) divided by its density ( $\rho_{\text{polymer}}$ ), which is also a function of temperature, pressure, and CO<sub>2</sub> concentration.

After sufficient equilibrium time, when the CO<sub>2</sub> volume in the pump becomes constant and independent of time, the corresponding weight fraction is treated as the solubility.

### 6.2.3. Shear Viscosity Characterization

The shear viscosity of PS and PS/clay nanocomposites without CO<sub>2</sub> at 1atm and 200°C was measured under the dynamic frequency sweep mode using the Rheometrics Mechanical Spectrometer (RMS 800).

As shown in Figure 6.2, by using a slit die rheometer, 2 mm thick and 20 mm wide, attached on the extrusion foaming line, shear viscosities of polymer melts at high pressures with and without CO<sub>2</sub> were measured at 180°C. Three pressure transducers, with a distance of 25mm between each other, were used to measure the pressure profile

along the slit die and one thermocouple was used to monitor the melt temperature. A metered amount of CO<sub>2</sub> was injected into the extruder barrel, controlled by the syringe pump (ISCO 260D). The shear rate was varied by changing screw rotation speed, i.e., the melt flow rate. The shear stress, shear rate, and shear viscosity were calculated based on the method described in reference [228]. The backpressure was controlled by a backpressure valve connected to the outlet of the slit die. The high pressure created by the backpressure valve keeps the CO<sub>2</sub> dissolved in the polymer matrix without phase separation during the measurement. To eliminate the influence of pressure on the shear viscosity, a backpressure of 6.895MPa (1000psi) was maintained at the position of the last pressure transducer for all measurements with different CO<sub>2</sub> concentrations.

#### **6.2.4. Microcellular Foaming and Cell Structure Analysis**

The microcellular foaming extrusion was performed on a two-stage single-screw extruder (HAAKE Rheomex 252P) with a capillary die (diameter: 0.5 mm, and length: 10 mm). CO<sub>2</sub> was delivered by a syringe pump (ISCO 260D). The foamed extrudate flows freely out to the air and vitrifies.

Cell size and cell density are determined by analyzing images obtained from scanning electron micrographs (SEM).

## 6.3. Results and Discussion

### 6.3.1. Solubility of CO<sub>2</sub> in Pure Polystyrene

In Figure 6.3, a CO<sub>2</sub> sorption curve at 120°C and 15 MPa is shown. A typical measurement at one temperature and one pressure takes about 6-12 hours. As the sorption experiment proceeds, the CO<sub>2</sub> volume in the pump decreases quickly at the beginning and then gradually levels off to a constant equilibrium value. The weight fraction of CO<sub>2</sub> in the polymer was also shown in the figure. To shorten the measurement time, the most effective way is to increase the contact surface between the gas and polymer and decrease the diffusion distance of the gas. For example, thin polymer disks can be loaded in the high-pressure vessel in shelves.

To ensure accurate experimental data, the density of CO<sub>2</sub> and polymer/CO<sub>2</sub> solution was determined carefully. The density of CO<sub>2</sub> is sensitive to both temperature and pressure, especially in the supercritical region. During the experiment, the CO<sub>2</sub> in the syringe pump is well insulated and controlled so that the temperature fluctuation is only  $\pm 0.2^\circ\text{C}$ . One digital pressure gage, which accuracy is as high as 0.035% of the highest applied pressure (5000 psi), was used to get accurate reading of pressure. As the first approximation, the density of the polystyrene/CO<sub>2</sub> phase was calculated based on the density of the pure polystyrene at the same temperature. It is found that the density of polystyrene is 1.029 grams/cm<sup>3</sup> at room temperature and 0.882 grams/cm<sup>3</sup> at melting state (200°C), based on which the density at other temperatures in between was linearly interpolated. Thus, qualitative measurement of solubility by a volumetric method was successfully accomplished.

As shown in Figure 6.4, the solubility of CO<sub>2</sub> in polystyrene (Dow 685D) was measured at two temperatures (120 and 200°C) in a pressure range from 5 to 15 MPa with an increment of 2.5 MPa. 120°C is a common foaming temperature for polystyrene in industry and 200°C is the normal processing temperature of polystyrene. Other operating temperatures should be in between. These results from the volumetric method are compared with the literature data from the gravimetric method (Figure 2.6). A fairly good agreement was achieved that the experimental results at 120°C are located between the two literature curves (100 and 150°C) and the experimental results at 200°C nearly overlap the literature data at the same temperature.

Sanchez-Lacombe equation of state was used to fit the experimental data and the binary interaction parameters ( $\delta_{ij}$ ) calculated at these two temperatures were compared with those fitted from the literature data at other temperatures. Then the fitting  $\delta_{ij}$  values were averaged to obtain 0.0249 because we found they change irregularly in a narrow range (0.0165 to 0.0359) for temperature varying from 35 to 200°C. At a typical foaming condition (175°C and 10.34 MPa), the solubility is calculated to be 3.82%, 3.62%, and 3.36% when the  $\delta_{ij}$  is the lowest (0.0165), the average (0.0249) and the highest (0.0359) respectively. Therefore not a big error was introduced by applying the average value for all the temperatures. This averaged  $\delta_{ij}$  was applied to predict the shear viscosity of PS with different CO<sub>2</sub> concentrations.

## 6.3.2. Shear Viscosity of PS/CO<sub>2</sub> Solution

### 6.3.2.1. Viscosity Measurement

To model a polymer melt flow and to design a foaming extrusion die, shear viscosity as a function of shear rate, temperature, pressure, and CO<sub>2</sub> concentration must be characterized.

Shear viscosities at the atmospheric pressure and different temperatures for pure polystyrene (AtoFina CX 5197) are shown in Figure 6.5(a). The data was measured using the Rheometrics Mechanical Spectrometer (RMS 800) with the parallel plate geometry. The curves can be shifted to a master curve (Figure 6.5(b)) and the shift factors ( $a_T$ ) follow the WLF equation

$$\log(a_T) = -\frac{11.11 \times (T - 373.2)}{(49.94 + T - 373.2)} \quad (6.2)$$

where the temperature (T) has a unit in Kelvin.

By using the slit die attached on the single-screw extruder, viscosity measurements at 180°C and different backpressures for pure polystyrene (AtoFina CX 5197) are shown in Figure 6.6. Backpressures (0, 1000, and 2000 psi) used for these measurements are indicated in the figure caption. At each backpressure, viscosities at different shear rates were measured. Here, the backpressures are selected as the reference pressure that will be used to compare the influence of pressure on the viscosity. It was shown that the melt becomes significantly more viscous at a higher backpressure.

The data for polystyrene with dissolved CO<sub>2</sub> at 180°C (Figure 6.7(a)) shows that viscosity decreases as gas content increases. The viscosity curves of the polystyrene/CO<sub>2</sub>

solutions are similar in shape to the viscosity curve of the pure polystyrene. The backpressure was controlled to be 1000 psi, a constant value for all shear rates. At this backpressure, CO<sub>2</sub> can be kept in the solution to avoid phase separation. The superposition master curve shifted to 0% CO<sub>2</sub> is shown in Figure 6.7(b). The shifting factors (Figure 6.7(c)) are found to be comparable with those from shifting the literature data [167]. The viscosity decreases a lot when only a small amount of CO<sub>2</sub> is dissolved in polystyrene. Then the decrease slows in the high CO<sub>2</sub> content range (>1% CO<sub>2</sub>).

#### **6.3.2.2. Viscosity Prediction**

As described above, carbon dioxide affects the viscosity of polymer melts following a similar mechanism to the temperature and pressure, predominantly through a change in free volume. Consequently, a constitutive equation consisting of the zero shear viscosity ( $\eta_0$ ), which expresses the shear thinning behavior, can be integrated with Doolittle's equation and the Sanchez-Lacombe equation of state to predict the shear viscosity changing with shear rate, temperature, pressure, and CO<sub>2</sub> concentration. Here, Doolittle's equation relates the zero shear viscosity to the free volume fraction. The free volume as a function of temperature, pressure, and CO<sub>2</sub> concentration can be calculated by using the Sanchez-Lacombe equation of state.

Areerat et al. [170, 185] built a model to predict the viscosity of LDPE/CO<sub>2</sub> solution. This model (Appendix D) was applied to fit the experiment data we obtained for PS/CO<sub>2</sub> solution. Instead of expressing the free volume fraction as a function of temperature, pressure, and CO<sub>2</sub> concentration, as applied by Areerat et al., we calculated

the free volume fraction directly from the specific volume of the PS/CO<sub>2</sub> solution, which can be computed by using the Sanchez-Lacombe equation of state.

The shear viscosity curve of pure PS measured on the RMS 800 rheometer at 180°C without CO<sub>2</sub> and pressure was fitted to a simplified Cross-Carreau model to determine the necessary parameters, including the hard-core specific volume of polystyrene ( $V_{poly}^0$ ), the coefficients ( $A$  and  $B$ ) in the Doolittle's equation, and the constants ( $n$  and  $\tau$ ) in the Cross-Carreau model. Note that these parameters listed above are independent of temperature, pressure, and CO<sub>2</sub> concentration. The results are listed in Table 6.1. The hard-core specific volume of CO<sub>2</sub> applied was 0.589 cm<sup>3</sup>/g. Using the Sanchez-Lacombe equation of state, the specific volume of PS or PS/CO<sub>2</sub> solution at different temperature, pressure, and CO<sub>2</sub> concentration was calculated, according to which the free volume fraction and the zero shear viscosity were obtained (Table 6.2). Finally, the calculated zero shear viscosity and the necessary parameters ( $n$  and  $\tau$ ) were substituted back into the simplified Cross-Carreau model to predict the shear viscosity at high shear rates.

Predictions at different temperatures (160, 180, and 200°C) without CO<sub>2</sub> and backpressure are shown in Figure 6.8(a). Fairly good fitting was obtained at the high shear rate region. At the same temperature (180°C) and different backpressures (0, 1000, and 2000 psi), good fitting was also achieved in Figure 6.8(b). However, for the data with different CO<sub>2</sub> concentration at 180°C and 1000 psi, good fitting (Figure 6.8(c)) was only found at low CO<sub>2</sub> concentrations (0.5 and 1 wt.%). At high CO<sub>2</sub> concentrations, it seems that the Sanchez-Lacombe EOS overestimates the volume swelling or the hard-core specific volume selected for CO<sub>2</sub> is too small.

### 6.3.3. Comparison Between Three Polystyrenes

Viscosity is an important parameter in the foaming process. However, from the classical nucleation theory, viscosity does not have direct influence on the nucleation. Viscosity affects nucleation indirectly by changing the pressure drop or pressure drop rate in the extrusion die. To study the effect of viscosity on the foam structure, three polystyrenes with different viscosity dependence on shear rate (Figure 6.9) were foamed at 200°C and different flow rates (and hence, different pressure drops and pressure drop rates) to investigate the effect of viscosity on the foam nucleation and growth. The CO<sub>2</sub> concentration was maintained at a high level (4 wt%) to provide sufficient amount of gas and a stable processing condition.

The cell size and cell density were plotted versus the pressure drop in Figure 6.10(a). With the decrease of viscosity, curves of cell size shift to high pressure, which means the low-viscosity polystyrene needs a high environmental pressure to form the same foam cell size. This is reasonable because the environmental pressure opposes the foam cell growth. If the environmental pressure is the same, the low-viscosity polystyrene will form larger bubbles. On the other hand, curves of cell density tend to merge together, which implies that viscosity affects nucleation indirectly by changing the pressure drop or pressure drop rate in the extrusion die. One would get the same cell density at the same pressure drop for polystyrenes with different shear viscosities (or molecular weight). The high pressure drops obtained by the low viscosity polystyrene are due to its higher flow rates at the same screw rotation speed. However, when the cell size and cell density were plotted versus the pressure drop rate (Figure 6.10(b)), the three curves collapse to one curve. Thus, it is indicated that the pressure drop rate is more

crucial in deciding the cell size than the viscosity. As discussed in Chapter 4, the pressure drop rate determines how fast and how large a supersaturation can be achieved because the pressure drop in the extrusion die is not an instantaneous process.

Figure 6.11 shows the foam morphology of the three polystyrenes at two screw rotation speeds. The cell size in the high-viscosity polystyrene is larger and cell density is lower than those in the low-viscosity polystyrenes at the same screw rotation speed. Again, the reason is mainly because the high-viscosity polystyrene creates a slower flow rate and thus a smaller pressure drop rate at the same screw rotation speed. No doubt that the cell density is lower for a smaller pressure drop rate, while the cell size is larger since the same amount of gas is shared by fewer cells.

#### **6.3.4. Effect of Nano-clay on CO<sub>2</sub> Sorption and Viscosity**

As discussed in Chapter 5, nanocomposite foams have many unique properties, such as improved microcellular structure, higher tensile modulus, enhanced fire retardance, and better barrier properties. To understand the interaction between nano-clay and CO<sub>2</sub> and also the synergistic effects of nano-clay and CO<sub>2</sub> on the viscosity, the CO<sub>2</sub> sorption in PS/nano-clay composites and the shear viscosity with and without CO<sub>2</sub> were studied.

#### 6.3.4.1. CO<sub>2</sub> Sorption of PS/Nano-Clay Composites

To study the effect of nano-clay on CO<sub>2</sub> solubility and diffusivity, experiments of CO<sub>2</sub> sorption and desorption were performed only at low temperatures because of experimental difficulties. At high temperatures, the temperature control and also the accurate reading of pressure and volume are extremely difficult. The absorption measurement was carried out at 50°C and the desorption was at room temperature. Here, we hypothesize that the trends obtained at low temperatures will hold true at high temperatures, such as 200°C, the real foaming temperature. The experimental procedure was similar to that employed by Berens et al. [236]. A high-pressure vessel in which flat plate samples (length: 44~51 mm, width: 8.1~8.8 mm, and thickness: 0.37~0.43 mm) of PS or PS/nano-clay composites were loaded was connected to a syringe pump. The samples were saturated with CO<sub>2</sub> at 10 MPa and 50°C for 24 hours. They were then quickly taken out of the high-pressure vessel and placed on a high-resolution balance. The CO<sub>2</sub> desorption curve (weight loss with time) was recorded. From this desorption curve, CO<sub>2</sub> solubility at 50°C was obtained by extrapolating the data back to time zero and CO<sub>2</sub> diffusivity at room temperature was also calculated.

Figure 6.12 shows CO<sub>2</sub> desorption curves of three samples, PS, PS/5% 20A, and PS/5% MHABS. After releasing the pressure in the high-pressure vessel, the samples still remained unfoamed due to the low temperature applied, and thus the dimensions of the samples keep unchanged. By extrapolating the desorption data back to time zero, the solubility of CO<sub>2</sub> in PS, PS/5% 20A, and PS/5% MHABS at 50°C and 10 MPa was found to be 8.5, 8.5, and 8.8 wt.%, respectively. Carbon dioxide exhibits a slightly higher solubility in the exfoliated PS nanocomposite. Additionally, the diffusivity at

room temperature was calculated based on the three desorption curves by assuming a one-dimensional diffusion (the thickness was much smaller than the other two dimensions). The results are  $5 \times 10^{-7}$ ,  $3 \times 10^{-7}$ , and  $3 \times 10^{-7}$  cm<sup>2</sup>/sec for PS, PS/5% 20A, and PS/5% MHABS respectively. Obviously, the addition of nano-clay can slow down the CO<sub>2</sub> diffusion out of the sample.

#### **6.3.4.2. Shear Viscosity of PS/20A Nanocomposite**

Shear viscosities of PS/5 wt.% 20A nanocomposite with and without CO<sub>2</sub> were measured under backpressures in a slit die. The die temperature was 180°C and five shear rates were selected for each CO<sub>2</sub> concentration. Compared to pure PS, the viscosity of the nanocomposite is not sensitive to the backpressure, showing the same value for the two methods with and without backpressure. A possible explanation is that the clay disperses in the polymer matrix and occupies the free volume that originally exists between PS molecules. The decrease of the free volume, a lower compressibility, makes the viscosity to be less sensitive to the pressure change.

Figure 6.13 summarizes the results with different CO<sub>2</sub> concentrations (1, 2, and 3 wt.%) under a backpressure of 1000 psi (6.895 MPa). Comparing the data with and without CO<sub>2</sub>, it was found that the shear viscosity decreases with an increase in the CO<sub>2</sub> concentration, a well-known phenomenon of viscosity reduction because the dissolution of CO<sub>2</sub> enlarges the free volume and improves the molecular mobility. An interesting observation is the synergistic effects of nano-clay and CO<sub>2</sub> on the viscosity. Without CO<sub>2</sub>, the melt viscosity of the nanocomposites is higher than that of pure PS. However, an opposite trend is observed when 2 to 3 wt.% CO<sub>2</sub> is dissolved. The shear viscosity of

PS/5% 20A nanocomposite is lower than that of PS. A possible explanation is that more CO<sub>2</sub> may be adsorbed on the surface of the nano-clay to lubricate the melt flow. Further study at other clay concentrations, temperatures, and pressures is being conducted in our lab to better understand the interaction between CO<sub>2</sub> and nanocomposites.

#### **6.4. Conclusions**

Two important parameters in the polystyrene/CO<sub>2</sub> extrusion foaming process, solubility and viscosity, were measured experimentally and fitted to models at various conditions.

The solubility, which decides CO<sub>2</sub> concentration limit and the nucleation onset, is measured by the volumetric method. Experimental data is then fitted to the Sanchez-Lacombe equation of state. The binary interaction parameters ( $\delta_{ij}$ ) calculated at these two temperatures were compared with those fitted from the literature data at other temperatures and then applied to predict shear viscosity.

The viscosity reduction by injecting CO<sub>2</sub> in the polystyrene is measured by connecting a slit die rheometer with backpressure control to the extruder. The viscosity at several temperatures, pressures, CO<sub>2</sub> concentrations, and shear rates were obtained. The superposition technique can be used to shift the viscosity data to one master curve. By integrating the Cross-Carreau model, Doolittle's equation, and the Sanchez-Lacombe equation of state, shear viscosities at different temperatures, pressures, and low CO<sub>2</sub> concentrations were successfully predicted in the high shear rate region.

Three polystyrenes with different shear viscosities were foamed at the same conditions. The viscosity shows influence mainly on the cell size, while indirect effect on the cell nucleation by changing the pressure drop or pressure drop rate in the extrusion die. It is also shown that the pressure drop rate is more crucial in deciding cell size and cell density.

When nano-clay was blended in polystyrene, the viscosity of the nanocomposite becomes less sensitive to the backpressure. The same viscosity reduction behavior was obtained as the CO<sub>2</sub> was dissolved and an even lower shear viscosity than that of PS was observed at high CO<sub>2</sub> concentrations.

Hard core specific volume (cm <sup>3</sup> /g)		Doolittle's eq.		Cross_Carreau model	
$V_{CO2}^0$	$V_{poly}^0$	A (Pa.sec)	B	$\tau$ (Pa)	$n$
0.589	0.8034	4.13E-08	5.65169	18196.84	0.3403

Table 6.1. Parameters in the viscosity prediction model.

Temperature (°C)	Pressure (psi)	$w_g$ (wt.%)	$V^0(w_g)^{(1)}$	$V(T, P, w_g)^{(2)}$	$f(T, P, w_g)^{(3)}$	$\eta_0(\text{Pa}\cdot\text{sec})^{(4)}$
180	1000	0	0.8034	1.0171	0.2102	19708.24
180	1000	0.5	0.8023	1.0186	0.2124	14913.63
180	1000	1	0.8012	1.0203	0.2147	11144.32
180	1000	2	0.7991	1.0238	0.2195	6286.055
180	1000	3	0.7969	1.0275	0.2244	3594.327
180	1000	4	0.7948	1.0313	0.2293	2082.779
180	0	0	0.8034	1.0243	0.2157	9879.377
180	2000	0	0.8034	1.0106	0.2050	38625.68
160	0	0	0.8034	1.0110	0.2054	36896.47
200	0	0	0.8034	1.0385	0.2264	2864.979

- (1) hard core specific volume:  $V^o(w_g) = w_g V_{CO_2}^o + (1 - w_g) V_{poly}^o$   
(2) specific volume of PS/CO<sub>2</sub> solution calculated from Sanchez-Lacombe EOS  
(3) free volume fraction:  $f(T, P, \omega_g) = 1 - V^0(\omega_g) / V(T, P, \omega_g)$   
(4) zero-shear viscosity from Doolittle's equation:  $\eta_0 = A \exp(B / f(T, P, \omega_g))$

Table 6.2. Shear viscosity prediction.

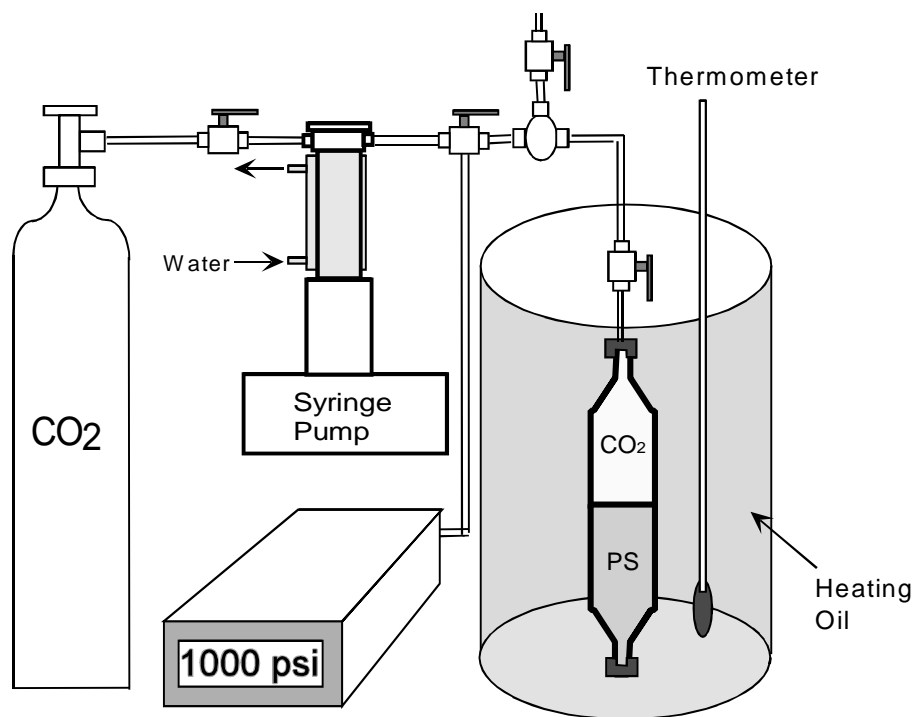


Figure 6.1. Volumetric method for solubility measurement.

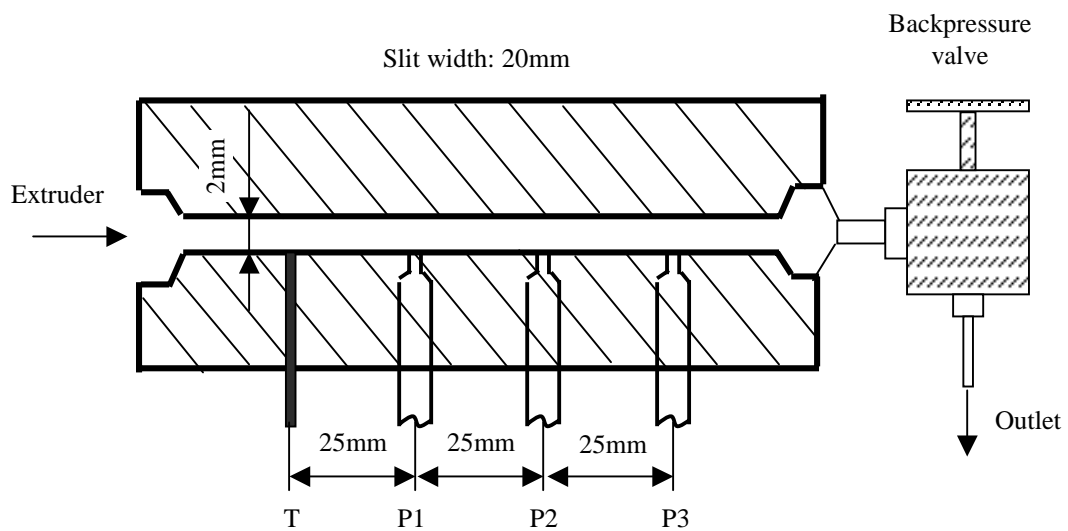


Figure 6.2. Side view of the slit die used for viscosity characterization under pressure.

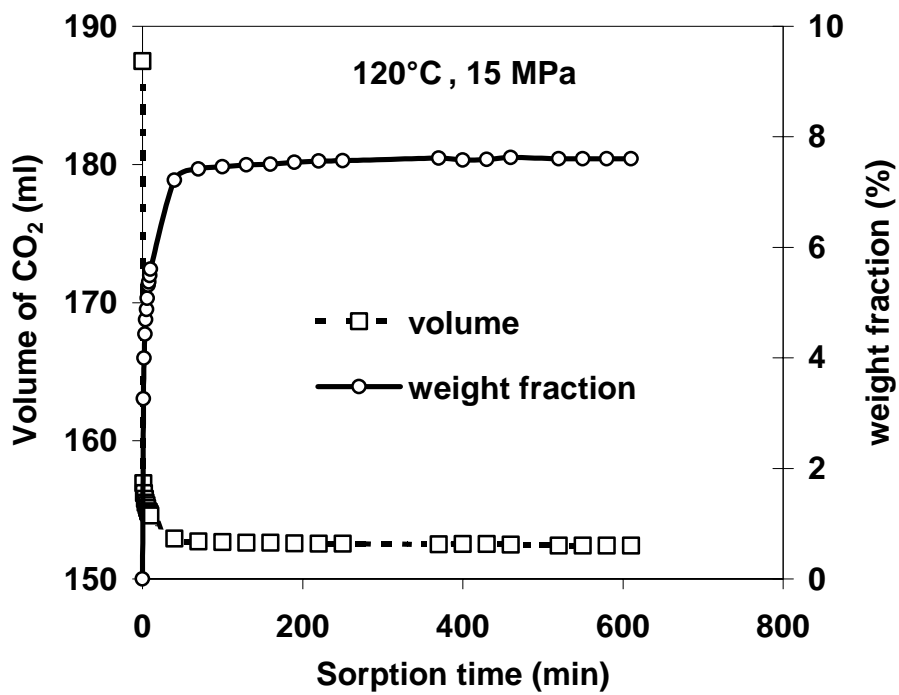


Figure 6.3. Sorption curve of CO<sub>2</sub> in polystyrene at 120°C and 15 MPa.

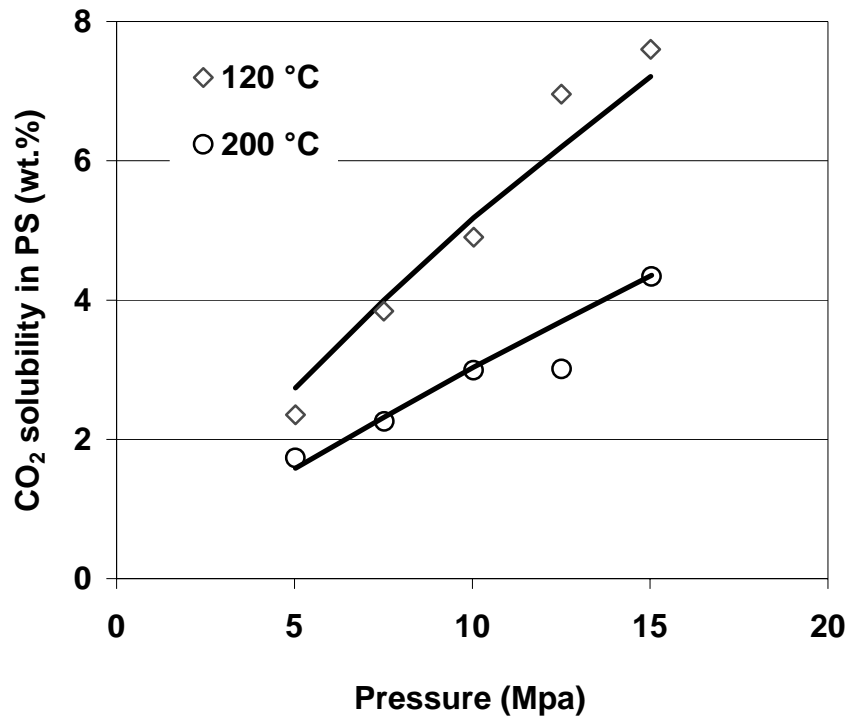
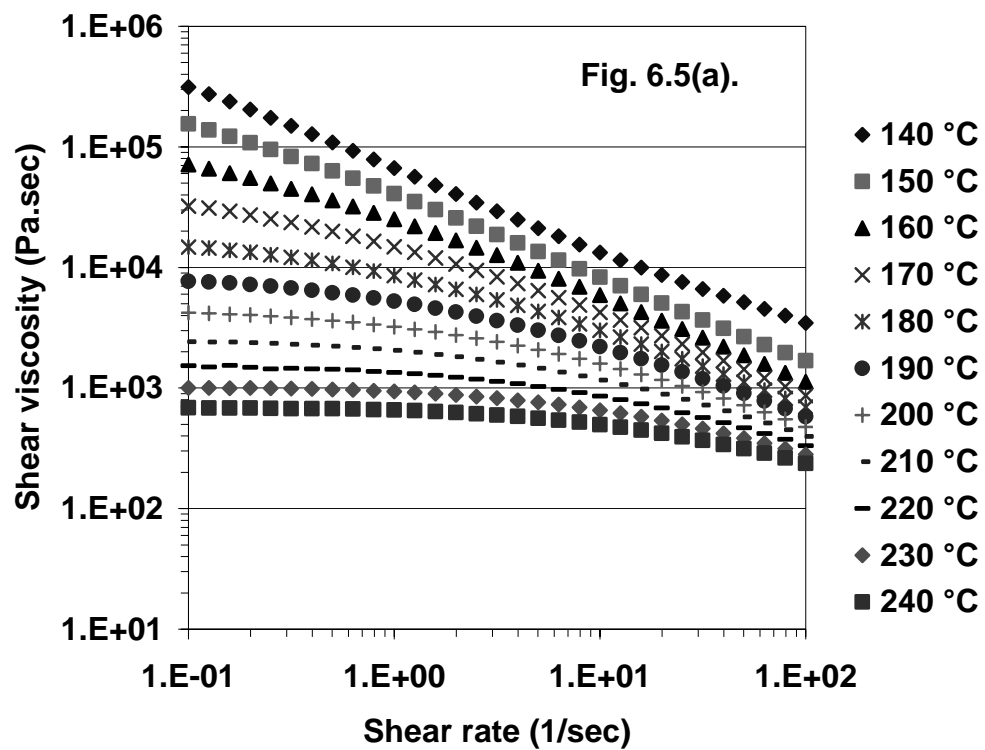


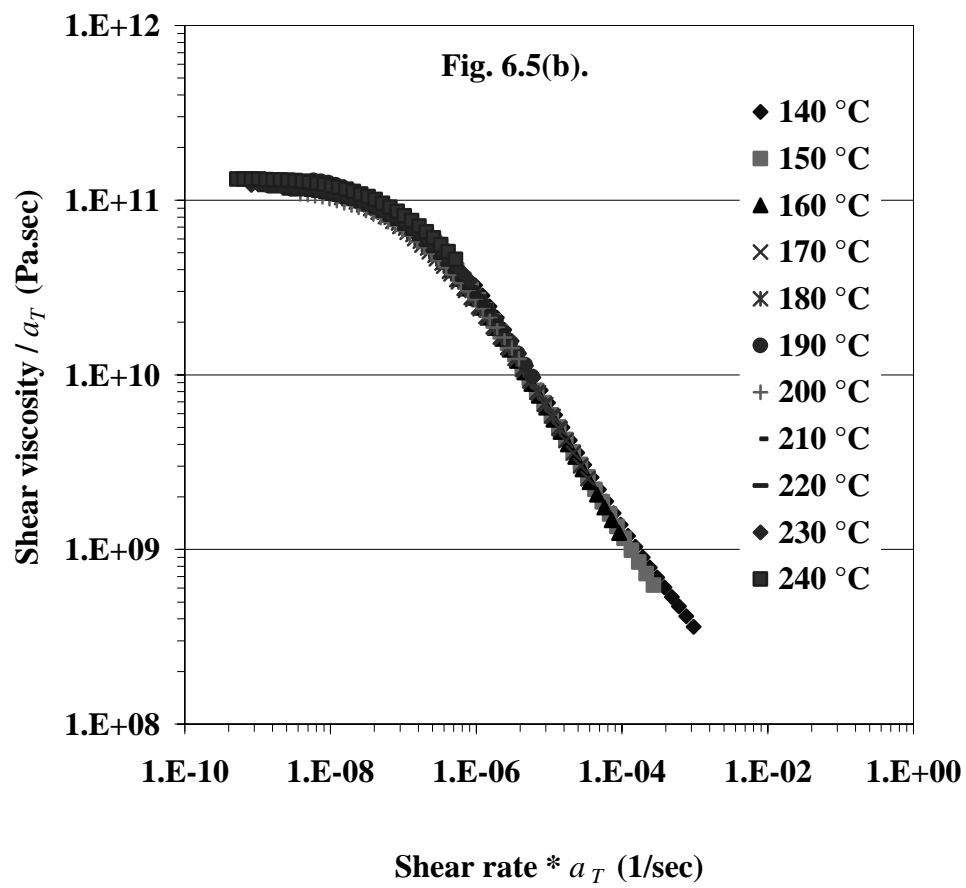
Figure 6.4. Solubility data of CO<sub>2</sub> in polystyrene (solid lines: fitting curves using the Sanchez-Lacombe equation of state).



(continued)

Figure 6.5. (a) Shear viscosities of polystyrene at different temperatures; (b) master curve shifted to  $T_g$ .

Figure 6.5 continued



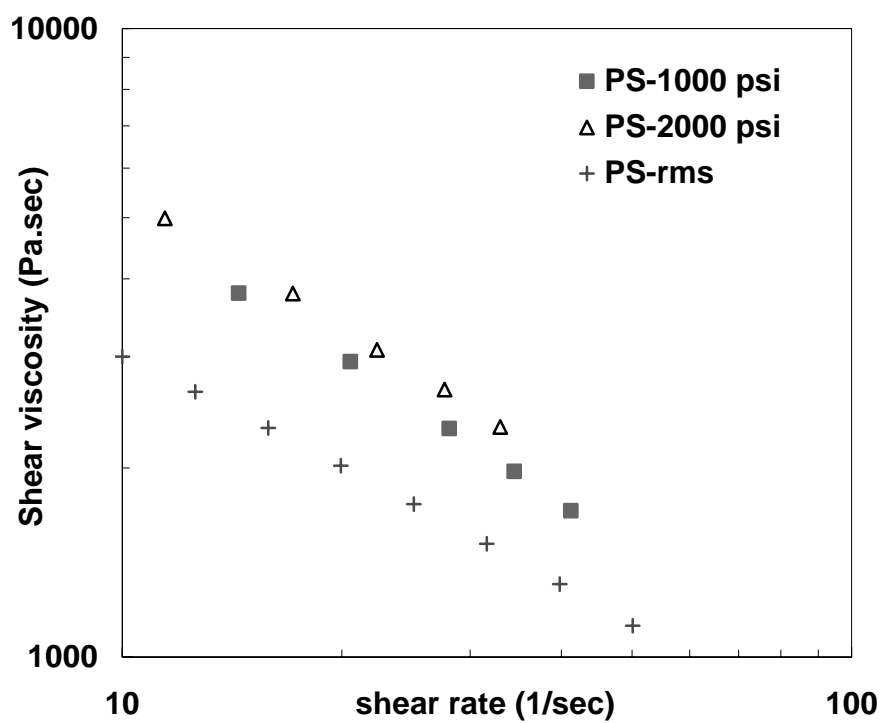
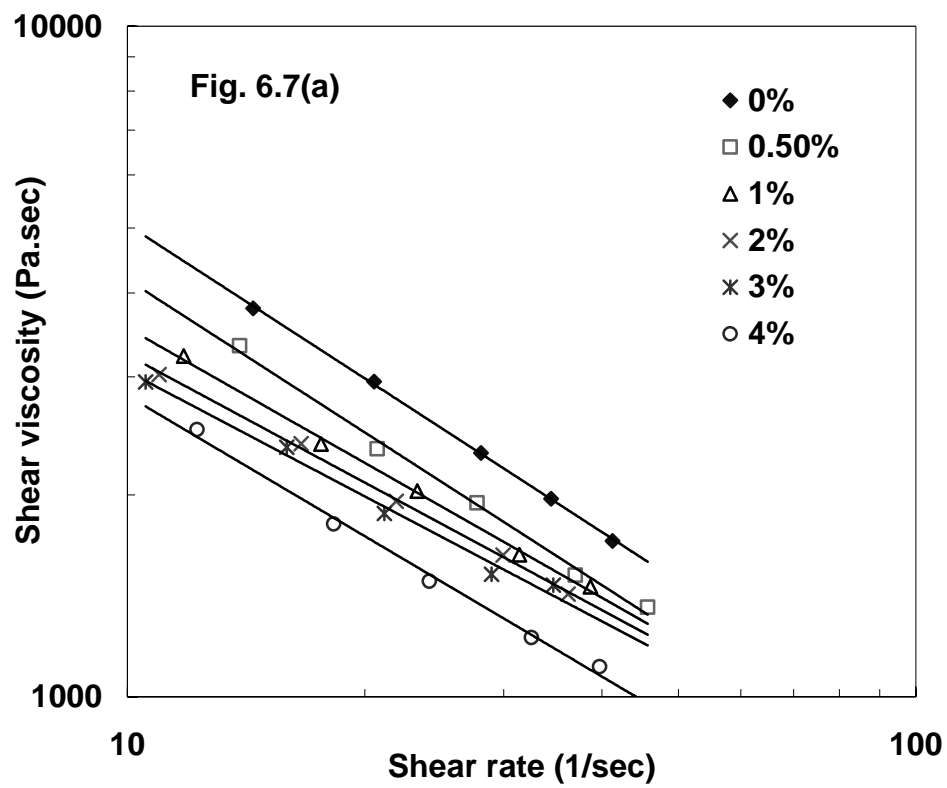


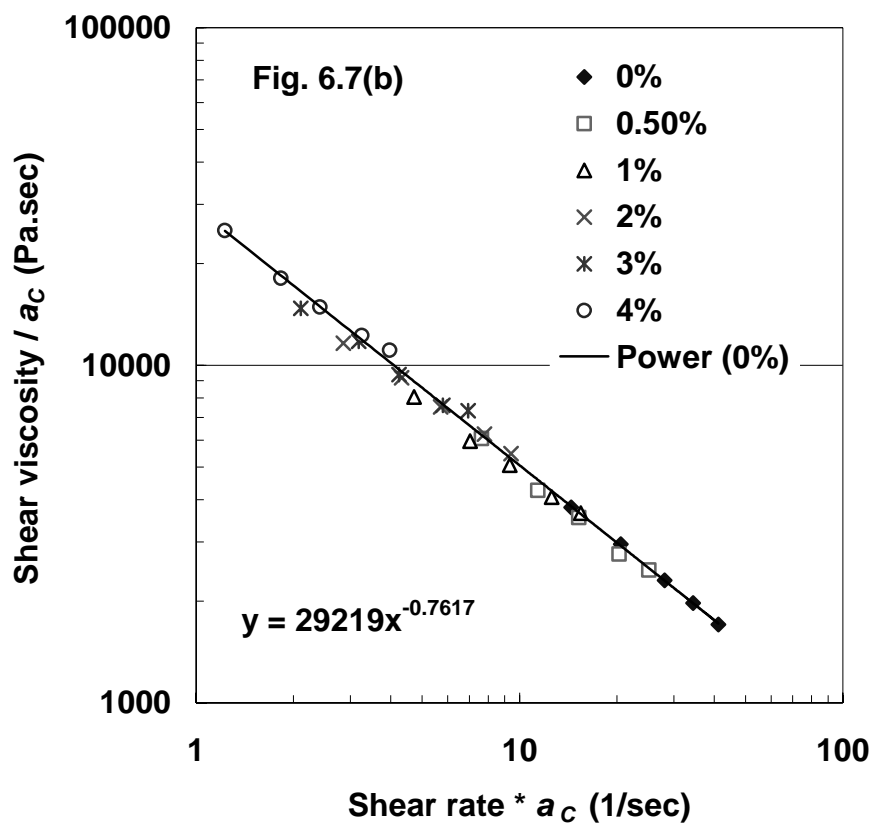
Figure 6.6. Effect of backpressure on the shear viscosity of pure polystyrene at 180°C (PS-rms means the measurement was performed on RMS 800).



(continued)

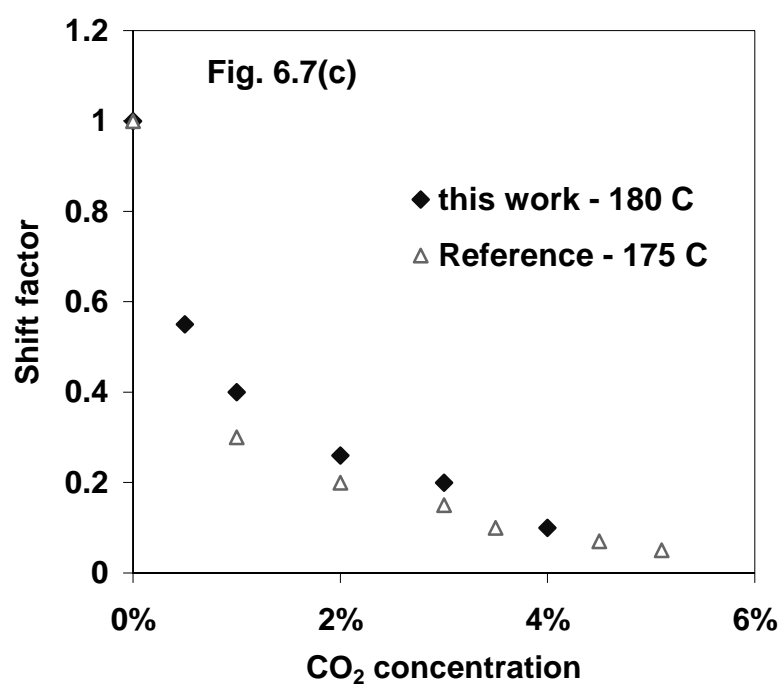
Figure 6.7. (a) Effect of CO<sub>2</sub> content on the shear viscosity of polystyrene at 180°C; (b) Master curve shifted to 0%; and (c) Shift factors.

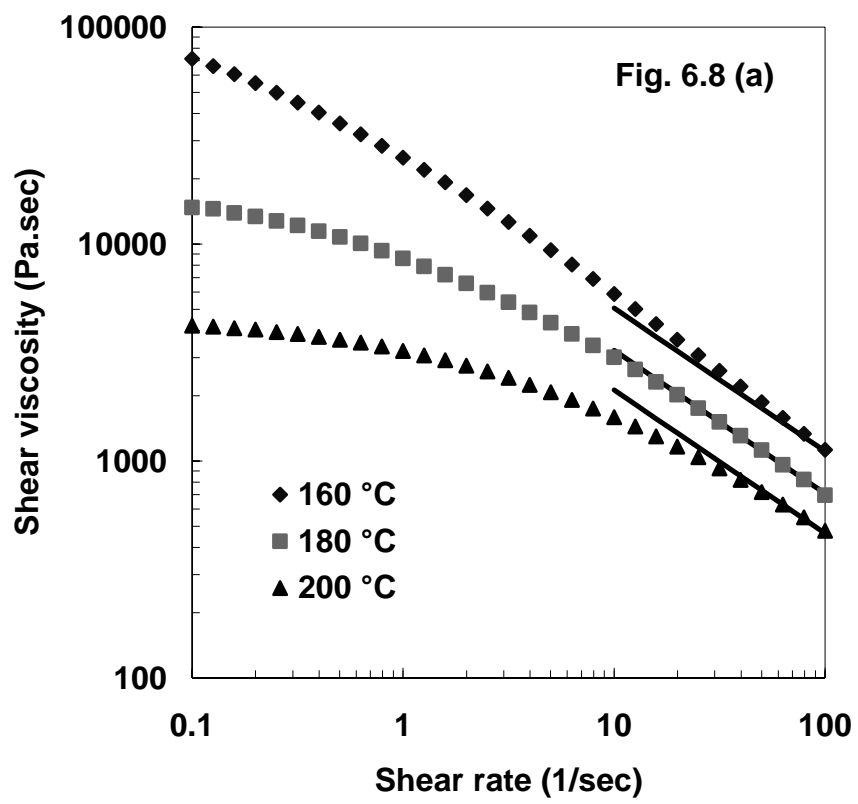
Figure 6.7 continued



(continued)

Figure 6.7 continued

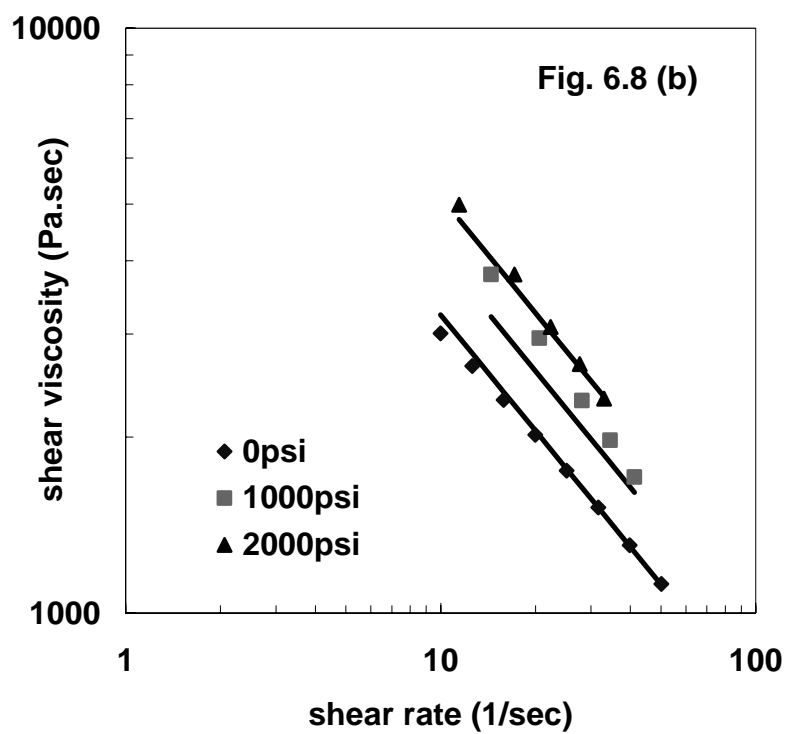




(continued)

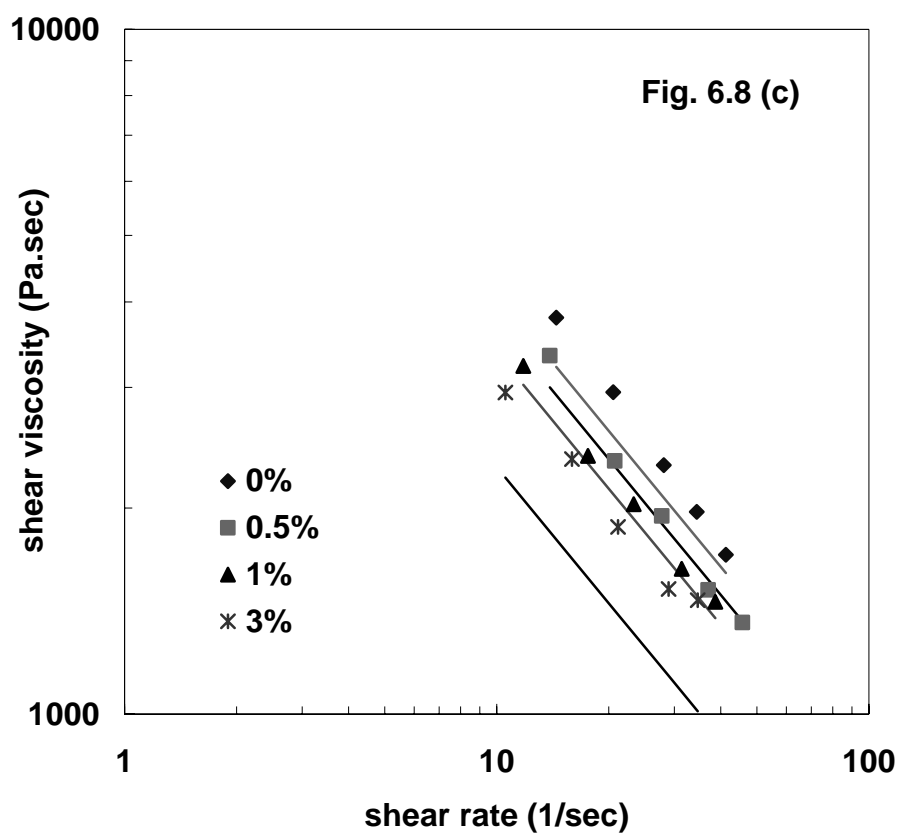
Figure 6.8. Viscosity prediction at different temperatures (a), pressures (b), and CO<sub>2</sub> concentrations (c).

Figure 6.8 continued



(continued)

Figure 6.8 continued



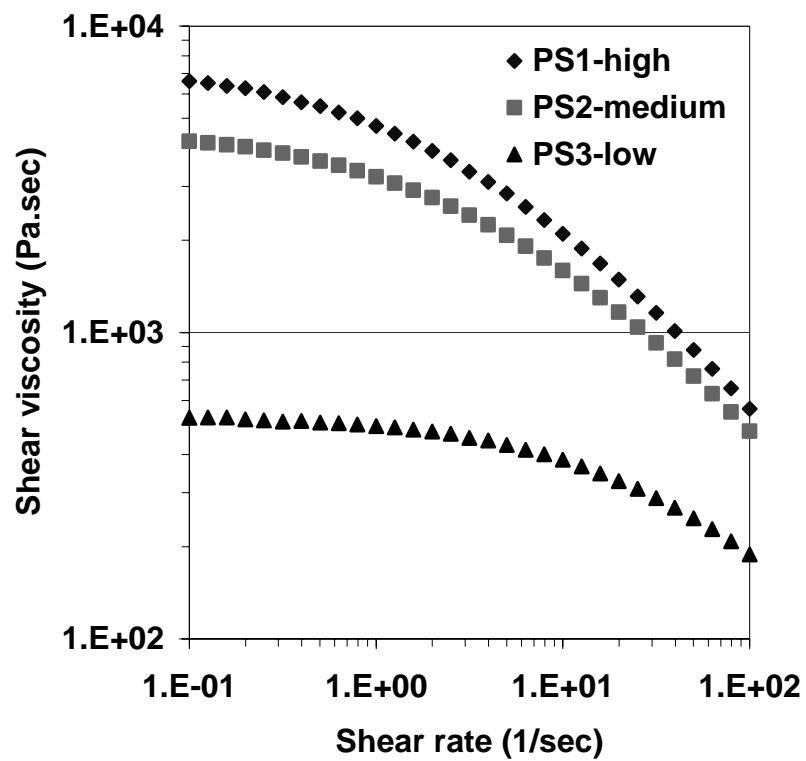
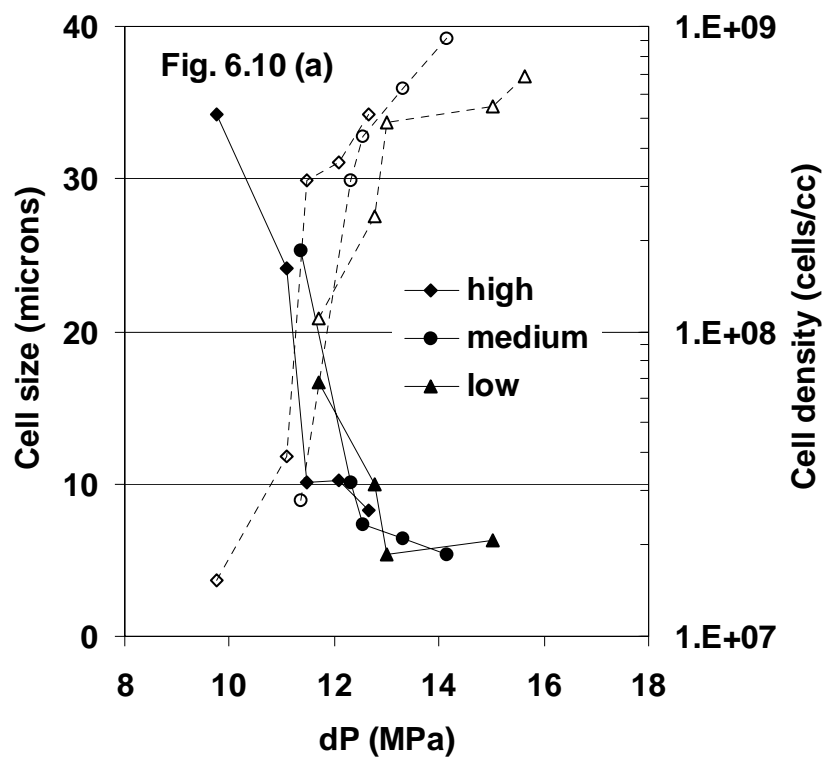


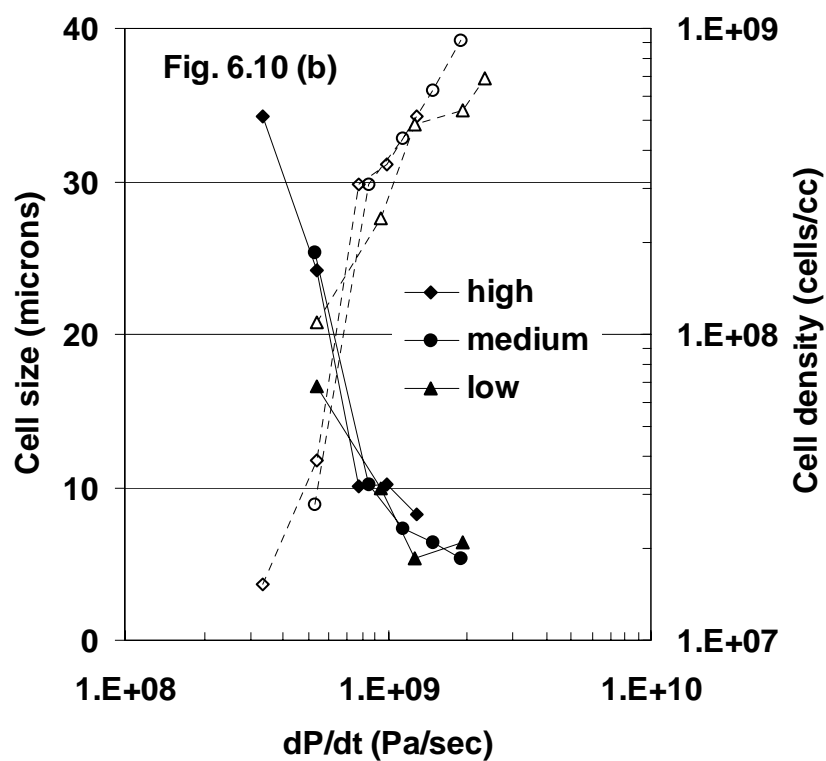
Figure 6.9. Shear viscosity of three polystyrene resins at 200°C without CO<sub>2</sub> and backpressure.



(continued)

Figure 6.10. Cell size (solid symbols) and cell density (open symbols) versus pressure drop (a) and pressure drop rate (b) at 200°C for three polystyrenes with different shear viscosities.

Figure 6.10 continued



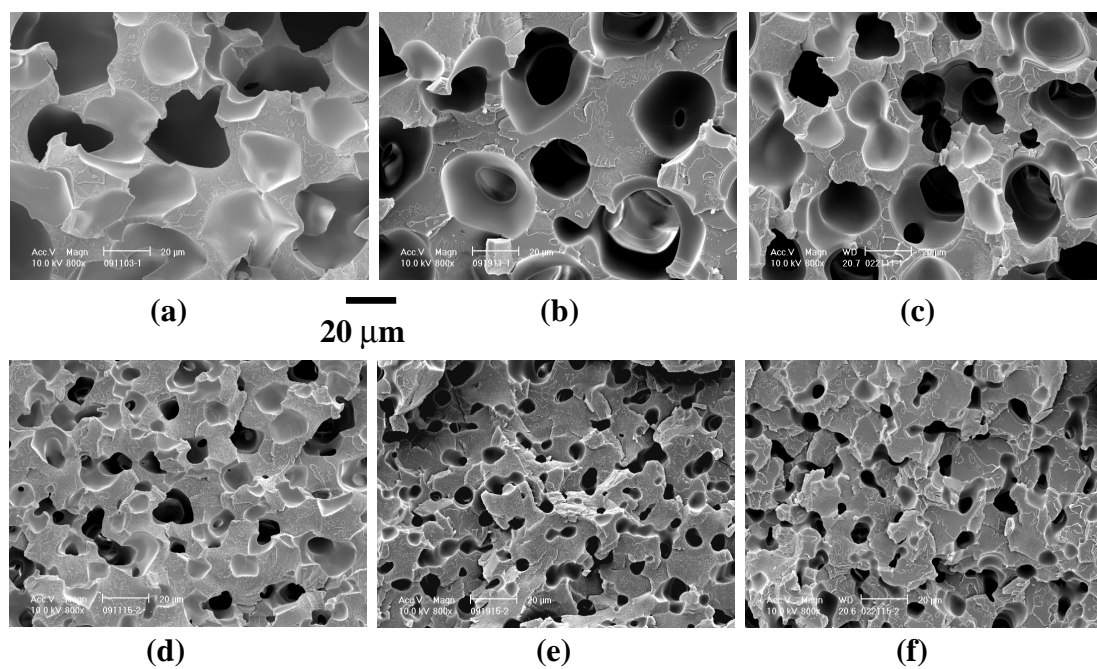


Figure 6.11. Cell morphology of the three polystyrenes at 200°C and different screw rotation speeds: (a) high viscosity, 10 rpm; (b) medium viscosity, 10 rpm; (c) low viscosity, 10 rpm; (d) high viscosity, 30 rpm; (e) medium viscosity, 30 rpm; and (f) low viscosity, 30 rpm.

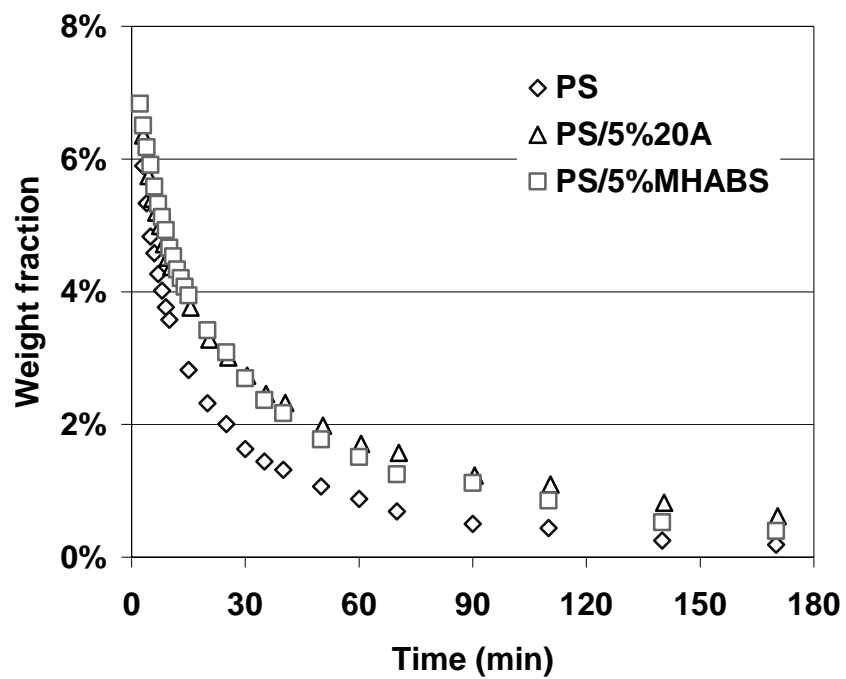
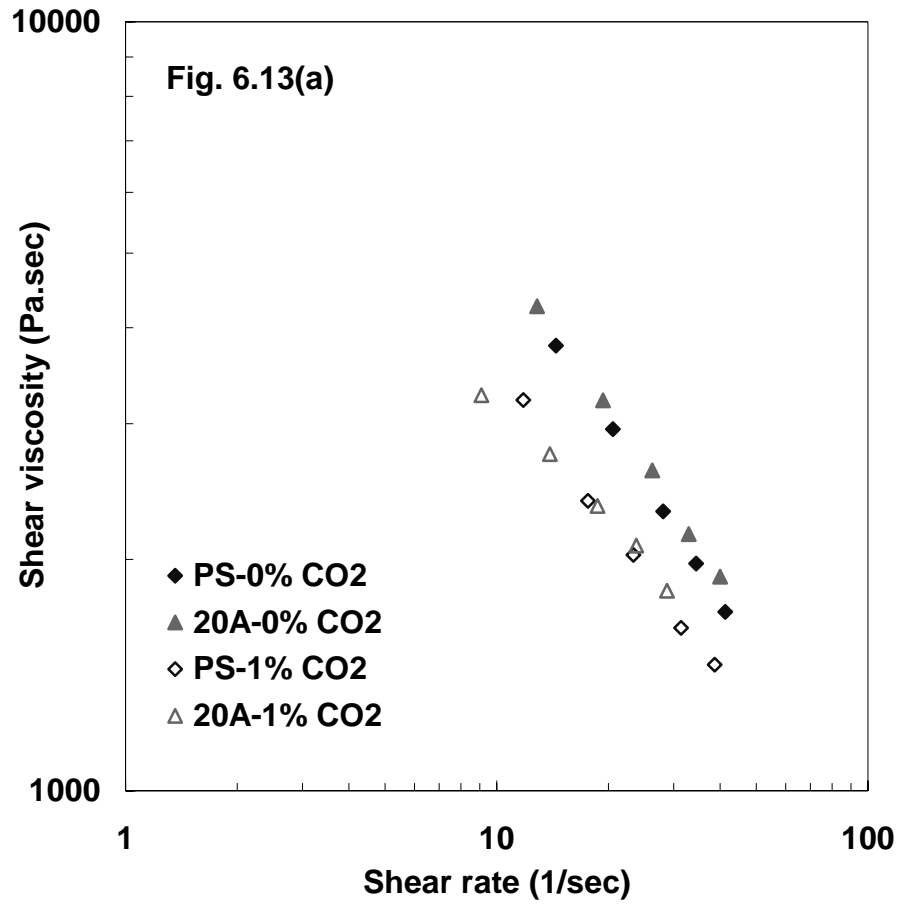


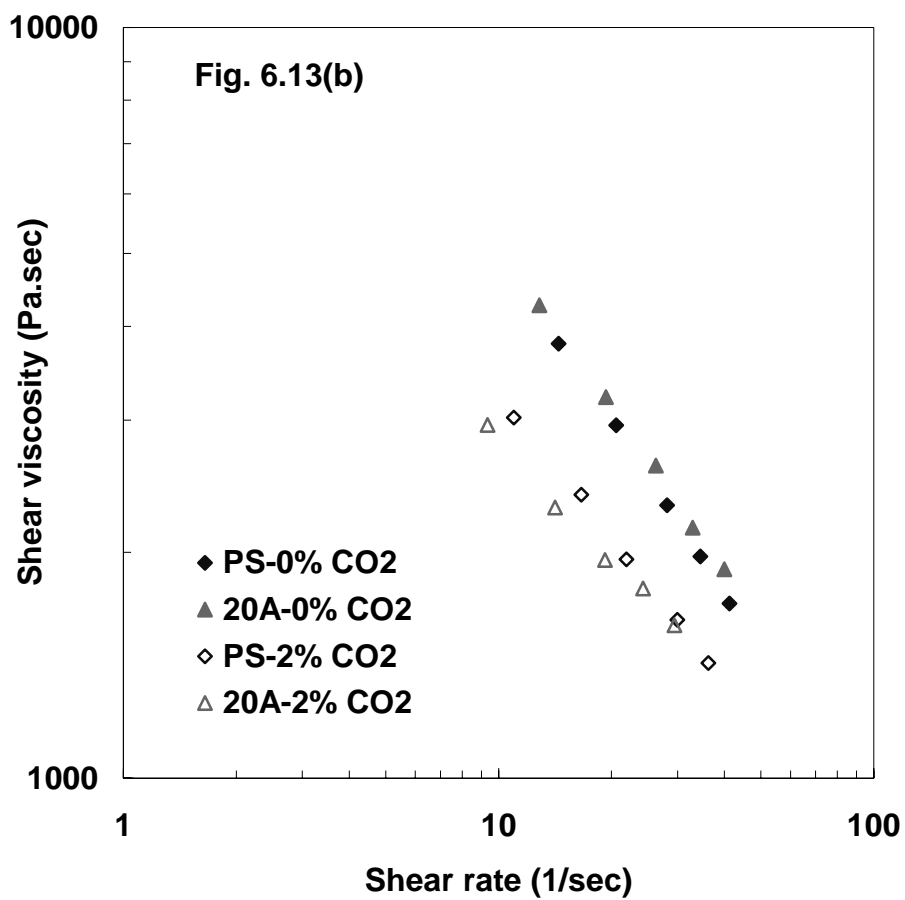
Figure 6.12. CO<sub>2</sub> desorption from PS and PS nanocomposites.



(continued)

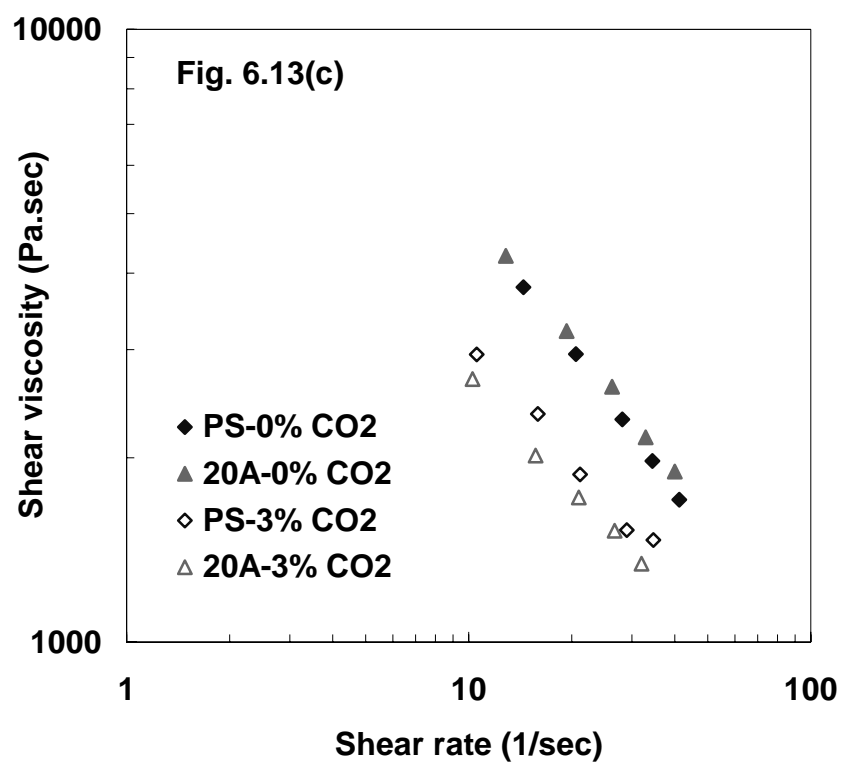
Figure 6.13. Shear viscosity of PS and PS/clay nanocomposites at 180°C with (a) 1 wt.%; (b) 2 wt.%; and (c) 3 wt.% CO<sub>2</sub>.

Figure 6.13 continued



continued

Figure 6.13 continued



## CHAPTER 7

### CONCLUSIONS AND RECOMMENDATIONS

#### 7.1. Conclusions

Microcellular foams of polystyrene and polystyrene nanocomposites were produced continuously applying carbon dioxide as the foaming agent in an extrusion system. The contraction flow in the extrusion die was simulated with the FLUENT computational code to predict profiles of pressure, temperature, viscosity, and velocity. To perform the simulation, the necessary physical properties of the CO<sub>2</sub>/polymer system, such as viscosity and solubility, were characterized and fitted to various theoretical models, which were latterly substituted into the flow simulation. Systematic experiments were performed to verify effects of three key operating conditions: CO<sub>2</sub> content, pressure drop or pressure drop rate, and foaming temperature on the foam cell structure. Experimental results are compared with simulations and both are used to gain insight into the foaming process. To obtain microcellular foams with even smaller cell size and larger cell density, and to create versatile properties, nanocomposite foams were produced.

To accomplish the computational simulation of the polymer flow in the foaming extrusion die and to understand the plasticization effect of CO<sub>2</sub> on polymer melts, two important parameters, solubility and viscosity, were first measured and fitted to various models.

- (1) Solubility of CO<sub>2</sub> in PS was measured by the open volumetric method at 120 and 200°C. Experimental data were then fitted with the Sanchez-Lacombe equation of state. The binary interaction parameters ( $\delta_{ij}$ ) calculated at these two temperatures were compared with those fitted from the literature data at other temperatures and was applied to predict the shear viscosity.
- (2) The viscosity reduction by injecting CO<sub>2</sub> in the polystyrene was measured by connecting a slit die rheometer with backpressure control to the extruder. The viscosity at several temperatures, pressures, CO<sub>2</sub> concentrations, and shear rates was characterized. The superposition technique was used to shift the data to one master curve and the shift factors of temperature and CO<sub>2</sub> concentration were calculated. By integrating the cross-carreau model, the Doolittle's equation, and the Sanchez-Lacombe equation of state, shear viscosities at different temperatures, pressures, and low CO<sub>2</sub> concentrations were successfully predicted in the high shear rate region.

- (3) When nano-clay was blended in polystyrene, the viscosity of the nanocomposite becomes not sensitive to the backpressure. The same viscosity reduction behavior was observed as the CO<sub>2</sub> was dissolved and an even lower shear viscosity than that of pure PS was observed at high CO<sub>2</sub> concentrations.

From the simulation results via the computational fluid dynamics code (FLUENT), the pressure profile in the die was computed by assuming no phase separation. The position of nucleation onset in the capillary die was then determined. For each simulation, only one variable among the CO<sub>2</sub> concentration, foaming temperature, and flow rate was changed and the other two were kept the same.

- (1) A higher CO<sub>2</sub> concentration, a higher foaming temperature, or a slower flow rate brings forward the nucleation onset to the die entrance, which indicates a longer cell growth distance.
- (2) Upon simulation, a lower pressure drop and pressure drop rate was obtained at a higher CO<sub>2</sub> concentration, a higher foaming temperature, or a slower flow, which indicates a lower nucleation rate.
- (3) Operating conditions which offer a late nucleation onset (i.e., a short cell growth time) and a high pressure drop rate (i.e., a high nucleation rate) simultaneously has the highest possibility to create small cell size and high cell density.

Influences of operating conditions on the cell structure of pure polystyrene were systematically studied by experiments. When the pressure drop in the die is larger than 16 MPa and the pressure drop rate is around  $10^9$  Pa/sec at a foaming temperature of 160°C, microcells with diameter less than 10 microns and cell density greater than  $10^9$  cells/cc were successfully extruded.

- (1) A higher pressure drop or pressure drop rate in the die results in smaller cell size and greater cell density.
- (2) Below the solubility limit, cell size decreases and cell density increases with the increase of CO<sub>2</sub> concentrations.
- (3) The influence of foaming temperature is complex because it affects nearly all parameters in the cell nucleation and growth. The foaming temperature shows a great influence to the foam morphology. Open and closed cell structures can be generated at different foaming temperatures. However, the cell size and cell density exhibit greater dependence on the pressure drop rate than the foaming temperature. The cell size and cell density at different foaming temperatures merge onto one curve when they are plotted versus the pressure drop rate.
- (4) Three polystyrenes with different shear viscosities were foamed at the same conditions. The viscosity shows influence mainly on the cell size, while indirect effect on the cell nucleation by changing the pressure drop or pressure drop rate in the extrusion die. It is also shown that the pressure drop rate is more crucial in deciding cell size and cell density.

To obtain microcellular foams with even smaller cell size (or larger cell density) and to create versatile properties, nanocomposite foams were produced. The resulting foam structure was compared with that of pure polystyrene and polystyrene/talc composite. Combining nanocomposites and the extrusion foaming process provides a new technique for the design and control of cell structure in microcellular foams.

- (1) At a screw rotation speed of 10 rpm and a die temperature of 200°C, the addition of a small amount (i.e., 5 wt.%) of intercalated nano-clay greatly reduces cell size from 25.3 to 11.1  $\mu\text{m}$  and increases cell density from  $2.7 \times 10^7$  to  $2.8 \times 10^8$  cells/cm<sup>3</sup>. Once exfoliated, the nanocomposite exhibits the highest cell density ( $1.5 \times 10^9$  cells/cm<sup>3</sup>) and smallest cell size (4.9  $\mu\text{m}$ ) at the same particle concentration.
- (2) Open cell structure was observed in intercalated nanocomposite foams at high clay concentrations. The structure of heterogeneous nucleated cells is affected by the orientation and dispersion of the clay.
- (3) Compared with the polystyrene foams, nanocomposite foams can provide superior performance, including higher tensile modulus, better surface quality, enhanced fire retardance, and improved barrier properties.
- (4) The addition of nano-clay was found to increase the shear viscosity of polymer melts without CO<sub>2</sub>.

## 7.2. Recommendations

The following topics are recommended in the continuing studies:

(1) Production of nano-sized foam cells

Now, there still exists a gap about the relationship between the cell size and the mechanical strength. However, nano-sized foams would show better properties than micron-sized foams, including mechanical strength, optical, thermal, and electrical properties. Nano-sized cells may give transparent foam products with high mechanical strength.

(2) Scale-up of microcellular foaming extrusion

Extrusion of microcellular foams with cell size smaller than 10  $\mu\text{m}$  and cell density larger than  $10^9$  cells/cm<sup>3</sup> still stays in the stage of research. Usually a very small extrusion die is applied to create the necessary high pressure. It has to be scaled up if microcellular foams are designed to replace the pure polymer for producing products like sheets, pipes, and films. The nanocomposite foam provides a high probability to realize the scale-up.

(3) Microcellular foams of other polymers

No doubt that different polymers have different applications due to their own unique properties. Microcellular foaming different polymers can offer new applications of microcellular foams.

(4) Foams with high volume expansion ratio

As a limitation of CO<sub>2</sub> as the foaming agent, high volume expansion ratio (or low density) is difficult to achieve due to the relatively high diffusivity of CO<sub>2</sub>. Hence, it becomes important to improve the barrier properties of polymer matrix and to properly design the foaming die.

(5) Interaction between nanocomposites and CO<sub>2</sub>

In this study, nano-clay shows a great influence on the cell structure and the shear viscosity. To unveil the mechanism behind these phenomena, interaction between nanocomposites and CO<sub>2</sub> is necessary to be investigated, such as the solubility, diffusivity, free volume, and so on. It is also important to know whether the influence comes from the surface modifier or the nano-particle itself.

(6) Understanding cell coalescence

In this study, it is found high cell density and sufficient gas and time for cell growth are crucial for the formation of open-cell foams. It is helpful to understand the formation of open-cell foams from the aspect of cell coalescence. How the cell wall, a polymer film between two growing bubbles, thins down and finally disappears, highly depending on the rheological behavior of the polymer/gas solution, is an interesting phenomenon to be known.

(7) Mechanism of nucleation

The classical nucleation theory is widely used to relate the cell nucleation rate to the operating conditions and material properties. However, the classical nucleation theory is always found not consistent with the experimental results quantitatively, sometimes even qualitatively.

Therefore, it becomes urgent to develop an improved theoretical model for cell nucleation. Furthermore, it is also beneficial to build an easy-operating experimental technique to measure the nucleation.

(8) Foaming simulation in a die

At present, the foam cell growth is relatively well understood and models for fluids with complex rheological behavior have been developed. This makes it possible to combine models of cell nucleation and cell growth within flow simulations to figure out which condition is important in deciding the foam structure, and then to guide the die design.

## REFERENCES

1. Kumar, V. and J.E. Weller, *Microcellular Foams*, in *Polymeric Foams: Science and Technology*, K.C. Khemani, Editor. 1997. p. 101-114.
2. Klempner, D. and K.C. Frisch, eds. *Handbook of Polymeric Foams and Foam Technology*. . 1991, Oxford University Press: Munich; Vienna; New York.
3. Landrock, A.H., *Handbook of Plastic Foams: Types, Properties, Manufacture and Applications*. 1995, Miller Road, Park Ridge, New Jersey: Noyes Publications.
4. Khemani, K.C., *Polymeric Foams: Science and Technology*. 1997: ACS Symposium Series.
5. Lee, S.-T., *Foam Extrusion: Principles and Practice*. 2000, Lancaster, PA: Technomic Publishing Company, Inc.
6. Owens-Corning, Private communication.
7. Aubert, J.H. and R.L. Clough, Low-density, microcellular polystyrene foams. *Polymer*, 1985. 26(13): p. 2047-54.
8. Dixon, D.J., K.P. Johnston, and R.A. Bodmeier, Polymeric materials formed by precipitation with a compressed fluid antisolvent. *AIChE Journal*, 1993. 39(1): p. 127-39.
9. AJ, W.R.P., M. Sasthav, and H.M. Cheung, Microcellular polymeric materials from microemulsions: control of microstructure and morphology. *Journal of Applied Polymer Science*, 1993. 47(3): p. 499-511.
10. Martini-Vvedensky, J.E., N.P. Suh, and F.A. Waldman, Microcellular closed cell foams and their method of manufacture. 1984.US 4,473,665

11. Park, C.B., N.P. Suh, and D.F. Baldwin, Method for Providing Continuous Processing of Microcellular and Supermicrocellular Foamed Materials. 1999.US 5,866,053
12. Martini-Vvedensky, J.E., F.A. Waldman, and N.P. Suh, The production and Analysis of Microcellular Thermoplastic Foams. *SPE-ANTEC*, 1982. 28: p. 674-676.
13. Park, C.B., D.F. Baldwin, and N.P. Suh, Formation and application of polymer/gas mixtures in continuous processing of microcellular polymers. *MD (Am. Soc. Mech. Eng.)*, 1994. 53: p. 109-24.
14. Doroudiani, S., C.B. Park, and M.T. Kortschot, Processing and characterization of microcellular foamed high-density polyethylene/isotactic polypropylene blends. *Polym. Eng. Sci.*, 1998. 38(7): p. 1205-1215.
15. Kumar, V. and J.E. Weller, A Process to Produce Microcellular PVC. *Intern. Polymer Processing*, 1993. VIII(1): p. 73-80.
16. Kumar, V. and J. Weller, Production of Microcellular Polycarbonate Using Carbon Dioxide for Bubble Nucleation. *Journal of Engineering for Industry*, 1994. 116: p. 413-420.
17. Kumar, V. and H.G. Schirmer, Semi-Continuous Production of Solid State Polymeric Foams. 1997. US 5,684,055
18. Kumar, V. and H.G. Schirmer, Semi-continuous production of solid-state PET foams. *SPE-ANTEC*, 1995. 53rd(Vol. 2), p. 2189-92.
19. Park, C.B. and N.P. Suh, Filamentary extrusion of microcellular polymers using a rapid decompressive element. *Polym. Eng. Sci.*, 1996. 36(1): p. 34-48.
20. Park, C.B., D.F. Baldwin, and N.P. Suh, Effect of the pressure drop rate on cell nucleation in continuous processing of microcellular polymers. *Polym. Eng. Sci.*, 1995. 35(5): p. 432-40.
21. Park, C.B., D.F. Baldwin, and N.P. Suh, Cell nucleation by rapid pressure drop in continuous processing of microcellular plastics. *MD (Am. Soc. Mech. Eng.)*, 46(*Use of Plastics and Plastic Composites*), 1993. 46: p. 537-52.
22. Park, C.B. and N.P. Suh, Rapid Polymer/Gas Solution Formation for Continuous Production of Microcellular Plastics. *Journal of Manufacturing Science and Engineering*, 1996. 118: p. 639-645.
23. Trexel, [www.trexel.com](http://www.trexel.com).

24. Xu, J., Reciprocating-Screw Injection Molding Machine for Microcellular Foam. *SPE-ANTEC*, 2001: p. 449-453.
25. Jacobsen, K. and D. Pierick, Microcellular Foam Molding: Advantages and Application Examples. *SPE-ANTEC*, 2000: p. 1929-33.
26. Moore, S., Foam Molding Resurgence: Sparks Competition among Processes. *Modern Plastics*, Nov., 2001: p. 23-25.
27. Kishbaugh, L.A., K.J. Levesque, A.H. Guillemette, L. Chen, J. Xu, and K.T. Okamoto, Fiber-Filler Molded Articles. 2002.WO 02/26482 A1
28. Sumarno, Y. Sato, S. Takishima, and H. Masuoka, Production of Polystyrene Microcellular Foam Plastics and a Comparison of Late- and Quick-Heating. *Journal of Applied Polymer Science*, 2000. 77: p. 2383-2395.
29. Arora, K.A., A.J. Lesser, and T.J. McCarthy, Preparation and Characterization of microcellular polystyrene foams processed in supercritical carbon dioxide. *Macromolecules*, 1998. 31(14): p. 4614-4620.
30. Arora, K.A., A.J. Lesser, and T.J. McCarthy, Compressive behavior of microcellular polystyrene foams processed in supercritical carbon dioxide. *Polymer Engineering and Science*, 1998. 38(12): p. 2055-62.
31. Park, C.B., A.H. Behraves, and R.D. Venter, Low density microcellular foam processing in extrusion using CO<sub>2</sub>. *Polym. Eng. Sci.*, 1998. 38(11): p. 1812-1823.
32. Handa, Y.P. and Z. Zhang, A New Technique for Measuring Retrograde Vitrification in Polymer-Gas Systems and for Making Ultramicrocellular Foams from the Retrograde Phase. *Journal of Polymer Science: Part B: Polymer Physics*, 2000. 38: p. 716-725.
33. Handa, Y.P., Z. Zhang, and B. Wong, Solubility, Diffusivity, and Retrograde Vitrification in PMMA-CO<sub>2</sub>, and Development of Sub-micron Cellular Structures. *Cellular Polymers*, 2001. 20(1): p. 1-16.
34. Goel, S.K. and E.J. Beckman, Generation of microcellular polymeric foams using supercritical carbon dioxide. I Effect of pressure and temperature on nucleation. *Polym. Eng. Sci.*, 1994. 34(14): p. 1137-47.
35. Goel, S.K. and E.J. Beckman, Generation of microcellular polymeric foams using supercritical carbon dioxide. II: Cell growth and skin formation. *Polym. Eng. Sci.*, 1994. 34(14): p. 1148-56.

36. Goel, S.K. and E.J. Beckman. *Generation of Microcellular Polymers using Supercritical CO<sub>2</sub>*. in *Cell. Polym., Int. Conf. 2nd*. 1993. Heriot-Watt University, Edinburgh, U. K.
37. Goel, S.K. and E.J. Beckman, Nucleation and Growth in Microcellular Materials: Supercritical CO<sub>2</sub> as Foaming Agent. *AICHE Journal*, 1995. *41*(2): p. 357-367.
38. Goel, S.K. and E.J. Bechman, Plasticization of poly(methyl methacrylate) (PMMA) networks by supercritical carbon dioxide. *Polymer*, 1993. *34*(7): p. 1410.
39. Holl, M.R., M. Ma, V. Kumar, and R.R. Kwapisz, The effect of additives on microcellular PVC foams: part 1 - effect on processing and microstructure. *Cell. Polym.*, 1998. *17*(4): p. 271-283.
40. Matuana, L.M., C.B. Park, and J.J. Balatinez, Cell morphology and property relationships of microcellular foamed PVC/wood-fiber composites. *Polym. Eng. Sci.*, 1998. *38*(11): p. 1862-1872.
41. Matuana, L.M., C.B. Park, and J.J. Balatinez, Characterization of Microcellular Foamed Plastic/Cellulosic Fiber Composites. *Annu. Tech. Conf. - Soc. Plast. Eng. 56th (Vol. 2)*, 1998. 2: p. 1968-1974.
42. Itoh, M., A. Kabumoto, N. Yoshida, and M. Okada, Microcellular Foaming Behaviors of Thermally Stable Non-Crystalline Polymers. *MD, Cellular and Microcellular Materials, ASME*, 1994. *53*: p. 139-145.
43. Krause, B., H.J.P. Sijbesma, P. Munuklu, N.F.A. Van der Vegt, and M. Wessling, Bicontinuous Nanoporous Polymers by Carbon Dioxide Foaming. *Macromolecules*, 2001. *34*: p. 8792-8801.
44. Krause, B., M. Kloth, N.F.A. Van der Vegt, and M. Wessling, Porous Monofilaments by Continuous Solid-state Foaming. *Ind. Eng. Chem. Res.*, 2002. *41*: p. 1195-1204.
45. Sun, H. and J.E. Mark, Preparation and Some Mechanical Properties of Microcellular Polysulfone Foam. *Polymer Preprints*, 2001. *42*(1): p. 630-631.
46. Sun, H., N. Venkatasubramanian, M.D. Houtz, J.E. Mark, and F.E. Arnold, Study of Modified Polysulfone/polybenzimidazole Composites and Their Application as Microcellular Foams. *Polymer Preprints*, 2002. *43*(1): p. 471-472.
47. Baldwin, D.F., N.P. Suh, and M. Shimbo, Gas Dissolution and Crystallization in Microcellular Thermoplastic Polymers. *MD-Vol. 38, Cellular Polymers, ASME*, 1992: p. 109-128.

48. Kumar, V., S. Eddy, and R. Murrar, *SPE-ANTEC*, 1996. 42: p. 1920-1925.
49. Kumar, V., S. Eddy, and R. Murrar, *Polymer Preprints, ACS*, 1996. 37: p. 779-780.
50. Park, C.B. and L.K. Cheung, A study of cell nucleation in the extrusion of polypropylene foams. *Polym. Eng. Sci.*, 1997. 37(1): p. 1-10.
51. Behraves, A.H., C.B. Park, and R.D. Venter, Challenge to the production of low-density, fine-cell HDPE foams using CO<sub>2</sub>. *Cell. Polym.*, 1998. 17(5): p. 309-326.
52. Lee, M., C.B. Park, and C. Tzoganakis, Extrusion of PE/PS blends with supercritical carbon dioxide. *Polymer Engineering and Science*, 1998. 38(7): p. 1112-20.
53. Doroudiani, S., C.B. Park, and M.T. Kortschot, Effect of the crystallinity and morphology on the microcellular foam structure of semicrystalline polymers. *Polym. Eng. Sci.*, 1996. 36(21): p. 2645-2662.
54. Park, C.B., Y. Liu, and H.E. Naguib, Challenge to Fortyfold Expansion of Biodegradable Polyester Foams by Using Carbon Dioxide as a Blowing Agent. *Journal of Vinyl & Additive Technology*, 2000. 6(1): p. 39-48.
55. Martinache, J.D., J.R. Royer, S. Siripurapu, F.E. Henon, J. Genzer, S.A. Khan, and R.G. Carbonell, Processing of Polyamide 11 with Supercritical Carbon Dioxide. *Ind. Eng. Chem. Res.*, 2001. 40: p. 5570-77.
56. DeSimone, J.M., S.A. Khan, J.R. Royer, R.J. Spontak, and T.A. Walker, Method of Making Foamed Materials using Surfactants and Carbon Dioxide. 2002.US 6,403,663.
57. Siripurapu, S., Y.J. Gay, J.R. Royer, J.M. DeSimone, R.J. Spontak, and S.A. Khan, Generation of Microcellular Foams of PVDF and Its Blends Using Supercritical Carbon Dioxide in A Continuous Process. *Polymer*, 2002. 43: p. 5511-20.
58. Bucknall, C.B., *Toughened Plastics*. 1977: Applied Science Publ., Barking, Engl.
59. Bubeck, R.A., D.J. Buckley, Jr., E.J. Kramer, and H.R. Brown, Modes of deformation in rubber-modified thermoplastics during tensile impact. *J. Mater. Sci.*, 1991. 26(23): p. 6249-59.

60. Borggreve, R.J.M., R.J. Gaymans, and H.M. Eichenwald, Impact behavior of nylon-rubber blends. 6. Influence of structure on voiding processes; toughening mechanism. *Polymer*, 1989. 30(1): p. 78-83.
61. van der Sanden, M.C.M., H.E.H. Meijer, and P.J. Lemstra, Deformation and toughness of polymeric systems: 1. The concept of a critical thickness. *Polymer*, 1993. 34(10): p. 2148-54.
62. van der Sanden, M.C.M., H.E.H. Meijer, and P.J. Lemstra, Deformation and toughness of polymeric systems: 2. Influence of entanglement density. *Polymer*, 1993. 34(14): p. 2961-70.
63. Barlow, C., V. Kumar, B. Flinn, R.K. Bordia, and J. Weller, Impact strength of high density solid-state microcellular polycarbonate foams. *Journal of Engineering Materials and Technology*, 2001. 123(2): p. 229-233.
64. Barlow, C., V. Kumar, B. Flinn, R.K. Bordia, and J. Weller, Experiments on the Impact Strength of Microcellular Polycarbonate. *MD-Vol 82, Porous, Cellular and Microcellular Materials, ASME*, 2001.
65. Collias, D.I., D.G. Baird, and R.J.M. Borggreve, Impact toughening of polycarbonate by microcellular foaming. *Polymer*, 1994. 35(18): p. 3978-83.
66. Collias, D.I. and D.G. Baird, Impact behavior of microcellular foams of polystyrene and styrene-acrylonitrile copolymer, and single-edge-notched tensile toughness of microcellular foams of polystyrene, styrene-acrylonitrile copolymer, and polycarbonate. *Polym. Eng. Sci.*, 1995. 35(14): p. 1178-83.
67. Collias, D.I. and D.G. Baird, Tensile toughness of microcellular foams of polystyrene, styrene-acrylonitrile copolymer, and polycarbonate, and the effect of dissolved gas on the tensile toughness of the same polymer matrixes and microcellular foams. *Polym. Eng. Sci.*, 1995. 35(14): p. 1167-77.
68. Matuana, L.M., C.B. Park, and J.J. Balatinecz, Structures and Mechanical Properties of Microcellular Foamed Polyvinyl Chloride. *Cellular Polymers*, 1998. 17(1): p. 1-16.
69. Kumar, V., Microcellular Plastics: Does Microcellular Structure Always Lead to an Improvement in Impact Properties? *SPE-ANTEC*, 2002. 60th(Vol. 2): p. 1892-96.
70. Juntunen, R.P., V. Kumar, J.E. Weller, and W.P. Bezubic, Impact strength of high density microcellular poly(vinyl chloride) foams. *Journal of Vinyl & Additive Technology*, 2000. 6(2): p. 93-99.

71. Juntunen, R.P., V. Kumar, and C. Barlow, Impact strength of high relative density Carbon Dioxide Blown Crystallizable Poly(ethylene terephthalate) microcellular foams. *Cellular Polymers*, 2000. 19(1): p. 25-38.
72. Seeler, K.A. and V. Kumar, The Effect of Annealing on the Mechanical Properties of Microcellular Polycarbonate. *MD-vol. 53, Cellular and Microcellular Materials, ASME*, 1994: p. 269-282.
73. Seeler, K.A. and V. Kumar, Tension-tension fatigue of microcellular polycarbonate: initial results. *J. Reinf. Plast. Compos.*, 1993. 12(3): p. 359-76.
74. Seeler, K.A. and V. Kumar, Effect of CO<sub>2</sub> Saturation and Desorption on the Fatigue Life of Polycarbonate. *MD, Use of Plastics and Plastic Composites: Materials and Mechanics Issues, ASME*, 1993. 46: p. 439-454.
75. Kumar, V., M. VanderWel, J. Weller, and K.A. Seeler, Experimental characterization of the tensile behavior of microcellular polycarbonate foams. *Journal of Engineering Materials Technology*, 1994. 116(4): p. 439-45.
76. Weller, J.E., M. Ma, R. Montecillo, and V. Kumar, The tensile properties of microcellular PVC: the effects of additives and foam density. *SPE-ANTEC*, 1997. 55th(Vol. 2): p. 2055-2059.
77. Kumar, V., J.E. Weller, M. Ma, R. Montecillo, and R.R. Kwapisz, The effect of additives on microcellular PVC foams: part II. tensile behavior. *Cellular Polymers*, 1998. 17(5): p. 350-361.
78. Kumar, V. and J.E. Weller, Producing Polycarbonate Foams of Constant Density and Different Average Cell Size. *MD-Vol. 53, Cellular and Microcellular Materials, ASME*, 1994: p. 255-267.
79. Cha, S.W., N.P. Suh, D.F. Baldwin, and C.B. Park, Microcellular Thermoplastic Foamed with Supercritical Fluid. 1992.US 5,158,986
80. Kumar, V. and N.P. Suh, A process for making microcellular thermoplastic parts. *Polym. Eng. Sci.*, 1990. 30(20): p. 1323-9.
81. Rodeheaver, B.A. and J.S. Colton, Open-Celled Microcellular Thermoplastic Foam. *Polymer Engineering and Science*, 2001. 41(3): p. 380-400.
82. Park, C.B., A.H. Behraves, and R.D. Venter, A strategy for the suppression of cell coalescence in the extrusion of microcellular high-impact polystyrene foams. *ACS Symp. Ser., 669(Polymeric Foams)*, 1997: p. 115-129.

83. Chen, L., H. Sheth, and X. Wang, Effect of shear stress and pressure drop rate on microcellular foaming process. *Journal of cellular plastics*, 2001. 37: p. 353-363.
84. Handa, Y.P. and Z. Zhang, Mew Pathway to Microcellular and Ultramicrocellular Polymeric Foams. *MD-Vol. 82, Porous, Cellular and Microcellular Materials*, ASME, 1998: p. 1-4.
85. Condo, P.D., I.C. Sanchez, C.G. Panayiotou, and K.P. Johnston, Glass Transition Behavior Including Retrograde Vitrification of Polymers with Compressed Fluid Diluents. *Macromolecules*, 1992. 25: p. 6119.
86. Condo, P.D., D.R. Paul, and K.P. Johnston, Glass Transition of Polymer with Compressed Fluid Diluents: Type II and III Behavior. *Macromolecules*, 1994. 27: p. 365-371.
87. Lan, T., P.D. Kaviratna, and T. Pinnavaia, *J. Chem. Mater.*, 1994. 6: p. 573.
88. Okada, A. and A. Usuki, *Mater. Sci. Eng.*, 1995. C3: p. 109.
89. Kojima, Y., A. Usuki, M. Kawasumi, A. Okada, Y. Fukushima, T. Kurauchi, and O. Kamigaito, *J. Mater. Res.*, 1993. 8: p. 1185.
90. Zeng, C. and L.J. Lee, Poly(methyl methacrylate) and Polystyrene/Clay Nanocomposites Prepared by in-Situ Polymerization. *Macromolecules*, 2001. 34: p. 4098-4103.
91. Wang, H., C. Zeng, M. Elkovitch, L.J. Lee, and K.W. Koelling, Processing and properties of polymeric nano-composites. *Polymer Engineering and Science*, 2001. 41(11): p. 2036-2046.
92. Svoboda, P., C. Zeng, H. Wang, L.J. Lee, and D.L. Tomasko, Morphology and mechanical properties of polypropylene/organoclay nanocomposites. *Journal of Applied Polymer Science*, 2002. 85(7): p. 1562-1570.
93. Nam, P.H., P. Maiti, M. Okamoto, T. Kotaka, T. Nakayama, M. Takada, M. Ohshima, A. Usuki, N. Hasegawa, and H. Okamoto, Foam Processing and Cellular Structure of Polypropylene/Clay Nanocomposites. *Polymer Engineering and Science*, 2002. 42(9): p. 1907-1918.
94. Nam, P.H., M. Okamoto, P. Maiti, T. Kotaka, T. Nakayama, M. Takada, M. Ohshima, A. Usuki, N. Hasegawa, and H. Okamoto, Biaxial Flow-Induced Alignment of Silicate Layers in Polypropylene/Clay Nanocomposite Foam. *Nano Letters*, 2001. 1(9): p. 503-505.

95. Wilson, P.S., Structural foam composite having nano-particle reinforcement and method of making the same. 2000.WO0037242
96. Fibiger, R.F., M.A. Barger, K.W. Suh, H.C. Tung, W. Liang, G.A. Mackey, and J.A. Schomaker, Nanocomposite Articles and Process for Making. 2000.WO0047657
97. Steeman, P.A.M., P.E.L. Voets, and E.M.A. Van, Extruded Nanocomposite Moulded Part Comprising at Least a Polycondensate and A Nano-Filler and A Process for Its Production. 2001.WO0118107
98. Mikos, A.G. and J.S. Temenoff, Formation of Highly Porous Biodegradable Scaffolds for Tissue Engineering. *Journal of Biotechnology*, 2000. 3(2): p. 1-6.
99. Sheridan, M.H., L.D. Shea, M.C. Peters, and D.J. Mooney, Bioabsorbable polymer scaffolds for tissue engineering capable of sustained growth factor delivery. *Journal of Controlled Release*, 2000. 64: p. 91 - 102.
100. Mooney, D.J., D.F. Baldwin, N.P. Suh, J.P. Vacanti, and R. Langer, Novel Approach to Fabricate Porous Sponges of Poly(D,L-Lactic-co-Glycolic Acid) without the Use of Organic Solvents. *Biomaterials*, 1996. 17(14): p. 1417-22.
101. Kumar, V., Potential of Porous Microcellular Polymers in Biomaterials Research. *MD-Vol. 82, Porous, Cellular and Microcellular Materials, ASME*, 1998: p. 5-7.
102. Mitchell, M.A. and A.S. Tomlin, Hydrophilic/Oleophilic Microcellular Foam and Method foam Making Same. 1999.US 5,900,437
103. Mikos, A.G., G. Sarakinos, S.M. Leite, J.P. Vacanti, and R. Langer, Laminated Three-Dimensional Biodegradable Foams for Use in Tissue Engineering. *Biomaterials*, 1993. 14(5): p. 323-330.
104. Shimidt, C.D., K.W. Suh, D.D. Imeokparia, B.A. Malone, and K. Franklin, Extruded, Open-Cell Microcellular Alkenyl Aromatic Polymer Foams, Process for Making, and Articles Made Therefrom. 1999.US 5,869,544
105. Huang, Q., B. Seibig, and D. Paul, Melt Extruded Open-Cell Microcellular Foams for Membrane Separation: Processing and Cell Morphology Relationship. *Journal of Cellular Plastics*, 2000. 36: p. 112-125.
106. Park, C.P., Soft Ethylenic Polymer Blend Foams. 1980.US 4,215,202
107. Bland, D.G., G.D. Rose, W.G. Stobby, S.W. Mork, T.G. Staples, and G.D. McCann, Absorbent, Extruded Thermoplastic Foam. 1998.WO 98/56430

108. Bland, D.G., G.D. Rose, W.G. Stobby, S.W. Mork, T.G. Staples, and G.D. McCann, Absorbent, extruded open-celled thermoplastic foam. 2000.US 6,071,580
109. Park, C.P., Lightly Crosslinked Polyethylene Polystyrene Blend Foams and Process for Making. 1986.US 4,605,682
110. Kim, D.W. and K.S. Kim, Investigation of the Radiation Crosslinked Foams Produced from Metallocene Polyolefin Elastomers/Polyethylene Blend. *Journal of Cellular Plastics*, 2001. 37: p. 333-352.
111. Graff, G., Noval Technologies Boost Performance Profile of Polyolefin Foams. *Modern Plastics*, 2000(3): p. 80-82.
112. Ramesh, N.S., New Products Made from Ethylene-Styrene Interpolymer/LDPE Blend Foams for Various Applications. *Foams 2000, Second International Conference on Thermoplastic Foam, Parsippany, New Jersey, October 24-25, 2000*, 2000: p. 102-107.
113. Nagata, T., M. Tanigaki, and M. Ohshima, In-Line NIR Sensing of CO<sub>2</sub> Concentration for Polymer Extrusion Foaming Processes. *Polymer Engineering and Science*, 2000. 40: p. 1843-1849.
114. Nagata, T., M. Tanigaki, and M. Ohshima, In-Line NIR Sensing of CO<sub>2</sub> Concentration in Polymeric Foaming Extrusion Process. *Journal of Cellular Plastics*, 2002. 38: p. 11-30.
115. Tatibouet, J., R. Gendron, A. Hamel, L. Piche, and A. Sahnoune, Application of Ultrasonic Sensors in the Study of Physical Foaming Agents such as CO<sub>2</sub> for PS Foam Extrusion. *Foamplas 2000*, 2000: p. 271-292.
116. Cooper, A.I., Polymer Synthesis and Processing Using Supercritical Carbon Dioxide. *J. Mater. Chem.*, 2000. 10(2): p. 207-234.
117. Kazarian, S.G., Polymer Processing with Supercritical Fluids. *Polymer Science, Series C*, 2000. 42(1): p. 78.
118. Tipnis, S.J., A review on the Applications of Supercritical Fluids in Polymer Processing. *Popular Plastics & Packaging*, 2001. January(77-79).
119. Kirby, C.F. and M.A. Mchugh, Phase Behavior of Polymers in Supercritical Fluid Solvents. *Chem. Rev.*, 1999. 99: p. 565-602.

120. Kazarian, S.G., M.F. Vincent, F.V. Bright, C.L. Liotta, and C.A. Eckert, Specific Intermolecular Interaction of Carbon Dioxide with Polymers. *J. Am. Chem. Soc.*, 1996. *118*: p. 1729-36.
121. Kazarian, S.G., M.F. Vincent, and C.A. Eckert, Infrared cell for supercritical fluid-polymer interactions. *Rev. Sci. Instrum.*, 1996. *67*: p. 1586.
122. Kazarian, S.G., Polymers and Supercritical Fluids: Opportunities for Vibrational Spectroscopy. *Macromol. Symp.*, 2002. *184*: p. 215-228.
123. Kazarian, S.G., N.H. Brantley, and C.A. Eckert, In Situ Spectroscopy of CO<sub>2</sub>-Induced Plasticization of Glassy Polymers. *SPE-ANTEC*, 1998: p. 1415-17.
124. Drohmann, C. and E.J. Beckman, Phase Behavior of Polymers containing Ether Groups in Carbon Dioxide. *Journal of Supercritical Fluids*, 2002. *22*: p. 103-110.
125. Shieh, Y.-T., J.-H. Su, G. Manivannan, P.H.C. Lee, S.P. Sawan, and W. Dale Spall, Interaction of Supercritical Carbon Dioxide with Polymers. II. Amorphous Polymers. *J. of Appl. Polym. Sci.*, 1996. *59*: p. 707.
126. Shieh, Y.-T., J.-H. Su, G. Manivannan, P.H.C. Lee, S.P. Sawan, and W. Dale Spall, Interaction of Supercritical Carbon Dioxide with Polymers. I. Crystalline Polymers. *J. of Appl. Polym. Sci.*, 1996. *59*: p. 695.
127. Sawan, S.P., Y.-T. Shieh, J.-H. Su, G. Manivannan, and W. Dale Spall, Evaluation of Supercritical Fluid Interactions with Polymeric Materials. *Supercritical Fluid Cleaning*, 1998: p. 121-161.
128. Wissinger, R.G. and M.E. Paulaitis, Swelling and Sorption in Polymer-CO<sub>2</sub> Mixtures at Elevated Pressures. *Journal of Polymer Science: Part B: Polymer Physics*, 1987. *25*: p. 2497-2510.
129. Wissinger, R.G. and M.E. Paulaitis, Molecular Thermodynamic Model for Sorption and swelling in Glassy Polymer-CO<sub>2</sub> System at Elevated Pressures. *Ind. Eng. Chem. Res.*, 1991. *2530*: p. 842-851.
130. Sato, Y., K. Fujiwara, T. Takikawa, Sumarno, S. Takishima, and H. Masuoka, Solubilities and diffusion coefficients of carbon dioxide and nitrogen in polypropylene, high-density polyethylene, and polystyrene under high pressures and temperatures. *Fluid phase equilibria*, 1999. *162*: p. 261-276.
131. Sato, Y., T. Takikawa, S. Takishima, and H. Masuoka, Solubility and diffusion coefficient of carbon dioxide in poly(vinyl acetate) and polystyrene. *The journal of Supercritical fluids*, 2001. *19*: p. 187-198.

132. Zhang, Q., M. Xanthos, and S.K. Dey, In-line measurement of gas solubility in polystyrene and polyethylene terephthalate melts during foam extrusion. *MD (Am. Soc. Mech. Eng.)* , 82(*Porous, Cellular and Microcellular Materials*), 1998(75-83).
133. Sanchez, I.C. and R.H. Lacombe, An Elementary Molecular Theory of Classical Fluids. *Pure Fluids. J. Phys. Chem.*, 1976. 80(21): p. 2352.
134. Sanchez, I.C. and R.H. Lacombe, An Elementary Equation of State for Polymer Liquids. *Polymer Letters Edition*, 1977. 15: p. 71-75.
135. Sanchez, I.C. and R.H. Lacombe, Statistical Thermodynamics of Polymer Solutions. *Macromolecules*, 1978. 11(6): p. 1145-1156.
136. Kiszka, M.B., M.A. Meilchen, and M.A. Mchugh, Modeling High-Pressure Gas-Polymer Mixtures Using the Sanchez-Lacombe Equation of State. *Journal of Applied Polymer Science*, 1988. 36: p. 583-597.
137. Kiran, E., Y. Xiong, and W. Zhuang, Modeling Polyethylene Solutions in Near and Supercritical Fluids Using the Sanchez-Lacombe Model. *The Journal of Supercritical Fluids*, 1993. 6: p. 193-203.
138. Garg, A., E. Gulari, and C.W. Manke, Thermodynamics of Polymer Melts Swollen with Supercritical Gases. *Macromolecules*, 1994. 27: p. 5643-5653.
139. Sperling, L.H., *Introduction to physical polymer science*. 1986, New York: Wiley Interscience.
140. DiMarzio, E.A. and J.H. Gibbs, Molecular interpretation of glass temperature depression by plasticizers. *Journal of Polymer Science: Part A*, 1963. 1: p. 1417-1428.
141. DiMarzio, E.A., J.H. Gibbs, P.D. Fleming, III, and I.C. Sanchez, Effects of pressure on the equilibrium properties of glass-forming polymers. *Macromolecules*, 1976. 9(5): p. 763-771.
142. Gibbs, J.H. and E.A. DiMarzio, Nature of the glass transition and the glass state. *The Journal of Chemical Physics*, 1958. 28(3): p. 373-383.
143. Chiou, J.S., J.W. Barlow, and D.R. Paul, Plasticization of Glassy Polymers by CO<sub>2</sub>. *J. of Appl. Polym. Sci.*, 1985. 30: p. 2633.
144. Chow, T.S., Molecular interpretation of glass transition temperature of polymer-diluent systems. *Macromolecules*, 1980. 13(2): p. 362-4.

145. Chow, T.S., Glass transition temperature of polymer-diluent systems. *Ferroelectrics*, 1980. 30(1-4): p. 139-45.
146. Wissinger, R.G. and M.E. Paulaitis, Glass Transition in Polymer/CO<sub>2</sub> Mixture at Elevated Pressures. *Journal of Polymer Science: Part B: Polymer Physics*, 1991. 29: p. 631-633.
147. Hwang, Y.D. and S.W. Cha, The Relationship between Gas Absorption and the Glass Transition Temperature in A Batch Microcellular Foaming Process. *Polymer Testing*, 2002. 21: p. 269-275.
148. Li, H., Y. Yang, L.J. Lee, and D.L. Tomasko, Interfacial Tension and Glass Transition Depression Measurement for Polymers Under High Pressure CO<sub>2</sub>. *DMII Conference Paper 2003*, 2003.
149. O'Neill, M.L. and Y.P. Handa, Assignment of the Glass Transition. *ASTM STP 1249, R. J. Seyler, Eds.; American Society for Testing and Materials: Philadelphia, 1994*.
150. Zhang, Z. and Y.P. Handa, *Journal of Polymer Science: Part B: Polymer Physics*, 1998. 36: p. 977-982.
151. Chiou, J.S., J.W. Barlow, and D.R. Paul, Polymer Crystallization Induced by Sorption of CO<sub>2</sub> Gas. *J. of Appl. Polym. Sci.*, 1985. 30: p. 3911.
152. Baldwin, D.F. and N.P. Suh, Microcellular poly(ethylene terephthalate) and crystallizable poly(ethylene terephthalate): characterization of process variables. *Annu. Tech. Conf. - Soc. Plast. Eng.*, 1992. 50: p. 1503-7.
153. Kumar, V. and O.S. Gebizlioglu, Carbon Dioxide--Induced Crystallization in PET Foams. *SPE-ANTEC*, 1991: p. 1297.
154. Kumar, V. and O.S. Gebizlioglu, Thermal and Microscopy Studies of CO<sub>2</sub>-induced Morphology in Crystalline PET Foams. *SPE-ANTEC*, 1992: p. 1536.
155. Mizoguchi, K., T. Hirose, Y. Naito, and Y. Kamiya, *Polymer*, 1987. 28: p. 1298.
156. Handa, Y.P., Z. Zhang, and B. Wong, Effect of compressed CO<sub>2</sub> on phase transitions and polymorphism in syndiotactic polystyrene. *Macromolecules*, 1997. 30(26): p. 8499-8504.
157. Takada, M., M. Tanigaki, and M. Ohshima, Effects of CO<sub>2</sub> on crystallization kinetics of polypropylene. *Polymer Engineering and Science*, 2001. 41(11): p. 1938-1946.

158. Royer, J.R., J.M. DeSimone, and S.A. Khan, Carbon Dioxide-Induced Swelling of Poly(dimethylsiloxane). *Macromolecules*, 1999. 32: p. 8965-73.
159. Webb, K.F. and A.S. Teja, Solubility and diffusion of carbon dioxide in polymers. *Fluid phase equilibria*, 1999. 158-160: p. 1029-1034.
160. Wong, B., Z. Zhang, and Y.P. Handa, High-Precision Gravimetric Technique for Determining the Solubility and Diffusivity of Gases in Polymers. *Journal of Polymer Science: PartB: Polymer Physics*, 1998. 36: p. 2025-32.
161. Li, H., L.J. Lee, and D.L. Tomasko, Interfacial Tension Between Polystyrene(PS) and SC CO<sub>2</sub>. *2002 Midwest Thermodynamics and Statistical Mechanics Meeting, Carnegie Mellon University, Pittsburgh, PA, MAy 13-14, 2002, ORGANIZERS: David Sholl, J. Karl Johnston, 2002.*
162. Han, C.D. and C.Y. Ma, Rheological properties of mixtures of molten polymer and fluorocarbon blowing agent. I. Mixtures of low-density polyethylene and fluorocarbon blowing agent. *J. Appl. Polym. Sci.*, 1983. 28(2): p. 831-50.
163. Han, C.D. and C.Y. Ma, Rheological properties of mixtures of molten polymer and fluorocarbon blowing agent. II. Mixtures of polystyrene and fluorocarbon blowing agent. *J. Appl. Polym. Sci.*, 1983. 28(2): p. 851-60.
164. Gerhardt, L.J., A. Garg, Y.C. Bae, C.W. Manke, and E. Gulari. *Effect of dissolved carbon dioxide on the viscosity of liquid poly(dimethylsiloxane) (PDMS)*. in *Theor. Appl. Rheol., Proc. Int. Congr. Rheol., 11th.* 1992.
165. Gerhardt, L.J., C.W. Manke, and E. Gulari, Rheology of polydimethylsiloxane swollen with supercritical carbon dioxide. *J. Polym. Sci., Part B: Polym. Phys.*, 1997. 35(3): p. 523-534.
166. Gerhardt, L.J., A. Garg, C.W. Manke, and E. Gulari, Concentration-dependent Viscoelastic Scaling Models for Polydimethylsiloxane Melts with Dissolved Carbon Dioxide. *Journal of Polymer Science: Part B: Polymer Physics*, 1998. 36: p. 1911-1918.
167. Kwag, C., C.W. Manke, and E. Gulari, Rheology of Molten Polystyrene With Dissolved Supercritical and Near-critical Gases. *J. Polym. Sci., Part B: Polym. Phys.*, 1999. 37(19): p. 2771-2781.
168. Lee, M., C.B. Park, and C. Tzoganakis, On-line measurement of PS/CO<sub>2</sub> solution viscosities. *Annu. Tech. Conf. - Soc. Plast. Eng. , 55th(Vol. 2)*, 1997. 2: p. 1991-1995.

169. Lee, M., C.B. Park, and C. Tzoganakis, Measurements and Modeling of PS/Supercritical CO<sub>2</sub> Solution Viscosities. *Polymer Engineering and Science*, 1999. 39(1): p. 99-109.
170. Areerat, S., T. Nagata, and M. Ohshima, Measurement and Prediction of LDPE/CO<sub>2</sub> Solution Viscosity. *Accepted by Polymer Engineering and Science*, 2002.
171. Areerat, S., Y. Hayata, R. Katsumoto, T. Kegasawa, H. Egami, and M. Ohshima, Solubility of carbon dioxide in polyethylene/titanium dioxide composite under high pressure and temperature. *Journal of Applied Polymer Science*, 2002. 86(2): p. 282-288.
172. Elkovitch, M.D., L.J. Lee, and D.L. Tomasko, Effect of supercritical carbon dioxide on PMMA/Rubber and Polystyrene/Rubber Blending: Viscosity Ratio and Phase Inversion. *Polym. Eng. Sci.*, 2001. 41(12): p. 2108-2125.
173. Elkovitch, M.D., L.J. Lee, and D.L. Tomasko, Effect of supercritical carbon dioxide on morphology development during polymer blending. *Polym. Eng. Sci.*, 2000. 40(8): p. 1850-1861.
174. Elkovitch, M.D., D.L. Tomasko, and L.J. Lee, Supercritical carbon dioxide assisted blending of polystyrene and poly(methyl methacrylate). *Polym. Eng. Sci.*, 1999. 39(10): p. 2075-2084.
175. Royer, J.R., J.M. DeSimone, and S.A. Khan, High-pressure rheology and viscoelastic scaling predictions of polymer melts containing liquid and supercritical carbon dioxide. *Journal of Polymer Science, Part B: Polymer Physics*, 2001. 39(23): p. 3055-3066.
176. Royer, J.R., Y.J. Gay, J.M. Desimone, and S.A. Khan, High-pressure rheology of polystyrene melts plasticized with CO<sub>2</sub>: experimental measurement and predictive scaling relationships. *Journal of Polymer Science, Part B: Polymer Physics*, 2000. 38(23): p. 3168-3180.
177. Lee, M., C. Tzoganakis, and C.B. Park, Effects of Supercritical CO<sub>2</sub> on the Viscosity and Morphology of Polymer Blends. *Advances in Polymer Technology*, 2000. 19(4): p. 300-311.
178. Gendron, R., L.E. Daigneault, and L.-M. Caron, Rheological Behavior of Polystyrene/Blowing Agent Mixtures. *SPE-ANTEC*, 1996: p. 1118-1122.
179. Gendron, R. and L.E. Daigneault, Rheological Behavior of Mixtures of Various Polymer Melts with CO<sub>2</sub>. *SPE-ANTEC*, 1997: p. 1096-1100.

180. Gendron, R. and A. Correa, The Use of On-Line Rheometry to Characterize Polymer Melts Containing Physical Blowing Agents. *Cellular Polymers*, 1998. 17(2): p. 93-113.
181. Royer, J.R., Y.J. Gay, M. Adam, J.M. DeSimone, and S.A. Khan, Polymer melt rheology with high-pressure CO<sub>2</sub> using a novel magnetically levitated sphere rheometer. *Polymer*, 2002. 43(8): p. 2375-2383.
182. Oh, J.-H., J.T. Lindt, and M.H. Ottoy, A Novel Couette Viscometer for Polymer Solutions in Supercritical Fluids. *SPE-ANTEC*, 2002: p. 1920-23.
183. Doolittle, A.K., Studies in Newtonian Flow. II. The Dependence of the Viscosity of Liquids on Free-Space. *Journal of Applied Physics*, 1951. 22(12): p. 1471-75.
184. Kelley, F.N. and B. F., Viscosity and Glass Temperature Relations for Polymer-Diluent Systems. *Journal of Polymer Science*, 1961. L: p. 549-556.
185. Areerat, S., T. Nagata, and M. Ohshima, Measuring and Modeling of Viscosity Depression Induced by CO<sub>2</sub> Dissolution. *PPS-18 (Polymer Processing Society 18th Annual Meeting) in Guimaraes, Portugal*, June 16-20, 2002.
186. Ladin, D., C.B. Park, S.S. Park, and H.E. Naguib, Measurements and modeling of rheological properties of biodegradable PBS/CO<sub>2</sub> solutions. *Annu. Tech. Conf. - Soc. Plast. Eng.*, 58th(Vol. 2), 2000: p. 1955-1977.
187. Cogswell, F.N., Converging flow of polymer melts in extrusion dies. *Polym. Eng. Sci.*, 1972. 12(1): p. 64-73.
188. Xue, A. and C. Tzoganakis, Rheological Properties of Polystyrene/Supercritical CO<sub>2</sub> Solution from an Extrusion Slit Die. *In preparation*, 2002.
189. Xue, A. and C. Tzoganakis, Measurement of entrance pressure drop of polystyrene/supercritical CO<sub>2</sub> solutions. *SPE-ANTEC*, 2001. 59th(Vol. 1): p. 1022-1026.
190. Abraham, F.F., *Advances in Theoretical Chemistry, Suppl. 1: Homogeneous Nucleation Theory. The Pretransition Theory of Vapor Condensation*. 1974, New York, N. Y: Academic.
191. Laaksonen, A., V. Talanquer, and D.W. Oxtoby, Nucleation: Measurements, Theory, and Atmospheric Applications. *Annu. Rev. Phys. Chem.*, 1995. 46: p. 489-524.
192. Colton, J.S. and N.P. Suh, The nucleation of microcellular thermoplastic foam with additives. Part I. Theoretical considerations. *Polym. Eng. Sci.*, 1987. 27(7): p. 485-92.

193. Colton, J.S. and N.P. Suh, The nucleation of microcellular thermoplastic foam with additives. Part II. Experimental results and discussion. *Polym. Eng. Sci.*, 1987. 27(7): p. 493-9.
194. Colton, J.S. and N.P. Suh, Nucleation of microcellular foam: theory and practice. *Polym. Eng. Sci.*, 1987. 27(7): p. 500-3.
195. Lee, J.G. and R.W. Flumerfelt, A Refined Approach to Bubble Nucleation and Polymer Foaming Process: Dissolved Gas and Cluster Size Effects. *Journal of Colloid and Interfacial Science*, 1996. 184: p. 335-348.
196. Punnathanam, S. and D.S. Corti, Homogeneous Bubble Nucleation in Stretched Fluids: Cavity Formation in the Superheated Lennard-Jones Liquid. *Ind. Eng. Chem. Res.*, 2002. 41: p. 1113-1121.
197. Han, J.H. and C.D. Han, Bubble Nucleation in Polymeric Liquids. I. Bubble Nucleation in Concentrated Polymer Solution. *Journal of Polymer Science: Part B: Polymer Physics*, 1990. 28: p. 711-741.
198. Han, J.H. and C.D. Han, Bubble Nucleation in Polymeric Liquids. II. Theoretical Considerations. *Journal of Polymer Science: Part B: Polymer Physics*, 1990. 28: p. 743-761.
199. Xu, X. and S.-y. Wu, Nucleation Model of Plastics Foam: Analysis and Computer Simulation. *Materials Science & Engineering (Cailiao Kexue Yu Gongcheng)*, 1999. 17(2): p. 39-41, 22.
200. Xu, X. and S.-y. Wu, Analysis of the nucleation of plastic foaming: a new model of nucleation with the theory of thermal fluctuation. *Gaofenzi Cailiao Kexue Yu Gongcheng*, 1999. 15(6): p. 38-40, 44.
201. Ramesh, N.S., D.H. Rasmussen, and G.A. Campbell, The Heterogeneous Nucleation of Microcellular Foams Assisted by the Survival of Microvoids in Polymers Containing Low Glass Transition Particles. Part 1: Mathematical Modeling and Numerical Simulation. *Polym. Eng. Sci.*, 1994. 34(22): p. 1685-1697.
202. Ramesh, N.S., D.H. Rasmussen, and G.A. Campbell, The Heterogeneous Nucleation of Microcellular Foams Assisted by the Survival of Microvoids in Polymers Containing Low Glass Transition Particles. Part 2: Experimental Results and Discussion. *Polym. Eng. Sci.*, 1994. 34(22): p. 1698-1706.
203. Lee, S.-T., Nucleation in Thermoplastic Foam Extrusion. *MD-Vol. 53, Cellular and Microcellular Materials, ASME*, 1994. 53: p. 71-81.

204. Lee, S.-T. and Y. Kim, Shear and Pressure Effects on Extruded Foam Nucleation. *SPE-ANTEC*, 1998: p. 3527-32.
205. Shafi, M.A., K. Joshi, and F.R. W., Bubble size distributions in freely expanded polymer foams. *Chemical Engineering Science*, 1997. 52(4): p. 635-644.
206. Shafi, M.A., J.G. Lee, and R.W. Flumerfelt, Prediction of Cellular Structure in free Expansion Polymer Foam Processing. *Polymer Engineering and Science*, 1996. 36(14): p. 1950-59.
207. Hoshi, K., J.G. Lee, M.A. Shafi, and R.W. Flumerfelt, Prediction of Cellular Structure in free Expansion of Viscoelastic Media. *Journal of Applied Polymer Science*, 1998. 67: p. 1353-68.
208. Amon, M. and C.D. Denson, A Study of the Dynamics of Foam Growth: Analysis of the Growth of Closely Spaced Spherical Bubbles. *Polymer Engineering and Science*, 1984. 24(13): p. 1026-1034.
209. Amon, M. and C.D. Denson, A Study of the Dynamics of Foam Growth: Simplified Analysis and Experimental Results for Bulk Density in Structure Foam Molding. *Polymer Engineering and Science*, 1986. 26(3): p. 255-67.
210. Patel, R.D., Bubble growth in a viscous Newtonian liquid. *Chemical Engineering Science*, 1980. 35: p. 2352-2356.
211. Papanastasiou, A.C., L.E. Scriven, and C.W. Macosko, Bubble growth and collapse in viscoelastic liquids analyzed. *Journal of Non-Newtonian Fluid Mechanics*, 1984. 16: p. 53-75.
212. Arefmenesh, A. and S.G. Advani, Diffusion-induced growth of a gas bubble in a viscoelastic fluid. *Rheologica Acta*, 1991. 30: p. 274-283.
213. Ramesh, N.S., *Foam Growth in Polymers*, in *Foam Extrusion: principles and Practice*, S.-T. Lee, Editor. 2000, Technomic: Lancaster, Basel.
214. Baldwin, D.F., C.B. Park, and N.P. Suh, Microcellular Sheet Extrusion System Process Design Models for Shaping and Cell Growth Control. *Polym. Eng. Sci.*, 1998. 38(4): p. 674-688.
215. Shafi, M.A. and F.R. W., Initial Bubble Growth in Polymer Foam Processes. *Chemical Engineering Science*, 1997. 52(4): p. 627-633.

216. Shimoda, M., I. Tsujimura, M. Tanigaki, and M. Ohshima, Polymeric Foaming Simulation for Extrusion Processes. *Journal of Cellular Plastics*, 2001. 37: p. 517-536.
217. Shimoda, M., M. Tanigaki, and M. Ohshima, Polymeric Foaming simulation for extrusion processes. *Foams 2000, 2nd International Conference on Thermoplastic Foam, Parsippany, New Jersey, Oct. 24-25, 2000*, 2000: p. 91-101.
218. Everage, A.E.J. and R.L. Ballman, Extensional viscosity of amorphous polystyrene. *Journal of Applied Polymer Science*, 1976. 20: p. 1137-1141.
219. Wagner, M.H., H. Bastian, P. Hachmann, J. Meissner, S. Kurzbeck, M. H., and L. F., The strain-hardening behavior of linear and long-chain-branched polyolefin melts in extensional flows. *Rheol. Acta*, 2000. 39: p. 97-109.
220. Sato, Y., M. Yurugi, K. Fujiwara, S. Takishima, and H. Masuoka, Solubilities of carbon dioxide and nitrogen in polystyrene under high temperature and pressure. *Fluid Phase Equilibria*, 1996. 125(1-2, 4th Asian Thermophysical Properties Conference, 1995): p. 129-138.
221. Zhang, Q., M. Xanthos, and S.K. Dey, Parameters affecting the in-line measurement of gas solubility in thermoplastic melts during foam extrusion. *SPE-ANTEC*, 2000: p. 1891-1895.
222. Doroudiani, S., M.T. Kortschot, and C.B. Park, Structure and mechanical properties study of foamed wood fiber/polyethylene composites. *Annu. Tech. Conf. - Soc. Plast. Eng.*, 55th, 1997. 2: p. 2046-2050.
223. Baldwin, D.F., C.B. Park, and N.P. Suh, A processing system for the extrusion of microcellular polymer sheets: shaping and cell growth control. *MD (Am. Soc. Mech. Eng.)*, 1994. 53: p. 85-107.
224. Cheung, L.K., C.B. Park, and A.H. Behraves, ,, Effect of branched structure on the cell morphology of extruded polypropylene foams. I: Cell nucleation. *Annu. Tech. Conf. - Soc. Plast. Eng.*, 54th(Vol. 2), 1996. 2: p. 1941-1947.
225. Pop-Iliev, R., C.B. Park, G. Liu, and F. Liu, Control of the melt strength of polypropylene in rotational foam molding. *Annu. Tech. Conf. - Soc. Plast. Eng.*, 58th(Vol. 2), 2000. 2: p. 1896-1907.
226. Elkovitch, M.D., L.J. Lee, and D.L. Tomasko. *Viscosity reduction of polymers by the addition of supercritical carbon dioxide in polymer processing*. in *Annu. Tech. Conf. - Soc. Plast. Eng.* 1998.

227. Elkovitch, M.D., D.L. Tomasko, and L.J. Lee, Supercritical carbon dioxide assisted blending of polystyrene and poly(methyl methacrylate). *Polym. Eng. Sci.*, 1999. 39(10): p. 2075.
228. Macosko, C.W., *Rheology: Principles, Measurements, and Applications*. 1994: VCH publishers, Inc.
229. Tadmor, Z. and C.G. Gogos, *Principles of Polymer Processing*. 1979, New York, N. Y.: Wiley-Interscience.
230. Han, X., K.W. Koelling, D.L. Tomasko, and L.J. Lee, Process Optimization in Microcellular Foam Extrusion. *Annu. Tech. Conf. - Soc. Plast. Eng.*, 2001. 2: p. 1741-1745.
231. Han, X., K.W. Koelling, D.L. Tomasko, and L.J. Lee, Continuous microcellular polystyrene foam extrusion with supercritical CO<sub>2</sub>. *Polymer Engineering and Science*, 2002. 42(11): p. 2094-2106.
232. Park, C.B., L.K. Cheung, and S.-W. Song, The Effect of Talc on Cell Nucleation in Extrusion Foam Processing of Polypropylene with CO<sub>2</sub> and Isopentane. *Cellular Polymers*, 1998. 17(4): p. 221-251.
233. Chen, L., R. Straff, and X. Wang, Effect of filler size on cell nucleation during foaming process. *ANTEC - SPE*, 2001. 2: p. 1732-1736.
234. Zeng, C. and L.J. Lee, Polymer layered silicate nanocomposites prepared by a two-stage method. *SPE-ANTEC*, 2001: p. 2213-2217.
235. Zeng, C., X. Han, and L.J. Lee, Preparation and Cell Morphology of Poplymer Clay Nanocomposite Foams by Carbon Dioxide. *Preparation and Cell Morphology of Poplymer Clay Nanocomposite Foams by Carbon Dioxide*, Paper in Preparation.
236. Berens, A.R., G.S. Huvard, R.W. Korsmeyer, and F.W. Kung, Application of compressed carbon dioxide in the incorporation of additives into polymers. *J. Appl. Polym. Sci.*, 1992. 46(2): p. 231-242.
237. Vaia, R.A. and E.P. Giannelis, *Macromolecules*, 1997. 30: p. 7990.
238. Vaia, R.A. and E.P. Giannelis, *Macromolecules*, 1997. 30: p. 8000.
239. Balazs, A., C. Singh, and E. Zhulina, *Macromolecules*, 1998. 31: p. 8370.

240. Han, X., A.R. Baxter, K.W. Koelling, D.L. Tomasko, and L.J. Lee, Influences of solubility and viscosity in the polystyrene/CO<sub>2</sub> microcellular foaming extrusion. *SPE-ANTEC*, 2002. *60th*(Vol. 2): p. 1910-1914.

## APPENDIX A

### MIXING RULES OF THE SANCHEZ-LACOMBE EQUATION OF STATE FOR A BINARY SYSTEM

Using the Sanchez-Lacombe equation of state (See Eq. 2.1 & Eq. 2.2), the solubility of CO<sub>2</sub> in polystyrene (PS) was calculated in Chapter 3 and the specific volume (i.e., density) of PS or PS/CO<sub>2</sub> solution was calculated in Chapter 6. In these calculations, the characteristic parameters of the PS/CO<sub>2</sub> solution, such as close-packed molar volume  $v^*$ , pressure  $P^*$ , temperature  $T^*$ , and the lattice size  $r^*$ , are given by the following mixing rules [136, 137] based on the corresponding characteristic parameters of the individual substance.

$$v^* = \phi_i^0 v_i^* + \phi_j^0 v_j^* \quad (\text{A.1})$$

$$\phi_i^0 = \frac{m_i / (\rho_i^* v_i^*)}{\sum_j m_j / (\rho_j^* v_j^*)} \quad (\text{A.2})$$

$$P^* = \sum_j \sum_i \phi_i \phi_j P_{ij}^* \quad (\text{A.3})$$

$$P_{ij}^* = \{P_i^* P_j^*\}^{1/2} (1 - \delta_{ij}) \quad (\text{A.4})$$

$$\phi_i = \frac{m_i / (\rho_i^*)}{\sum_j m_j / (\rho_j^*)} \quad (\text{A.5})$$

$$T^* = \left\{ \frac{\phi_i / \tilde{T}_i + \gamma \phi_j / \tilde{T}_j}{\phi_i + \gamma \phi_j} - \phi_i \phi_j X \right\} T \quad (\text{A.6})$$

$$\gamma = \frac{v_i^*}{v_j^*} \quad (\text{A.7})$$

$$X = \frac{(P_i^* + P_j^* - 2P_{ij}^*) v^*}{RT} \quad (\text{A.8})$$

$$r = \frac{r_i^0 x_i v_i^* + r_j^0 x_j v_j^*}{v^*} \quad (\text{A.9})$$

In these equations,  $\delta_{ij}$  is the binary interaction parameter;  $x_i$  and  $x_j$  are the mole fractions;  $m_i$  and  $m_j$  are the weight fractions;  $\phi_i$  and  $\phi_j$  are the volume fractions. For a binary system consisting of CO<sub>2</sub> and polystyrene, the chemical potential of CO<sub>2</sub> in the solution should be equal to that of pure gas phase when the system is at equilibrium.

$$\mu_1^{mix}(T, P, \phi_1) = \mu_1^G(T, P) \quad (\text{A.10})$$

The chemical potential of CO<sub>2</sub> is then calculated by

$$\begin{aligned} \mu_1 = & RT \{ \ln \phi_1 + (1 - r_1 / r_2) \phi_2 + r_1^0 \tilde{\rho} X_1 \phi_2^2 \} \\ & + r_1^0 RT \{ -\tilde{\rho} / \tilde{T}_1 + \tilde{P}_1 \tilde{v} / \tilde{T}_1 \\ & + \tilde{v} [(1 - \tilde{\rho}) \ln(1 - \tilde{\rho}) + \tilde{\rho} \ln \tilde{\rho} / r_1^0] \} \end{aligned} \quad (\text{A.11})$$

$$X_1 = \frac{(P_1^* + P_2^* - 2P_{12}^*) v_1^*}{RT}$$

Based on these equations, two computational codes in Fortran were compiled. One is to calculate  $\delta_j$  when the solubility is known as a function of temperature and pressure (See Appendix B). The other is to calculate the solubility when  $\delta_j$  is known (See Appendix C).

## APPENDIX B

### FORTRAN CODE TO DETERMINE $\delta_{IJ}$ BY KNOWING SOLUBILITY

```
c *****
c * By using Sanchez-Lacombe model, the interaction factor delta
c * can be evaluated by this program at a certain temperature Tc
c * and different pressures P(100).
c * 1 -- CO2, 2 -- polymer, 3 -- mixture of CO2 and polymer.
c * Pt,Tt,Rout -- reduced pressure, temp, and density
c * Ps,Ts,Rous -- charateristic parameters in the EOS
c * vs -- closed packed mer volume
c * r0 -- the number of sites occupied by an r-mer
c * pMu1,mMu1 -- chemical potential of CO2 in pure & mixed state*
c * m -- weight fration, phi -- volume fraction **
c * step1, step2: increase for delta and weight ratio
c * error1,error2: error control for weight ratio and chem. poten.
c * time1, time2: do-loop calculation times control

c main program

real T,MW(3),Ps(3),Ts(3),Rous(3),error1,delta,step1,Tc
real P(100),m1(100),m2(100),RouL(100),RouV(100),expm1(100)
real probe1,probe2,sum
integer count1,time1

open(210,file='psT200delta2.dat',status='new')

c input the working temperature and characteristic parameters of EOS

Tc=200
T=273.15+Tc
Ps(1)=5670.0*101325.0
Ps(2)=3523.0*101325.0
Ps(3)=0.0
Ts(1)=305.0
Ts(2)=735.0
Ts(3)=0.0
Rous(1)=1.510e3
Rous(2)=1.105e3
Rous(3)=0.0
```

```
MW(1)=44.0e-3
MW(2)=500.0
```

- c input the experimental pressures (Pa) and weight ratios.

```
N=4
P(1)=729*6894.757
P(2)=1090*6894.757
P(3)=1453*6894.757
c P(4)=1816*6894.757
P(4)=2178*6894.757
```

- ```
expm1(1)=0.0235
expm1(2)=0.0424
expm1(3)=0.0429
c expm1(4)=0.0701
expm1(4)=0.0760
```

- c looking for a delta between -1 and 1 with a smallest step of 1e-4

```
error1=0.00001
count1=1
delta=-1.0
step1=0.1
time1=21

do 300, j=1,4
  sum=error1+1
  probe2=sum+1
  do while(sum.gt.error1.and.count1.le.time1)
    count1=count1+1
    call content(N,T,P,delta,Ps,Ts,Rous,MW,m1,m2,RouV,RouL)
    sum=0
    do 150, i=1,N
      sum=sum+(m1(i)-expm1(i))**2
150    continue
    WRITE(210,*)'SUM=',sum,'delta=',delta,m1(5),expm1(5)
    If(sum.lt.probe2) then
      probe1=delta
      probe2=sum
    else
      endif
      delta=delta+step1
    end do
    delta=probe1-step1
    step1=step1*0.1
    count1=1
300 continue
  delta=probe1
  call content(N,T,P,delta,Ps,Ts,Rous,MW,m1,m2,RouV,RouL)
```

- c Outputs

```
WRITE(210,*)'SUM=',probe2,'delta=',probe1
```

```

write(210,*)' P (psi) T (C) expm1 m1 delta'
do 208,i=1,N
  write(210,215)P(i)/6.8948e3,T-273.15,expm1(i),m1(i),delta
208 continue
215 format(1X,F9.2,2X,F6.2,2X,F9.7,2X,F9.7,2X,F10.6)
write(210,*)' P(psi) m1 m2 Rouv RouL'
do 155, i=1,N
  write(210,156)P(i)/6.8948e3,m1(i),m2(i),RouV(i),RouL(i)
155 continue
156 format(1X,F9.2,2X,F9.7,2X,F9.7,2X,F10.5,2X,F10.5)
end

```

c \*Here weight ratio will be calculated with a given delta\*

```

Subroutine content(N,T,P,delta,Ps,Ts,Rous,MW,m1,m2,RouV,RouL)
real T,Ptr,MW(3),Ps(3),Ts(3),Rous(3),vs(3),r0(3),Pt,Tt,Rout
real phi(2),pMu1,mMu1,delta,P12
real Pstr,MWtr,vstr,r0tr,Roustr,Tstr,step2,error2,Tc
real P(100),m1(100),m2(100),m(2),RouL(100),RouV(100)
integer count,time,N

Do 120, i=1,100
  m1(i)=0.000001
  m2(i)=1-m1(i)
  RouL(i)=0
  RouV(i)=0
120 continue

Do 5, I=1,2
  Pstr=Ps(I)
  Tstr=Ts(I)
  Roustr=Rous(I)
  MWtr=MW(I)
  call convert(1,Pstr,Tstr,Roustr,MWtr,r0tr,vstr)
  r0(I)=r0tr
  vs(I)=vstr
5 continue

error2=200.0
count=1
time=5001
step2=1.0/(time-1)

do 145,i=1,N
  Ptr=P(i)
  m(1)=1.0e-6
  m(2)=1-m(1)

```

c To obtain the chemical potential for the pure CO<sub>2</sub> phase

```

Pstr=Ps(1)
Tstr=Ts(1)
Roustr=Rous(1)
call reducing(1,Ptr,T,Rou,Pstr,Tstr,Roustr,Pt,Tt,Rout)

```

```

r0tr=r0(1)
call density(0,Pt,Tt,Rout,r0tr)
call reducing(2,Ptr,T,Rou,Pstr,Tstr,Roustr,Pt,Tt,Rout)
RouV(i)=Rou
P12=0.0
phi(1)=1.0
phi(2)=0.0
call chempo(T,Ptr,Rout,Ts,Ps,P12,vs,phi,r0,pMu1)
mMu1=pMu1+error2*10.0
do while(ABS(pMu1-mMu1).gt.error2.and.count.lt.time)
  count=count+1

```

c To get the CO<sub>2</sub> chemical potential in the mixture

```

  call mixing(Ps,Ts,Rous,MW,vs,m,delta,T,r0,P12,phi)
  Pstr=Ps(3)
  Tstr=Ts(3)
  call reducing(1,Ptr,T,Rou,Pstr,Tstr,Roustr,Pt,Tt,Rout)
  r0tr=r0(3)
  call density(1,Pt,Tt,Rout,r0tr)
  call chempo(T,Ptr,Rout,Ts,Ps,P12,vs,phi,r0,mMu1)
8   m(1)=m(1)+step2
   m(2)=1-m(1)
  end do
  MWtr=MW(3)
  vstr=vs(3)
  call convert(2,Pstr,Tstr,Roustr,MWtr,r0tr,vstr)
  call reducing(2,Ptr,T,Rou,Pstr,Tstr,Roustr,Pt,Tt,Rout)
  RouL(i)=Rou
  m1(i)=m(1)
  m2(i)=m(2)
  count=1
145 continue
  return
  end

```

c \* Here all the characteristic parameters will be calculated.

```

Subroutine convert(N,Ps,Ts,Rous,MW,r0,vs)
real Ps,Ts,Rous,MW,r0,vs,epslns
integer N
gasR=8.314
If(N.eq.1) then
  epslns=gasR*Ts
  vs=epslns/Ps
  r0=MW/(Rous*vs)
else
  epslns=gasR*Ts
  vs=epslns/Ps
  Rous=MW/(r0*vs)
end If
return
end

```

c \* Here transfer the T,P to be reduced value.

```

subroutine reducing(N,P,T,Rou,Ps,Ts,Rous,Pt,Tt,Rout)
real P,T,Ps,Ts,Rous,Pt,Tt,Rout,Rou
integer N
If(N.eq.1) then
  Pt=P/Ps
  Tt=T/Ts
else
  Rou=Rout*Rous
end If
return
end

```

c \* Mixing rules for vstar, Pstar, Tstar, and rstar.

```

subroutine mixing(Ps,Ts,Rous,MW,vs,m,delta,T,r0,P12,phi)
real Ps(3),Ts(3),Rous(3),MW(3),m(2),delta,T,r0(3),P12,phi(2)
real vs(3),sum,P(2,2),gasR,Tt(2),phi0(2)
gasR=8.314
sum=0
do 10, i=1,2
  sum=sum+m(i)/(Rous(i)*vs(i))
10 continue
do 20, i=1,2
  phi0(i)=m(i)/(Rous(i)*vs(i))/sum
20 continue
vs(3)=0.0
do 25,i=1,2
  vs(3)=vs(3)+phi0(i)*vs(i)
25 continue

sum=0
do 30, i=1,2
  sum=sum+m(i)/Rous(i)
30 continue
do 40, i=1,2
  phi(i)=m(i)/Rous(i)/sum
40 continue
P(1,2)=(Ps(1)*Ps(2))*0.5*(1-delta)
P(2,1)=P(1,2)
P(1,1)=Ps(1)
P(2,2)=Ps(2)
P12=P(1,2)
Ps(3)=0
Do 60, j=1,2
  Do 50, i=1,2
    Ps(3)=Ps(3)+phi(i)*phi(j)*P(i,j)
50 continue
60 continue
X=(Ps(1)+Ps(2)-2*P(1,2))*vs(3)/(gasR*T)
gama=vs(1)/vs(2)
do 70,i=1,2
  Tt(i)=T/Ts(i)

```

```

70  continue
    Ts(3)=(phi(1)/Tt(1)+gama*phi(2)/Tt(2))/(phi(1)+gama*phi(2))
    Ts(3)=(Ts(3)-phi(1)*phi(2)*X)*T

    sum=0
    do 80, i=1,2
        sum=sum+m(i)/MW(i)
80  continue
    r0(3)=0
    do 85,i=1,2
        r0(3)=r0(3)+r0(i)*vs(i)*(m(i)/MW(i)/sum)/vs(3)
85  continue
    MW(3)=1/(m(1)/MW(1)+m(2)/MW(2))
    return
end

```

c \* To obtain the chemical potential of CO<sub>2</sub> with diff. contents.

```

subroutine chempo(T,P,Rout,Ts,Ps,P12,vs,phi,r0,Mu1)
real Ps(3),vs(3),phi(3),r0(3),T,Ts(3),Rout,Mu1
real vt,gasR,P12,Tt1,Term1,Term2,Pt1,X1
gasR=8.314
vt=1/Rout
Tt1=T/Ts(1)
Pt1=P/Ps(1)
X1=(Ps(1)+Ps(2)-2*P12)*vs(1)/(gasR*T)
Term1=(log(phi(1))/log(2.718))+r0(1)*Rout*X1*phi(2)**2
Term1=Term1+(1-r0(1)*vs(1)/(r0(2)*vs(2)))*phi(2)
Term2=(1-Rout)*log(1-Rout)/log(2.718)
Term3=Rout*(log(Rout)/log(2.718))/r0(1)
Term2=-Rout/Tt1+Pt1*vt/Tt1+vt*(Term2+Term3)
Mu1=gasR*T*(Term1+r0(1)*Term2)
return
end

```

c \* To solve the EOS and get three reduced densities which should  
c \* be bw. 0 & 1. Attn: F(0)>0.

```

subroutine density(N,Pt,Tt,Rout,r)
real Pt,Tt,Rout,r,root(3),step,tol,F
integer N

Rout=0.001
step=0.0001
tol=0.00001

Do 100,i=1,3
    root(i)=0
    Do 105, j=1,10001
        If(Rout.le.1.0) then
            F=1.0-exp(-(Rout**2+Pt)/Tt-(1-1/r)*Rout)-Rout
            If(ABS(F).gt.tol) then
                If((((i.eq.1).or.(i.eq.3)).and.(F.lt.0))
+                 .or.((i.eq.2).and.(F.gt.0))) then

```

```

        Rout=Rout-step
        step=step*0.1
        Rout=Rout+step
    else
        Rout=Rout+step
    endif
else
    root(i)=Rout
    step=0.0001
    Rout=Rout+step
    goto 100
endif
else
    root(i)=Rout
    step=0.0001
    Rout=Rout+step
    goto 100
endif
105 continue
100 continue

If (N.eq.1) then
    Do 110, i=1,3
        If (root(i).gt.1.0) then
            root(i)=-1.0
        else
            endif
110 continue
        Rout=amax1(root(1),root(2),root(3))
    else
        Rout=amin1(root(1),root(2),root(3))
        If(Rout.gt.1.0) then
            Rout=-1.0
        else
            endif
        endif
    endif
return
end

```

## APPENDIX C

### FORTRAN CODE TO COMPUTE SOLUBILITY BY KNOWING $\delta_{LJ}$

```
c *****
c * By using Sanchez-Lacombe model, solubility can be solved
c * at a certain temperature Tc
c * and different pressures P(100).
c * 1 -- CO2, 2 -- polymer, 3 -- mixture of CO2 and polymer.
c * Pt,Tt,Rout -- reduced pressure, temp, and density
c * Ps,Ts,Rous -- charateristic parameters in the EOS
c * vs -- closed packed mer volume
c * r0 -- the number of sites occupied by an r-mer
c * pMu1,mMu1 -- chemical potential of CO2 in pure & mixed state*
c * m -- weight fration, phi -- volume fraction **
c * step1, step2: increase for delta and weight ratio
c * error1,error2: error control for weight ratio and chem. poten.
c * time1, time2: do-loop calculation times control

c   main program

      real T,MW(3),Ps(3),Ts(3),Rous(3),delta,Tc
      real P(100),m1(100),m2(100),RouL(100),RouV(100)

      open(210,file='psTPw.dat',status='new')

c   input the working temperature and characteristic parameters of EOS

      Tc=0
      T=273.15+Tc
      Ps(1)=5670.0*101325.0
      Ps(2)=3523.0*101325.0
      Ps(3)=0.0
      Ts(1)=305.0
      Ts(2)=735.0
      Ts(3)=0.0
      Rous(1)=1.510e3
      Rous(2)=1.105e3
      Rous(3)=0.0
      MW(1)=44.0e-3
      MW(2)=500.0
```

c input the experimental pressures (Pa) and weight ratios.

```
P(1)=6894.757*100
N=50
delta=0.023611
do 802, j=2,N
    P(j)=P(j-1)+6894.757*100
802 continue

write(210,*)`delta=', delta
do 801, k=1,30

    call content(N,T,P,delta,Ps,Ts,Rous,MW,m1,m2,RouV,RouL)

    write(210,*)` P (psi)  T (C)  m1, m2  RouV  RouL`
    do 208,i=1,N
        write(210,215)P(i)/6.8948e3,T-273.15,m1(i),m2(i),RouV(i),RouL(i)
208    continue
215    format(1X,F6.1,1X,F5.1,2(1X,F9.7),2(2X,F10.5))

        T=T+10
801 continue
end
```

c \*Here weight ratio will be calculated with a given delta\*

```
Subroutine content(N,T,P,delta,Ps,Ts,Rous,MW,m1,m2,RouV,RouL)
real T,Ptr,MW(3),Ps(3),Ts(3),Rous(3),vs(3),r0(3),Pt,Tt,Rout
real phi(2),pMu1,mMu1,delta,P12
real Pstr,MWtr,vstr,r0tr,Roustr,Tstr,step2,error2,Tc
real P(100),m1(100),m2(100),m(2),RouL(100),RouV(100)
integer count,time,N

Do 120, i=1,100
    m1(i)=0.000001
    m2(i)=1-m1(i)
    RouL(i)=0
    RouV(i)=0
120 continue

Do 5, I=1,2
    Pstr=Ps(I)
    Tstr=Ts(I)
    Roustr=Rous(I)
    MWtr=MW(I)
    call convert(1,Pstr,Tstr,Roustr,MWtr,r0tr,vstr)
    r0(I)=r0tr
    vs(I)=vstr
5    continue

error2=200.0
count=1
time=5001
```

```

step2=1.0/(time-1)

do 145,i=1,N
  Ptr=P(i)
  m(1)=1.0e-6
  m(2)=1-m(1)
c To obtain the chemical potential for the pure CO2 phase
  Pstr=Ps(1)
  Tstr=Ts(1)
  Roustr=Rous(1)
  call reducing(1,Ptr,T,Rou,Pstr,Tstr,Roustr,Pt,Tt,Rout)
  r0tr=r0(1)
  call density(0,Ptr,Tt,Rout,r0tr)
  call reducing(2,Ptr,T,Rou,Pstr,Tstr,Roustr,Pt,Tt,Rout)
  RouV(i)=Rou
  P12=0.0
  phi(1)=1.0
  phi(2)=0.0
  call chempo(T,Ptr,Rout,Ts,Ps,P12,vs,phi,r0,pMu1)
  mMu1=pMu1+error2*10.0
  do while(ABS(pMu1-mMu1).gt.error2.and.count.lt.time)
    count=count+1
c To get the CO2 chemical potential in the mixture
  call mixing(Ps,Ts,Rous,MW,vs,m,delta,T,r0,P12,phi)
  Pstr=Ps(3)
  Tstr=Ts(3)
  call reducing(1,Ptr,T,Rou,Pstr,Tstr,Roustr,Pt,Tt,Rout)
  r0tr=r0(3)
  call density(1,Ptr,Tt,Rout,r0tr)
  call chempo(T,Ptr,Rout,Ts,Ps,P12,vs,phi,r0,mMu1)
8   m(1)=m(1)+step2
   m(2)=1-m(1)
  end do
  MWtr=MW(3)
  vstr=vs(3)
  call convert(2,Pstr,Tstr,Roustr,MWtr,r0tr,vstr)
  call reducing(2,Ptr,T,Rou,Pstr,Tstr,Roustr,Pt,Tt,Rout)
  RouL(i)=Rou
  m1(i)=m(1)
  m2(i)=m(2)
  count=1
145 continue
  return
end

```

c \* Here all the characteristic parameters will be calculated.

```

Subroutine convert(N,Ps,Ts,Rous,MW,r0,vs)
real Ps,Ts,Rous,MW,r0,vs,epsilons
integer N
gasR=8.314
If(N.eq.1) then
  epsilons=gasR*Ts

```

```

    vs=epslns/Ps
    r0=MW/(Rous*vs)
else
    epslns=gasR*Ts
    vs=epslns/Ps
    Rous=MW/(r0*vs)
end If
return
end

```

c \* Here transfer the T,P to be reduced value.

```

subroutine reducing(N,P,T,Rou,Ps,Ts,Rous,Pt,Tt,Rout)
real P,T,Ps,Ts,Rous,Pt,Tt,Rout,Rou
integer N
If(N.eq.1) then
    Pt=P/Ps
    Tt=T/Ts
else
    Rou=Rout*Rous
end If
return
end

```

c \* Mixing rules for vstar, Pstar, Tstar, and rstar.

```

subroutine mixing(Ps,Ts,Rous,MW,vs,m,delta,T,r0,P12,phi)
real Ps(3),Ts(3),Rous(3),MW(3),m(2),delta,T,r0(3),P12,phi(2)
real vs(3),sum,P(2,2),gasR,Tt(2),phi0(2)
gasR=8.314
sum=0
do 10, i=1,2
    sum=sum+m(i)/(Rous(i)*vs(i))
10 continue
do 20, i=1,2
    phi0(i)=m(i)/(Rous(i)*vs(i))/sum
20 continue
vs(3)=0.0
do 25,i=1,2
    vs(3)=vs(3)+phi0(i)*vs(i)
25 continue

sum=0
do 30, i=1,2
    sum=sum+m(i)/Rous(i)
30 continue
do 40, i=1,2
    phi(i)=m(i)/Rous(i)/sum
40 continue
P(1,2)=(Ps(1)*Ps(2))**0.5*(1-delta)
P(2,1)=P(1,2)
P(1,1)=Ps(1)
P(2,2)=Ps(2)
P12=P(1,2)

```

```

Ps(3)=0
Do 60, j=1,2
  Do 50, i=1,2
    Ps(3)=Ps(3)+phi(i)*phi(j)*P(i,j)
50  continue
60  continue
X=(Ps(1)+Ps(2)-2*P(1,2))*vs(3)/(gasR*T)
gama=vs(1)/vs(2)
do 70,i=1,2
  Tt(i)=T/Ts(i)
70  continue
Ts(3)=(phi(1)/Tt(1)+gama*phi(2)/Tt(2))/(phi(1)+gama*phi(2))
Ts(3)=(Ts(3)-phi(1)*phi(2)*X)*T

sum=0
do 80, i=1,2
  sum=sum+m(i)/MW(i)
80  continue
r0(3)=0
do 85,i=1,2
  r0(3)=r0(3)+r0(i)*vs(i)*(m(i)/MW(i)/sum)/vs(3)
85  continue
MW(3)=1/(m(1)/MW(1)+m(2)/MW(2))
return
end

```

c \* To obtain the chemical potential of CO<sub>2</sub> with diff. contents.

```

subroutine chempo(T,P,Rout,Ts,Ps,P12,vs,phi,r0,Mu1)
real Ps(3),vs(3),phi(3),r0(3),T,Ts(3),Rout,Mu1
real vt,gasR,P12,Tt1,Term1,Term2,Pt1,X1
gasR=8.314
vt=1/Rout
Tt1=T/Ts(1)
Pt1=P/Ps(1)
X1=(Ps(1)+Ps(2)-2*P12)*vs(1)/(gasR*T)
Term1=(log(phi(1))/log(2.718))+r0(1)*Rout*X1*phi(2)**2
Term1=Term1+(1-r0(1)*vs(1)/(r0(2)*vs(2)))*phi(2)
Term2=(1-Rout)*log(1-Rout)/log(2.718)
Term3=Rout*(log(Rout)/log(2.718))/r0(1)
Term2=-Rout/Tt1+Pt1*vt/Tt1+vt*(Term2+Term3)
Mu1=gasR*T*(Term1+r0(1)*Term2)
return
end

```

c \* To solve the EOS and get three reduced densities which should  
c \* be bw. 0 & 1. Attn: F(0)>0.

```

subroutine density(N,Pt,Tt,Rout,r)
real Pt,Tt,Rout,r,root(3),step,tol,F
integer N

Rout=0.001
step=0.0001

```

```

tol=0.00001

Do 100,i=1,3
  root(i)=0
  Do 105, j=1,10001
    If(Rout.le.1.0) then
      F=1.0-exp(-(Rout**2+Pt)/Tt-(1-1/r)*Rout)-Rout
      If(ABS(F).gt.tol) then
        If((((i.eq.1).or.(i.eq.3)).and.(F.lt.0))
+       .or.((i.eq.2).and.(F.gt.0))) then
          Rout=Rout-step
          step=step*0.1
          Rout=Rout+step
        else
          Rout=Rout+step
        endif
      else
        root(i)=Rout
        step=0.0001
        Rout=Rout+step
        goto 100
      endif
    else
      root(i)=Rout
      step=0.0001
      Rout=Rout+step
      goto 100
    endif
  105  continue
100  continue

  If (N.eq.1) then
    Do 110, i=1,3
      If (root(i).gt.1.0) then
        root(i)=-1.0
      else
        endif
    110  continue
    Rout=amax1(root(1),root(2),root(3))
  else
    Rout=amin1(root(1),root(2),root(3))
    If(Rout.gt.1.0) then
      Rout=-1.0
    else
      endif
    endif
  return
end

```

## APPENDIX D

### DEVELOPMENT OF VISCOSITY PREDICTION MODEL

Carbon dioxide affects the viscosity of polymer melts following a similar mechanism to the temperature and pressure, predominantly through a change in free volume. Doolittle's equation relates the zero shear viscosity,  $\eta_0$ , to the free volume fraction as following:

$$\eta_0 = A \exp\left(\frac{B}{f(T, P, \omega_g)}\right) \quad (\text{D.1})$$

where A and B are unique constant parameters for the polymer.  $f(T, P, \omega_g)$  denotes the free volume fraction, a function of temperature, pressure, and CO<sub>2</sub> concentration:

$$f(T, P, \omega_g) = \frac{V(T, P, \omega_g) - V^0(\omega_g)}{V(T, P, \omega_g)} \quad (\text{D.2})$$

Here,  $V(T, P, \omega_g)$  is the specific volume of the polymer at temperature T, pressure P, and gas concentration  $\omega_g$ . It can be calculated from the Sanchez-Lacombe equation of state (Equation 2.1 & 2.2).  $V^0$  is the hardcore specific volume of the binary mixture and can be calculated by a weight average of the hardcore specific volume of CO<sub>2</sub> ( $V_{CO_2}^o$ ) and polymer ( $V_{poly}^o$ ):

$$V^o(w_g) = w_g V_{CO_2}^o + (1 - w_g) V_{poly}^o \quad (D.3)$$

As shown in reference [170, 185],  $V_{CO_2}^o$  was selected to be  $0.589 \text{ cm}^3/\text{g}$  and  $V_{poly}^o$  was evaluated by fitting the shear viscosity data with a simplified Cross-Carreau Model. The Cross-Carreau Model is expressed as

$$\eta(\dot{\gamma}) = \frac{\eta_0}{\left(1 + \left(\frac{\eta_0 \dot{\gamma}}{\tau}\right)^a\right)^{\frac{1-n}{a}}} \quad (D.4)$$

At high shear rates when  $\frac{\eta_0 \dot{\gamma}}{\tau} \gg 1$ , Equation (D.4) can be simplified as

$$\eta(\dot{\gamma}) \cong \eta_0^n \left(\frac{\dot{\gamma}}{\tau}\right)^{n-1} \quad (D.5)$$

where  $\dot{\gamma}$  is the shear rate,  $n$ ,  $\tau$  and  $a$  are constants determined by the material.

By substituting Equation (D.1) into Equation (D.5), a new equation can be obtained by rearrangement:

$$\eta = \exp((n \ln A - (n-1) \ln \tau) + \frac{nB}{f(T, P, w_g)}) \dot{\gamma}^{n-1} \quad (D.6)$$

For pure polymer at atmospheric pressure without gas sorption, the free volume fraction can be expressed as:

$$f(T) = 1 - \frac{V_{poly}^0}{V(T)} = 1 - V_{poly}^0 \rho(T) \quad (D.7)$$

Therefore, we can fit a viscosity curve measured at atmospheric pressure without gas sorption with Equation (D.6) combined with Equation (D.7) to determine the parameters  $A$ ,  $B$ ,  $n$ ,  $\tau$ , and  $V_{poly}^o$ . Density ( $\rho(T)$ ) can be calculated from Sanchez-Lacombe equation of state for pure polymer at atmospheric pressure.

Note that the parameters  $A$ ,  $B$ ,  $n$ , and  $\tau$  are not affected by temperature, pressure, and CO<sub>2</sub> concentration; they are all included into the free volume fraction and then the zero shear viscosity.

By substituting all the parameters  $A$ ,  $B$ ,  $n$ ,  $\tau$ , and the calculated  $f(T, P, \omega_g)$  from Equation (D.2) back into equation (D.6), viscosities at the specific temperature, pressure, and CO<sub>2</sub> concentration ( $T, P, w_g$ ) can be predicted at various shear rates.

## **APPENDIX E**

### **DESIGN OF THE CAPILLARY FOAMING DIE**

The first step of this study was to design a capillary die to realize the high pressure drop and pressure drop rate. The design procedure follows the steps below:

1) Pressure drop and pressure drop rate

Microcellular foaming requires a high value for both the pressure drop and the pressure drop rate. By summarizing the information in the literature, the pressure drop and the pressure drop rate were designed to be 4000 psi and  $10^9$  pa/sec, respectively.

2) Flow rate

The flow rate was selected according to the processing capability of the single screw extruder (HAAKE 252P), which is from 1 to 10 lb/hr. We simply picked up the lowest value, 1 lb/hr, to ensure the required pressure drop and pressure drop rate can be achieved even at the lowest flow rate.

3) Rheological behavior of the polymer melt

Only the shear-thinning behavior of the polymer melt was considered, which follows the power law model:

$$\eta = m \dot{\gamma}^{n-1} \quad (\text{E.1})$$

where  $\eta$  is the shear viscosity,  $\dot{\gamma}$  is the shear rate,  $n$  is the power law index, and  $m$  is a constant.

4) Dimension of the die

The relationship between the pressure drop and the dimension of the capillary die was derived from the equations of motion simplified for the power law model fluid.

$$\Delta P = \frac{2mL}{R} \left[ \frac{(1+3n)Q}{n\pi R^3} \right]^n \quad (\text{E.2})$$

where  $\Delta P$  is the pressure drop,  $L$  is the length of the die,  $R$  is the radius, and  $Q$  is the volumetric flow rate. The pressure drop rate was determined from the residence time  $\Delta t$ :

$$\frac{\Delta P}{\Delta t} = \frac{\Delta P}{L/v} = \frac{\Delta P}{L/(Q/\pi R^2)} = 2m \left[ \frac{(1+3n)}{n} \right]^n \left[ \frac{Q}{\pi R^3} \right]^{n+1} \quad (\text{E.3})$$

Note that the pressure drop rate is independent of the length of the die and only decided by the radius. A similar result can be obtained for the slit die that the pressure drop rate is independent of the length and only decided by the opening of the rectangular channel.

During the design, we also need to consider the manufacturing limit on dimensions. Usually it is hard to make a long capillary die with a very small diameter.

The calculation results are shown in Figure E.1. Both the pressure drop and pressure drop rate reduces quickly with the increase of the die diameter. To get a pressure drop rate higher than  $10^9$  Pa/sec, a diameter smaller than 0.5 mm is needed. Considering the difficulties in manufacturing, the length of the die was selected to be 10 mm, which can satisfy the pressure requirement ( $>4000$  psi). In Figure E.2, both quantities were calculated again at different mass flow rates to check the design flexibility. Finally, a capillary die with a diameter of 0.5 mm and a length of 10 mm was selected. Figure E.3 gives a schematic of the designed capillary die.

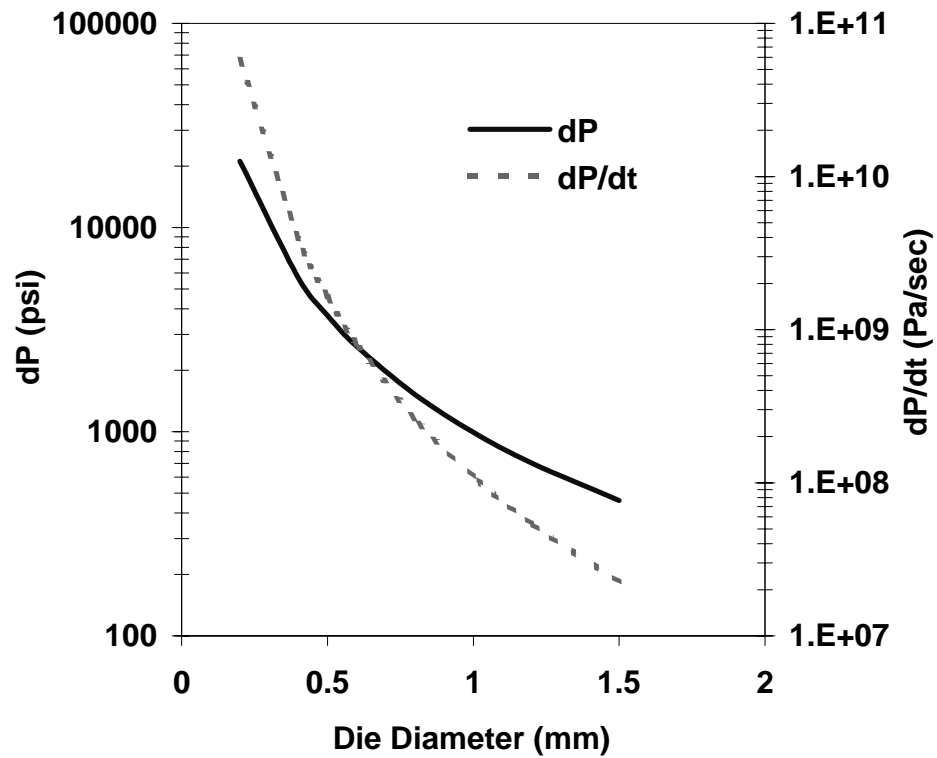


Figure E.1. Pressure drop and pressure drop rate with different diameter of the capillary die (PS, Power Law Model:  $m=17,420 \text{ Pa}\cdot\text{s}^{0.30}$ ,  $n=0.30$ , length  $L=10 \text{ mm}$ ,  $q = 1 \text{ lb/hr}$ ).

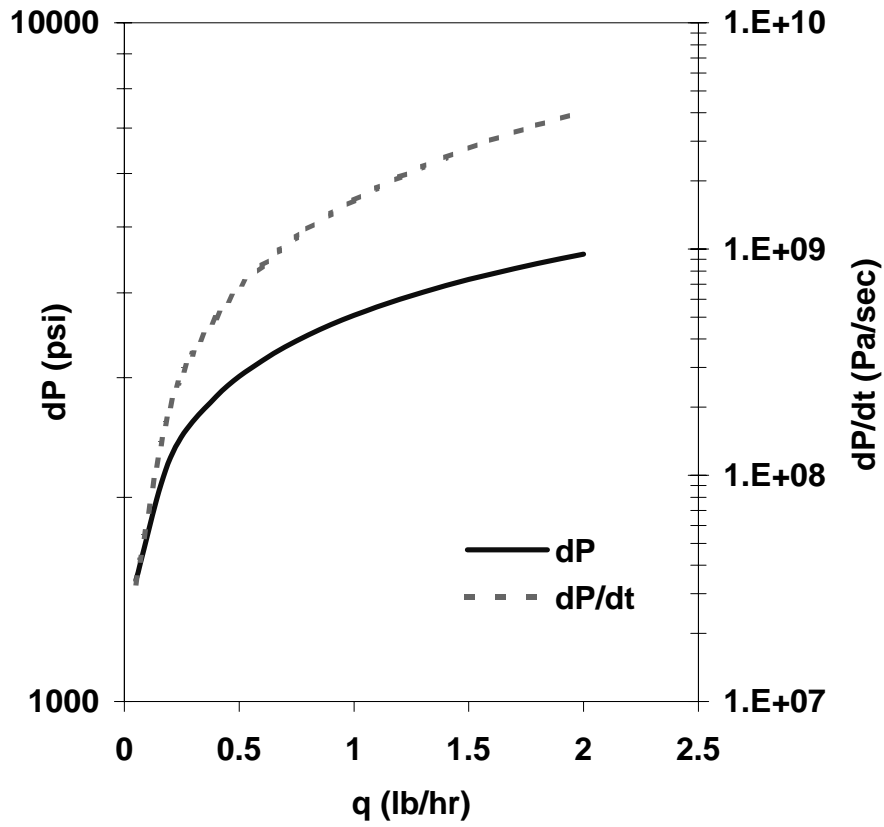


Figure E.2. Pressure drop and pressure drop rate with different flow rate (PS, Power Law Model:  $m=17,420 \text{ Pa}\cdot\text{s}^{0.30}$ ,  $n=0.30$ ,  $L=10 \text{ mm}$ ,  $D = 0.5 \text{ mm}$ ).

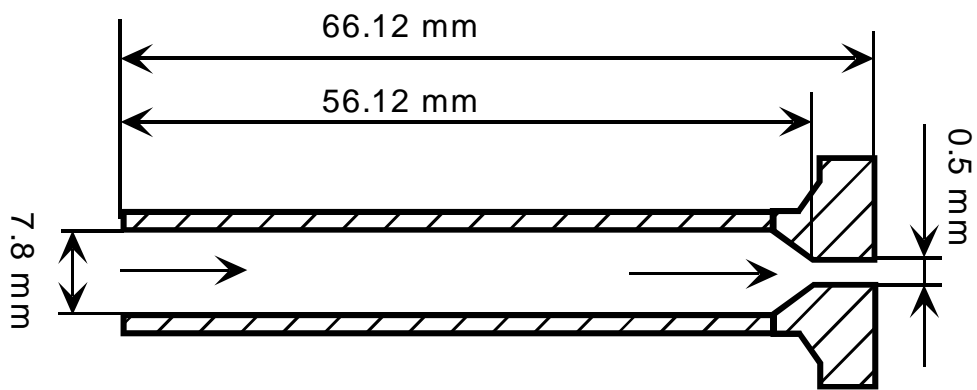


Figure E.3. Dimension of the designed capillary die.

## **APPENDIX F**

### **FLOW SIMULATION IN THE DIE: EFFECT OF TEMPERATURE**

To understand the extrusion foaming process, it is important to study the flow, the cell nucleation and growth in the foaming die. As discussed in Chapter 3, the position of nucleation onset was determined and the effect of CO<sub>2</sub> concentration at 175°C was shown. Here, we continue this discussion to study how foaming temperature affects the position of nucleation onset. Two temperatures, 150 and 175°C, are selected with constant CO<sub>2</sub> concentration of 5 wt.%.

Via a computational fluid dynamics code (FLUENT), the pressure profile in the die was determined at the two temperatures by assuming that there is no phase separation. After that, the Sanchez-Lacombe equation of state was applied to calculate the CO<sub>2</sub> saturation concentration (solubility) at each pressure obtained above. The position of nucleation onset is where the actual CO<sub>2</sub> concentration that is physically blended into the polymer melt becomes higher than the saturation concentration of the local pressure.

## F.1. Computations

### F.1.1. Fluent Simulation of the Contraction Flow

To determine the pressure profile in the die, and as a first approximation, to locate the position of nucleation onset, the Fluent computational code was applied to combine the equations of motion with the energy balance and the rheological model by assuming that the CO<sub>2</sub>/PS solution flows through the die without phase separation. As shown in Figure F.1, the die insert used in this work contains two sections: a guiding hollow tube (D = 7.8mm, L = 56.12mm) and a capillary nozzle (D = 0.5mm, L = 10mm). Therefore, a contraction flow exists through the insert.

The shear-thinning behavior of the CO<sub>2</sub>/PS solution is expressed as the Carreau model:

$$\frac{\eta - \eta_{\infty}}{\eta_0 - \eta_{\infty}} = \frac{1}{\left(1 + \left(\lambda \dot{\gamma}\right)^2\right)^{(1-n)/2}} \quad (\text{F.1})$$

Where  $\eta$ ,  $\eta_0$ ,  $\eta_{\infty}$  are shear viscosity, zero shear viscosity and infinite shear viscosity respectively.  $n$  is the power law index and  $\lambda$  is a constant.

By fitting the experimental viscosity data obtained by Kwag et al. [167], we determine the parameters in the Carreau model, which are shown in Table F.1.  $\eta_{\infty}$  is set to be zero. This model was then put into the Fluent computational code to characterize the rheological behavior of the CO<sub>2</sub>/polystyrene mixture.

During the calculation, the CO<sub>2</sub>/polystyrene mixture was assumed to be a one-phase solution and the heat capacity was a function of temperature ( $C_p$  (J/kg.K) = 1182.03 + 1.7714 T (K)), but the thermal conductivity was a constant ( $k = 0.15$  W/m.K) [227]. The temperature on the wall and at the entrance was set to be 150 or 175°C and an exit flow rate of 0.4536 kg/hr (1 lb/hr) was selected.

### **F.1.2. Calculation of CO<sub>2</sub> Solubility**

The Sanchez-Lacombe equation of state has been shown successfully to model the sorption of high-pressure gases in amorphous polymers or polymer melts. The solubility is determined by equating the chemical potential of CO<sub>2</sub> in the polymer at a given temperature and pressure to that in the gas phase. During the calculation, the gas phase is assumed pure, i.e., the polymer is insoluble in the gas. The binary interaction parameters ( $\delta_{ij}$ ) were selected by fitting the Sanchez-Lacombe EOS with the literature solubility experimental data [128-131] at different temperatures. Then the fitting  $\delta_{ij}$  values were averaged to obtain 0.0249 because we found they change irregularly in a narrow range (0.0165 to 0.0359) for temperature varying from 35 to 200°C. At a typical foaming condition (175°C and 10.34 MPa), the solubility is calculated to be 3.82%, 3.62%, and 3.36% when the  $\delta_{ij}$  is the lowest (0.0165), the average (0.0249) and the highest (0.0359) respectively. Therefore not a big error was introduced by applying the average value for all the temperatures. This value was assumed independent of temperature.

## **F.2. Flow Simulation in the Die**

### **F.2.1. Pressure Drop**

Because of the large ratio in diameter between the guiding tube and the capillary nozzle, the pressure drop concentrates in the capillary nozzle. The pressure is nearly constant from the insert entrance to the capillary nozzle entrance (0 to 56.12 mm), and then it drops quickly through the nozzle (56.12 to 66.12 mm). In the calculations, we only considered the shear viscosity in the calculation, although extensional viscosity is also important in a contraction flow. Figure F.2 demonstrates the effect of die temperature on the pressure drop with 5 wt.% of CO<sub>2</sub> dissolved in the polystyrene. When the die temperature decreases from 175 to 150°C, the pressure drop through the die increases as a result of viscosity increase.

In Figure F.2, we also tried to label the nucleation onset, which is defined as the position that the solution reaches saturation. The actual concentration of CO<sub>2</sub> in the polymer is decided by the experimental condition. At some point in the die the actual concentration will become greater than the saturation concentration due to the latter decrease of the pressure in the die. The point at which these concentrations are equal is where the polymer begins to be supersaturated with CO<sub>2</sub> and nucleation becomes theoretically possible. The saturated CO<sub>2</sub> content, which are the thick lines in the figure, was calculated with the Sanchez-Lacombe equation of state according to the local pressure (the thin lines) at different positions along the centerline at the corresponding die temperature. The horizontal dashed lines represent the actual CO<sub>2</sub> concentration in

polystyrene (5 wt.%), and the intersection of the vertical dashed lines and the length-axis represents the onset position where the solution becomes saturated. This position can be treated as the point where bubble nucleation and growth begin.

Figure F.3 exhibits how the pressure drop and the average pressure drop rate change with CO<sub>2</sub> content and temperature. With the same flow rate, both qualities decrease with increasing CO<sub>2</sub> content and temperature. The influence of CO<sub>2</sub> content is more significant at the lower temperature (150°C). Furthermore, the pressure drop or pressure drop rate decreases more quickly at low CO<sub>2</sub> concentration region.

### **F.2.2. Position of Nucleation Onset**

For a batch foaming system, the processing pressure is always the saturation pressure at the given temperature because the sample is placed in a pressurized vessel for a sufficient long time to ensure saturation is achieved before the pressure is released. But for a continuous foaming process, the pressure at the die entrance sometimes is higher than the saturated pressure to maintain a single-phase solution and stable flow. Therefore, nucleation does not occur until the solution becomes saturated at some position in the die. We believe the nucleation rate is highest just beyond this point because of the high concentration of the gas. As shown in Figure F.4, the more CO<sub>2</sub> in the melt, the earlier the bubbles begin to nucleate and grow. In other words, a high CO<sub>2</sub> content gives more nuclei, but a longer time for bubble growth. Although the influence of temperature to the nucleation is complex, a lower die temperature postpones the nucleation to a position near the exit at the same CO<sub>2</sub> content and flow rate.

### F.2.3. Consistency between Simulation and Experimental Observations

For microcellular foaming which purpose is to form bubbles as small as possible, a nucleation position near the die exit may be favorable. The cell structure can be frozen right after nucleation (before full growth) due to the temperature decrease out of the die.

In Table F.2, the influence of the operating conditions, such as CO<sub>2</sub> concentration, temperature, and flow rate, on the pressure drop rate and the nucleation position is summarized. A high flow rate postpones the nucleation (↓) to the die exit (which has been experimentally shown by Tsujimura et al. [216, 217]) and increases the pressure drop rate (↑) simultaneously, while a high CO<sub>2</sub> concentration at the same foaming temperature or a high foaming temperature with the same CO<sub>2</sub> concentration brings forward the nucleation position near the die entrance and reduces the pressure drop rate. A later nucleation onset indicates a shorter cell growth time and a higher pressure drop rate induces a higher nucleation rate. Therefore, only conditions that postpone the nucleation to the die exit (↓) and increase the pressure drop rate (↑) simultaneously will have the high possibility to create small cells and large cell density.

Experimental observations in Chapter 3 and 4 can be qualitatively explained by the simulation results above. For example, a high CO<sub>2</sub> concentration is favorable to form open cells, a direct result of the long cell growth time, which is consistent with the simulation result that a high CO<sub>2</sub> concentration offers an early nucleation onset. At high screw rotation speed, a low foaming temperature can nucleate a small cell size and large cell density because the low foaming temperature postpones the nucleation to the die exit and increases the pressure drop rate. This explanation is also applicable to the increase of flow rate, which directly postpones the nucleation and increases the pressure drop rate.

As a result, the cell size decreases and the cell density increases. This is one reason why it is a more effective method to get microcellular foams by increasing the entrance pressure through speeding up the flow rate compared with changing CO<sub>2</sub> concentration and foaming temperature only.

However, the complexity of a foaming procedure determines that we cannot explain all phenomena by the position of nucleation onset. For example, an early nucleation, which means a longer cell growth time, does not always indicate the formation large bubbles because cell nucleation and cell growth are a pair of competitive processes on the aspect of gas consumption. When the available amount of gas is shared by more nucleated bubbles growing simultaneously, smaller bubble size is possible.

To further understand the thermodynamic change in a foaming die, profiles of pressure, solubility and glass transition temperature ( $T_g$ ) are plotted together in Figure F.5. As the polymer/gas solution flows through the die, the solubility decreases as a consequence of the pressure drop, which provides the driving force for phase separation. At the same time, the glass transition temperature increases with the decrease of CO<sub>2</sub> concentration in the polymer matrix. This increase in  $T_g$  can promote the frozen of cell structure as soon as the temperature is lower than the  $T_g$  at the corresponding CO<sub>2</sub> concentration.

### **F.3. Estimation of Critical Size of Nucleated Cells**

Based on Equation 2.11, the critical cell size was estimated in Figure F.6. The interfacial tension was 0.0173 N/m selected according to the experimental data of high molecular weight PS at high pressures in Figure 2.9. The critical cell size was calculated at different supersaturation pressures ranging from 1 Pa to 20 MPa. Obviously, the critical cell size decreases exponentially with the increase of the supersaturation pressure. For example, the critical cell size is 3.5 cm at the supersaturation pressure of 1 Pa and 1.7 nm at 20 MPa. Once the foam cell size is beyond the critical cell size, foam cells will grow spontaneously.

| 150°C             | 1 wt%   | 2 wt%   | 3 wt%   | 3.5 wt% | 4.5 wt% | 5 wt%   |
|-------------------|---------|---------|---------|---------|---------|---------|
| $\eta_0$ (Pa.sec) | 27340.6 | 20091.5 | 7177.9  | 3149.5  | 3360.9  | 2972.6  |
| $\lambda$         | 0.9398  | 0.6076  | 0.1913  | 0.0749  | 0.09168 | 0.1358  |
| n                 | 0.4508  | 0.3102  | 0.3311  | 0.3972  | 0.3604  | 0.3738  |
| 175°C             | 1 wt%   | 2 wt%   | 3 wt%   | 3.5 wt% | 4.5 wt% | 5.1 wt% |
| $\eta_0$ (Pa.sec) | 1969.4  | 1577.9  | 1139.3  | 614.2   | 548.5   | 334.4   |
| $\lambda$         | 0.07102 | 0.0584  | 0.04956 | 0.02292 | 0.02614 | 0.01496 |
| n                 | 0.4099  | 0.3703  | 0.428   | 0.4271  | 0.4409  | 0.4553  |

Table F.1. Parameters in the Carreau model

|                     | CO <sub>2</sub> concentration | Temperature | Flow rate |
|---------------------|-------------------------------|-------------|-----------|
|                     | ↑                             | ↑           | ↑         |
| dP/dt               | ↓                             | ↓           | ↑         |
| nucleation position | ↑                             | ↑           | ↓         |

Table F.2. Influence of the operating conditions on the pressure drop rate and the nucleation position (the up arrow means an increase in the specific value or a earlier nucleation)

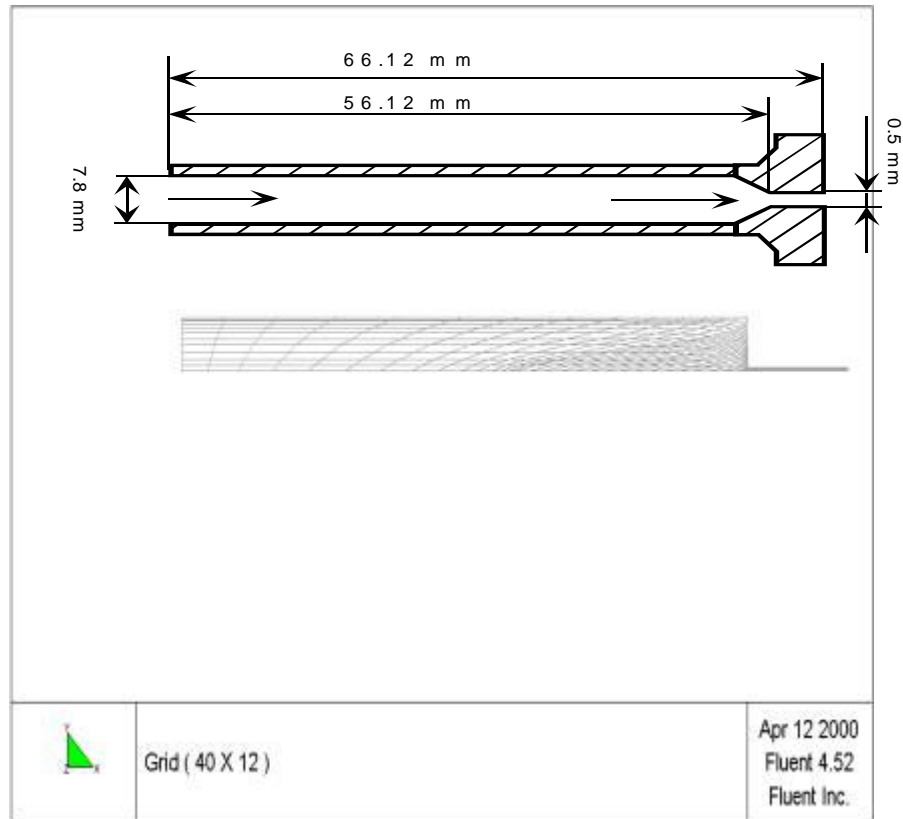


Figure F.1. Geometry and grid in the Fluent simulation.

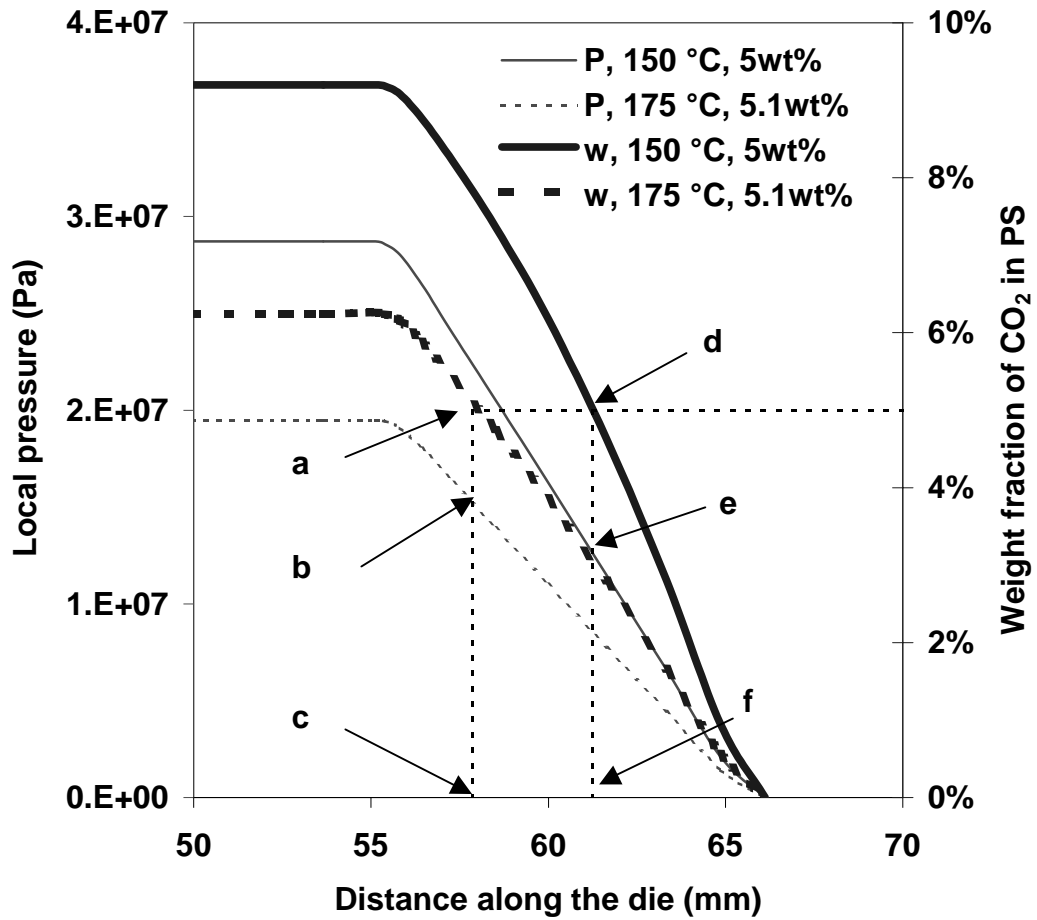


Figure F.2. Profiles of pressure and saturation CO<sub>2</sub> weight fraction along the die nozzle at different die temperatures (150 and 175°C) and same CO<sub>2</sub> concentration (5 wt.%). Points a and d: saturation concentration; b and e: local pressure when the solution becomes saturated; c and f: nucleation onset position.

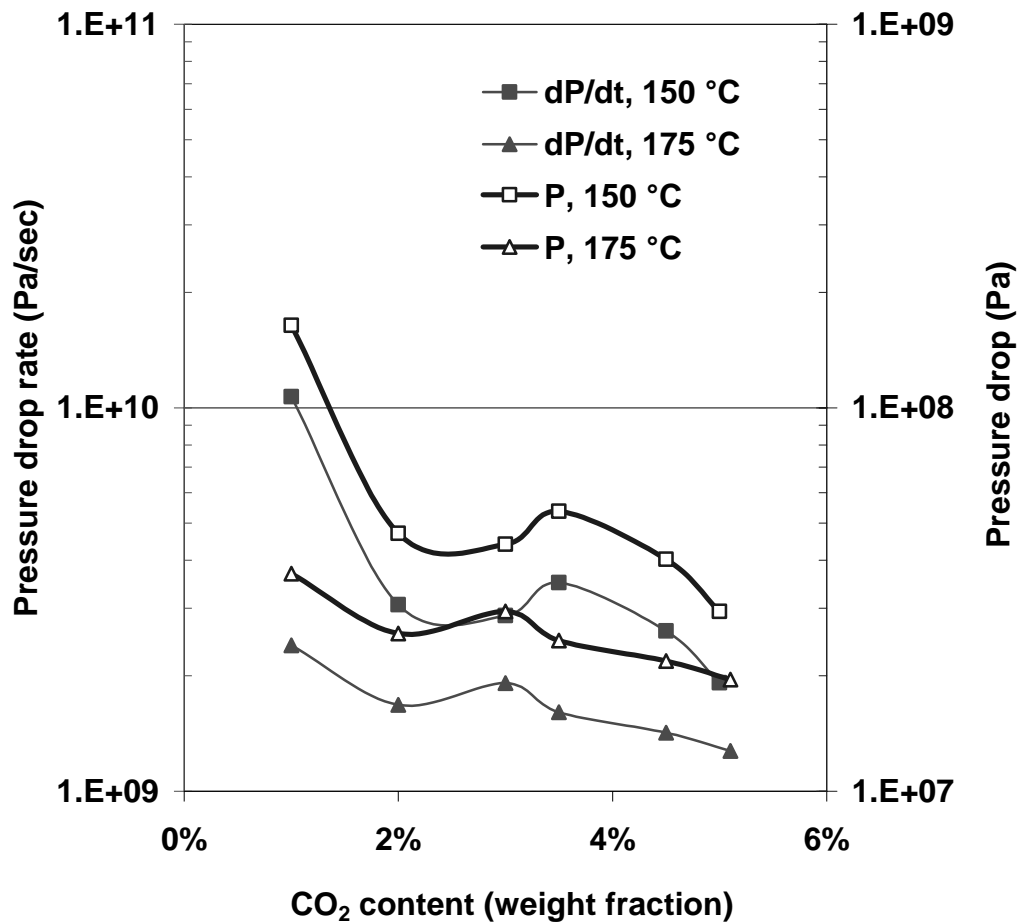


Figure F.3. The influence of CO<sub>2</sub> content on the pressure drop and pressure drop rate (5 wt.% CO<sub>2</sub>).

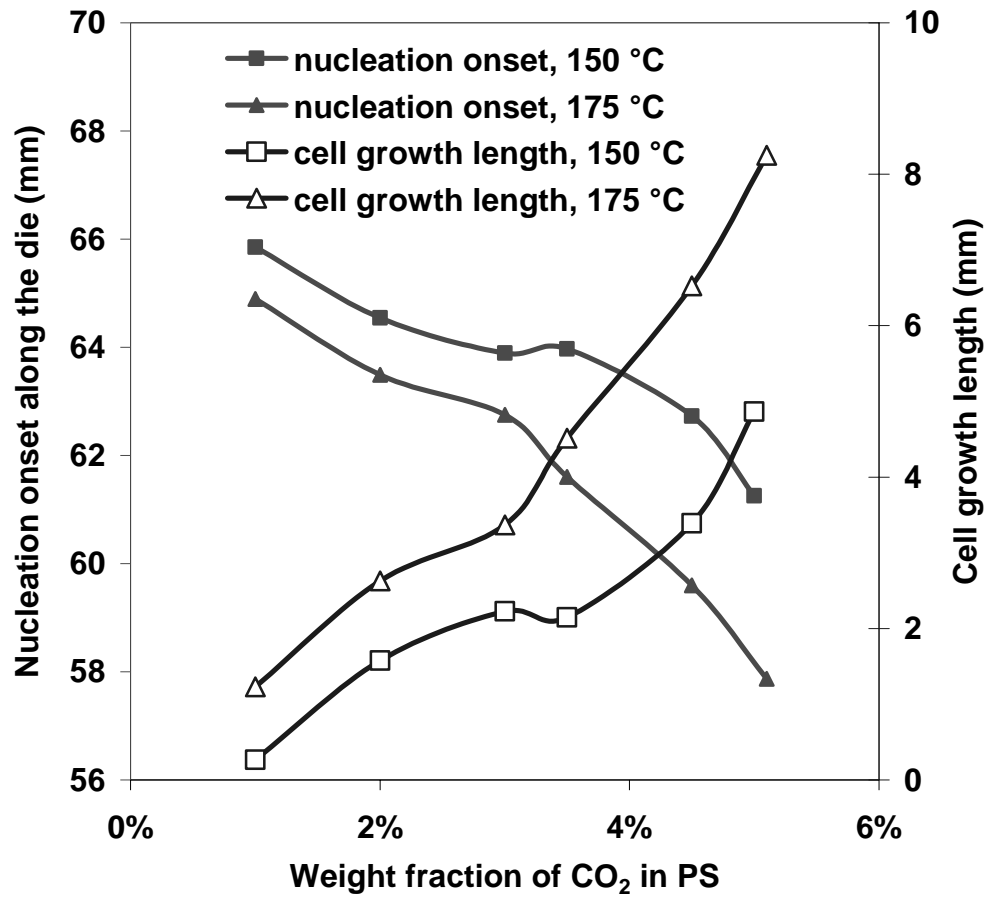


Figure F.4. Effects of die temperature on the nucleation onset position and the cell growth length (5 wt.% CO<sub>2</sub>).

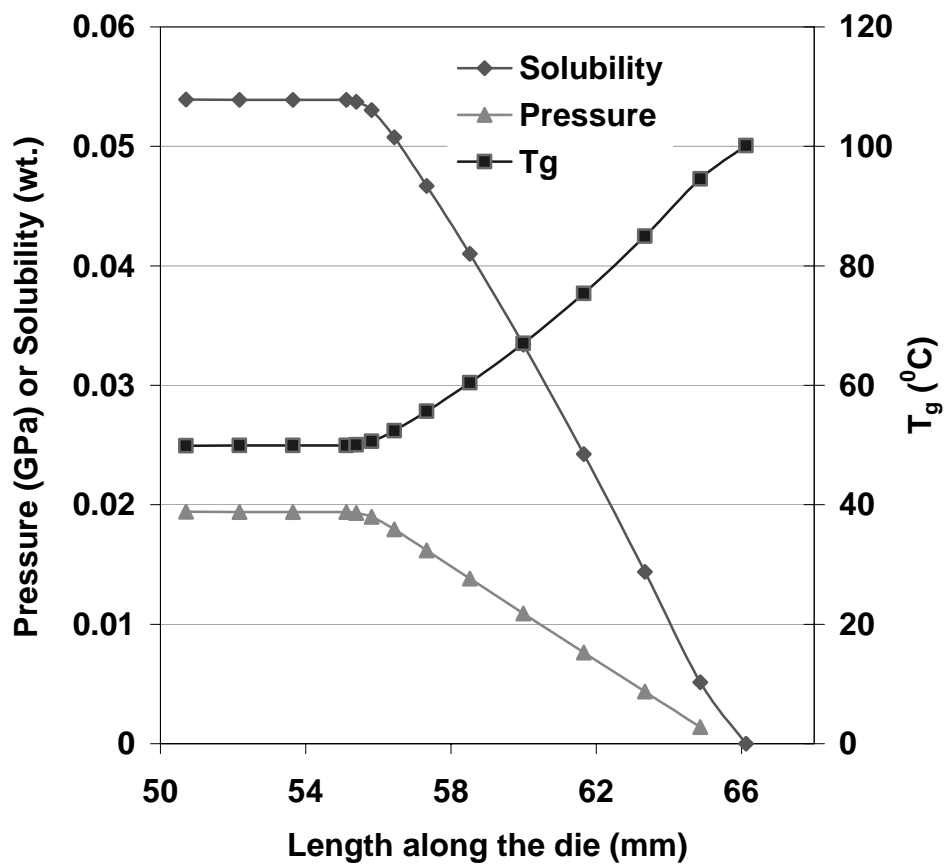


Figure F.5. Profiles of pressure, solubility, and glass transition temperature in the die during flow.

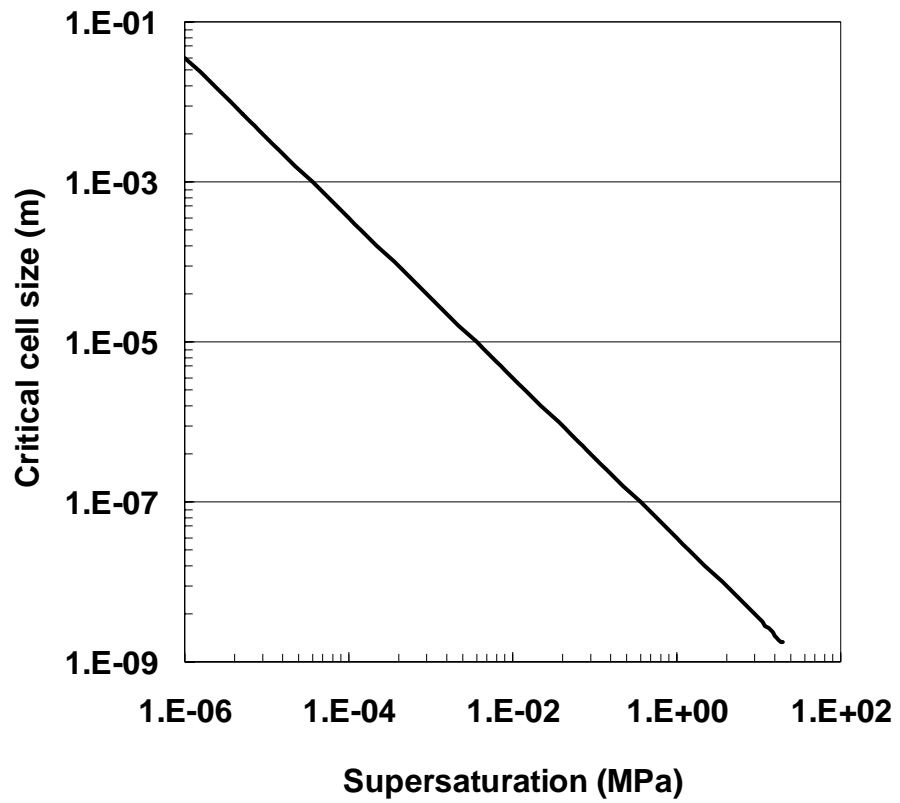


Figure F.6. Estimation of critical cell size at different supersaturation pressures.

## APPENDIX G

### MICROCELLULAR FOAM EXTRUSION WITH FILLERS: TALC AND ALUMOXANE NANO-PARTICLE

Talc, non-aluminous magnesian silicate hydroxide ( $\text{Mg}_3\text{Si}_4\text{O}_{10}(\text{OH})_2$ ), is a very common nucleating agent in the foaming industry. Low bulk density talc provided by Owens-Corning was applied in this study. Figure G.1 gives the particle size and distribution of talc in the PS matrix.

Alumoxane nano-particle was donated by TDA Research, Inc. Alumoxanes are versatile materials that contain aluminum, oxygen, and a variety of subgroups depending on the application. Their properties can be modified by changing the identity of the subgroup. Figure G.1 gives the particle size and distribution of alumoxane in the PS matrix. The small black spherical dots are the alumoxane particles.

In this section, talc and alumoxane were blended into polystyrene (AtoFina CX 5197) as the nucleating agent. The blends were then foamed at 200°C on a single screw extruder (HAAKE 252p) with a capillary die of 0.5 mm in diameter and 10 mm in length. The resulted foams were compared with those of pure PS and PS nanocomposites as shown in Chapter 5.

### **G.1. Talc**

Polystyrene with different talc concentrations were foamed at 200°C, 4 wt.% CO<sub>2</sub>, and 20 rpm. Cell size and cell density of the foam samples were plotted in Figure G.2. For the samples containing talc, the cell size decreases and the cell density increase with the increase of talc concentration. However, all of them show larger cell size and lower cell density than the pure PS foam at the same conditions. Therefore, the hypothesis that the total nucleation rate is the summation of homogeneous and heterogeneous nucleation rate is questionable. The total heterogeneous nucleation sites are not as many as the homogeneous nucleation sites at the same foaming conditions without addition of talc. This trend can be seen more clearly in Figure G.3.

The PS/5 wt.% talc blend was also foamed at different screw rotation speeds (i.e., different pressure drops). The cell structures are shown in Figure G.4. With the increase of screw rotation speed, the cell size decreases and the cell density increases. The results are summarized in Figure G.5 that also includes other nucleating agents. Again, only at low pressure drop or pressure drop rate (Figure G.5 (b) and (d)) is talc effective to enhance the nucleation compared with pure PS due to the heterogeneous nucleation sites are more than the homogeneous nucleation sites. On contrary, at high pressure region where the driving force for homogeneous nucleation is large, the addition of talc is not helpful to increase the nucleation. This also shows that the influence of pressure on homogeneous nucleation is greater than that on heterogeneous nucleation. After adding talc, the foam structure becomes less sensitive to the operating conditions, which benefits the cell structure control to get uniform cell size distribution.

## **G.2. Alumoxane Nano-Particle**

Alumoxane nano-particles were used as nucleating agent for PS foams to determine if all nano-sized particles can obtain similar foam structure. In other words, if there exists other factors, such as the particle shape, distribution, and surface modifier, affecting the nucleation efficient other than particle size.

The change of cell size and cell density with pressure drop and pressure drop rate are also included in Figure G.5. Figure G.6 shows the SEM pictures of PS/5 wt.% alumoxane samples foamed at different screw rotation speeds. With the increase of screw rotation speed, the pressure drop and pressure drop rate increase. This causes the cell density to increase and cell size to decrease. However, from the aspect to nucleate microcellular foams with small cell size, alumoxane works not as good as talc and nano-clays. A possible reason is that it is hard to disperse nano-sized particles of alumoxane uniformly in the PS matrix.

A unique characteristic of the PS/alumoxane foams is the formation of bimodal cell size distribution (Figure G.7 (a)) in which the big cells are probably from homogeneous nucleation and the small cells are from heterogeneous nucleation on the nano-sized alumoxane particles.

## **G.3. Formation of Bimodal Cell Size Distribution**

As discussed above, an obvious bimodal cell size distribution is formed in the PS/alumoxane foams (Figure G.7 (a)). The big cells are larger than 13 microns, on the order of the homogeneous nucleated PS cells at low pressures, and the small cells are smaller than 200 nm, comparable with the size of alumoxane particles.

Figure G.7 (b) shows SEM micrographs of PS/talc foams at high magnifications. Small cells around 1  $\mu\text{m}$  can be also found due to the large particle size of talc.

As a comparison, Figure G.8 shows the SEM micrographs at high magnifications for both the intercalated PS/5 wt.% 20A nanocomposite foam and the exfoliated PS/5 wt.% MHABS nanocomposite foam. For intercalated nanocomposite foams, cells ( $< 500$  nm) nucleate and grow around clay tactoids, while in exfoliated nanocomposites, very fine cells seem to nucleate and grow around single clay platelets. In both cases, cells are stretched according to the particle shape, like a cigar. In comparison, the nucleated cells around alumoxane and talc are spherical because of small particle aspect ratio.

#### **G.4. Shear Viscosity**

Shear viscosities of PS/5% talc and PS/5% alumoxane were measured by using the RMS 800 rheometer at 200°C and compared with that of pure PS and PS/5% 20A in Figure G.9. Talc exhibits almost no effect on PS viscosity, especially at low shear rates. Alumoxane uniformly enhances the viscosity of PS at all shear rates, as the curve is nearly parallel to that of PS. However the nanocomposite consisting of PS/5% 20A shows the highest shear viscosity and earliest shear-thinning behavior.

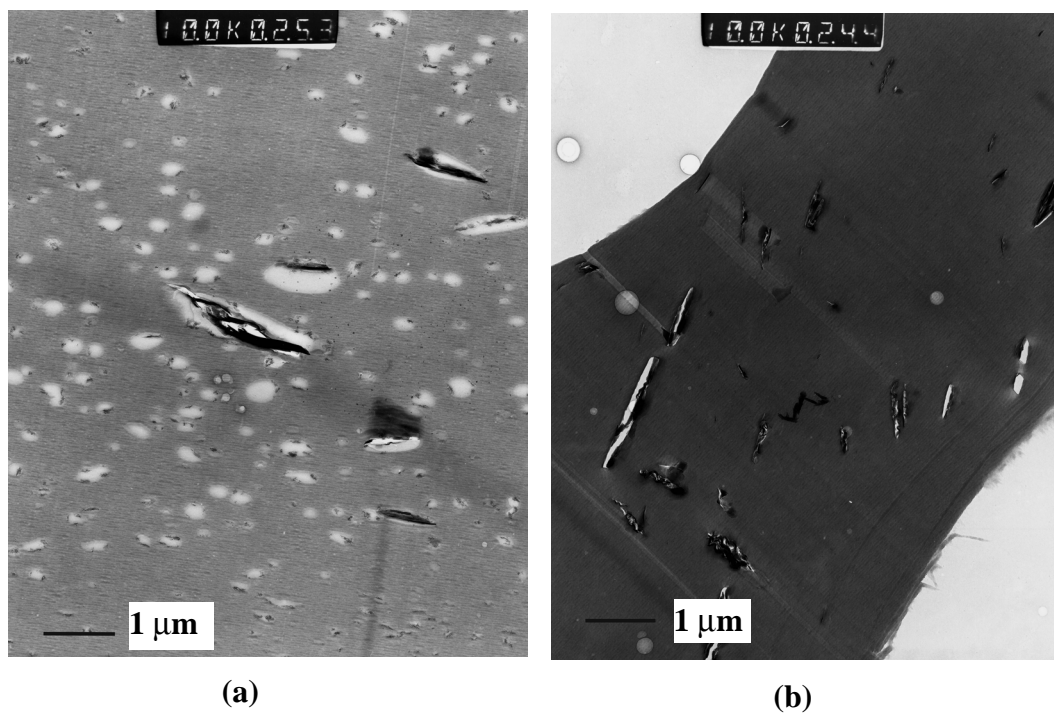


Figure G.1. TEM pictures of PS foams with (a) 5 wt.% alumoxane nano-particle and (b) 5 wt.% talc at 200°C, 4 wt.% CO<sub>2</sub> and 20 rpm (The black dots in the pictures are the filler particles).

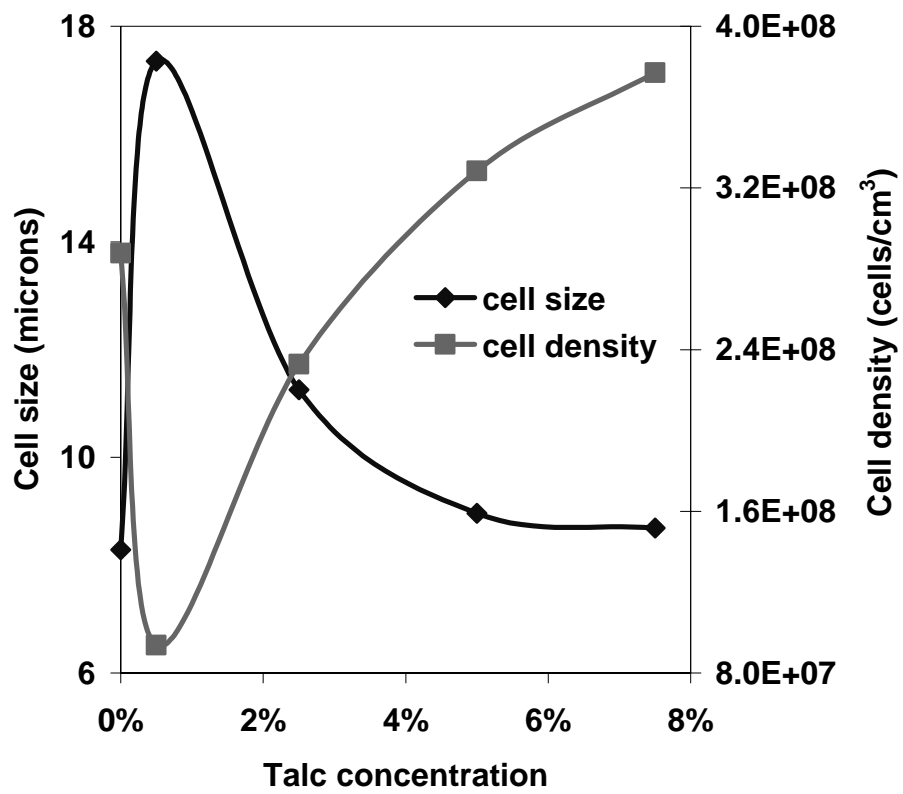


Figure G.2. Cell size and cell density with different talc concentration at 200°C, 4 wt.% CO<sub>2</sub> and 20 rpm.

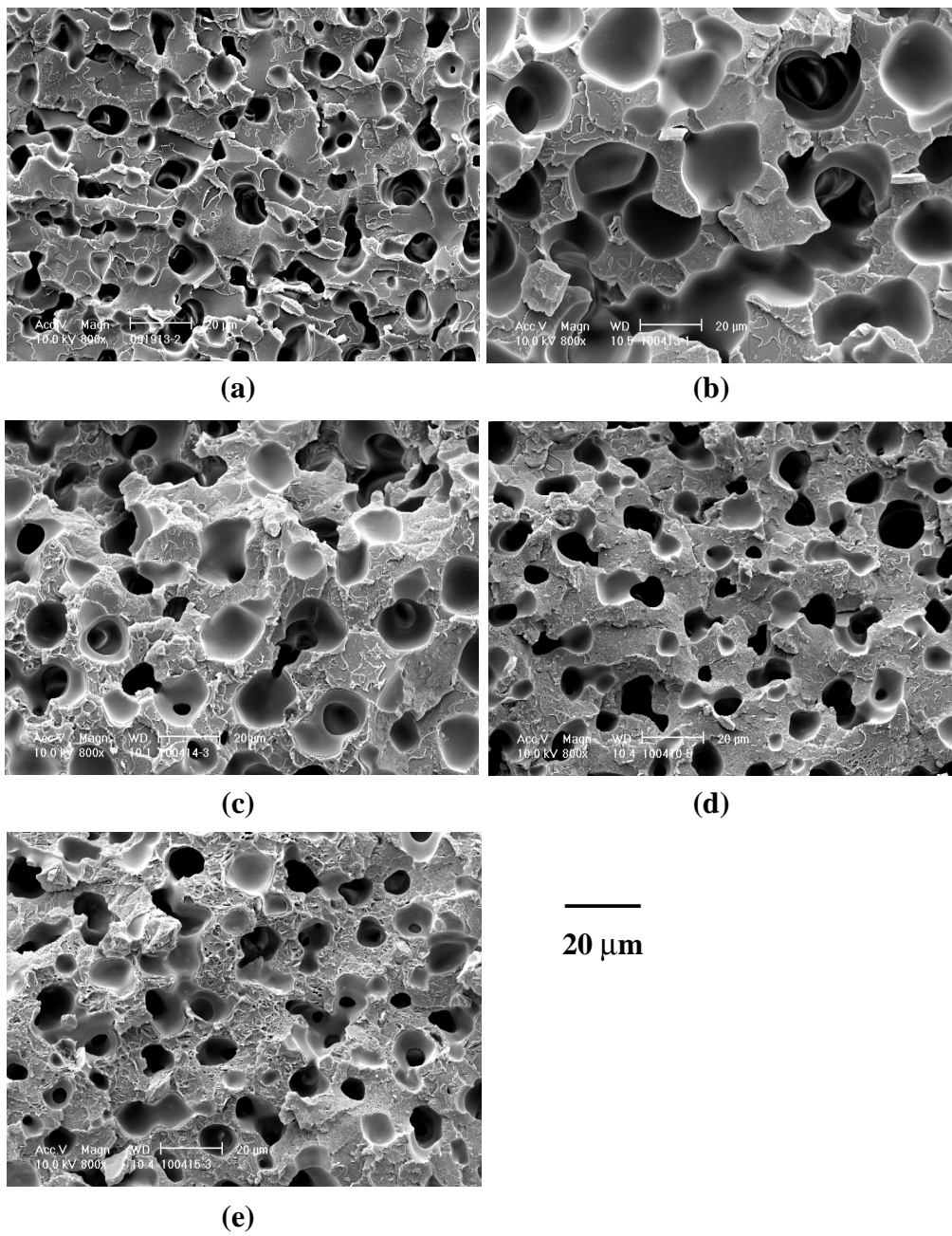


Figure G.3. SEM pictures of PS foams with different talc concentration at 200°C, 4 wt.% CO<sub>2</sub> and 20 rpm: (a) 0, (b) 0.5, (c) 2.5, (d) 5, and (e) 7.5 wt.%.

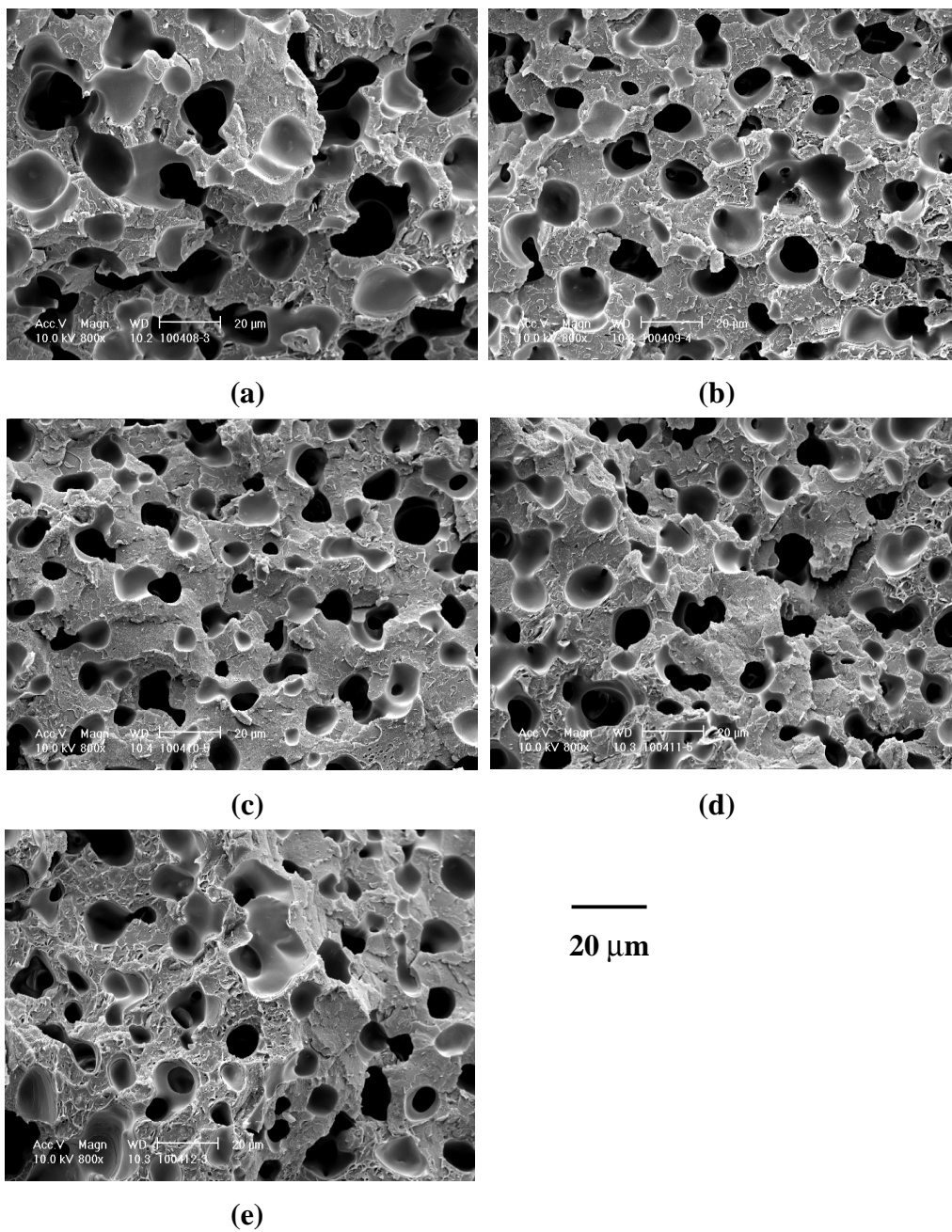
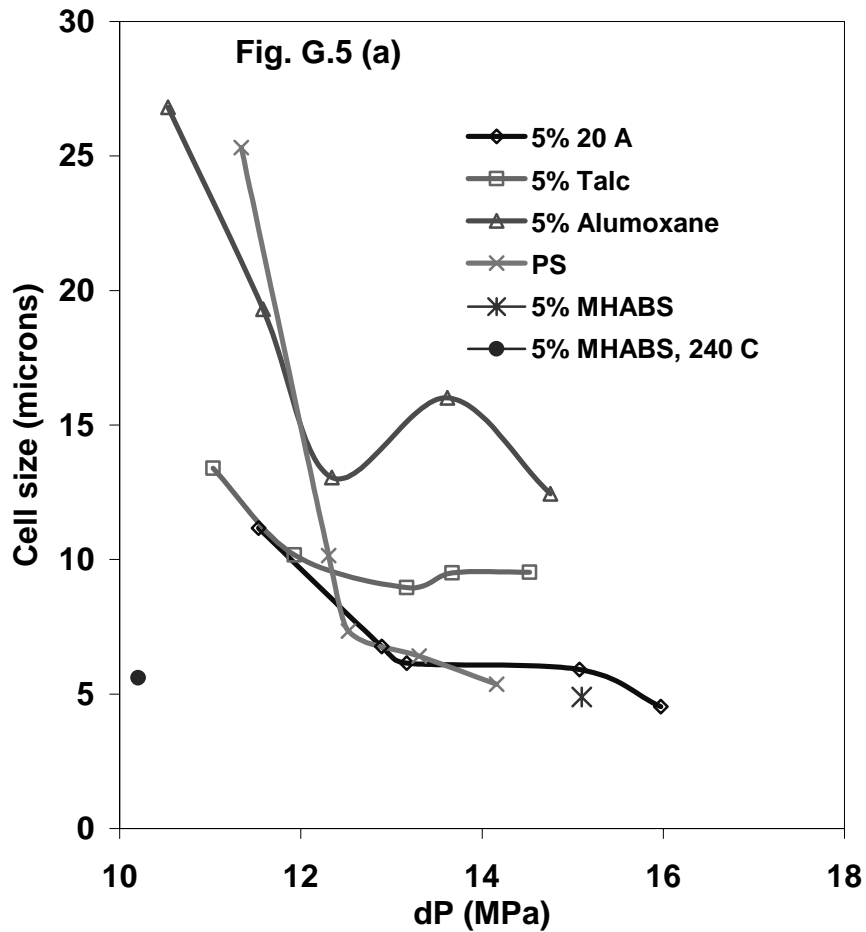


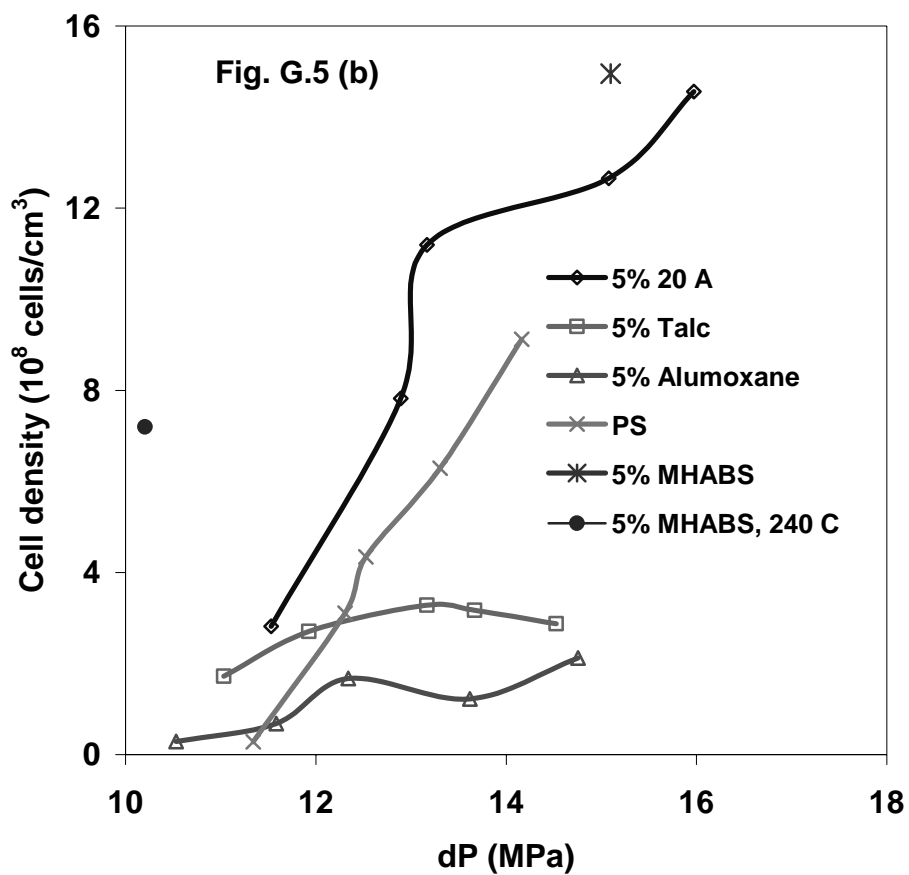
Figure G.4. SEM pictures of PS foams with 5 wt.% talc at 200°C, 4 wt.% CO<sub>2</sub> and different screw rotation speeds: (a) 10, (b) 15, (c) 20, (d) 25, and (e) 30 rpm.



(continued)

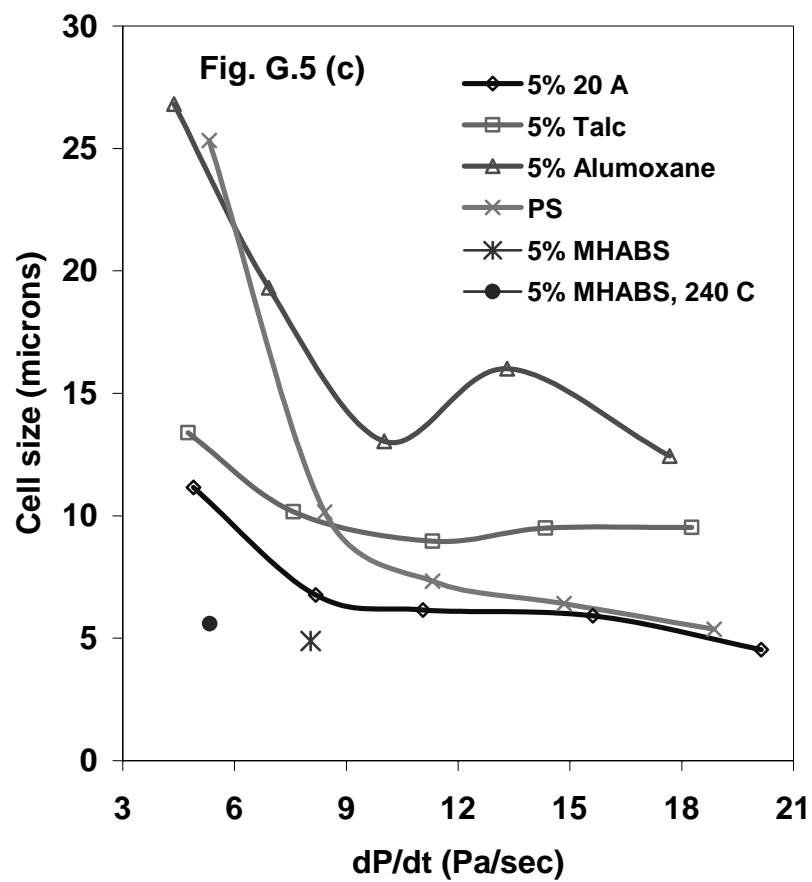
Figure G.5. Comparison of PS foams with 5 wt.% of different fillers at 200°C, 4 wt.% CO<sub>2</sub> (except one data point of MHABS is at 240°C): (a) cell size vs. pressure drop, (b) cell density vs. pressure drop, (c) cell size vs. pressure drop rate, and (d) cell density vs. pressure drop rate.

Figure G.5 continued



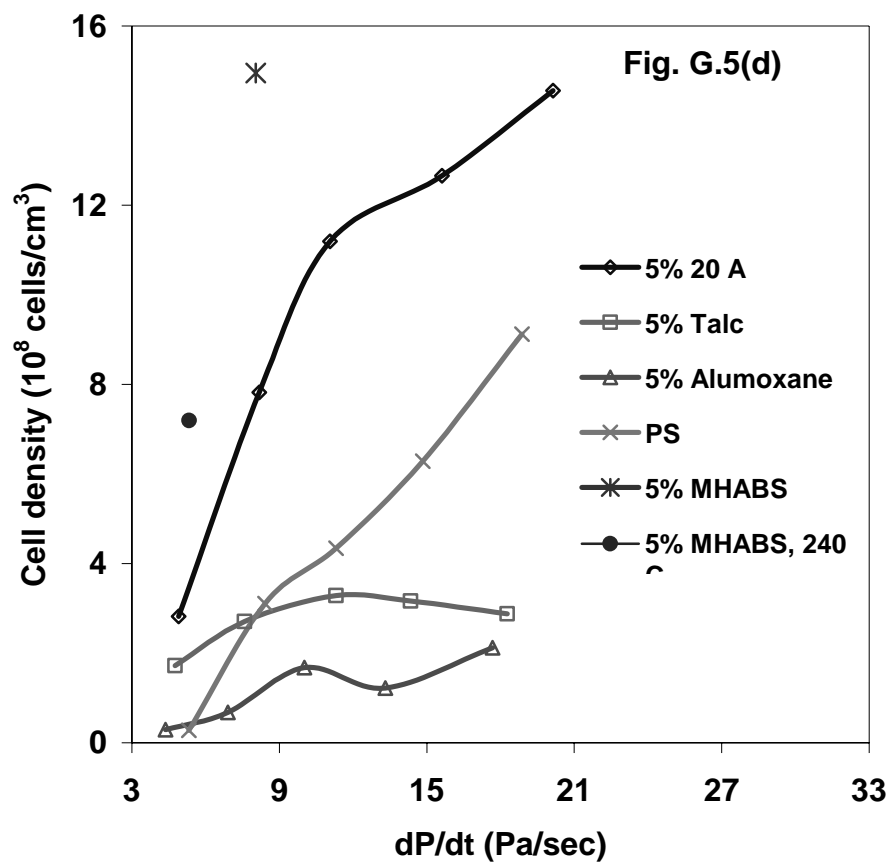
(continued)

Figure G.5 continued



(continued)

Figure G.5 continued



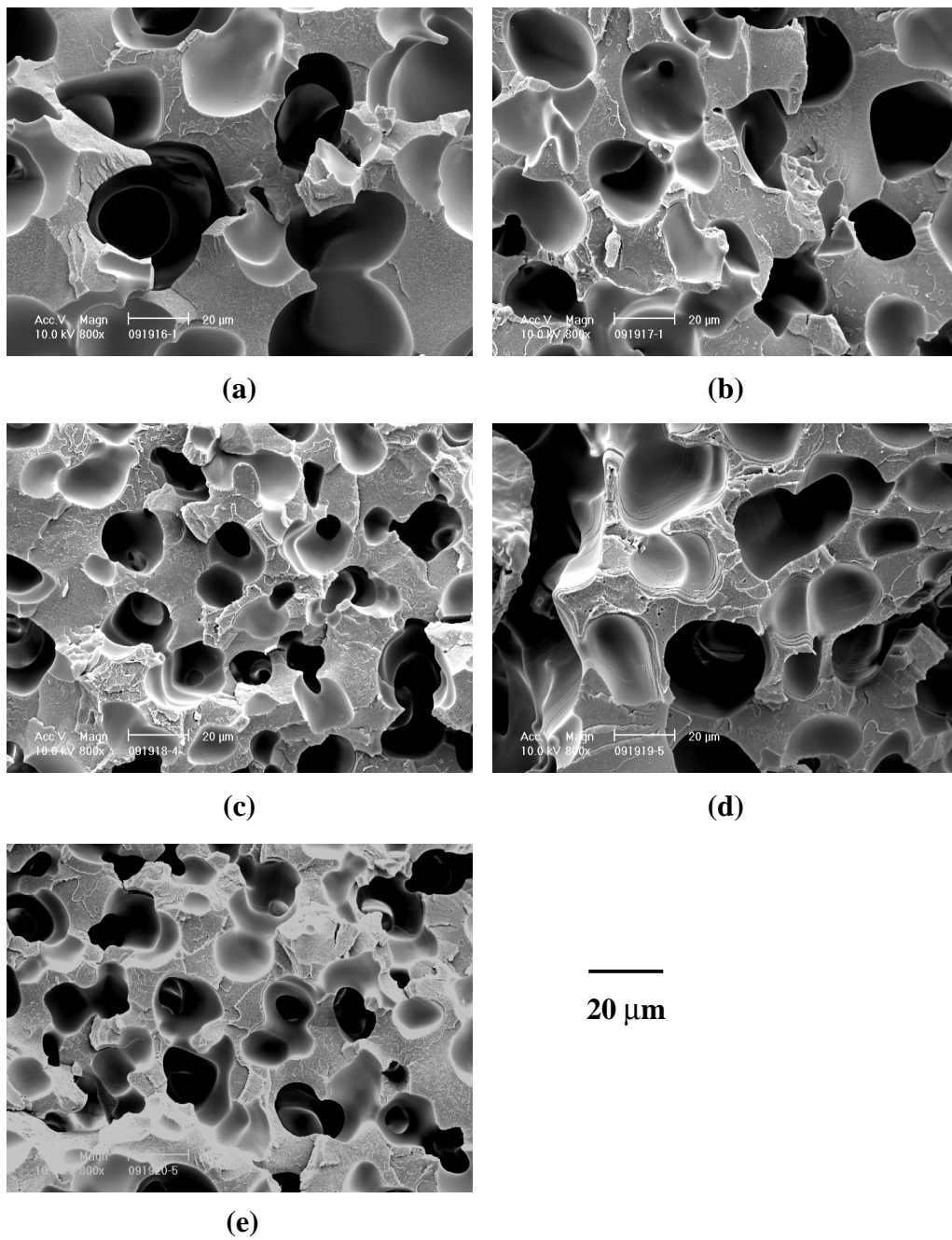


Figure G.6. SEM pictures of PS foams with 5 wt.% alumoxane at 200°C, 4 wt.% CO<sub>2</sub> and different screw rotation speeds: (a) 10, (b) 15, (c) 20, (d) 25, and (e) 30 rpm.

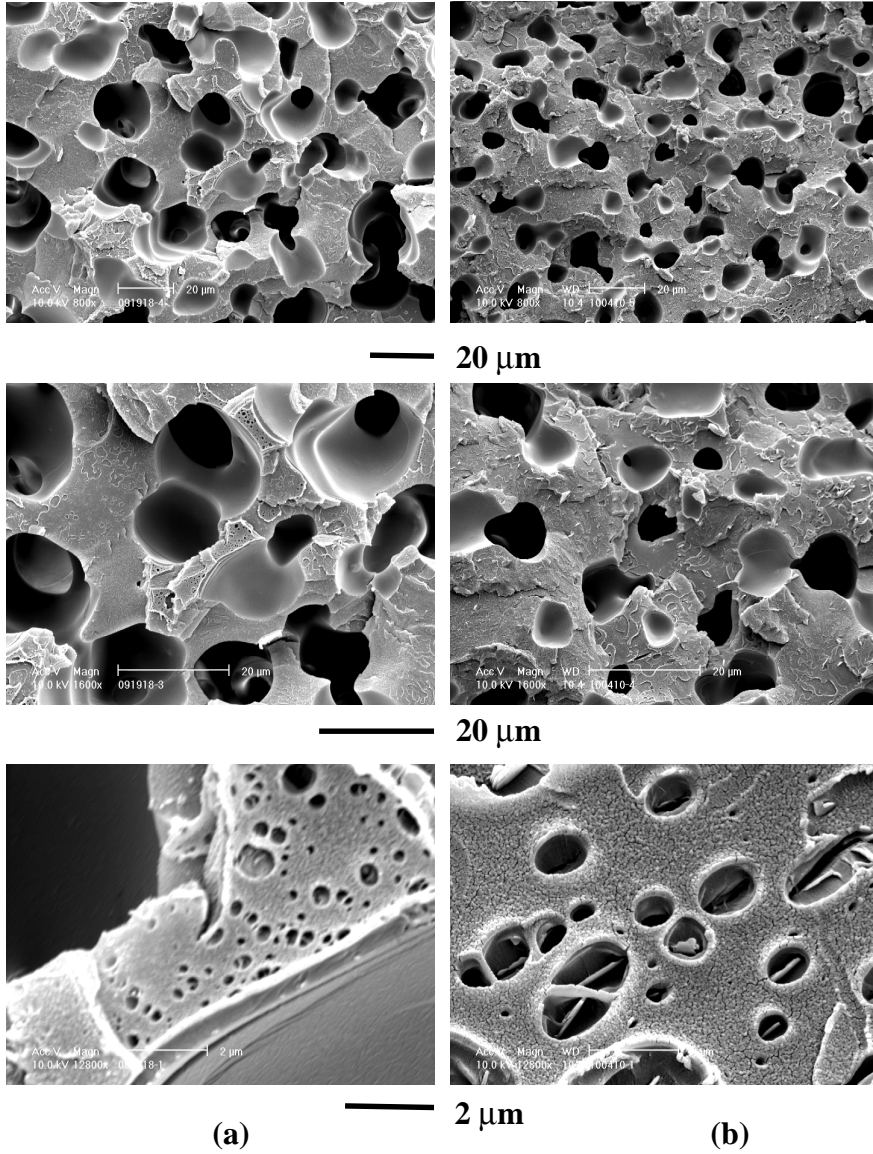


Figure G.7. SEM pictures of PS foam with (a) 5 wt.% alumoxane and (b) 5 wt.% talc at 200°C, 4 wt.% CO<sub>2</sub> and different magnifications.

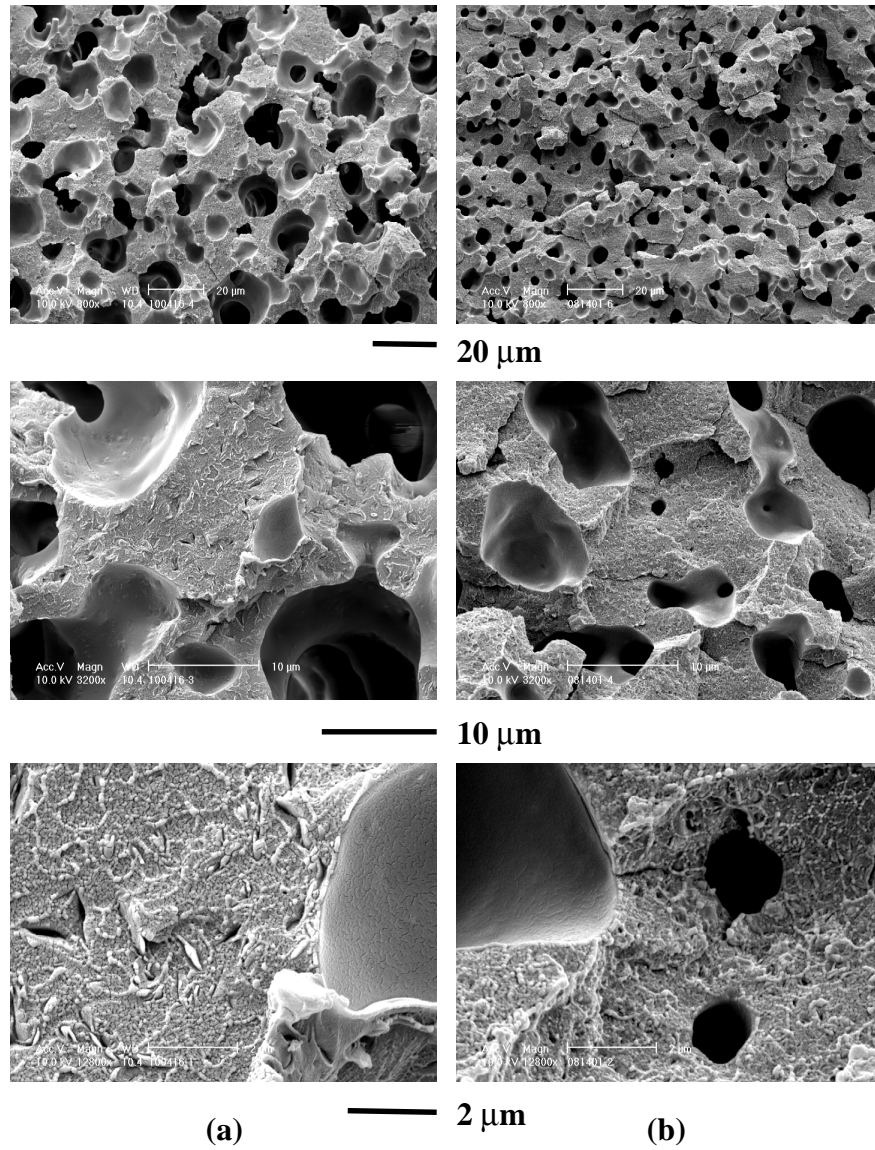


Figure G.8. SEM pictures of PS foam with (a) 5 wt.% 20A and (b) 5 wt.% MHABS at 200°C, 4 wt.% CO<sub>2</sub> and different magnifications.

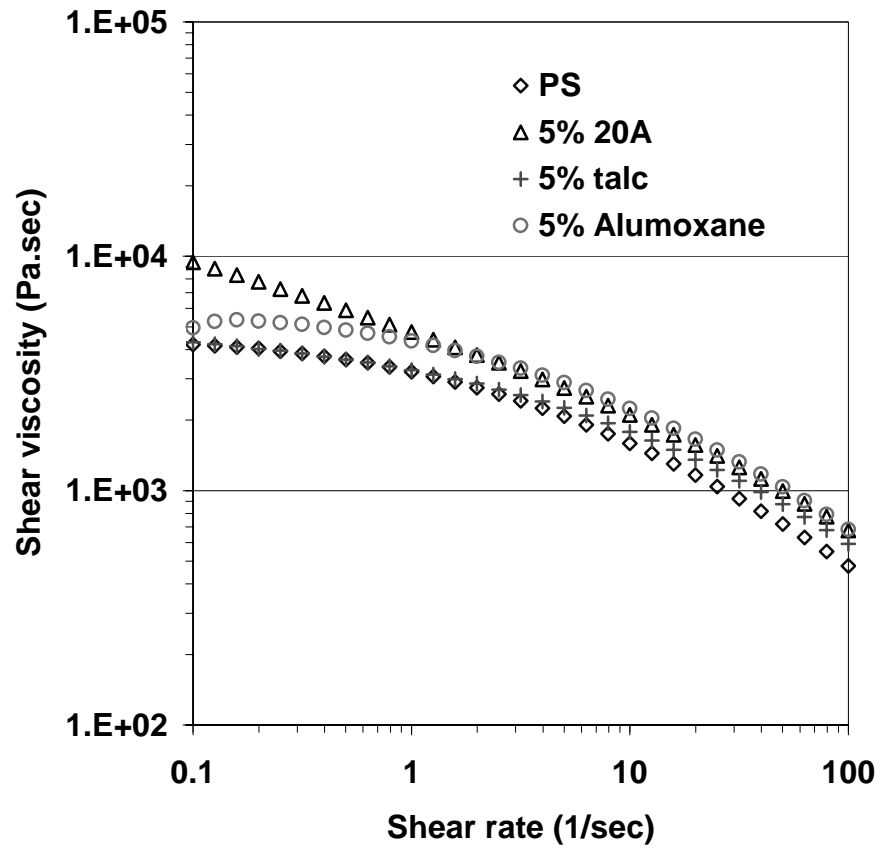


Figure G.9. Shear viscosity of PS with different fillers at 200°C.

## APPENDIX H

### FOAM EXTRUSION WITH H142B/22

H142B/22 is a blend of two hydrogenated chlorofluorocarbons (HCFCs) and widely used in present foaming industries. Under working conditions, it has a good solubility in polystyrene and high theoretical expansion efficiency. The permeability of H142b/22 in polystyrene is very low, which assures the maintenance of the insulation properties with time. However, because of its ozone depletion potential) and of Global Warming Potential, it will be eventually banned in the near future. Some physical properties of Forane H142B/22 from Atofina Chemicals Inc. are listed below.

H142B/22 (CClF<sub>2</sub>CH<sub>3</sub>/CHClF<sub>2</sub> 60/40 blend): specific gravity: 1.16 g/cm<sup>3</sup> at 21°C; vapor pressure: 79.4 psi at 21°C; and boiling point: -28°C

It is important to compare the foaming effect of H142B/22 with that of CO<sub>2</sub> to understand the difficulties by using CO<sub>2</sub> as the foaming agent.

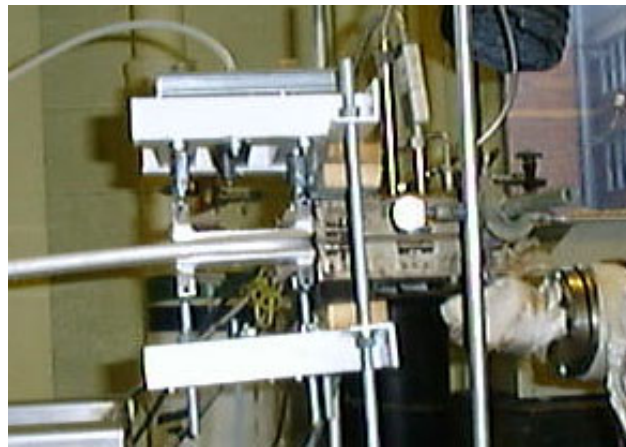
As shown in Figure H.1, PS (AtoFina CX 5197) and PS/talc/20A blends were foamed by both CO<sub>2</sub> and H142B/22 on a twin-screw extruder (Leiztriz-27). A slit die (L×W×H: 100×20×2 mm) was used as the foaming die and a shaping die (Figure H.1 (b)) consisting of two parallel plates was used to control the shape of the foam products. With the shaping die, the foaming agent is further prevented from diffusing out of the polymer matrix and therefore a larger volume expansion ratio can be obtained.

Figure H.2 shows the cross section of ten samples foamed by CO<sub>2</sub> and H142B/22. Because the solubility limit, 6 wt.% CO<sub>2</sub> and 10 wt.% of H142B/22 were injected into polymer melts. Due to the molecular weight of CO<sub>2</sub> (44 g/mole) is only about half of that of H142B/22, a similar theoretical volume expansion ratio should be achieved for the two different concentrations. However, a much smaller cross-section area is given in Figure H.2 for the CO<sub>2</sub> foamed samples. The large diffusivity that comes from the small molecules of CO<sub>2</sub> is believed to be the reason. Much CO<sub>2</sub> diffuses out of the polymer and is lost into the air. This provides a good application of nano-clay in CO<sub>2</sub> foamed samples to improve barrier properties. The cell structures of the ten samples are given in Figure H.3. The cell size of CO<sub>2</sub> foamed samples is smaller than that of H142B/22 foamed samples at the same composition. Nano-clay is also effective as a nucleating agent when H142B/22 was used as the foaming agent (Figure H.3(c) to (f) or (g) to (j)). The competition between talc and nano-clay as nucleation sites makes foam cells become larger when more talc was added, compared Figures H.3 (d)-(f) with the corresponding Figures H.3 (h)-(j).

Figure H.4 shows the cell structure of the foam samples produced on the pilot plant line of Owens-Corning. Different amount of nano-clay (15A, Southern Clay) was applied to control the cell size and cell density. Regular polygonal foam cells were obtained. The addition of nano-clay offers another means to control the cell structure (Figure H.5). Sometimes the strut, the connection section of three adjacent bubbles, is important in deciding the foam properties, such as the heat transfer coefficient. Figure H.6 gives two examples of the strut structure.



**(a)**

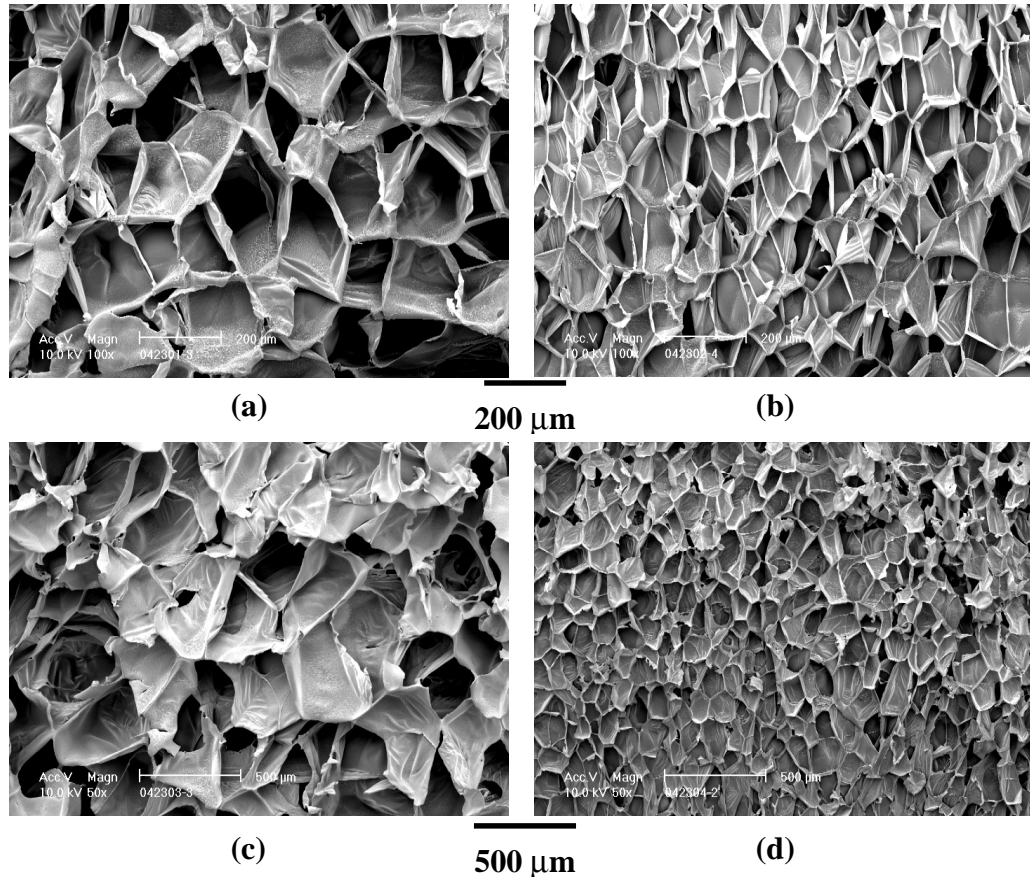


**(b)**

Figure H.1. Experimental setup for PS foam extrusion on a twin-screw extruder by using H142B/22 as the foaming agent: (a) entire setup, and (b) enlargement of the foaming die and shaping die.



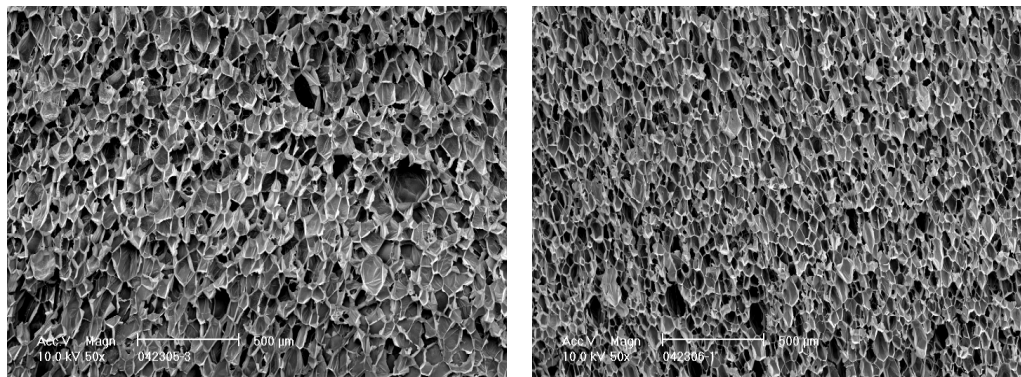
Figure H.2. Comparison between CO<sub>2</sub> and H142B/22 as foaming agent. The composition of the 10 samples from left to right is (a) PS/0.2% talc /6% CO<sub>2</sub>, (b) PS/0.2% talc /5% 20A/6% CO<sub>2</sub>, (c) PS/0.5% talc /10% H143B/22, (d) PS/0.5% talc /2.5% 20A/11% H143B/22, (e) PS/0.5% talc /5% 20A/11% H143B/22, (f) PS/0.5% talc /7.5% 20A/11% H143B/22, (g) PS/1% talc/11% H143B/22, (h) PS/1% talc/2.5% 20A/11% H143B/22, (i) PS/1% talc/5% 20A/11% H143B/22, and (j) PS/1% talc/7.5% 20A/11% H143B/22 (the percentage is in weight).



(continued)

Figure H.3. Comparison of cell structure between CO<sub>2</sub> and H142B/22 as foaming agent. The composition of the 10 samples is (a) PS/0.2% talc /6% CO<sub>2</sub>, (b) PS/0.2% talc /5% 20A/6% CO<sub>2</sub>, (c) PS/0.5% talc /10% H143B/22, (d) PS/0.5% talc /2.5% 20A/10% H143B/22, (e) PS/0.5% talc /5% 20A/10% H143B/22, (f) PS/0.5% talc /7.5% 20A/10% H143B/22, (g) PS/1% talc/10% H143B/22, (h) PS/1% talc/2.5% 20A/10% H143B/22, (i) PS/1% talc/5% 20A/10% H143B/22, and (j) PS/1% talc/7.5% 20A/10% H143B/22 (the percentage is in weight).

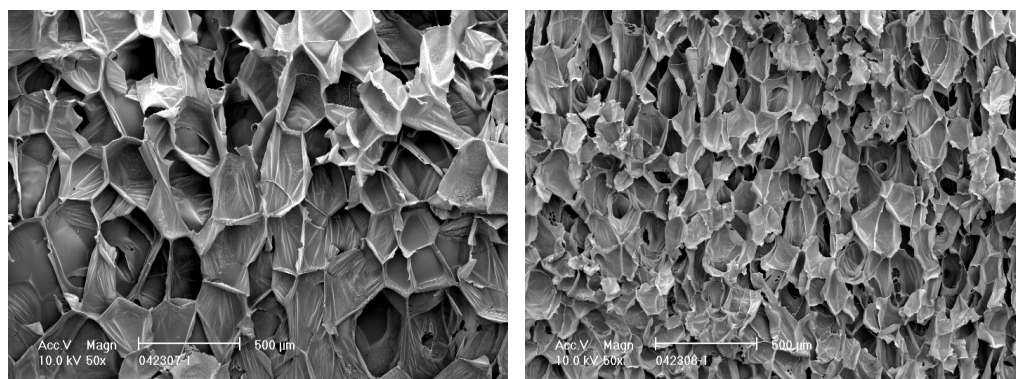
Figure H.3 continued



(e)

500 μm

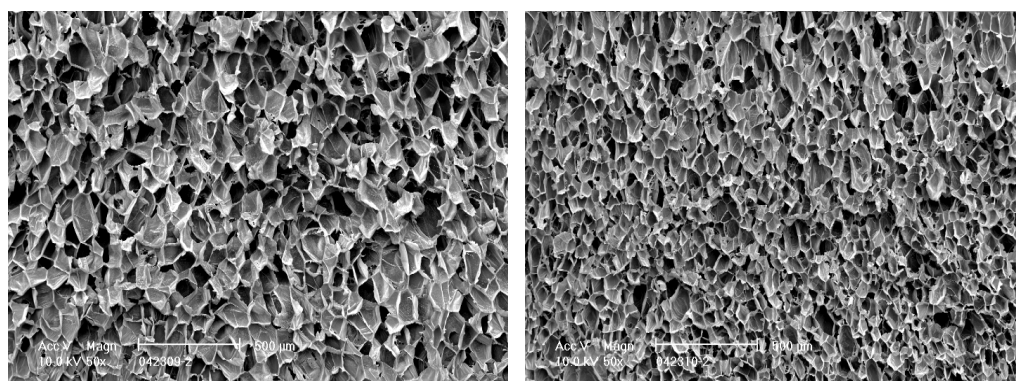
(f)



(g)

500 μm

(h)



(i)

500 μm

(j)

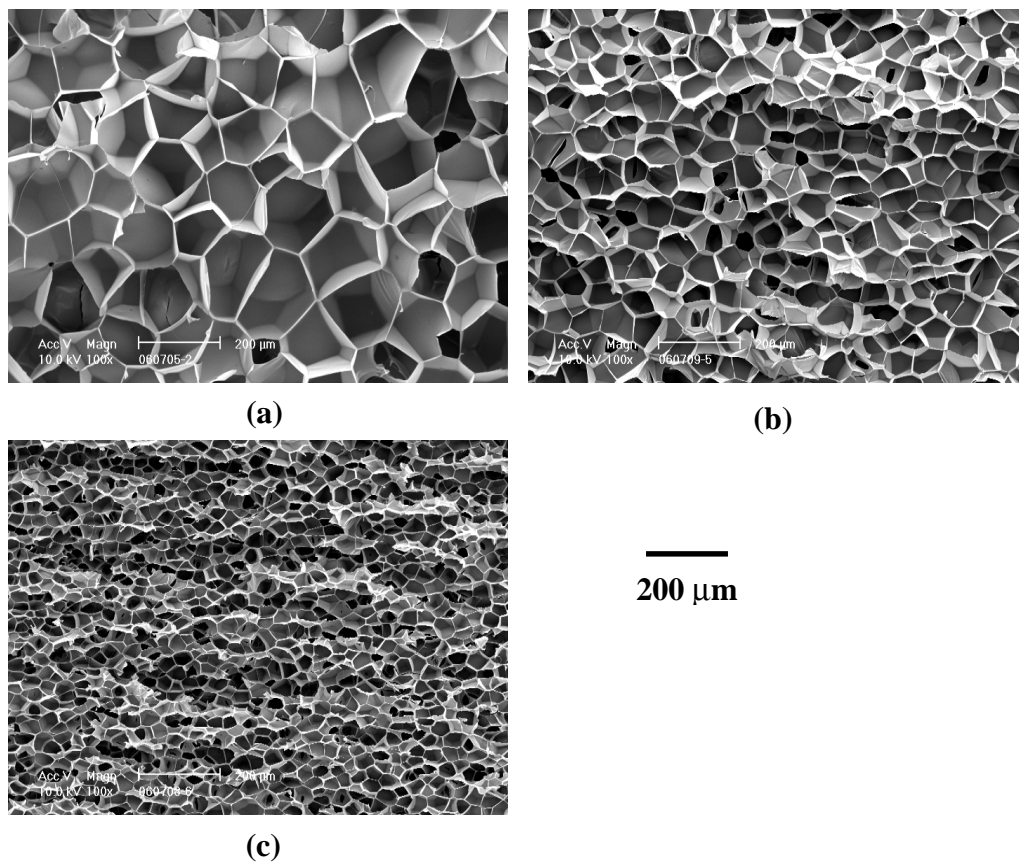


Figure H.4. SEM pictures of PS foam with talc and nano-clay by using H142B/22 as the foaming agent: (a) 0.8 wt.% talc, (b) 0.5 wt.% 15A, and (c) 2.5 wt.% 15A (pilot plant products of Owens-Corning).

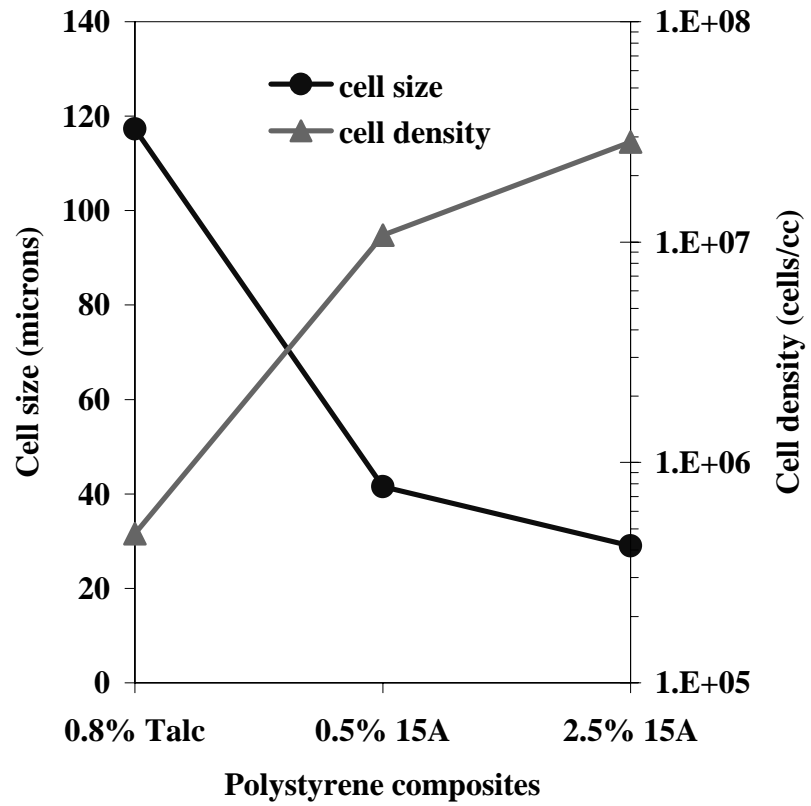


Figure H.5. Cell size and cell density of PS foam with talc and nano-clay by using H142B/22 as the foaming agent (pilot plant products of Owens-Corning).

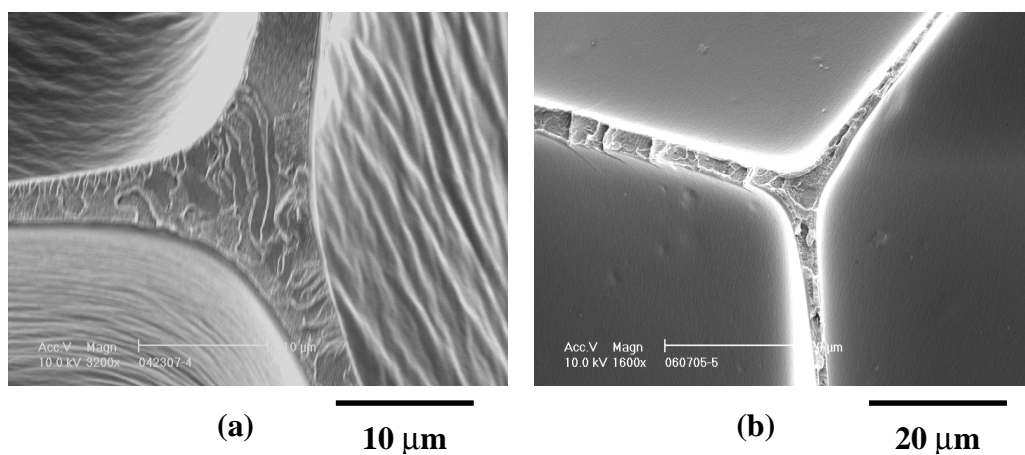


Figure H.6. Strut structure of PS foam by using H142B/22 as the foaming agent: (a) PS/1% talc/10% H143B/22, and (b) PS/0.8 wt.% talc (pilot plant product of Owens-Corning).

## APPENDIX I

### BATCH FOAMING

Compared with a continuous foaming extrusion process, batch foaming is convenient to study foams of different polymers due to small quantity of material needed. The pressure drop rate for a batch foaming, on the order of  $10^6$  Pa/sec, is much lower than that of a foaming extrusion process when a small die is used, which is on the order of  $10^9$  Pa/sec for a capillary die of 0.5 mm in diameter. However, when a large die is used, the pressure drop rates for the continuous foaming extrusion and the batch foaming are comparable.

In this section, we mainly focus on the batch foaming process to study the effect of nano-clay dispersion on the foam structure for both polystyrene (PS) and poly(methyl methacrylate) (PMMA).

The setup for batch foaming is very similar to the one to measure the solubility, which is shown in Figure 6.1. The only modification is to change the high-pressure vessel to be 3/8" or 1/2" stainless steel tubing. During the experiment, the saturation temperature and the foaming temperature were same, 120°C, higher than the glass transition temperature. The saturation pressure was 2000 psi. First, polymer rod samples of 2-3 mm in diameter were put in the tubing and sealed. Then CO<sub>2</sub> was induced and

pressurized to 2000 psi. After the samples were saturated over 24 hours at 120°C, the pressure was released in 3-4 seconds. Without changing the temperature (120°C), 30 seconds were given for foam cell growth. Finally the foam structure was frozen by emerging the foam sample into ice water.

Materials in this section to be compared are pure polymer (PS or PMMA), intercalated nanocomposite (polymer with 5 wt.% 20 A), and exfoliated nanocomposite (polymer with 5 wt.% MHABS). The preparation of these nanocomposites is introduced in Chapter 5. The PS used is AtoFina CX 5197 (melt index: 4.5) and the PMMA used is Plaskolite PL-25.

The foam structures of PS and PS nanocomposites are shown in Figure I.1. The corresponding cell size and cell density are summarized in Figure I.2. The addition of nano-clay can really increase the cell density and reduce the cell size. The better the nano-clay disperses in the polymer matrix, the more nucleation sites provided. As a result, the exfoliated nanocomposite creates the highest cell density and smallest cell size. Compared with the foams produced by extrusion in Figure 5.9, the cell density from the batch process is still low mainly due to the low pressure drop rate.

As a comparison, PMMA and PMMA nanocomposites were also foamed at the same conditions (Figure I.3 and I.4). A similar trend of cell size and cell density with nano-clay dispersion was obtained. However, it is found the cell density is much higher and the cell size is much smaller than the corresponding PS sample. It is well-known that the solubility of CO<sub>2</sub> in PMMA is much higher than that in PS because a stronger interaction exists between CO<sub>2</sub> and the carbonyl groups in PMMA. This increases the nucleation rate. Although more gas is available for foam cell growth, it is shared by a

much larger quantity of cells. Therefore, smaller cells were still formed. Furthermore, the interaction improves the interface between the clay and CO<sub>2</sub> and provides a lower nucleation interfacial tension. Consequently, the nucleation efficient of the nano-clay is enhanced as well. Additionally, some open-cell structure was observed on SEM micrographs, which is mainly because the huge cell density increases the possibility for cell impingement and cell coalescence.

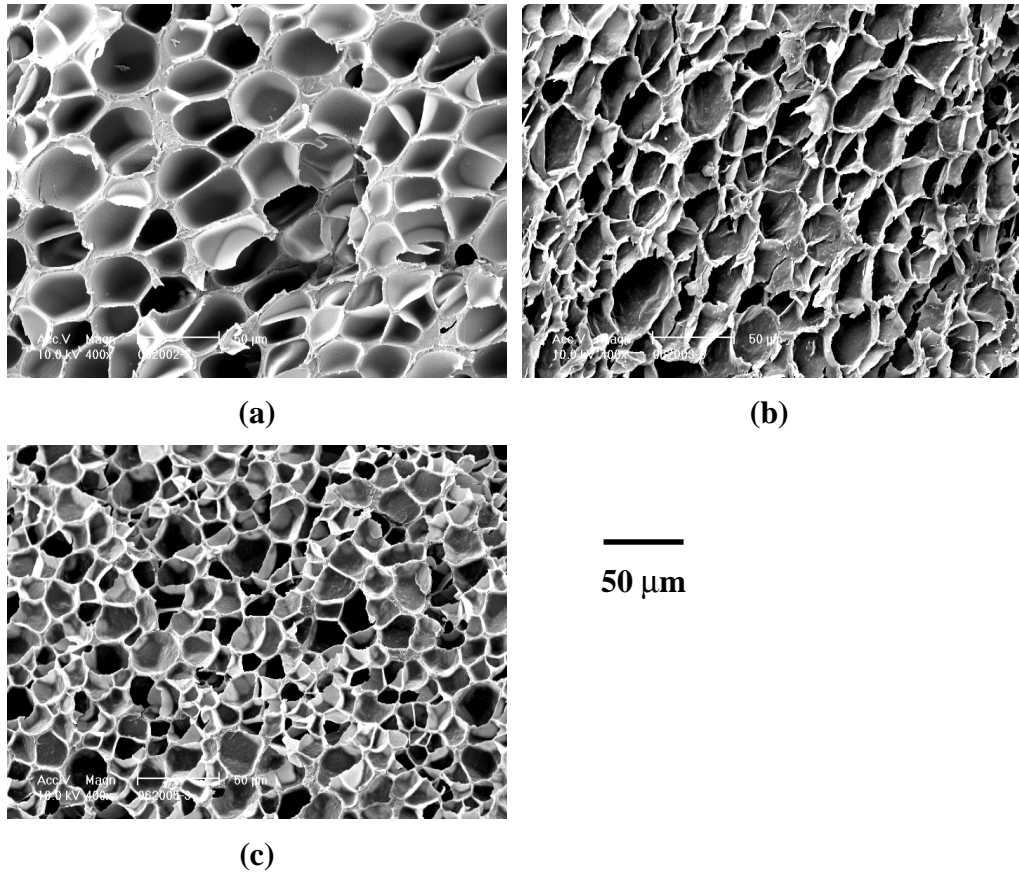


Figure I.1. Batch foaming at 120°C and 2000 psi saturation pressure to determine the effect of nano-clay dispersion on PS nanocomposite foams by using CO<sub>2</sub> as foaming agent: (a) PS, (b) PS/5 wt.% 20A intercalated nanocomposite, and (c) PS/5 wt.% MHABS exfoliated nanocomposite.

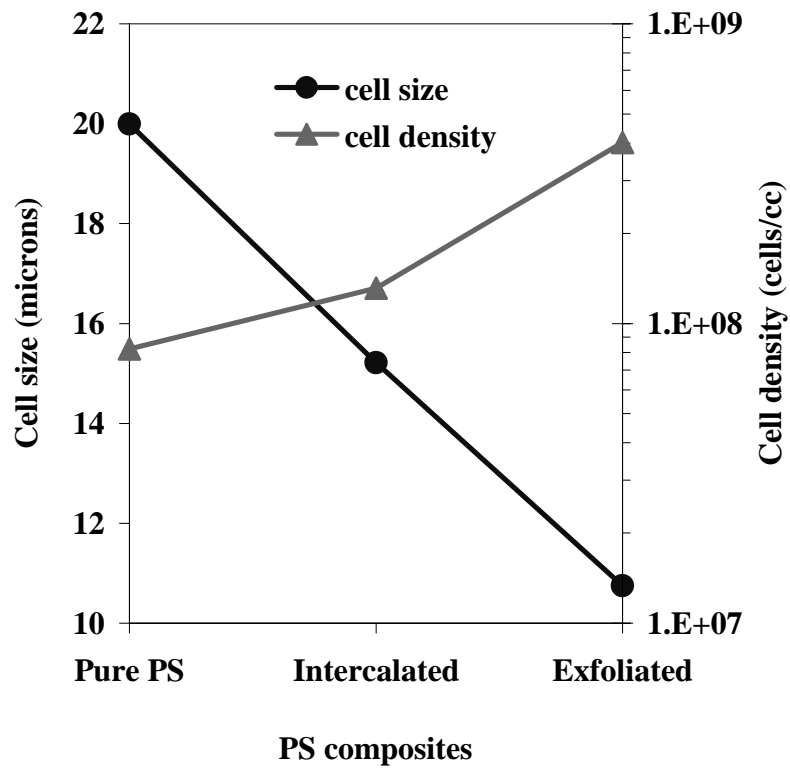


Figure I.2. Cell size and cell density of different PS nanocomposite foams (batch foaming at 120°C and 2000 psi saturation pressure by using CO<sub>2</sub> as foaming agent).

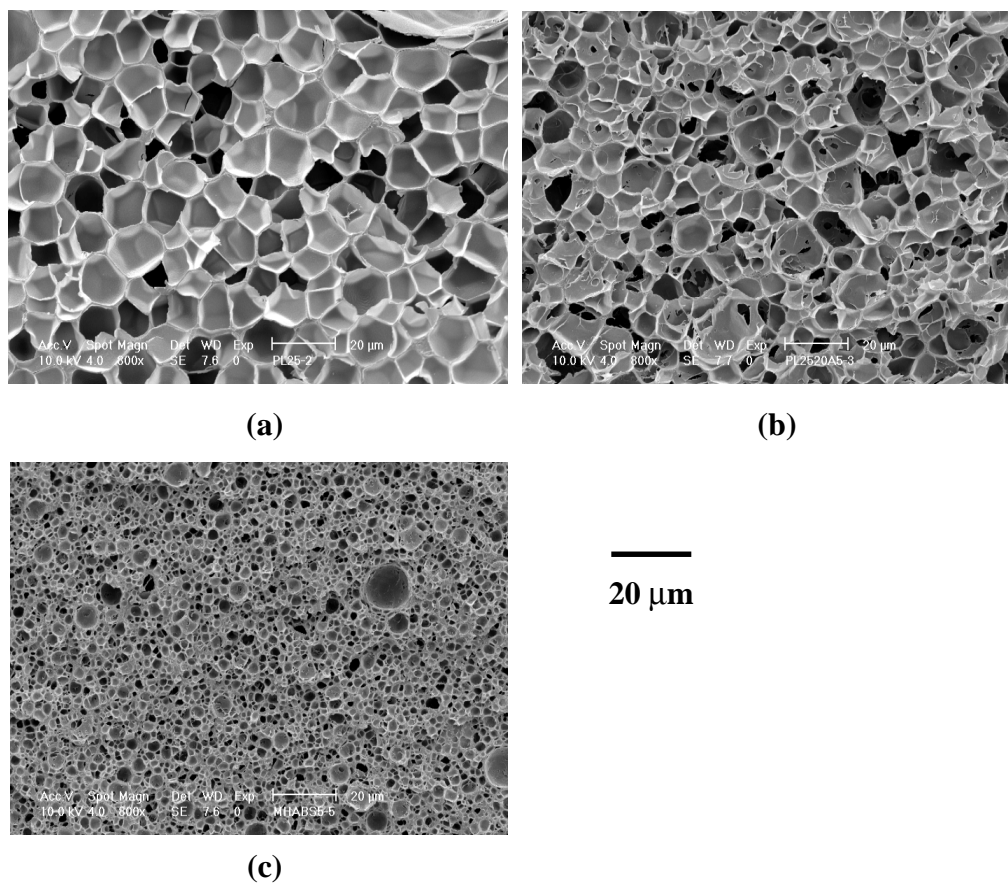


Figure I.3. Batch foaming at 120°C and 2000 psi saturation pressure to determine the effect of nano-clay dispersion on PMMA nanocomposite foams by using CO<sub>2</sub> as foaming agent: (a) PMMA, (b) PMMA/5 wt.% 20A intercalated nanocomposite, and (c) PMMA/5 wt.% MHABS exfoliated nanocomposite.

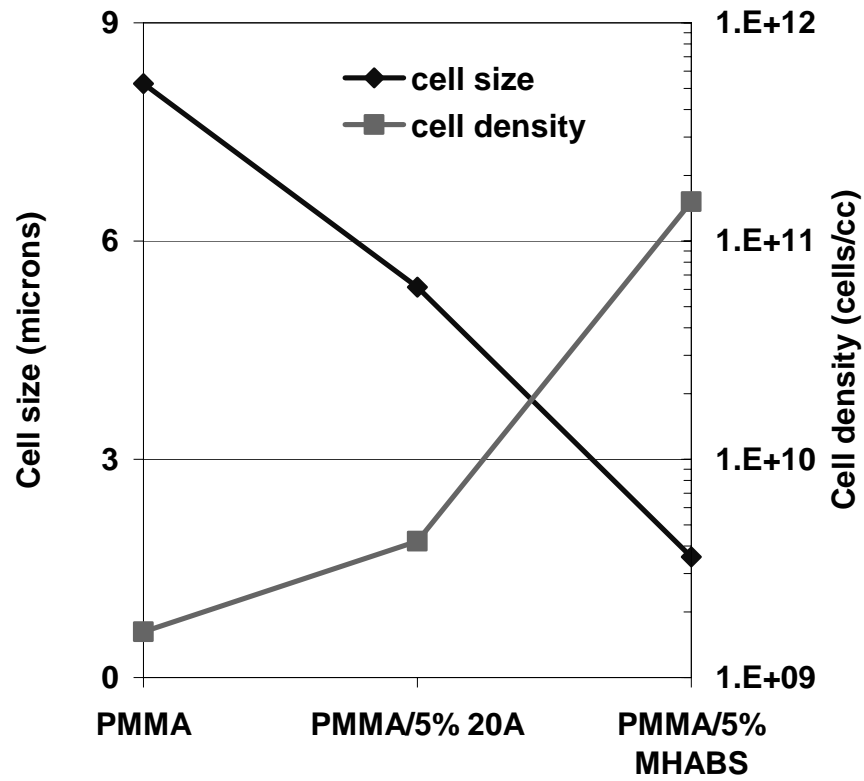


Figure I.4. Cell size and cell density of different PMMA nanocomposite foams (batch foaming at 120°C and 2000 psi saturation pressure by using CO<sub>2</sub> as foaming agent).